A MATHEMATICAL MODEL FOR GAS MIGRATION IN NATURAL AND ENGINEERED BARRIERS FOR RADIOACTIVE WASTE DISPOSAL

ELIAS ERNEST DAGHER

Thesis submitted to the University of Ottawa
in partial Fulfillment of the requirements for the
Doctorate in Philosophy degree in Environmental Engineering

Faculty of Engineering
University of Ottawa

ABOUT THE AUTHOR

Elias. E. Dagher, Ph.D.

Elias is currently pursuing studies in a Ph.D. in Environmental Engineering at the University of Ottawa. His research focuses on studying the migration of gas through bentonite seals and host rock formations which provide containment of nuclear waste in deep geological repositories. Elias had formerly completed a B.ASc in Chemical Engineering, a B.Sc in Biochemistry, and an M.Eng in Environmental Engineering, having completed his project entitled, "Numerical Modelling of Coupled Heat Transfer and Groundwater Flow: Applications to Tailings Management Facility in Permafrost Environments in Northern Canada".

Elias had worked as an Environmental Protection Specialist at the Canadian Nuclear Safety Commission for 8 years, before transitioning to a Geoscience Assessment Officer in 2017. His responsibilities have included assuring compliance through desktop reviews and inspections at regulated nuclear facilities, establishing operational controls on releases to the environment, and formalizing and implementing an environmental protection framework at nuclear facilities. His responsibilities have also included conducting technical assessments of waste water treatment systems and air pollution control technologies at nuclear facilities, conducting dispersion modelling and dose assessments to members of the public, and conducting statistical and geospatial analysis on effluent and environmental monitoring data for a wide-range of applications. As a geoscience assessment officer, Elias has contributed to the review of several safety cases for radioactive waste disposal projects, has participated in international workshops related to geological waste disposal, and is developing the Strategic Research Agenda for Canada's Nuclear Regulator. Elias is also a dispersion specialist in Canada's Nuclear Emergency Operations Center.

ACKNOWLEDGEMENTS

These works are dedicated to the many that supported me along the way. To my supervisors Dr. Julio Ángel Infante Sedano and Dr. Thanh Son Nguyen for helping feed my curiosity, shape my mind, and steer me on this journey. To my CNSC family for their strong belief in me and unwavering support (A. McAllister, K. Sauvé, M. Rinker, P. Thompson, T. Jamieson, P. Elder, R. Jammal). To my family, Lillian (mother), Michel (father), Duve (identical twin brother), and Gaetano (brother), who have forever been my strength and the model for which I've tried to live my life. To my wife Jessica, whose patience and hard work earned this Doctorate alongside me. Finally, a special thanks to my mentor Son, whose relentless and strong push…always in the right direction, guided me throughout. I thank you.

PREFACE

This research has been supported by a contribution from the Canadian Nuclear Safety Commission. This research continues to be, in part, a contribution to Task A of the international working group for the DEvelopment of COupled models and their VALidation against EXperiments (DECOVALEX-2019). This task, led by the British Geological Survey (BGS) and with experimental data provided by the BGS, further attempts to identify the physical HM mechanisms required to adequately model dilatancy-controlled gas migration.

The works presented here are original works by the author with guidance and supervision provided by the author's supervisors Dr. T. S. Nguyen and Dr. J. A. Infante-Sedano. Conceptualization, Dagher and Nguyen; methodology, Dagher and Nguyen; software, Dagher; validation, Dagher, Nguyen and Infante Sedano; verification, Dagher and Nguyen; formal analysis, Dagher; investigation, Dagher and Nguyen; resources, Infante Sedano; data curation, Dagher, Nguyen and Infante Sedano; writing—original draft preparation, Dagher; writing—review and editing, Nguyen and Infante Sedano; visualization, Dagher; supervision, Nguyen and Infante Sedano; project administration, Infante Sedano; funding acquisition, Infante Sedano.

Through the works presented herein, the author seeks an understanding of the processes governing two-phase flow in a swelling geomaterial at critical gas pressures which may exceed the material strength of the soil, and for which dilation and dilation-controlled gas flow is expected to occur. The author investigates a number of processes influencing two-phase flow through a series of original contributions. In the first contribution, the author builds upon the hydro-mechanical mathematical model originally proposed by Nguyen and Le [1], by extending the model to incorporate diffusion and identify the shift from diffusion dominated to advection dominated gas transport. Additionally, the author chooses to adopt Bishop's effective stress principle applying a Chi parameter as described by Khalili and Khabbaz [2]. This provides improved relationship between suction and the AEV for expansive soils. The mathematical model is numerically applied to simulate one dimensional gas flow through near-saturated swelling soil under constant volume boundary condition instead of sedimentary rock.

The second original contribution is through the derivation of steady-state and transient analytical solutions for poregas pressure and displacement of a 1-dimensional gas flow experiment under constant volume boundary condition. Part of the analytical solution was identified as analogous to the analytical solution for transient diffusion through a plane sheet as provided by Crank [3]. Verification of the numerical model in COMSOL Multiphysics® was then performed.

The third original contribution provided by the author is to identify the impact of several processes on two-phase flow, including the influence of material heterogeneity, the Klinkenberg "slip flow" effect, and introduction a swelling strain to facilitate shrinkage of the bentonite under increasing unsaturated conditions.

The fourth original contribution investigates the highly HM coupled nature of this two-phase flow problem, by assessing three different types of mechanical deformation (i.e., plasticity, damage and non-localization) and the resulting effect on two-phase flow. Through model comparison, key features of each model provide further insight into the significant mechanisms controlling two-phase flow. Specific conclusions for future studies have also been synthesized.

ABSTRACT

This work provides a comprehensive assessment into the processes governing two-phase flow in a swelling geomaterial under critical gas pressures whereby the material strength of the soil may be exceeded and for which dilation and dilation-controlled gas flow is expected to occur. The author first provides background on the importance of understanding such processes in the safe geological disposal of radioactive waste. This is followed by a review of experimental studies to describe mechanisms of gas migration processes through natural (host rock formations) and engineered barrier materials, and an evaluation of existing studies that have attempted to numerically model multi-phase flow in expansive soils. Finally, the author provides a literary synthesis of the hydraulic and mechanical behaviour of bentonite clays observed in laboratory experiments under saturated and unsaturated conditions.

The novel contribution of this work is then presented through a series of articles. The author first develops a fully-coupled hydro-mechanical (HM) mathematical model for advective-diffusive visco-capillary controlled two-phase flow through a geomaterial and applies it to simulate a 1-dimensional (1D) flow problem using the Finite Element Method (FEM) commercial code COMSOL Multiphysics®. The model results are compared to experimental data and although several key-features of the experimental results were realized, additional flow mechanisms would be necessary to achieve complete gas breakthrough of the sample.

In the second article, a verification study is performed, whereby analytical solutions for a 1D steady-state and 1D transient gas flow problem under constant volume boundary conditions were derived. Successful verification of the numerical model was completed by comparing the pore-gas pressure evolution and stress evolution to that of the results of the analytical solution, which showed near-perfect agreement.

Building upon the authors original mathematical model, an investigation of enhanced processes and characteristics which may be contributing to dilation-controlled gas flow were conducted. These processes included the introduction of material heterogeneity, consideration of the Klinkenberg "slip flow" effect, and the presence of a swelling strain, and were applied to simulate the same 1D flow problem. The results showed significant improvement over the previous work, including observing complete breakthrough and matching experimental stress evolution. However, the results showed a high degree of gas saturation within the sample and a plug outflow behavior, which were not characteristic of dilation-controlled gas flow.

To further improve the mathematical model, the author conducted a detailed investigation of the highly coupled relationship between mechanical deformation and flow. This included assessing the effect of plasticity, damage, and non-localization to dilation-controlled gas flow, while incorporating the knowledge gained from previous studies. These advanced mathematical models were applied to numerically simulate 1D flow and a 3D spherical flow under constant boundary conditions. Some results demonstrated very good agreement with experimental data and provide further understanding of the processes involved.

The collection of this research provides much needed insight into the possible mechanisms controlling two-phase flow and the capability of continuum models to do so. The intent of this research is to expand the literature further and provide a few steps closer in the development of a robust numerical model that can be used to support long-term safety assessments for radioactive waste disposal, by correctly capturing major features of two-phase flow.

TABLE OF CONTENTS

CHAPTER 1: INTRODUCTION

In a deep geological repository (DGR) for the long-term containment of radioactive waste, gas will be generated through a number of processes including the degradation of organic matter, radioactive decay of the waste (e.g., radon), corrosion of metals producing hydrogen gas (H_2), and the radiolysis of water producing H_2. If production exceeds the containment capacity of the engineered barriers or host rock, a discrete gas phase could migrate through the engineered barriers and/or the host rock. The preferential migration pathway of these radioactive gases might be through the access and ventilation shafts, as these components are typically part of the repository design, and also through the excavation damage zone around those shafts and emplacement rooms. Migration through these pathways could potentially expose people and the environment to radioactivity. Expansive soils, such as bentonite-based materials, are currently the preferred choice of seal materials used for those shafts. Understanding the long-term performance of bentonite/these seals as barriers against gas migration is an important component in the design and long-term safety assessment of a DGR.

This thesis provides a comprehensive assessment into the problem of two-phase flow of both gas and water, in order to provide insight into mechanisms controlling gas migration in low permeability swelling geomaterials. In **Chapter 2**, the author first provides background on the safety features of a deep geological repository for nuclear waste, including the multi-barrier approach, and functions of the engineered barrier system. This is followed by a review of experimental studies that have been published to date to describe mechanisms of gas migration processes through natural (host rock formations) and engineered barrier materials, including substantial evidence supporting the formation of localized preferential flow-pathways and dilation of clay occurring under high gas pressures. The author then provides an evaluation of existing studies that have attempted to numerically model multi-phase flow in expansive soils their successes and limitations in model validation.

Since two phases (gas and fluid) will be present simultaneously in the seal materials, an understanding of unsaturated soil mechanics and an investigation into the behaviour of the bentonite clays, commonly used as seal materials, under saturated and unsaturated conditions is required. This study will further investigate the current research to date that has assessed experimental (laboratory) studies related to the flow and mechanical behaviour of bentonite clays under these conditions. This will include an introduction to bentonite clays and their application in engineering practices, followed by an examination of studies to date that have assessed the soil-water characteristic curve (SWCC) behaviour, swelling behaviour (which makes bentonites so distinguishable amongst clays), swelling pressure and volume change behaviour, shear strength behaviour, and flow behaviour of bentonite clays.

The novel contribution provided by this study is then presented through a series of Chapters where each chapter corresponds to a publication on the subject of the development of a mathematical model to describe two-phase flow. The mathematical model has been developed using a systematic approach with model complexity evolving as the study progresses, in order understand the contribution of different processes to two-phase flow and advanced hydro-mechanical models.

Chapter 3 presents the first paper entitled, "*Development of a mathematical model for gas migration (two-phase flow) in natural and engineered barriers for radioactive waste disposal*", whereby the author develops a fully-coupled hydro-mechanical (HM) linear-elastic mathematical model for advective-diffusive visco-capillary controlled two-phase flow through geomaterials in order to model the first two transport mechanisms proposed by Marschall et al. [4] [5]. The model is based on the theoretical framework of poromechanics, incorporates Darcy's Law for both the porewater and poregas, and a modified Bishop's effective stress principle. Using the Finite Element Method (FEM), a numerical model was used to simulate 1-dimensional (1D) flow through a confined cylindrical sample of near-saturated low-permeable soil under a constant volume boundary stress condition using COMSOL Multiphysics® (COMSOL) FEM software. The results of the numerical model are compared to those from a constant volume 1D flow experiment in order to validate the model. A number of parametric studies are investigated to assess the contribution of advection of poregas, diffusion of dissolved gas in porewater, advection of dissolved gas in porewater, and

inclusion of mechanical deformation (linear elasticity) on flow behaviour with increasing gas pressures over time. Additionally, sensitivity analyses are conducted to gain an understanding of the influence of a number of soil properties on flow behaviour, such as the effect of modifying the air-entry value (AEV), intrinsic permeability, and initial porosity of the soil specimen. Finally, the study investigates the use of a linear elastic damage model to better represent the experimental results.

Chapter 4 presents the findings of the second paper entitled, "*A Mathematical Model of Gas and Water Flow in a Swelling Geomaterial – Part 1. Verification with Analytical Solution*". In this paper, the authors conduct model verification of the numerical model presented in the first paper, in order to provide added confidence that the proposed mathematical model is being correctly implemented in the COMSOL® FEM software. This is performed through the derivation of analytical solutions for a 1D steady-state gas flow and 1D transient gas flow problem under constant volume boundary conditions. Using the FEM, the model is used to simulate 1D flow through a confined cylindrical sample of near-saturated low-permeability soil under a constant volume boundary stress condition. Verification of the numerical model is performed by comparing the pore-gas pressure evolution and stress evolution to that of the results of the analytical solution.

The verification study is followed by its companion paper in **Chapter 5** entitled, "*A Mathematical Model of Gas and Water Flow in a Swelling Geomaterial – Part 2. Process Simulation*". In this third paper the author conducts an analysis of additional processes which may contribute to two-phase flow in a swelling geomaterial. These processes include the introduction of material heterogeneity in both the pore space and permeability of the geomaterial, consideration of the Klinkenberg "slip flow" effect and its effect on an intrinsic gas permeability, and lastly, the presence of a linear swelling strain. Additionally, this paper investigates the formation of gas fingers and the conditions which promote their growth and shrinkage.

Chapter 6 introduces the fourth paper entitled, "*Influence of Stress-Strain Behaviour and Damage on Gas Transport in a Swelling Geomaterial*". In this paper, the authors expand on the previous works through more detailed investigation of the hydromechanical coupling of three mechanisms of mechanical deformation and their effect on two phase flow. These include application of a poro-elastic model with damage, a local poro-elastoplastic model with damage, and a non-local poro-elastoplastic model with damage. These models consider heterogeneity, Klinkenberg effect, and introduction of a non-linear swelling strain. Each model is then compared to experimental data for a 1D flow case and a 3D spherical flow case under constant boundary conditions. In addition, detailed stress path analyses are conducted for each model run in order to provide insight into their capabilities of representing dilation-controlled gas flow.

The collection of this research provides much needed insight into the possible mechanisms controlling two-phase flow and the capability of continuum models to do so. The intent of this research is to expand our knowledge of processes which may contribute to two-phase in the scientific literature and provide a robust numerical model that can be used to support long-term safety assessments for radioactive waste disposal, by correctly capturing major features of two-phase flow.

Full references of each paper are provided below:

1. E. E. Dagher, T. S. Nguyen and J. A. Infante Sedano, "Development of a mathematical model for gas migration (two-phase flow) in natural and engineered barriers for radioactive waste disposal," in *Multiple Roles of Clays in Radioactive Waste Confinement*, S. Norris, E. Neeft and M. Van Geet, Eds., London, Geological Society, Special Publications, 2018.

2. E. E. Dagher, J. A. Infante Sedano and T. S. Nguyen, "A Mathematical Model of Gas and Water Flow in a Swelling Geomaterial - Part 1 - Verification with Analytical Solution," *Minerals (2020)*, vol. 10, no. 1, article 30, 2020.

3. E. E. Dagher, J. A. Infante Sedano and T. S. Nguyen, "A Mathematical Model of Gas and Water Flow in a Swelling Geomaterial - Part 2 - Process Simulation," *Minerals (2020)*, vol. 10, no. 1, article 32, 2020.

4. E. E. Dagher, T. S. Nguyen and J. A. Infante Sedano, "Influence of Stress-Strain Behaviour and Damage on Gas Transport in a Swelling Geomaterial", in Special Publication of International Journal of Rock Mechanics and Mining Sciences, 2020. (submitted)

CHAPTER 2: LITERATURE REVIEW

1. Safety Features of a Deep Geological Repository for Nuclear Waste

1.1. Introduction to nuclear waste in Canada

In Canada, nuclear waste has been generating and accumulating since the 1930s when the Port Radium radium mine began operating in the Northwest Territories [6]. Since then Canada has become a sustainable nuclear country with operating nuclear facilities across the nuclear fuel cycle all producing various forms of radioactive waste. To-date, this waste, in the form of low-, intermediate-, and high-level radioactive waste has been primarily stored on-site of nuclear power plants or in below surface radioactive waste management facilities.

CSA Group standard N292.0-14, *General principles for the management of radioactive waste and irradiated fuel*, provides criteria used to classify radioactive waste. Low-level radioactive waste (LLRW) is comprised mainly of contaminated equipment from the operation of nuclear power plants. This includes protective equipment such as shoe covers and clothing, rags, mops, equipment and tools, and typically loses much of its radioactivity within 300 years. Intermediate-level radioactive waste (ILRW), is typically waste that has been exposed to alpha radiation, or that contains long-lived radionuclides in concentrations that require isolation and containment for a timeframe of over several hundred years. High-level radioactive waste (HLRW) consists of used nuclear fuel that has been declared as radioactive waste and generates significant heat via radioactive decay [7].

The Low-Level Radioactive Waste Management Office (LLRWMO), estimated that by the end of 2050 there would be more than 2.6 million m^3 of radioactive waste requiring long-term management, and the bulk of radioactive waste is LLRW. **Table 1** below provides waste inventory estimates by the end of 2011 and by the end of 2050.

Table 1. Waste Inventory Projections to 2011 and 2050 (adapted from LLRWMO, 2012)

Waste Category	Waste Inventory to the End of 2011	Waste Inventory to the End of 2050
High-Level Radioactive Waste (Nuclear Fuel Waste)	9,400 m3	20,000 m3
Intermediate-Level Radioactive Waste	33,400 m3	67,000 m3
Low-Level Radioactive Waste	2,343,000 m3	2,594,000 m3

Under the Nuclear Safety and Control Act (NSCA), the Canadian Nuclear Safety Commission (CNSC) was established to regulate nuclear activity in Canada. As part of its mandate, the CNSC was made responsible for ensuring the health and safety of the public and the environment through its regulation of nuclear facilities, which includes ensuring waste producers are managing their waste in a safe and responsible manner [8].

Although earlier programs existed [9], in 2002, to address the long-term management of Canada's nuclear fuel waste, the Nuclear Fuel Waste Act (NFWA) came into force. The NFWA outlined various responsibilities of the federal government and nuclear fuel waste owners, and resulted in the formation of the Nuclear Waste Management Organization (NWMO) as the responsible authority for managing Canada's long-term nuclear fuel waste management activities [10]. In 2007, the NWMO recommended that the Adaptive Phased Management (APM) approach be applied for the long-term management of nuclear fuel waste in Canada. The APM approach, is a phased management approach to identify a suitable site and design for the containment and isolation of the high-level radioactive waste in a deep geological repository (DGR) [11].

Since 2007, a DGR has been proposed by Ontario Power Generation (OPG), for the long-term management of low- and intermediate-level radioactive wastes. The project had gone through an Environmental Assessment, with public hearings taking place in 2013 and 2014. Currently no decision has been made by the Minister of the Environment to approve the project moving forward [12]. However, if the proposal is accepted, the CNSCs licensing process would need to ensure that OPG can design and implement a DGR for the long-term management of the waste in a manner that is safe and will protect the public and the environment for futures to come.

The concept of a DGR for the containment and isolation of radioactive waste is considered in many countries, including Canada, as the most viable method for the long-term management of the waste. Countries such as Finland, Sweden, France, Russia, and Germany are amongst those furthest along in the development of their national deep geological disposal programs for high-level radioactive waste. In identifying a long-term solution to manage the global radioactive waste, the international community, including Canada, have been assessing the technical practicability of a DGR for its long-term management. The primary purpose of a DGR is to contain and isolate wastes to minimize impact to the environment and radiological exposure to people. Since the 1990s, nuclear regulators, waste producers, responsible organizations, and academics across the international community have been exploring the use of a DGR for the long-term disposal and containment of nuclear wastes.

One such international collaboration is the DECOVALEX (DEvelopment of COupled models and their VALidation against Experiments) project. DECOVALEX, established in 1992, is an international research and model comparison collaboration, used to advance the understanding and modeling of various coupled thermo-hydro-mechanical-chemical (THMC) processes in geological systems [13]. Through their development, model performance is validated against the results of laboratory and field studies. This study is in part, in support to the work currently being done in DECOVALEX-2019.

1.2. A multi-barrier approach: natural and engineered barriers

The concept of defense-in-depth is one major safety principle that has been incorporated in the design of nuclear power plants. Similarly, this concept also exists within the design of a geological repository for the long-term disposal of radioactive waste. In the design of a DGR the use of a multi-barrier system or approach is considered [14, 15, 16].

The multi-barrier system consists of the natural barrier system, which consists of the host rock and subsurface environment, and the engineered barrier system which consists of the waste form itself, the waste package or canister, buffer materials, backfill and seals [16]. Each barrier component provides a 'safety function', which is a means for retaining and retarding the migration of radionuclides from the waste source [9].

1.3. Engineered barriers: bentonite seal and buffer

Of particular interest in this study, is the sealing and buffer materials being considered as part of the engineered barrier system design. Sellin and Leupin [9], conducted a detailed review of engineered barrier systems with a focus on swelling or expansive clays. From their review they described a number of desirable properties of the buffer material, which include having i) low hydraulic permeability/conductivity, ii) a self-sealing ability, and iii) durability of properties over the very long-term [9].

An important component of the engineered barrier is the buffer and seal. Their primary safety functions are to limit the transport of dissolved species to the canister that could cause the canister to corrode (i.e., chemical and/or biological activity), to prevent potential radionuclide release from a damaged canister, and to prevent advective transport of radionuclides in the near-field [9, 16]. In light of this, the

hydraulic conductivity of the buffer and sealing material should be low enough to ensure that diffusion is the dominant transport mechanism.

Much research since the early 1990s has focused on identifying a suitable material for the sealant and buffer. Swelling/expansive clays are being considered for use as a barrier material in nearly all countries [9]. Expansive clays such as bentonite have all three of the above safety functions. Bentonite, a montmorillonite-rich clay, has been studied extensively as a suitable buffer and sealant material due to its many favorable physical properties. These suitable properties will be described further in Section 3.

2. Multi-Phase Flow in Low Permeability Materials

2.1. Gas generation, migration and potential impacts to humans and the environment

The primary purpose of a DGR is to contain and isolate the wastes deep inside a suitable rock formation to ensure that no significant quantities of radioactivity would reach the surface environment [1]. If the migration of radionuclides from the waste source to the surface occurred, there could be potential impacts to human health and other ecological and non-ecological receptors as a result of the exposure to these radionuclides. Therefore, it is necessary to ensure future exposures to radioactivity are minimized.

To adequately develop a safety case for a DGR, consideration must be given to the relevant features, events, and processes (FEPs), and their impact on the primary objectives of a DGR [17, 18]. One such process with the potential means for radiological exposure to the biosphere is the generation of a significant amount of radioactive gas over time, which may migrate to the surface [19]. Gas could be generated through a number of processes including the degradation of organic matter, radioactive decay of the waste, corrosion of metals producing hydrogen gas (H_2), and the radiolysis of water producing H_2 [20, 21, 19].

If production exceeds the containment capacity of the engineered barriers or host rock, a discrete gas phase could form and these gases could migrate through the engineered barriers and/or the host rock [22, 9]. This gas will continue to accumulate over hundreds of years resulting in a build-up of gas pressure within the engineered and natural barriers. The preferential migration pathway of these radioactive gases, to potentially expose people and the environment to radioactivity, might be through the access and ventilation shafts and the excavation damage zones around the shafts, emplacement rooms and galleries of a DGR.

In recent years, a number of international projects have focused on the topics of gas generation and migration. In Europe, the Fate Of Repository GasEs (FORGE) project was undertaken to address key research areas on gas generation and migration, in order to better ascertain the mechanisms of each, and to support the safety case for a DGR [23, 19]. As part of the FORGE project, the Large scale gas injection test (Lasgit) was designed to study the impact of gas build-up and migration through an engineered barrier system (EBS) [23, 24].

2.2. Experimental studies on gas migration processes

Expansive or swelling soils, such as bentonite-based materials, are currently the preferred choice of seal materials used for an EBS. Understanding the long-term performance of these seals as barriers against gas migration is an important component in the design and long-term safety assessment of a DGR. The results of an increasing number of laboratory experiments have been published to try to explain the mechanisms involved in gas migration in natural and engineered barriers for radioactive waste. However, the current understanding of the mechanisms of gas migration in expansive clays are still not fully realized. Furthermore, as a result of the uncertainties in our current understanding, few studies have been able to model the experimental results.

An investigation of the gas transport processes in low-permeability clay material was described by Marschall et al. [5], and further investigated by Cuss et al. [20]. Marschall et al. [5] recognized that gas

transport through a porous medium is controlled by a number of the medium's hydraulic and mechanical characteristics such as the intrinsic permeability, porosity, and material strength. They identified the importance of the hydro-mechanical state of the rock or soil media (i.e., water saturation, porewater pressure, and stress state) and the gas pressure at focal points which could lead to microfracturing [5]. Marschall et al. [5], divided the basic transport mechanisms into four processes.

In the first process, the advective-diffusive transport of gas dissolved in the porewater is governed by Darcy's law for advective groundwater flow, Fick's law for the diffusion of dissolved gas due to concentration gradients in the porewater, and Henry's law which describes the solubility of gas in the porewater.

The second process of visco-capillary two-phase flow is related to the viscous and capillary forces (i.e., matric suction) which describe the underlying principles of unsaturated soil mechanics. Soil properties influencing this transport process are the porosity and soil compressibility. The air-entry value (AEV) or gas-entry pressure, which is the value of matric suction that must be exceeded before air recedes into the soil pores, is a controlling factor in this transport mechanism of two-phase flow. It is also a measure of the maximum pore-size in a soil, as water will migrate from and gas will enter through the largest pores first.

The third process is termed dilatancy-controlled gas flow. A wealth of laboratory and field-scale experimental studies have investigated gas transport processes through natural (host rock) and engineered barriers. These studies have provided considerable evidence suggesting that gas flow at gas pressures above a reference level is accompanied by the creation of pressure-induced preferential pathways and dilation of the clay, yet have not been able to determine the exact mechanisms which control gas entry, flow, and pathway sealing [25, 22, 26, 27, 28, 20, 23, 29].

Marschall et al. [5]., described this primary transport mechanism as dilatancy-controlled gas flow or "pathway dilation" and identified it as an important transport mechanism in clay soil or clay-rich rock with low tensile-strength. Dilatancy will occur when the gas pressure reaches a reference stress level acting on the clay medium, forcing the clay particles to align in a dispersed orientation, and resulting in the formation of microfractures accompanied by an increase in plastic deformation [30]. As a result, gas flow along these microfractures will be promoted due to the increased pore space. The presence of microfractures therefore leads to an increase in the intrinsic permeability of the material and in turn results in changes in the relationship between the capillary pressure (i.e., matric suction) and degree of saturation (i.e., Soil-Water Characteristic Curve (SWCC) of the material). As a result of dilatency-controlled gas flow, transport properties are now dependent on the stress-state and state of deformation of the soil.

Finally, gas transport along macroscopic fractures, also known as hydro- and gas-fracturing, becomes a significant transport mechanism when a macroscopic tensile fracture occurs. Unlike the formation of microfractures that result in dilatancy, these macroscopic fractures develop in low-tensile strength material when gas pressure build-up is rapid and becomes larger than the sum of the minimum principal stress and the tensile strength of the material (i.e., porewater displacement and formation of microfractures can no longer counter balance the gas production rate) [5].

Other considerations when conceptualizing the physical processes taking place during two-phase flow through a porous medium is the phenomena of viscous or gas fingering. The phenomena of gas fingering results from differences in the fluid viscosity of the liquid phase and of the gas phase. In these cases, the mobility ratio, M (generally the ratio of gas and liquid viscosities), between the gas phase and the liquid phase is less than one ($M < 1$) [31]. Since movement of the gas front is faster than the liquid front this will result in a displacement front (i.e., gas front is further than the liquid front). In a porous medium the gas front may result in the formation of gas 'fingers' [31].

As stated by Sahimi et al. (2006) a number of factors contribute to the effect of gas fingering. These include the displacement rate of the gas with the liquid, the heterogeneity of the porous medium and spatial variations of the porosity and permeability, the viscosity ratio between the gas and liquid, three-

dimensional dispersion within the porous medium, and the aspect ratio and boundary conditions representing the narrowness of the porous medium.

2.3. Modelling of multi-phase flow in radioactive waste disposal

In 1999, Rodwell et al. stated "there are few problems in geoscience more complex than the quantitative prediction of gas migration fluxes through an argillaceous rock formation" [32]. A number of studies have attempted to model gas migration in natural or engineered barrier systems. In 1998 the results of Phase 1 of the GAMBIT Club programme were published. Nash et al. [33] applied the theory of linear elastic fracture mechanics to develop a model of crack propagation through the clay. In this model, a continuous gas flow was applied to one face of the sample, and once gas breakthrough occurred, gas would flow through the sample and the dilation of gas pathways would be pore-gas pressure dependent. Phase 1 saw difficulties obtaining agreement between simulation and experimental results over the whole test sequence [33].

Phases 2 and 3 of the GAMBIT Club program further explored the refinement and extension of their earlier models, including the investigation of clay fabric effects (i.e., distinction between inter- and intra-stack pore space) and how to treat hysteresis effects [34]. Hoch et al. [34] examined results with three basic mechanisms that could describe flow i) gas flow governed by conventional concepts of capillary pressure and relative permeability, ii) microfissuring (dilation) of the clay, iii) macroscopic fracturing of the clay. However, these authors did not provide a unique explanation of the results in terms of the above mechanisms. They concluded that the current uncertainties associated with understanding the transport mechanisms, made it considerably difficult to establish an adequate model for gas migration [34]. The report also concluded that any further development of models of gas migration in bentonite will depend on obtaining better characterization of gas pathways as well as the couplings that exist in the clay between stress and strain, gas and water fluid pressures, and gas-filled porosity [34].

Fall et al. [35] developed a coupled hydro-mechanical model for simulating gas migration in host sedimentary rocks for nuclear waste repositories. Their study identified that high gas pressure can lead to mechanical damage and the formation of micro-cracks [35]. Their model was limited in part because they did not consider the elasto-plastic mechanical behaviour of the rock. Nguyen and Le [1] developed a mathematical model for gas migration in Opalinus clay. The inherent anisotropy due to bedding, and the elasto-plastic behaviour of the clay was considered in the model. The model was successfully validated against laboratory experiments and field gas injection tests, especially up to the dilatancy controlled flow phase. However, it was recognized that the last phase of gas flow controlled by macro-fractures needed further understanding.

In 2015, the Geological Society of London, published Special Publication 415 - entitled, *Gas Generation and Migration in Deep Geological Radioactive Waste Repositories*. This publication presented current research to date on experimental studies on gas migration and the development of models to describe gas behaviour in several systems of a DGR [19]. However, there is still much work to be done to understand the basic mechanisms and processes of two-phase flow, particularly dilatancy controlled gas flow through low-permeability swelling soils over the life-time of the repository. In doing so, the development of mathematical relations describing these processes is imperative, along with the development of suitable numerical models which can be used to support the design and long-term safety assessment of a DGR.

3. Physical Behaviours of Bentonite Clays under Saturated and Unsaturated Conditions

3.1. Applications of bentonite clays

Bentonite is montmorillonite-rich clay that has garnered attention in the international community for its use in various engineering applications [36, 37]. For geo-environmental practices, these applications

include as liner and cap systems in industrial and municipal landfill designs to reduce infiltration and protect groundwater, and as liners around contaminated sites which could be used to facilitate the removal of metal ions and improve the bio-availability of contaminated soils and ponds [37].

A significant amount of effort has gone into understanding the behaviour of bentonites in the application of engineered barriers, and more specifically, as a sealant for use in the deep geological disposal of radioactive wastes [38, 39, 36, 40]. The applications being considered in these long-term repositories include plugging of borehole, shaft and tunnel, sealing rock fractures, and the sealing of canisters containing radioactive waste [38, 36, 37, 1].

Before one can und understand the behaviour of bentonite as an engineered buffer material for a repository for nuclear waste, taking into account various site-specific conditions, a general understanding of its properties and behaviour under saturated and unsaturated conditions is required. Determination of the changes in water content, void ratio, the degree of saturation, and the effects of temperature on soil suction are necessary for quantitative assessments of volume change behaviour, hydraulic conductivity, the ion retention capacity, and the shear strength of unsaturated soils [41, 42, 43, 37]. This section provides a brief, non-extensive literature review of bentonite behaviour under saturated and unsaturated conditions, with a focus on those features (mainly hydraulic and mechanical) that are most relevant to this thesis.

3.2. Physical and chemical properties

Three studies conducted by Börgesson et al. [42], Ye et al. [44] and Tripathy et al. [37], examined the flow and/or mechanical behaviours of bentonite clays under unsaturated conditions. The physical and chemical properties of the bentonites were also examined, which include determining the grain size distribution of the clays, the montmorillonite content, the specific gravity of the soil and additional properties, which give bentonites their unique behaviours.

Börgesson et al. [42] conducted a number of laboratory tests performend on bentonite OT-9607, a natural sodium bentonite with grain sizes between 0.1 and 2 mm and a montmorillonite content of approximately 46% to assess the effects of temperature on various properties of bentonite OT-9607.

Ye et al. [44] investigated effects of temperature on SWCCs and unsaturated hydraulic conductivities under confined conditions, whereby temperature effects influence viscosity, density of water, and permeability. In their study, Gaomiaozi bentonite (GMZ01) from China was used with a dry density 1.7 g/cm^3 and a montmorillonite content of 75.4%.

Tripathy et al. [37] assessed the properties of three clays: sodium based American MX80 bentonite (65-82% montmorillonite content) [45], calcium based Greek Yellow bentonite, and British Speswhite kaolin (primarily composed of kaolinite) under unsaturated conditions. Properties of the two bentonites are provided in **Table 2**.

Table 2. Properties of two bentonite clays (MX80 and Yellow Bentonite) and Speswhite kaolin (adapted from Tripathy et al. (2014))

Properties	MX80 bentonite	Yellow bentonite	Speswhite kaolin
Specific gravity of soil solids, G_s	2.8	2.84	2.61
Liquid limit, w_L (%)	437	135	51.4
Plastic limit, w_P (%)	63	58	32
Shrinkage limit, w_S (%)	12.2	13.6	26.5
Specific surface area, S (m^2/g)	676	797	10
Cation exchange capacity (CEC), B (meq/100 g)	90.31	84.91	3.18

Na^{+}	51.24	7.66	1.06
Ca^{+2}	28.24	63.42	1.09
Mg^{+2}	9.43	12.97	0.66
K^{+}	1.4	0.86	0.37
Weighted average valence of exchangeable cations	1.42	1.9	1.55
Grain-size distribution (%)			
<75 μm	100	100	100
<2 μm	96.4	97.18	97.92

The primary differences between bentonites are the montmorillonite content and Cation Exchange Capacity (CEC), which is the number of exchangeable cations per dry weight, and is a measure of the soil fertility, nutrient retention capacity, and capacity to protect groundwater from cation contamination. These differences impact other properties of the soil including the liquid limit, w_L, which is the water content at which the behaviour of the soil chang-es from that of a soil to that of a liquid.

3.3. Soil-water retention characteristics

To assess the effects of temperature on the soil water retention characteristics, Börgesson et al. [42] measured the suction vs water content of the bentonite under both drying and wetting conditions using thermocouple psychrometers and measuring the relative humidity in the small air filled part of the chamber to calculate the suction. Their results showed that the effect of temperature on the soil water characteristic curve (SWCC) was small, and provided some insight to the water retention behaviour of bentonite.

Ye et al. [44] produced SWCCs for GMZ01 at temperatures of 20°C, 40°C, and 60°C. Similar to Börgesson et al. [42], their results showed that the effects of temperature was small, but that the water retention capacity decreases as temperature increases.

Tripathy et al. [37] assessed SWCC of three clays: MX80 bentonite, Yellow bentonite, and Speswhite kaolin (primarily composed of kaolinite) using three different techniques: axis-translation (pressure plate), vapour equilibrium (dessicator), and osmotic suction techniques. The axis-translation and vapour equilibrium techniques were used to measure the suction at levels from 0 to 1500 kPa, and from approximately 1000 to 300,000 kPa respectively, while the osmotic suction technique was used to compare its agreement to the pressure plate results. Good agreement between the techniques were obtained. The results and corresponding SWCC are provided by the author [37].

As it is more difficult to identify the Air-Entry Values (AEVs) from a water content vs suction SWCCs, Tripathy et al. [37] used the results of Clod tests, that were conducted to identify the shrinkage paths of the bentonite clays along with the SWCC, to determine the SWCCs in the form of suction vs degree of saturation. This allowed for the distinct identification of the AEVs of each clay. From the authors results, the AEVs of the two bentonite clays were 100 MPa compared to kaolinite clay at 0.700 MPa, demonstrating the high storage capacity of bentonites.

3.4. Flow behaviour

A number of physical properties make bentonite very suitable as a sealant. With respect to flow behaviour, the hydraulic conductivity of bentonite clays or clays rich in montmorillonite at low bulk densities has been shown to be lower compared to kaolinite or hydrous mica ("illite") clays, and at higher bulk densities bentonite clay is almost impermeable [38].

Pusch et al. [38] provided values of the hydraulic conductivity under saturated conditions for montmorillonite, hydrous mica, and kaolinite clays as a function of void ratio and bulk density. As

indicated from the figure, montmorillonite rich clays when highly compacted (bulk densities of 2.4 g/cm^3), will have hydraulic conductivity as low as 10^{-14} m/s with a void ratio of 0.2.

Börgesson et al. [42] examined the hydraulic conductivity of the bentonite OT-9607. To measure the hydarulic conductivity, they exposed the saturated buffer material to hydraulic gradient of 16,000 at three different temperatures, 25, 60, and 90°C, and determined that the influence of temperature is related to the change in viscosity of the water, while the intrinsic permeability remains constant. Their results yielded a hydraulic conductivity off 3.3×10^{-13} m/s at 60℃ [42].

Ye et al. [44] studied the effects of temperature on the hydraulic conductivity. In their study, they observed that at the onset of hydration of the sample, there was a slight decrease in the hydraulic conductivity, which approached a constant value as hydration continued. This was followed by a rapid increase in hydraulic conductivity as saturation approached. They noted that this rapid increase as it approached could be a result of changes in the soil microstructure.

3.5. Swelling/self-healing behaviour

The primary mechanical characteristics of bentonite, and its most fascinating property in the application as a buffer in the storage of radioactive wastes, is its ability to swell when it encounters water. Bentonite clays are generally applied as a highly compacted and dry granulated bentonite powder. As they take in water from their surrounding environment, they begin to swell (i.e., expansive clay) and form tight contact with the host rock and any other material, such as canisters storing radioactive waste [38]. Under saturated conditions, the effective stresses and pore-water pressures within the bentonite will reach equilibrium, and the resulting bentonite will have a very low hydraulic conductivity and a low ion diffusivity [38].

Furthermore, as a result of the swelling properties of bentonite, when densely compacted the clay has the ability to self-heal [38]. This phenomena was observed by Oscarson et al. [46], who examined the permeability and diffusivity of defected compacted bentonite plugs and noted that if cracked, compacted bentonite will swell and seal the cracks under the presence of water [38, 46, 47, 36].

Conceptually, in its use as a buffer material, as heat is generated, bentonite clay buffer will shrink and dry. Stresses will change and cracks or fractures may form. This will lead water infiltration from the host rock along the preferential flow channels and result in resaturation, swelling, and self-healing of the bentonite buffer [16].

In Madsen's [47] investigation of bentonite as a protective barrier for the safe storage of radioactive waste, Madsen observed that due to its swelling capacity (i.e., ability to self-heal) and low water-permeability, "bentonite forms a mechanical, hydraulic, and chemical protection zone (buffer zone) around emplaced waste canisters…and as a result, no convective water flow occurs." He concluded that the only potential for radionuclide transport following failure of the canisters would be through ion diffusion in stagnant pore-water until the diffusion front had crossed the bentonite layer, and that by the time significant concentrations of radionuclides had made it to the ground surface, long-lived radionuclides would have already decayed [47]. In addition to the mechanical, hydraulic, and chemical barrier provided because of it's swelling capacity, the same swelling nature of bentonite has been observed to reduce the potential for microbial activity in compacted bentonite clays, acting as a barrier from biological processes [48].

Börgesson et al. [42] examined the shrinkage of bentonite OT-9607, a Japanese bentonite, during the drying process, by measuring the volume of a number of compacted samples with different intitial water contents before and after drying at 110°C for 24 hours, and plotting the results in terms of volume before drying and volume after drying as a function of the initial water content. The results provided some insight to the shrinkage and potential swelling property of bentonite, whereby at desaturation a volume change of approximately 6% was identified.

Tripathy et al. [37], plotted void ratio as a function of suction for MX-80 bentonite, Yellow bentonite, and Speswhite kaolin. The characteristic behaviour of MX-80 bentonite was as expeceted, whereby a rapid decrease in the void ratio as suction increases was observed.

3.6. Swelling pressure behaviour

If confined to a constant volume and not allowed to swell, pressure within the bentonite clay, termed "swelling pressure" will develop during wetting [42]. Börgesson et al. [42] conducted swelling pressure tests, whereby samples of bentonite OT-9607 with an average dry density of 1.65 g/cm^3 were saturated with distilled water at one end, and swelling pressure was measured at the top using a load cell. A water pressure of 100 kPa was applied to the filter during the test. The results showed that a full swelling pressure of approximately 900 kPa was reached in about 60 days, with the largest increase in swelling pressure from 0 kPa to 600 kPa occuring within the first 5 days. As observed by the authors results, the swelling pressure is quite substantial. An understanding of the swelling pressure will therefore be necessary in the assessment of bentonite as a sealant for a DGR.

3.7. Shear strength and volume change behaviour

In the study conducted by Börgesson et al. [42], shear strength properties of saturated bentonite under undrained compression using triaxial tests were obtained. Under these conditions an increase in shear strength was observed (indicated by an increase in deviaotric stress), with an increase in the mean effective stress.

Since the primary application of interest is the long-term integrity of the bentonite seal in order to act as a long-term barrier for the migration radioactive gases, it is important to understand the shear strength behaviour under various stresses, which can be interpreted using a slow consolidated drained test. During the investigation of this paper, few studies could be found assessing the shear strength and volume change behaviour of bentonite under saturated and unsaturated conditions.

A study conducted by Seiphoori et al. [49] used an advanced double-wall cell triaxial test to characterize the thermo-hydro-mechanical behaviour of compacted granular MX-80 bentonite. This form of bentonite is a candidate buffer material in nuclear repository in Switzerland and many other countries. In the study, drained triaxial compression tests were performed on saturated and unsaturated MX-80 bentonite that were compacted at varying water contents and at a target dry density of 1.5 g/cm^3 [49].

The study assessed the volume change and shear strength behaviour at various suction values. With respect to the volume change behaviour, Seiphoori et al. [49] observed that for the unsaturated samples, there was a decrease in the compressibility with an increase in soil suction. The study also showed the influence of suction on shear strength, whereby an increase in strength (as indicated by the deviatoric stress) was observed with an increase in suction [49].

3.8. Overall behaviour of bentonite based geomaterials

The experimental results from the literature confirm that bentonite has ideal properties which make it suitable for use in various industrial applications, including in the use as a sealant and barrier against the migration of radioactive gases in the design of a DGR for nuclear wastes. In addition to the selected studies described above, there has been a wealth of information on the thermal, hydraulic and mechanical properties of bentonite that has come out of the Full-scale Engineered Barriers Experiment (FEBEX) [50].

CHAPTER 3: DEVELOPMENT OF A MATHEMATICAL MODEL FOR GAS MIGRATION (TWO-PHASE FLOW) IN NATURAL AND ENGINEERED BARRIERS FOR RADIOACTIVE WASTE DISPOSAL

Article

Development of a Mathematical Model for Gas Migration (Two-phase flow) in Natural and Engineered Barriers for Radioactive Waste Disposal

Elias Ernest Dagher [1,2], Thanh Son Nguyen [1,2] and Julio Ángel Infante Sedano [2,*]

[1] Canadian Nuclear Safety Commission (CNSC), Ottawa, ON, K1P 5S9, Canada;
[2] Department of Civil Engineering, University of Ottawa, Ottawa, ON K1N 6N5, Canada; e-mail@e-mail.com
* Correspondence: jinfante@uottawa.ca

Received: date; Accepted: date; Published: date

A Mathematical Model for Gas Migration (Two-phase Flow)

Abstract: In a deep geological repository (DGR) for the long-term containment of radioactive waste, gases could be generated through a number of processes. If gas production exceeds the containment capacity of the engineered barriers or host rock, these gases could migrate through these barriers and potentially expose people and the environment to radioactivity. Expansive soils, such as bentonite-based materials, are currently the preferred choice of seal materials. Understanding the long-term performance of these seals as barriers against gas migration is an important component in the design and long-term safety assessment of a DGR. This study proposes a hydro-mechanical linear poro-elastic visco-capillary mathematical model for advective-diffusive controlled two-phase flow through a low-permeability expansive soil. It is based on the theoretical framework of poromechanics, incorporates Darcy's Law for both the porewater and poregas, and a modified Bishop's effective stress principle. Using the Finite Element Method (FEM), the model was used to numerically simulate 1D flow through a low-permeability expansive soil. The results were verified against experimental results found in the current literature. Parametric studies were performed to determine the influence on the flow behaviour. Based on the results, the mathematical model looks promising and will be improved to model flow through preferential pathways.

Keywords: THMC modelling; model verification, multi-phase flow; gas migration; nuclear waste disposal; bentonite, expansive soils, swelling soils, swelling geomaterials

1. Introduction

In Canada, nuclear waste has been generating and accumulating since the 1930s when the Port Radium radium mine began operating in the Northwest Territories [50]. Since then Canada has become a sustainable nuclear country with operating nuclear facilities across the nuclear fuel cycle all producing various forms of radioactive waste. To-date, this waste, in the form of low-, intermediate-, and high-level radioactive waste has been primarily stored on-site of nuclear power plants or in below surface radioactive waste management facilities.

The Low-Level Radioactive Waste Management Office (LLRWMO), estimated that by the end of 2050 there would be more than 2.6 million m^3 of radioactive waste requiring long-term management in Canada,

the bulk of which is low-level radioactive waste. **Table 1** below provides waste inventory estimates by the end of 2011 and by the end of 2050.

Table 1. Canadian Waste Inventory Projections to 2011 and 2050 (adapted from LLRWMO, 2012)

Waste Category	Waste Inventory to the End of 2011	Waste Inventory to the End of 2050
High-Level Radioactive Waste (Nuclear Fuel Waste)	9 400 m^3	20 000 m^3
Intermediate-Level Radioactive Waste	33 400 m^3	67 000 m^3
Low-Level Radioactive Waste	2 343 000 m^3	2 594 000 m^3

In identifying a long-term solution to manage the global radioactive waste, the international community, including Canada, have been assessing the technical practicability of a Deep Geological Repository (DGR) for its long-term management. The primary purpose of a DGR is to contain and isolate wastes to minimize impact to the environment and radiological exposure to people.

To adequately design a safety case for a DGR, consideration must be given to the relevant features, events, and processes (FEPs), and their impact on the primary objectives of a DGR [17, 18]. One such process with the potential means for radiological exposure to the biosphere is the generation of radioactive gas which may migrate to the surface [19]. Gas could be generated through a number of processes including the degradation of organic matter, radioactive decay of the waste, corrosion of metals producing hydrogen gas (H_2), and the radiolysis of water producing H_2 [20, 21, 19]. If production exceeds the containment capacity of the engineered barriers or host rock, these gases could migrate through the engineered barriers and/or the host rock [22, 9]. The preferential migration pathway of these radioactive gases, to potentially expose people and the environment to radioactivity, might be through the access and ventilation shafts; as these components are typically part of the repository design.

In recent years, a number of international projects have focused on the topics of gas generation and migration. In Europe, the Fate Of Repository GasEs (FORGE) project was undertaken to address key research areas on gas generation and migration, in order to better ascertain the mechanisms of each, and to support the safety case for DGR [24, 23]. As part of the FORGE project, the Large scale gas injection test (Lasgit) was designed to study the impact of gas build-up and migration through an engineered barrier system (EBS) [23, 24].

Expansive or swelling soils, such as bentonite-based materials, are currently the preferred choice of seal materials used for an EBS. Understanding the long-term performance of these seals as barriers against gas migration is an important component in the design and long-term safety assessment of a DGR.

An investigation of the gas transport processes in low-permeability clay material was described by Marschall et al. [5], and further investigated by Cuss et al. [20]. Marschall et al. [5] recognized that gas transport through porous media is controlled by a number of the media's hydraulic and mechanical characteristics such as the intrinsic permeability, porosity, and material strength. They identified the importance of the hydro-mechanical state of the rock or soil media (i.e., water saturation, porewater pressure, and stress state) and the gas pressure at focal points which could lead to microfracturing [5]. Marschall et al. [5] divided the basic transport mechanisms into four processes conceptualized in **Figure 1**.

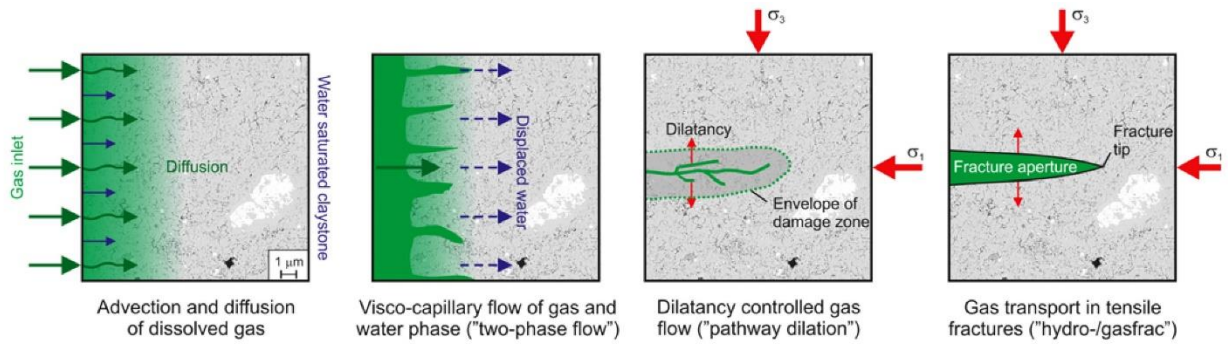

Figure 1. Four main processes of gas migration in clays (Cuss, et al., [20])

In the first process, the advective-diffusive transport of gas dissolved in the porewater is governed by Darcy's law for advective groundwater flow, Fick's law for the diffusion of dissolved gas due to concentration gradients in the porewater, and Henry's law which describes the solubility of gas in the porewater.

The second process of visco-capillary two-phase flow is related to the viscous and capillary forces (i.e., matric suction) which describe the underlying principles of unsaturated soil mechanics. Soil properties influencing this transport process are the pore size distribution and soil compressibility. The air-entry value (AEV) or gas-entry pressure, which is the value of matric suction that must be exceeded before air recedes into the soil pores, is a controlling factor in this transport mechanism of two-phase flow. It is also a measure of the maximum pore-size in a soil, as water will migrate from and gas will enter through the largest pores first.

A wealth of laboratory and field-scale experimental studies have investigated gas transport processes through natural (host rock) and engineered barriers. These studies have provided considerable evidence suggesting that gas flow at gas pressures above a reference level is accompanied by the creation of pressure-induced preferential pathways and dilation of the clay, yet have not been able to determine the exact mechanisms which control gas entry, flow, and pathway sealing [25, 22, 26, 27, 28, 20, 23, 29].

Marschall et al., [5] described this primary transport mechanism as dilatancy-controlled gas flow or "pathway dilation" and identified it as an important transport mechanism in clay soil or clay-rich rock with low tensile-strength. Dilatancy will occur when the gas pressure reaches a reference stress level acting on the clay medium, forcing the clay particles to align in a dispersed orientation, and resulting in the formation of microfractures accompanied by an increase in plastic deformation [30]. As a result, gas flow along these microfractures will be promoted due to the increased pore space. The presence of microfractures therefore leads to an increase in the intrinsic permeability of the material and in turn results in changes in the relationship between the capillary pressure (i.e., matric suction) and degree of saturation (i.e., SWCC of the material). As a result of dilatency-controlled gas flow, transport properties are now dependent on the stress-state and state of deformation of the soil.

Finally, gas transport along macroscopic fractures, also known as hydro- and gas-fracturing, becomes a significant transport mechanism when a macroscopic tensile fracture occurs. Unlike the formation of microfractures that result in dilatancy, these macroscopic fractures develop in low-tensile strength material when gas pressure build-up is rapid and becomes larger than the sum of the minimum principal stress and the tensile strength of the material (i.e., porewater displacement and formation of microfractures can no longer counter balance the gas production rate) [5].

A number of studies have attempted to model gas migration in natural or engineered barrier systems. In 1998 the results of Phase 1 of the GAMBIT Club program were published [33]. The main objective of the GAMBIT Club program was to establish a computational model that could represent the principle features of gas migration through compacted bentonite observed through experiments [33]. Nash et al. [33] applied

the theory of linear elastic fracture mechanics to develop a model of crack propagation through clay, whereby providing a continuous gas flow in a sample, following gas breakthrough, gas flow would be observed across the sample and dilation pathways occur. Phase 1 saw difficulties obtaining agreement between simulation and experimental results over the whole test sequence [33].

Phases 2 and 3 of the GAMBIT Club program further explored the refinement and extension of their earlier models, including the investigation of clay fabric effects (i.e., distinction between inter- and intra-stack pore space) and how to treat hysteresis effects [34]. Hoch et al. [34] examined results with three basic mechanisms that could describe flow i) gas flow governed by conventional concepts of capillary pressure and relative permeability, ii) microfissuring (dilation) of the clay, iii) macroscopic fracturing of the clay, but could not provide a unique explanation of the results in terms of these mechanisms. They concluded that the current uncertainties associated with understanding the transport mechanisms, made it considerably difficult to establish an adequate model for gas migration [34]. The report also concluded that any further development of models of gas migration in bentonite will depend on obtaining better characterisation of gas pathways as well as the couplings that exist in the clay between stress and strain, gas and water fluid pressures, and gas-filled porosity [34].

Fall et al. [35] developed a coupled hydro-mechanical model for simulating gas migration in host sedimentary rocks for nuclear waste repositories. Their study identified that high gas pressure can lead to mechanical damage and the formation of micro-cracks [35]. Their model was limited in part because they did not consider the elasto-plastic mechanical behaviour of the rock. Nguyen and Le [1]developed a mathematical model for gas migration in Opalinus clay. The inherent anisotropy due to bedding, and the elasto-plastic behaviour of the clay were considered in the model. The model was successfully validated against laboratory experiments and field gas injection tests, especially up to the dilatancy controlled flow phase. However, it was recognized that the last phase of gas flow controlled by macroscopic fractures need further understanding.

In 2015, the Geological Society of London, published Special Publication 415 - entitled, *Gas Generation and Migration in Deep Geological Radioactive Waste Repositories*. This publication presented current research to date on experimental studies on gas migration and the development of models to describe gas behaviour in several systems of a DGR [19]. However, there is still much work to be done to understand the basic mechanisms and processes of two-phase flow, particularly dilatancy controlled gas flow through low-permeability swelling soils over the life-time of the repository. In doing so, the development of mathematical relations describing these processes is imperative, along with the development of suitable numerical models which can be used to support the design and long-term safety assessment of a DGR.

Stemming from these international initiatives to understand gas migration and multi-phase flow in low permeability geomaterials, Task A of the current project phase of the international working group for the DEvelopment of COupled models and their VALidation against EXperiments (DECOVALEX-2019) was established. This task, led by the British Geological Survey (BGS), further attempts to identify the physical HM mechanisms required to adequately model dilatancy-controlled gas migration. This research is in part a contribution to Task A of DECOVALEX-2019.

This paper presents a fully-coupled, hydro-mechanical linear-elastic mathematical model for advective-diffusive visco-capillary controlled two-phase flow through geomaterials. The objective of the study is to gain an intricate understanding of the model processes and model parameters which can influence flow behaviour. A validation study is performed by numerically simulating experimental data from a 1-dimensional flow constant volume boundary condition experiment using the finite element method (FEM). This is followed by parametric studies and sensitivity analysis that are used to assess the effects of several features of the numerical model on the flow behaviour.

2. Mathematical Model

A hydro-mechanical (HM) model to describe the migration of gas (two-phase flow) through a low-permeable expansive soil was developed using the theoretical framework of poromechanics. The model follows the general formulation from Nguyen and Le [1], with the addition of the following features:

1. A Bishop's effective stress, with a χ parameter generalized from the work of Khalili and Khabbaz [2];
2. Gas dissolution into the liquid phase and subsequent gas migration from i) the advection of water, and ii) diffusion of gas through the liquid phase;
3. A relation for the Air-Entry Value (AEV), and corresponding Soil Water Characteristic Curves (SWCCs), as a function of changing porosity;
4. A relation of the intrinsic permeability, k_{ij}, as a function of changing porosity; and
5. Consideration of a damage model

The applicable constitutive relations and governing equations for conservation of momentum, water mass and gas mass are presented below.

2.1. Constitutive Relations for the Mechanical Behaviour

2.1.1. Bishop's modified effective stress principle

Many effective stress equations have been proposed to characterize the stress-state of an unsaturated soil or porous medium [1]. This paper proposes the use of Bishop's effective stress principle, which is dependent on both net normal stress and matric suction, and may be more suitable for expansive clay's, as described by equation (1).

$$\sigma' = (\sigma - p_g) + \chi(p_g - p_w) \tag{1}$$

where
σ' is the effective stress (Pa)
σ is the total normal stress (Pa)
p_g is the poregas pressure (Pa)
p_w is the porewater pressure (Pa)
$(\sigma - p_g)$ is the net normal stress (Pa)
$(p_g - p_w)$ is the matric suction (Pa)
χ is a parameter related to the degree of saturation of the soil (unitless)

Expanding and rearranging for σ

$$\sigma = \sigma' + (1 - \chi)p_g + \chi p_w \tag{2}$$

The porefluid pressure can be defined as,

$$\bar{p} = (1 - \chi)p_g + \chi p_w \tag{3}$$

Khalili and Khabbaz [2], proposed the following unique relationship for the determination of χ based on the ratio of suction over the air entry value, also termed the suction ratio,

$$\chi = \begin{cases} \left[\dfrac{(p_g - p_w)}{(p_g - p_w)_b}\right]^{-0.55}, & \text{if } (p_g - p_w) > (p_g - p_w)_b \\ 1, & \text{otherwise} \end{cases} \tag{4}$$

where $(p_g - p_w)_b$ is the air-entry value (AEV) of the soil and only applies when the matric suction > AEV [2].

2.1.2. Equation of poro-elasticity

The general form for the equation of poromechanics can be expressed by,

$$\sigma_{ij} = C_{ijkl}\varepsilon_{kl} + \alpha_B \bar{p}\delta_{ij} \tag{5}$$

where σ_{ij} total normal stress tensor acting on the soil element (Pa)
C_{ijkl} is the fourth order stiffness tensor
ε_{kl} is the strain tensor (unitless)
α_B is the Biot-Willis coefficient (unitless)
δ_{ij} is the Kronecker delta (identity tensor) (unitless)

Applying Hooke's Law for linear elasticity

$$\sigma_{ij} = 2G\varepsilon_{ij} + \lambda\varepsilon_{kk}\delta_{ij} + \alpha_B \bar{p}\delta_{ij} \tag{6}$$

where

$$\varepsilon_{ij} = \frac{1}{2}\left(u_{i,j} + u_{j,i}\right) = \frac{1}{2}\left(\frac{\partial u_i}{\partial x_j} + \frac{\partial u_j}{\partial x_i}\right) \tag{7}$$

$$\varepsilon_{kk} = u_{k,k} = \frac{\partial u_k}{\partial x_k} \tag{8}$$

where G is the shear modulus (Pa)
λ is the Lamé constant (Pa)
$\varepsilon_{kk}\left(= u_{k,k} = tr\varepsilon_{ij}\right)$ is the volumetric strain (unitless)
u_{ij} is the displacement tensor (m)
substituting into equation (6)

$$\sigma_{ij} = G\left(\frac{\partial u_i}{\partial x_j} + \frac{\partial u_j}{\partial x_i}\right) + \left(\lambda\frac{\partial u_k}{\partial x_k} + \alpha_B \bar{p}\right)\delta_{ij} \tag{9}$$

or in terms of Young's modulus, E, and Poisson's ratio, ν

$$\sigma_{ij} = \frac{E}{2(1+\nu)}\left(\frac{\partial u_i}{\partial x_j} + \frac{\partial u_j}{\partial x_i}\right) + \left(\frac{\nu E}{(1+\nu)(1-2\nu)}\frac{\partial u_k}{\partial x_k} + \alpha_B \bar{p}\right)\delta_{ij} \tag{10}$$

2.2. Constitutive Relations for the Hydraulic Behaviour

2.2.1. Equation for the Soil-Water Characteristic Curve

The Soil-Water Characteristic Curve (SWCC), describes the relationship between the degree of saturation, S or water content (θ or w) in the soil and the matric suction, s. A number of mathematical models can be used to model the behaviour of the SWCC. This paper utilizes the van Genuchten equation to model the SWCC. a specific soil fitted to model parameters a, n′, and m′ [51].

$$S_{e,w} = \begin{cases} \dfrac{1}{\left[1 + \left|a'\left(\frac{s}{\rho_w g}\right)\right|^{n'}\right]^{m'}}, s > 0 \\ 1, s \leq 0 \end{cases} \tag{11}$$

where $S_{e,w}$ is the effective degree of saturation of water
a', n', and m' are fitting parameters for the SWCC
ρ_w is the density of water (kg m^{-3})
g is the acceleration due to gravity (m s^{-2})
s is the matric suction $(p_g - p_w)$ (Pa)
The fitting parameter, a', is related to the AEV and can be expressed by equation (12)

$$a' = 0.5\frac{\rho_w g}{AEV} \tag{12}$$

The fitting parameter m' is related to fitting parameter n' by equation (13),

$$m' = 1 - \frac{1}{n'} \tag{13}$$

$S_{e,w}$ can be calculated from scaling the water saturation, S_w, with respect to the maximum degree of saturation, $S_{w,s}$, and the residual degree of saturation, $S_{w,r}$

$$S_{e,w} = \frac{S_w - S_{w,r}}{S_{w,s} - S_{w,r}} \tag{14}$$

From the fitted SWCC, the model can be used to predict the degree of saturation of water, S_w, from measuring the stress-state variable matric suction (or capillary pressure), s.

The degree of saturation of the gas phase, S_g, can be related to S_w via the following relationship.

$$S_g = 1 - S_w \tag{15}$$

It should be noted that the model does not consider entrapped gases which would be present if $S_{w,s} < 1$.

2.2.2. Equation for the Air-Entry Value as a function of pore size

Huang et al. [52], using data published by Laliberte et al. [53] showed that for sand, sandy loam, and silt loam, the logarithm of the AEV is linearly proportional to the void ratio or porosity at the AEV, as expressed by equation (16) and this linear relationship can be assumed for deformable unsaturated porous medium.

$$\log(s_{aev}) = \log(s'_{aev}) + m(e_{aev} - e'_{aev}) \tag{16}$$

where s_{aev} is the air-entry value (Pa) for a void ratio, e_{aev}
s'_{aev} is the arbitrary reference air-entry value (Pa) for a void ratio e'_{aev}
m is the slope of the s_{aev} - e_{aev} curve
It should be noted that the slope, m, is negative as an increase in the void ratio (i.e., pore-size) will result in a decrease in the AEV. In the current model, the swelling potential of expansive clays is not considered and therefore this relationship is considered reasonable for this study.
By re-arranging equation (16) we can express this relationship in terms of porosity,

$$\log(s_{aev}) = \log(s'_{aev}) + m\left(\frac{n_{aev}}{1 - n_{aev}} - \frac{n'_{aev}}{1 - n'_{aev}}\right) \tag{17}$$

2.2.3. Darcy's Law for two-phase flow

Darcy's Law for the water and gas phases are expressed by equation (18) and equation (19).

$$v_{iw} - v_{is} = -\frac{k_{ij}k_{rw}}{nS_w\mu_w}\left(\frac{\partial p_w}{\partial x_j} + \rho_w g\right) \quad (18)$$

$$v_{ig} - v_{is} = -\frac{k_{ij}k_{rg}}{nS_g\mu_g}\left(\frac{\partial p_g}{\partial x_j} + \rho_g g\right) \quad (19)$$

where p_w is the porewater pressure (Pa)
p_g is the poregas pressure (Pa)
$(v_{iw} - v_{is})$ is the velocity of water in the pores relative to the velocity of the soil matrix (m s^{-1})
$(v_{ig} - v_{is})$ is the velocity of gas in the pores relative to the velocity of the soil matrix (m s^{-1})
n porosity (m^3 voids · m^{-3} total)
μ_w dynamic viscosity of the water phase (Pa s or kg m^{-1} s^{-1})
μ_g dynamic viscosity of the gas phase (Pa s or kg m^{-1} s^{-1})
k_{ij} intrinsic permeability tensor of the porous medium (m^2)
k_{rw} relative permeability of the water phase (unitless)
k_{rg} relative permeability of the gas phase (unitless)
ρ_w density of water phase (kg m^{-3})
ρ_g density of the gas phase (kg m^{-3})

2.2.4. Intrinsic permeability as a function of porosity

Numerous equations have been proposed to describe the relationship of between intrinsic permeability, and measurable properties of soils such as the porosity and particle-size. The Kozeny-Carman equation can be used to express the intrinsic permeability as a function of porosity using the capillary tube (hydraulic radius) model, and is sufficient for laminar flow and low porefluid velocity [54]. The Kozeny-Carmen Equation is given by,

$$k_{ij} = \frac{1}{5S_0^2}\frac{n^3}{(1-n)^2} \quad (20)$$

where S_0 is the specific surface (surface exposed to fluid per unit solid volume) (m^2 m^{-3})

For fine-grained expansive clays, which have very small grain-sizes less than 2 μm, and are non-uniform, the Kozeny-Carman equation may not be appropriate [55] [56]. Pall and Moshenin [56], proposed a modification of equation (20) by taking the volume-surface mean diameter to better account for the non-uniformity of soil particles.

$$k_{ij} = \frac{D_{vs}^2}{180}\frac{n^3}{(1-n)^2} \quad (21)$$

where D_{vs} is the volume-surface mean diameter (m)

If the porosity and intrinsic permeability were known, the volume-surface mean diameter could be obtained by rearranging equation (21).

$$D_{vs} = \sqrt{180k_{ij}\frac{(1-n)^2}{n^3}} \quad (22)$$

In this study, the experimentally determined initial porosity and intrinsic permeability were used to calculate the volume-surface mean diameter of the soil sample. Any elastic deformations to the soil structure will influence the porosity, subsequently influencing the intrinsic permeability across the soil specimen.

2.2.5. Relative permeability of water and gas phases

The coefficient of permeability is strongly dependent on the degree of saturation, S_w. Using Mualem's Model [1], k_{rw} and k_{rg}, can be calculated using the following expressions:

$$\mathrm{k_{rw}} = \begin{cases} \mathrm{S_{e,w}^{L}}\left[1-\left(1-\mathrm{S_{e,w}^{1/m'}}\right)^{\mathrm{m'}}\right]^{2}, \mathrm{s} > 0 \\ 1, \mathrm{s} \le 0 \end{cases} \quad (23)$$

$$\mathrm{k_{rg}} = \left(1-\mathrm{S_{e,w}}\right)^{\mathrm{L'}}\left[1-\mathrm{S_{e,w}^{1/m'}}\right]^{2\mathrm{m'}} \quad (24)$$

where L' is the relative permeability function fitting parameter (unitless)

2.2.6. Diffusivity of gas in water through porous media

Diffusion of gas through the liquid phase of a porous medium can be expressed as an effective diffusivity, D_e,

$$\mathrm{D_e} = \mathrm{DnS_w}\tau \quad (25)$$

where D_e is the effective diffusivity of gas dissolved in water through porous media ($m^2\ s^{-1}$)

D is the diffusivity of gas in water ($m^2\ s^{-1}$)

n is the porosity (unitless)

τ is the tortuosity (unitless)

The tortuosity for gas diffusion through porous water can be calculated using the Millington and Quirk model [57] by,

$$\tau = \mathrm{n^{\frac{1}{3}}S_w^{\frac{7}{3}}} \quad (26)$$

2.2.7. Storage due to suction of water and gas (storage coefficient)

Storage terms are applied in the governing equations when differentiating $\frac{dS_w}{ds}$. The storage coefficient of water, C_w, can be calculated by differentiating the van Genuchten SWCC,

$$\mathrm{C_w} = \frac{\mathrm{dS_w}}{\mathrm{ds}} = \begin{cases} \frac{1}{\rho_w g}\cdot\frac{a'm'}{1-m'}\left(S_{w,s}-S_{w,r}\right)S_{e,w}^{1/m'}\left(1-S_{e,w}^{1/m'}\right)^{m'}, s > 0 \\ 0, s \le 0 \end{cases} \quad (27)$$

The storage coefficient of gas, $\mathrm{C_g}$, can be related to the storage coefficient of water by,

$$\mathrm{C_g} = \frac{\mathrm{dS_g}}{\mathrm{ds}} = \frac{\mathrm{d(1-S_w)}}{\mathrm{ds}} = -\frac{\mathrm{d(S_w)}}{\mathrm{ds}} = -\mathrm{C_w} \quad (28)$$

2.2.8. Bulk Modulus of water and gas

The bulk modulus of water, K_w, can be calculated as follows.

$$\mathrm{K_w} = -\mathrm{V_w}\frac{\mathrm{dp_w}}{\mathrm{dV_w}} = \rho_w\frac{\mathrm{dp_w}}{\mathrm{d}\rho_w} \quad (29)$$

The bulk modulus of gas, K_g, can be calculated as follows.

$$K_g = -V_g \frac{dp_g}{dV_g} = \rho_g \frac{dp_g}{d\rho_g} \tag{30}$$

From the ideal gas law,

$$\frac{p_g}{\rho_g} = \frac{RT}{M} \tag{31}$$

From Boyle's Law for isothermal conditions,

$$\frac{dp_g}{d\rho_g} = \frac{RT}{M} \tag{32}$$

substituting equation (32) back into equation (30)

$$K_g = \rho_g \frac{RT}{M} = p_g \tag{33}$$

2.3. Constitutive Relations of a Damage Model

A Damage model has been introduced based on that developed by Tang et al. [58] and adopted by Fall et al. [35], whereby an element under tension or compression will experience an elastic damage, D ($0 < D < 1$), when the stress of the element satisfies the strength criterion, and the element begins to fail. Failure results in a decrease in the elastic modulus and an increase in the intrinsic permeability, as expressed in this paper by equation (34) and equation (35), respectively,

$$E = E_0(1 - D^c) \tag{34}$$

where D is the damage (unitless)
E_0 is the Young's modulus before damage (Pa)
E is the Young's modulus after damage (Pa)

$$k_{ij} = k_{UD} + k_D \tag{35}$$

where k_{ij} is the permeability at any given time (m^2)
k_{UD} is the permeability before damage (m^2) and is expressed by equation (21)
k_D is the increase in permeability as a result of damage (m^2) and can be expressed by equation (36)

$$k_D = D^c(k_{max} - k_{UD}) \tag{36}$$

where k_{max} (m^2) is the maximum permeability obtained when $D = 1$
c is a smoothing coefficient (unitless) and may be calibrated anywhere from 2 to 20 depending on the mesh size and the rate of increase in damage
k_{max} and c, are determined through model calibration.

The criterion for D_t in multi-axial tension is expressed by equation (37), while the criterion for D_c in multi-axial compression is expressed by equation (38):

$$D_t = \begin{cases} 0 & \varepsilon \le \varepsilon_{t0} \\ 1 - \dfrac{f_{tr}}{E_0 \varepsilon} & \varepsilon_{t0} \le \varepsilon \le \varepsilon_{tu} \\ 1 & \varepsilon \ge \varepsilon_{tu} \end{cases} \tag{37}$$

$$D_c = \begin{cases} 0 & \varepsilon_{c0} \le \varepsilon \\ 1 - \dfrac{f_{cr}}{E_0 \varepsilon} & \varepsilon \le \varepsilon_{c0} \end{cases} \tag{38}$$

where ε is the strain (unitless)

ε_{tu} is the tensile strain corresponding to a complete material failure

ε_{t0} is the strain corresponding to the point of tensile strength

ε_{c0} is the strain corresponding to the compressive strength

f_{tr} is the residual tensile strength (Pa)

f_{cr} is the residual compressive strength (Pa)

Note for equation (37) and equation (38) the following sign convention is used: i) strain components and volumetric deformations are positive for expansion and negative for contraction; and ii) stress components are positive for tension and negative for compression.

2.4. Governing Equations

2.4.1. Conservation of Momentum (Quasistatic Equilibrium)

The total equilibrium equation for a cubical soil element can be expressed in tensor notation by equation (39).

$$\frac{\partial \sigma_{ij}}{\partial x_j} + F_{v,i} = 0 \tag{39}$$

where, σ_{ij} is the stress tensor (Pa)

$F_{v,i}$ is the volumetric body force tensor (kg m^{-2} s^{-2})

$\frac{\partial \sigma_{ij}}{\partial x_j}$ represents the change in normal and shear stresses across the soil element (kg m^{-2} s^{-2})

Substituting equation (9) and differentiating, the governing equation for the conservation of momentum using a linear poro-elasticity model is expressed by equation (40).

$$G\frac{\partial^2 u_i}{\partial x_j \partial x_j} + (G+\lambda)\frac{\partial^2 u_j}{\partial x_j \partial x_i} + \alpha_B(1-\chi)\frac{\partial p_g}{\partial x_i} + \chi\frac{\partial p_w}{\partial x_i} + F_{v,i} = 0 \tag{40}$$

2.4.2. Conservation of water mass

For a soil element depicted in **Figure 2**, the general equation for the conservation of water mass and gas mass (considering dissolution of gas in water and diffusion of dissolved gas in water) in porous media can be expressed by equation (41) and equation (42), respectively

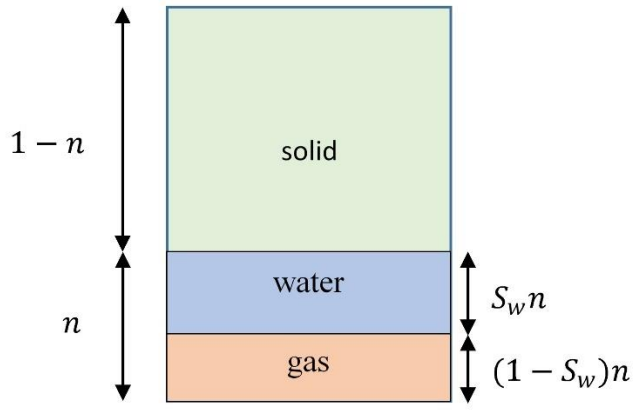

Figure 2. Control Volume and Phase Relations

$$\frac{\partial}{\partial x_i}\left(\rho_w n(v_{iw} - v_{is})\right) = -\frac{\partial(\rho_w n S_w)}{\partial t} \tag{41}$$

where,

$\frac{\partial(\rho_w n S)}{\partial t}$ is the rate of change of mass of water in the soil element over time (kg m^{-3} s^{-1})

$\frac{\partial}{\partial x_i}\left(\rho_w n(v_{iw} - v_{is})\right)$ is the net advective flux of water for the soil element (kg m^{-3} s^{-1})

Substituting in Darcy's (18), and solving the right-hand side of equation (41) results in the following governing equations for the conservation of water mass,

$$\frac{\partial}{\partial x_i}\left(\rho_w \frac{k_{ij} k_{rw}}{\mu_w}\left(\frac{\partial p_w}{\partial x_j} + \rho_w g_j\right)\right) = -\rho_w\left[n\left(\frac{dS_w}{ds}\right)\frac{\partial s}{\partial t} + n\frac{S_w}{K_w}\frac{\partial p_w}{\partial t} + S_w(1-n)\frac{\partial}{\partial t}\left(\frac{\partial u_k}{\partial x_k}\right)\right] \tag{42}$$

where K_w is the bulk modulus of water (Pa)

It should be noted that the right hand side of equation (42) is derived from the differentiation of $\frac{\partial(\rho_w n S_w)}{\partial t}$. The final term in equation (42) is multiplied by $(1 - n)$ which is derived from differentiating the equation for porosity,

$$n = \frac{V_v}{V} \tag{43}$$

where V_v is the volume of voids (m^{-3})

Using the Quotient Rule to differentiate,

$$\begin{aligned} dn = d\left(\frac{V_v}{V}\right) = \frac{dV_v V - V_v dV}{V^2} = \frac{dV_v}{V} - \frac{V_v}{V}\frac{dV}{V} = \frac{d(V - V_s)}{V} - n\frac{dV}{V} \\ = \frac{dV}{V}(1-n) - \frac{dV_s}{V} \end{aligned} \tag{44}$$

where, $\frac{dV}{V} = d\varepsilon_{kk}$, the volumetric strain, and where it is assumed that $\frac{dV_s}{V} \ll d\varepsilon_{kk}(1-n)$,

$$dn = d\left(\frac{V_v}{V}\right) = d\varepsilon_{kk}(1-n) = (1-n)\,\partial\left(\frac{\partial u_k}{\partial x_k}\right) \tag{45}$$

2.4.3. Conservation of gas mass

For a soil element depicted in **Figure 2**, the general equation for the conservation of gas mass in porous media can be expressed by (46), respectively

$$\begin{aligned} \frac{\partial\left(\rho_g n\left((v_{ig} - v_{is}) + H(v_{iw} - v_{is})\right)\right)}{\partial x_i} + \frac{\partial}{\partial x_i}\left(-D_e\frac{\partial}{\partial x_k}\left(\rho_g n(HS_w)\right)\right) \\ = -\frac{\partial\left(\rho_g n(1 - S_w + HS_w)\right)}{\partial t} \end{aligned} \tag{46}$$

where,

ρ_g, is the gas density (kg gas m^{-3})

$\frac{\partial}{\partial x_i}\left(\rho_g n\left((v_{ig} - v_{is}) + H(v_{iw} - v_{is})\right)\right)$ is the net advective flux of gas for the soil element (kg m^{-3} s^{-1})

$\frac{\partial}{\partial x_i}\left(-D_e\frac{\partial}{\partial x_k}\left(\rho_g n(HS_w)\right)\right)$ is the net diffusive flux of gas for the soil element (kg m^{-3} s^{-1})

$\frac{\partial(\rho_g n(1-S_w+HS))}{\partial t}$ is the rate of change of mass of gas in the soil element over time (kg m^{-3} s^{-1})

H is Henry's coefficient (kg species A m^{-3} in aqueous phase kg^{-1} species A m^3 in gas phase)

Substituting in Darcy's Law (19) and solving the right-hand side of equation (47), results in the following governing equation for the conservation of gas mass.

$$\frac{\partial\left(\rho_g\left(\frac{k_{ij}k_{rg}}{\mu_g}\left(\frac{\partial p_g}{\partial x_j}+\rho_g g\right)+H\frac{k_{ij}k_{rw}}{\mu_w}\left(\frac{\partial p_w}{\partial x_j}+\rho_w g\right)\right)\right)}{\partial x_i}+\frac{\partial}{\partial x_i}\left(-D_e\frac{\partial}{\partial x_k}\left(\rho_g n(HS_w)\right)\right) = -\rho_g\left[n(H-1)\left(\frac{dS_w}{ds}\right)\frac{\partial s}{\partial t}+\frac{n(1-S_w+HS_w)}{K_g}\frac{\partial p_g}{\partial t}+(1-S_w+HS_w)(1-n)\frac{\partial}{\partial t}\left(\frac{\partial u_k}{\partial x_k}\right)\right] \quad (47)$$

where K_g is the bulk modulus of the gas phase (Pa)

3. Numerical Model Description and Modelling Approach

3.1. Overview of the Numerical Model

A two-dimensional (2D) axisymmetric and three-dimensional (3D) time-dependent (i.e., transient) hydro-mechanical (HM) coupled multiphysics models were developed. The models simulate the simultaneous migration of gas and liquid (two-phase flow) in porous media, which are coupled to the linear poro-elastic behaviour of the solid matrix using the finite element method (FEM). The commercially available code COMSOL Multiphysics® was used to numerically solve the governing equations of the model.

The numerical model was based on an experimental setup conducted by the British Geological Survey (BGS) to assess the 1D flow through a saturated bentonite sample under a constant volume boundary stress condition [59]. In this experiment, a confined cylindrical sample of near-saturated bentonite was injected on one side with helium gas with increasing gas pressures over a period of 120 days. The other side was left at a constant water backpressure throughout the duration of the experiment. The experiment was conducted under isothermal conditions at a temperature of 293.15 K. During the experiment, a number of parameters where measured including the gas inflow and outflow, the porefluid pressure at defined porefluid arrays, and the total radial stresses at radial load cell arrays. The cylindrical specimen of MX-80 bentonite had a diameter of 60 mm and a length of 120 mm.

Table 2 provides the location of the monitoring sensors within the specimen. The BGS provided the experimental data that was used in the model validation [59].

Table 2. Model dimensions and location of the porefluid arrays

Sensor name	Measurement Type	Axial distance from injection face (mm)
Injection load cell	Total stress	0
Radial load cell 1	Total stress	15.2
Radial load cell 2	Total stress	60
Radial load cell 3	Total stress	104.8
Backpressure load cell	Total stress	120
Radial porewater array 1	Porefluid pressure	38.6
Radial porewater array 2	Porefluid pressure	60
Radial porewater array 3	Porefluid pressure	81.4
Central filter (Middle)	Porefluid pressure	60

3.2. Modelling Approach

The modelling approach included the simulation of a number of study scenarios. A validation study scenario S1 was run with the HM poro-elastic model for both 2D axisymmetric and 3D models. Several parametric studies were performed to assess the contribution of advection, diffusion and linear elastic deformation on flow behaviour (S2-S4). Similarly, sensitivity analyses were performed to identify the influence of changing the initial porosity, AEV, and intrinsic permeability on flow behaviour (S5-S10). Scenario S11 was run to determine whether better agreement with the experimental results could be obtained by inclusion of a damage model. Lastly, the effect of mesh size on the numerical solution was investigated by running S1 using a number of mesh sizes (S12). **Table 3** summarizes the simulations which were run.

Table 3. Base Study and Parametric Study Model Scenarios

Scenario Number	Model	Description	Porosity	Intrinsic permeability (m^2)	AEV (Pa)	SWCC fitting parameters		
						a′ (1/m)	**n′**	**m′**
S1-Validation	HM	Advection, dissolution and diffusion linear poro-elasticity	0.44	3.4E-21	8.0E+06	0.0006	2.04	0.51
Parametric studies								
S2	H	Advection, no dissolution, no diffusion	0.44	3.4E-21	8.0E+06	0.0006	2.04	0.51
S3	H	Advection, dissolution, no diffusion	0.44	3.4E-21	8.0E+06	0.0006	2.04	0.51
S4	H	Advection, dissolution, diffusion	0.44	3.4E-21	8.0E+06	0.0006	2.04	0.51
Sensitivity analysis								
S5	HM	↑ por	0.48	5.1E-21	6.2E+06	0.0008	2.04	0.51
S6	HM	↓ por	0.30	6.9E-22	1.6E+07	0.0003	2.04	0.51
S7	HM	↑ AEV	0.44	3.4E-21	2.0E+07	0.00025	2.04	0.51
S8	HM	↓ AEV	0.44	3.4E-21	5.0E+06	0.0006	2.04	0.51
S9	HM	↑ k_{ij}	0.44	1.0E-19	8.0E+06	0.0006	2.04	0.51
S10	HM	↓ k_{ij}	0.44	1.0E-22	8.0E+06	0.0006	2.04	0.51
S11	HM	Inclusion of a damage model	0.44	3.4E-21	8.0E+06	0.0006	2.04	0.51
S12	HM	Effect of mesh size	0.44	3.4E-21	8.0E+06	0.0006	2.04	0.51

3.3. Model Geometry and Mesh

The 2D-axisymmetric and 3D geometry and mesh sizes are presented in **Figure 3** and **Figure 4**, respectively. Due to the nature of axisymmetric models (i.e., rotates along a vertical axis), the 2D-axisymmetric model was configured vertically. As a result, the effects of gravity have been turned off for this specific configuration in COMSOL®, as it differs from the actual experimental set-up. The number of elements and degrees of freedom for each geometry are provided in **Table 4**.

Table 4. Number of Elements and Degrees of Freedom

Model Geometry	Mesh Qualifier	No. of Elements	Degrees of Freedom
2D Axisymmetric	Extremely Fine	8 886	117 132
3D	Normal	10 698	161 741

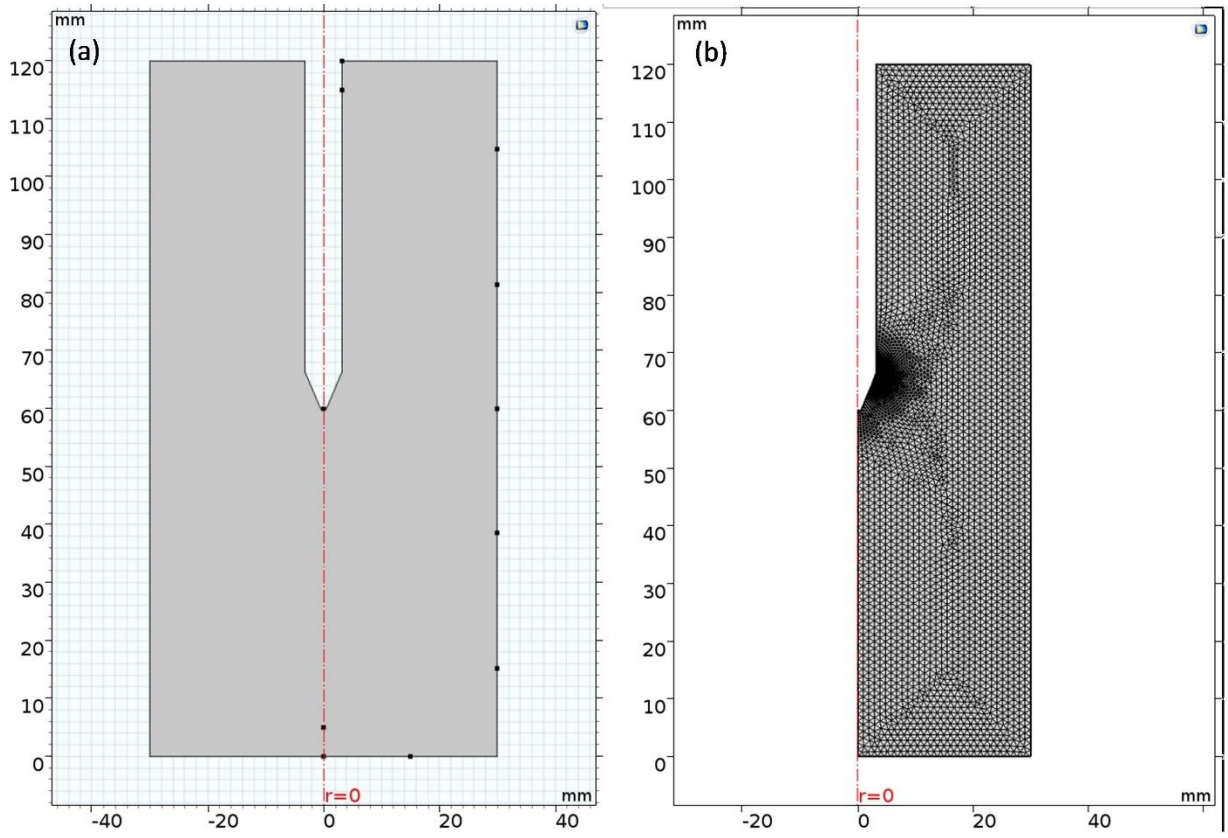

Figure 3. 2D-Axisymmetric Geometry and Meshing

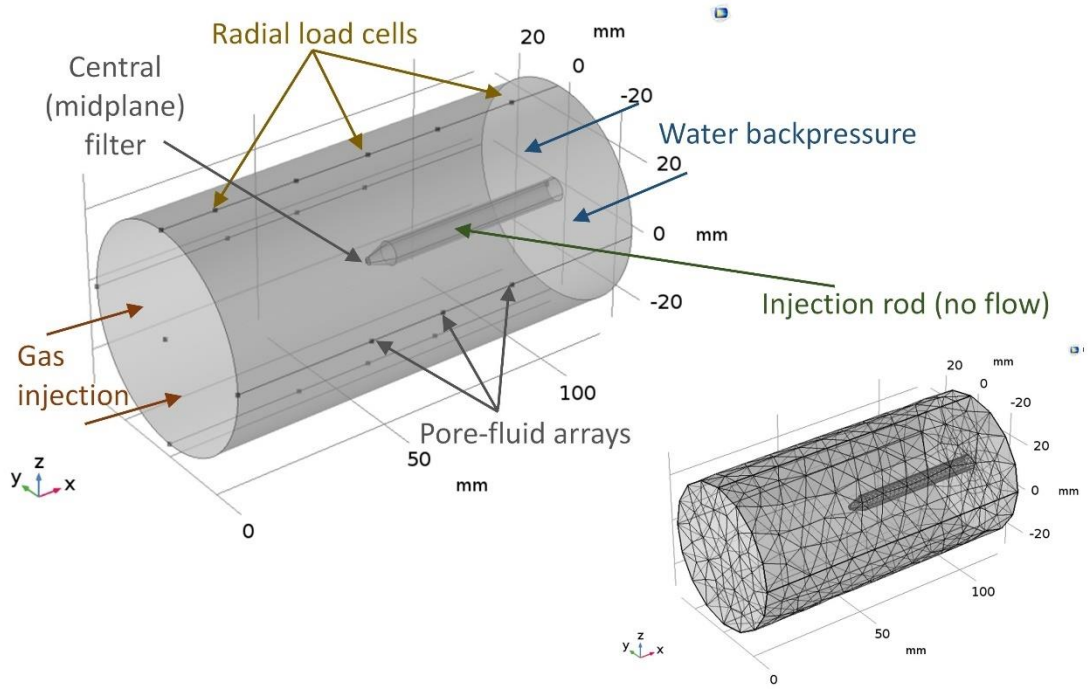

Figure 4. 3D Geometry and Meshing

3.4. Material Properties

Material properties for the solid bentonite MX-80 soil matrix, helium gas and water are provided in **Table** 5. Material properties were provided by BGS for the initial porosity, intrinsic permeability, Young's Modulus and Poisson ratio. The dry density of bentonite was calculated from the dry weight and volume of the bentonite sample. The volume-surface mean diameter, D_{vs}, was calculated from equation (22), and the initial tortuosity, τ, was calculated from equation (26).

Table 5. Material properties of the solid soil matrix and gas and liquid phases

Material	Parameter	Value
Solid Soil Matrix (Bentonite)	Saturated/intrinsic permeability, k_{ij} (m^2)	3.4E-21
	Dry density, ρ_d (kg m^{-3})	1 560
	Maximum degree of saturation, S_{w_s}	1
	Residual degree of Saturation, S_{w_r}	0.05
	Porosity, n	4.4E-01
	Young's Modulus, E (MPa)	307
	Poisson ratio, ν	0.4
	Bulk Modulus of bentonite, K_s (Pa)	2.0E+08
	Compression Index, $1/K_s$ (Pa^{-1})	5.0E-09
	Volume-surface mean diameter, D_{vs} (m) calculated based on equation (23)	1.5E-09
	Initial tortuosity, τ	0.69
Gas (Helium)	Density, ρ_g (kg m^{-3})	$p_g \frac{M}{RT}$
	Dynamic Viscosity @ 293.15 K (Pa·s)	2.0E-05

	Bulk Modulus of helium, K_g (Pa)	p_g
	Henry's Coefficient, H	0.0091
	Diffusivity of helium in water (m^2 s^{-1})	6.29E-09
	Diameter of helium gas particle, d_{he} (m)	1.0E-10
Liquid (Water)	Density, ρ_w (kg m^{-3})	1000
	Dynamic Viscosity @ 293.15 K (Pa s)	0.001
	Bulk Modulus of water, K_w (Pa)	2.2E+09
	Compression Index, $1/K_w$ (Pa^{-1})	4.55E-10

3.5. Boundary Conditions

The hydraulic and mechanical boundary conditions (BC) for gas transport, water transport, and momentum transport are provided below.

Gas Conservation BCs

For gas transport, a no flow Neumann BC, $\frac{\partial p_g}{\partial x_i} = 0$, was set at the radial boundaries. Dirichlet BCs were set at the gas injection pressure as a function of time for the lower boundary. The upper boundary was set at atmospheric pressure to allow for gas to flow out of the sample.

For the concentration of gas in porewater, $C_{g,\,H_2O}$, Dirichlet BCs were applied to the lower boundary as a function of the gas injection pressure and to the upper boundary based on an atmospheric pressure condition as follows; from the Ideal Gas Law

$$p_g V = nRT \tag{48}$$

$$p_g V = \frac{m_g}{M} RT \tag{49}$$

Re-arranging

$$\frac{m_g}{V} = \rho_g = p_g \frac{M}{RT} \tag{50}$$

where p_g is the poregas pressure (Pa)

Assuming instantaneous dissolution, the concentration of gas in the porewater can be calculated by multiplying equation (50) by Henry's coefficient, H, and the portion of water in a unit cell, nS_w

$$C_{g,\,H_2O} = \rho_g H(nS_w) \tag{51}$$

where $C_{g,\,H_2O}$ is the concentration of gas in water (kg gas m^{-3} water)

H is Henry's coefficient (kg species A m^{-3} in aqueous phase kg^{-1} species A m^3 in gas phase)

Water Conservation BCs

For water transport, a no flow Neumann BC, $\frac{\partial p_w}{\partial x_i} = 0$, was set for the lower and radial boundaries. A Dirichlet BC was set as the water backpressure for the upper boundary.

Momentum Conservation BCs

For the moment conservation equation, a roller constraint was applied along the upper, lower, and radial boundaries to represent a condition whereby the boundary is free to move in the tangential direction, but is fixed in the normal direction, simulating a constant volume condition, as per the experimental set-up.

The gas injection pressure and water backpressure Dirichlet BCs were imported from the experimental data provided by BGS and have been plotted in **Figure 5**(**a**), while the concentration of dissolved gas BCs have been plotted in **Figure 5**(**b**).

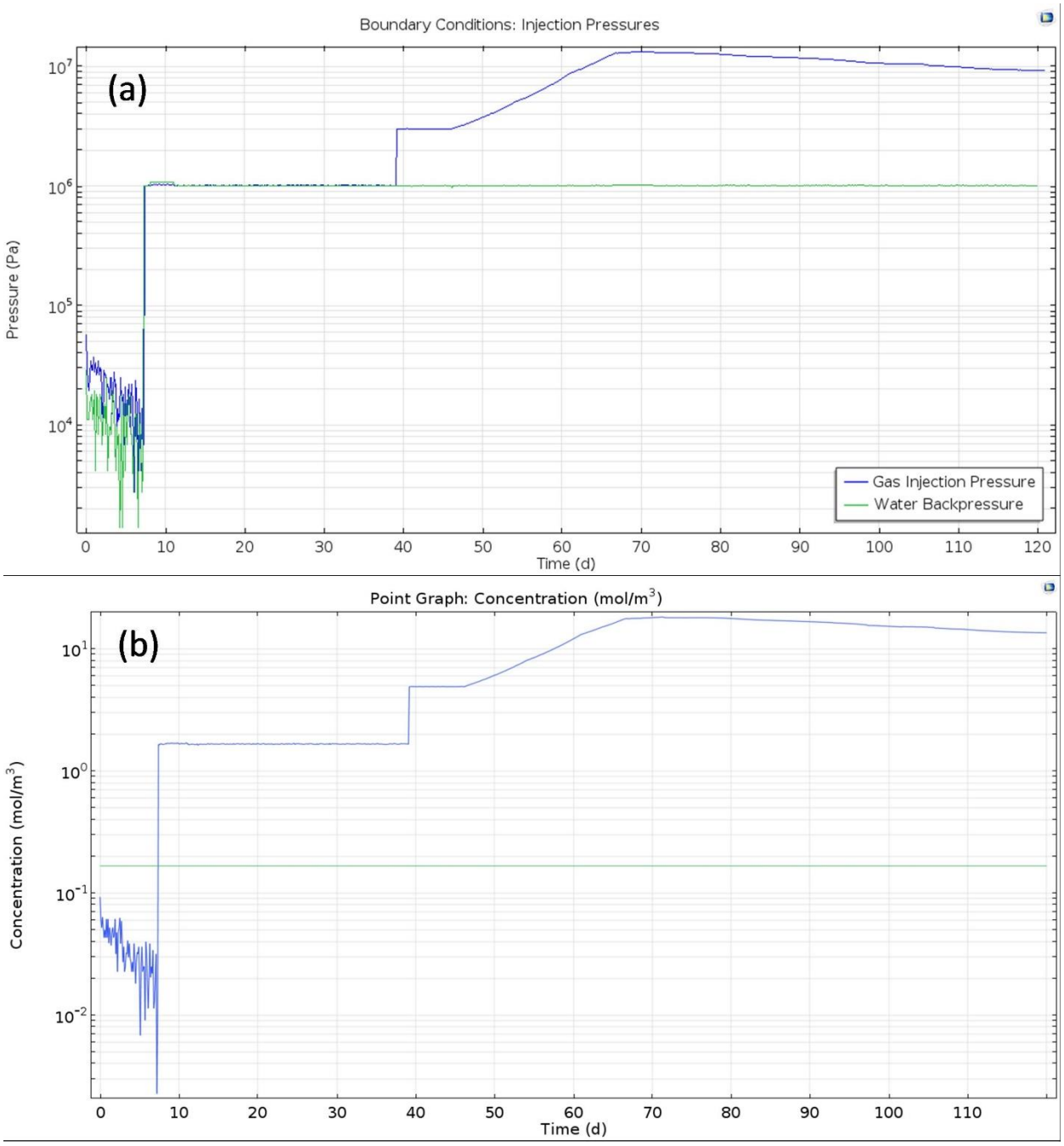

Figure 5. Dirichlet Boundary Conditions for the (a) lower gas injection pressure and upper water backpressure (b) lower and upper gas concentrations in porewater

3.6. Initial Value Conditions

The initial conditions at t = 0s across the domain are provided in **Table 6**, and are based on experimental data provided by BGS [59]. It should be noted that the bentonite sample was not fully saturated upon the start of the experiment but underwent a hydration phase which began on t=7.3 days and ended on t=39 days. Thereby an initial degree of saturation, $S_{w,inital}$, measured at 0.96 was used as the initial condition. This is important as the model assumes a continuous gas-phase throughout the specimen and does not account for entrapment of gas within the pore space.

Table 6. Initial Value Conditions

Parameter Name	Parameter	Initial Value Condition
Initial poregas pressure	$p_{g_{initial}}$	1.01E+05 Pa
Initial degree of saturation	$S_{w_{initial}}$	0.96
Initial suction (from SWCC)	$s_{initial}$	5.8E+06 Pa
Initial porewater pressure	$p_{w_{initial}}$	-5.7E+06 Pa
Initial displacement field	u_i	0 m
Initial stress	$\sigma_{0_{xx}} = \sigma_{0_{yy}} = \sigma_{0_{zz}}$	5.0E+05 Pa
Initial gas concentration in porewater @STP	$C_{g,\,H_2O}$	0.073 mol m^{-3}

3.7. Intrinsic Permeability, Air-Entry Value, Effective Diffusivity, Chi Parameter, Soil Water Characteristic Curves and Relative Permeability Functions

The intrinsic permeability, AEV and effective diffusivity as a function of porosity are provided in **Figure 6**. Khalili and Khabbaz's, χ-value, is displayed as a function of suction and AEV in **Figure 7**.

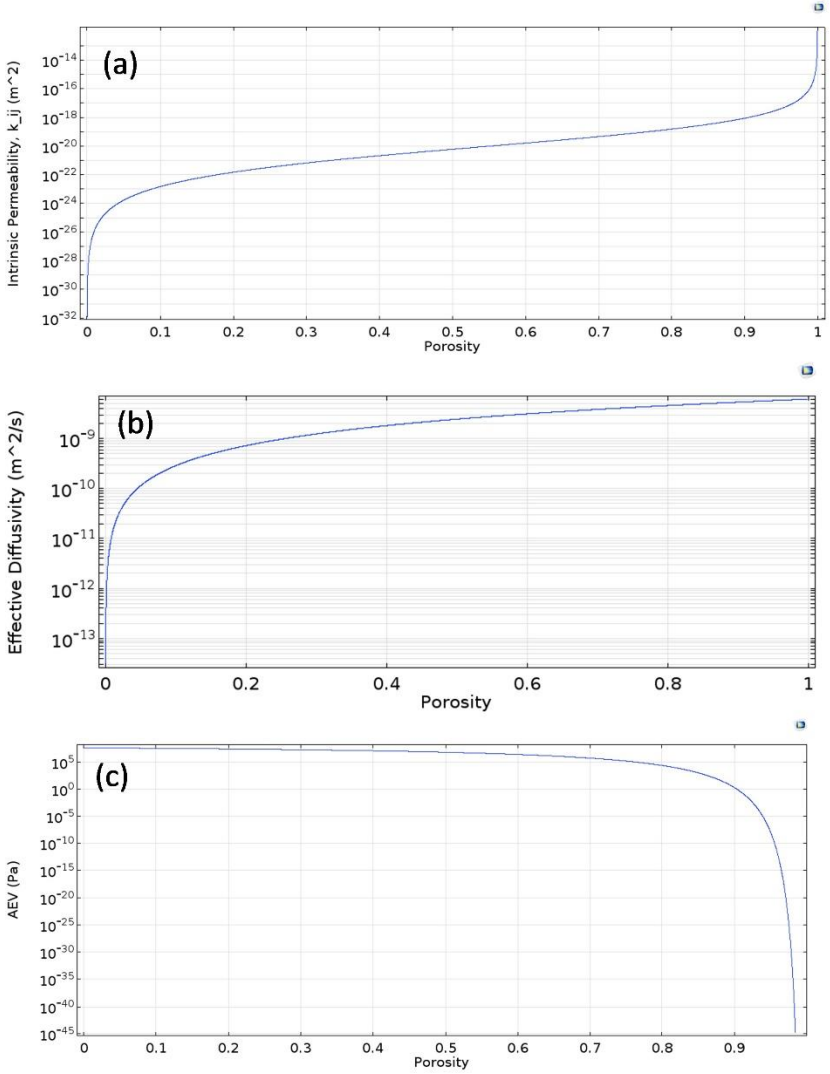

Figure 6. Intrinsic permeability (**a**), effectivity diffusivity (**b**) and AEV (**c**) curves as a function of porosity

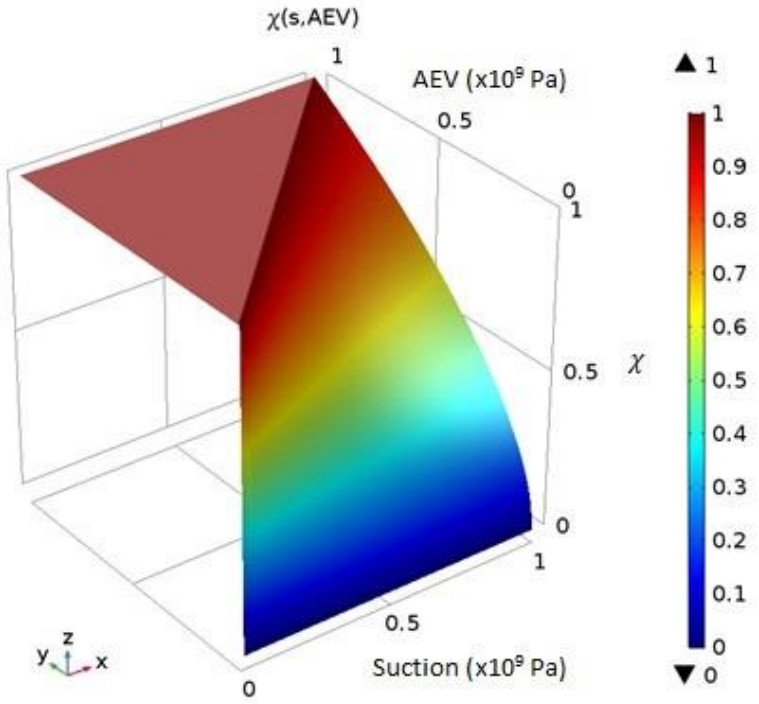

Figure 7. χ as a function of both AEV and suction

Table 7 lists the fitting parameters for the van Genuchten-Mualem model soil water characteristic curve (SWCC) and relative permeability function for the S1 validation study. Values for the van Genuchten SWCC fitting parameters were assessed from literature taking the calculated dry density of MX-80 bentonite [60, 39, 61, 37]. **Figure 8** and **Figure 9** depict the SWCC in the form of the effective degree of saturation and relative permeability of gas and water through bentonite as a function of suction.

Table 7. van Genuchten-Mualem SWCC and relative permeability function fitting parameters

Parameter	Value
SWCC fitting parameter, a′ (1/m)	0.00065*
SWCC fitting parameter, n′	2.04 [60]
SWCC fitting parameter, m′	0.51 [60]
Relative permeability function fitting parameter, L′	0.51†

*calculated from the calibrated AEV using equations (12) and (18) where $AEV = 8.0E6$ Pa and s'_{aev} = 3.46E7 Pa

†A value of $L' = 1$ was inputted by the user and required for COMSOL® to converge, and does not significantly change the relative permeability curves

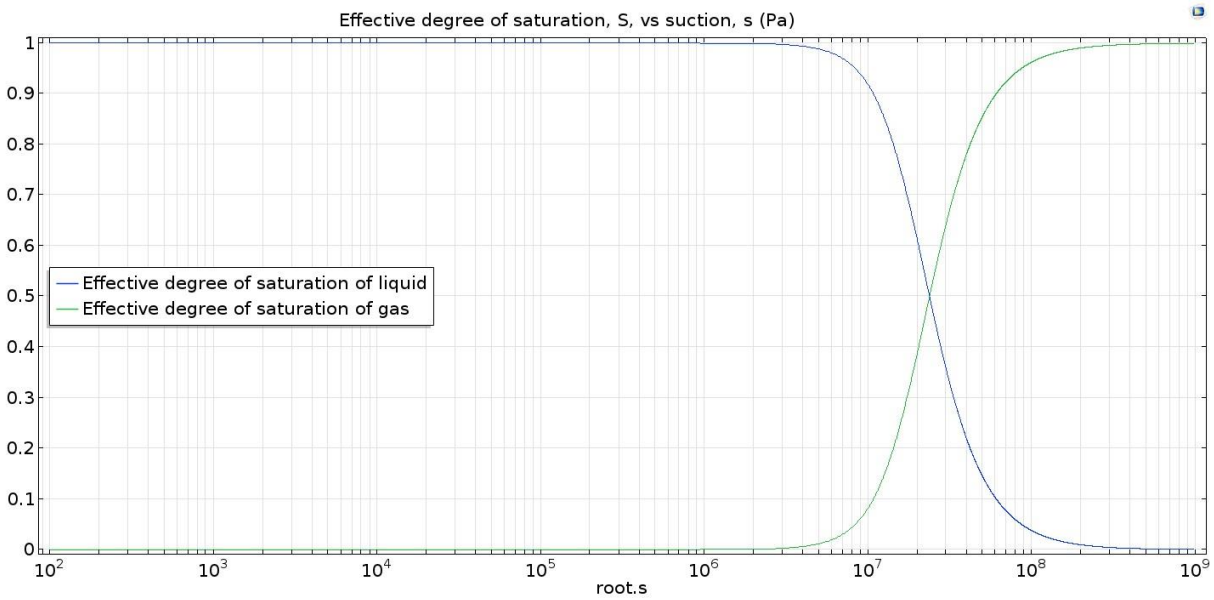

Figure 8. Soil water and soil gas characteristic curves for bentonite at n = 0.44

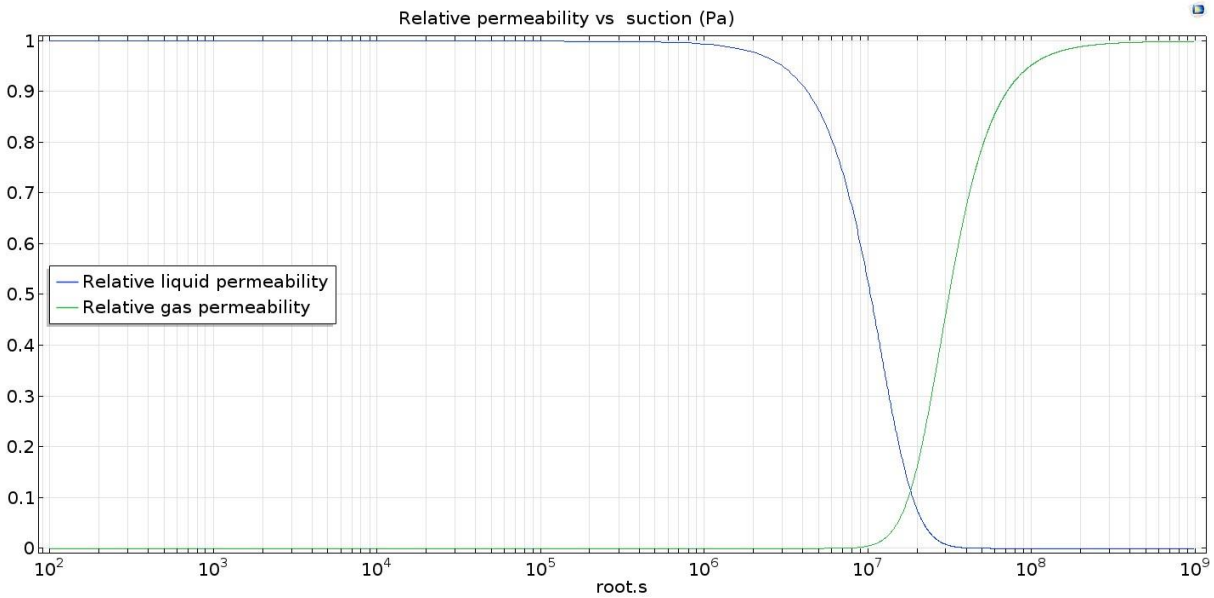

Figure 9. Relative permeability curves (water and gas) in bentonite vs suction at n = 0.44

4. Results and Discussion

In this section, the following sign convention is used: i) strain components and volumetric deformations are positive for expansion and negative for contraction; and ii) stress components and pressures are positive for compression and negative for tension.

4.1. S1: Validation Study

The results of the validation study are presented below. As shown in **Figure 10**, the proposed HM model was capable of simulating two-phase flow through the MX-80 bentonite specimen. Gas breakthrough (i.e., into the sample) was observed at 63.8 days when the gas-injection pressure of 8 MPa

corresponded to the AEV of the sample. Over the 120 day duration of the experiment gas migrated as a gas front through the first 5% of the sample.

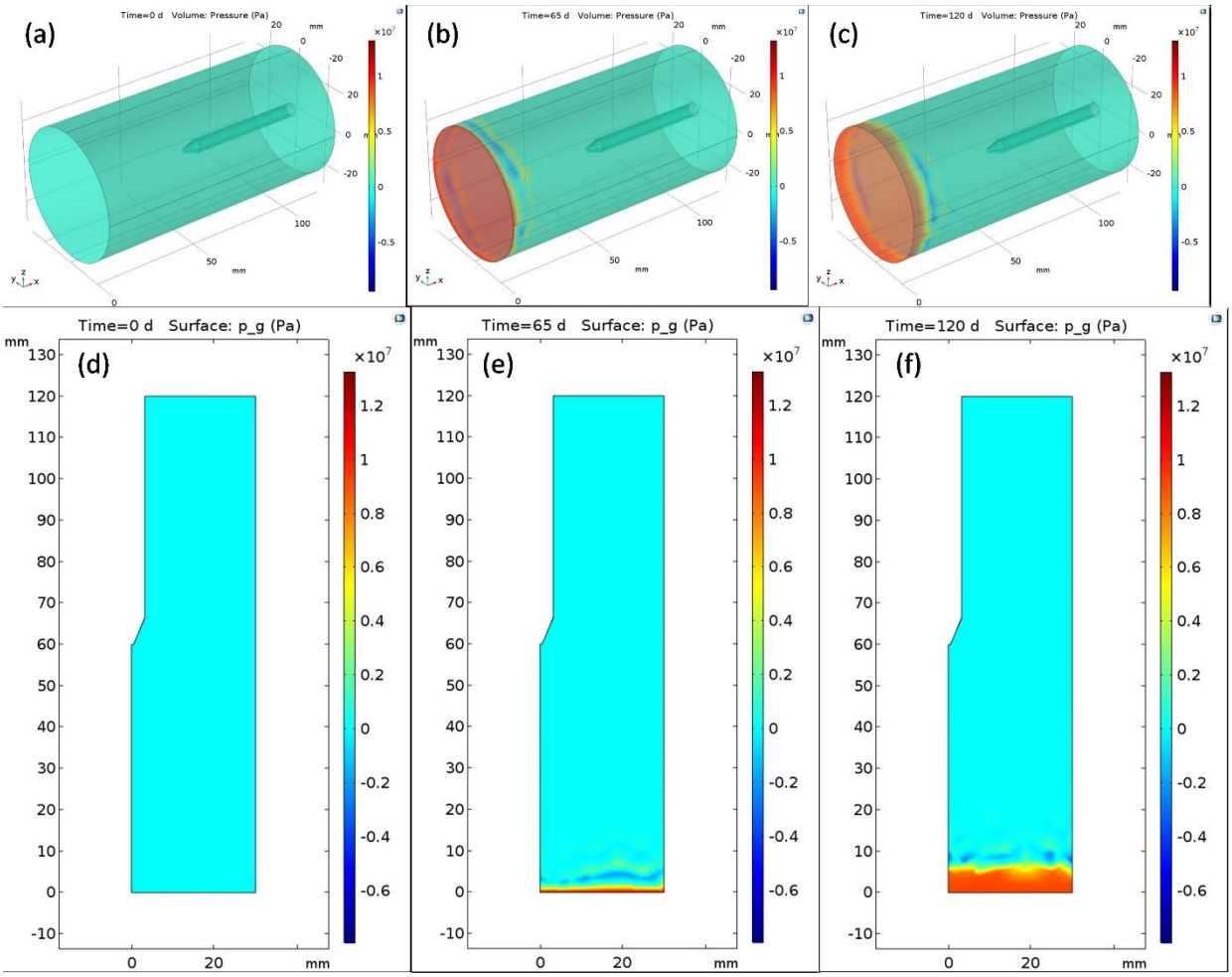

Figure 10. S1 Results – Gas migration through bentonite MX-80 sample. For the 3D model, at times (**a**) 0 *days*, (**b**) 65 days, and (**c**) 120 days; and for the 2D axisymmetric model, at times (**d**) 0 days, (**e**) 65 days, and (**f**) 120 days.

The 2D axisymmetric (2D) and 3D simulation results were compared against i) the experimental inflow and outflow profiles (**Figure 11**), ii) the experimental porefluid pressure profiles at the radial porewater arrays (**Figure 12**), and iii) the evolution of total stresses at the radial load cell arrays (**Figure 13**) over the 120 day study period.

Total gas flow into the sample is depicted in **Figure 11**(**a**). From the figure it is clearly observed that the onset of gas flow into the sample (i.e., gas breakthrough) occurs when the injection pressure reaches the AEV (around 63.8 days). The AEV was the only model parameter calibrated to match the experimental results, with the corresponding van Genuchten SWCC fitting parameter α' calculated from (12). The model was also able to reproduce the point in time when the gas injection pump was stopped, resulting in a rapid decline in gas inflow (71 days). The shape and timing of the modelled gas inflow curves matches the experimental data reasonably well, however, the peak magnitude of the modelled gas inflow was approximately half the magnitude of the experimental results. The fact that the simulation results of gas inflow were significantly lower than the experimental results, may be due to a lower modelled intrinsic

permeability at the breakthrough pressure. As the intrinsic permeability applied to the model was based on those measured by the BGS, it may be that some damage occurs at the breakthrough poregas pressure, which allow for a significant increase in poregas pressure. The 2D and 3D models were able to reproduce similar results to each other. Differences are likely due to mesh size and will be discussed further in scenario S12.

Figure 11(**b**) shows the experimental and modelled gas outflow. The experimental gas outflow results align with those of the inflow results, providing evidence that dilation-controlled gas flow is occurring, as the majority of gas moving into the system also leaves the system, with very little gas being stored within the system. Using the proposed model, no gas outflow was observed from the specimen, indicating that the model was not able to reproduce dilation-controlled gas flow, as could be observed via the peaks of the experimental dataset. This further supports the reasoning that inclusion of a damage model may be required to simulate the increase in gas permeability within the specimen in order to obtain gas breakthrough flow in-line with the experimental results.

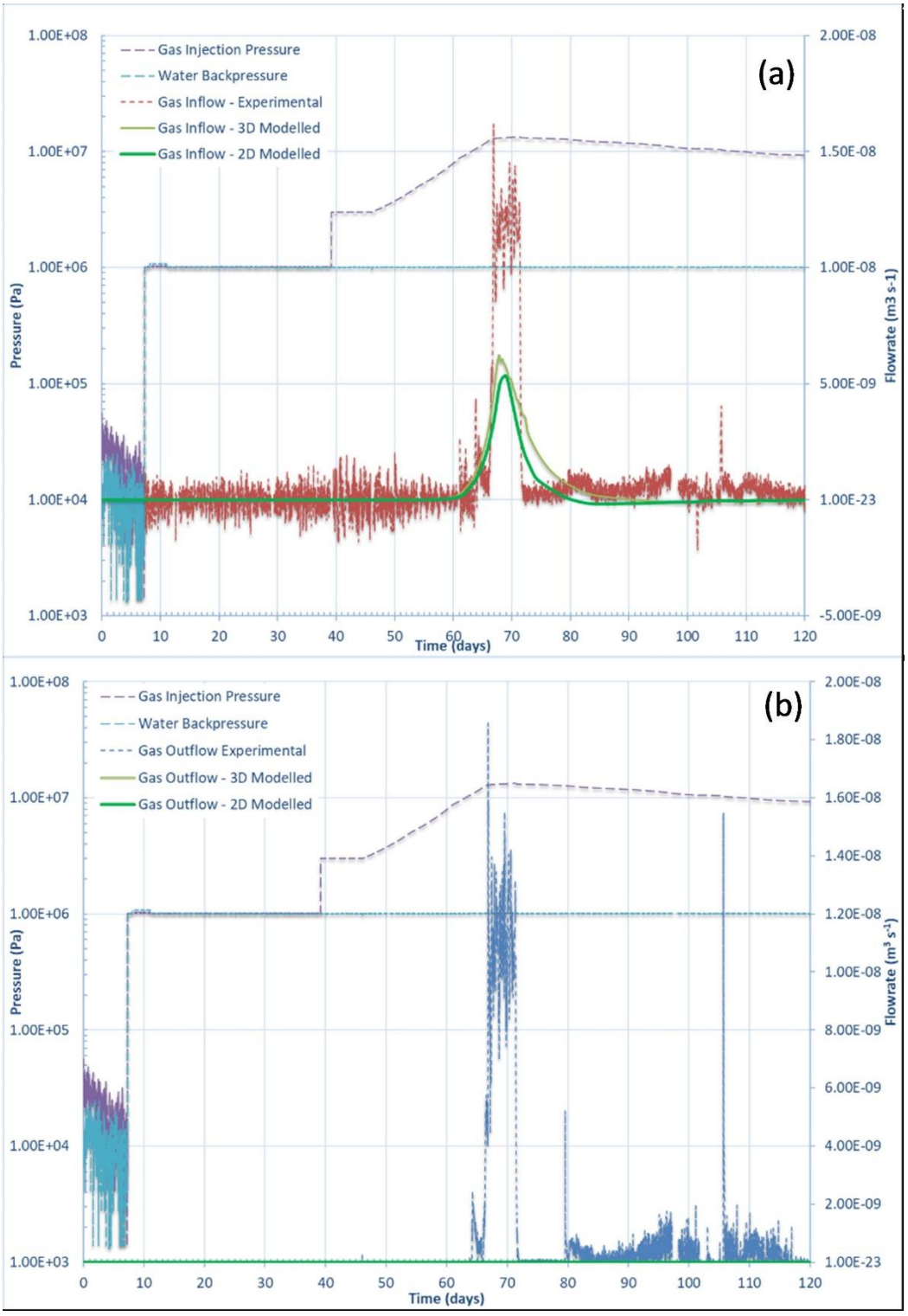

Figure 11. S1 Results – Gas (a) inflow and (b) outflow profiles over time

Similar results, though not all, are observed when comparing the porefluid pressure profiles obtained between the experimental and modelled results, as depicted in **Figure 12**(**a**). Following hydration of the sample which occurred between day 7.3 and day 39, gas testing began. At day 46 there is a sudden decrease

in porefluid pressure observed in the experimental results when the gas pressure into the system is ramped up. This is followed by an increase in porewater pressure in Porewater Array 1 and 2, while Porewater Array 3 continues to decrease. This initial decrease in porewater pressure could have occurred due to several factors. Supporting the notion that some damage or dilation may be occurring, an increase in the pore-space due to damage would result in a decrease in porewater pressure. Additionally, this could be further explained by the effect of suction, where the system attempts to maintain a capillary pressure close to zero. Unfortunately, these features were not able to be reproduced by the model and will be further investigated in scenario S11.

Once the gas injection pressure reaches the AEV however, increases in porefluid pressures at the porefluid arrays were observed in response to increasing gas injection pressures. At this point the model was able to adequately reproduce key features of the experimental results including both the shape and timing of changes in porefluid pressure. However, the extent of porefluid pressure build-up is not as large or as sharp as that depicted by the experimental results. Regarding the lower peak of the porefluid pressure profiles, this is to be expected as the model was not able to simulate gas flow through the porefluid pressure arrays, and therefore there is little contribution of poregas pressure to the porefluid pressure. As a result, the increase in porefluid pressure observed is dominated by the displacement of porewater by the poregas as it migrates through the front end of the bentonite specimen, creating a porewater pressure gradient.

This leads to another distinguishable feature; in the modelled results, following gas breakthrough into the sample, there is a clear separation in the porefluid pressure profiles between the three porewater arrays. This lag can be attributed to the time it takes for the displaced water to push through the soil column, and results in the increase in porefluid pressures. This is can be seen in the experimental results as well although less pronounced due to the use of a log scale in **Figure 12**(**a**).

The difference in the sharpness or steepness of the porefluid pressure profiles in comparison to the experimental results is also expected and can be partially attributed to the use of van Genuchten SWCC equation, which provides a continuous smooth function at the interface between the saturation zone and the desaturation zone (i.e., AEV). In addition to this, during analysis of the modelling results obtained using the 2D-axisymetric model vs 3D model, it was identified that mesh size plays a large role in the shape and steepness of the porefluid pressure profile at the AEV. This is further investigated in scenario S12.

In **Figure 12**(**b**), the results of the porefluid pressure profiles along the axial length of the soil specimen are presented. At the beginning of the simulation (t = 0 days), the modelled results show a negative porefluid pressure along the soil specimen. This is expected as the soil specimen was not fully saturated. During the hydration phase (day 7.3 to day 39), the porefluid pressures stabilize at 1 MPa, representing equilibrium with the defined BCs. Following a ramp up of gas injection pressures front from day 39 to day 63, a small increase in porefluid pressures at the gas injection front is observed (at t = 60 days). Once the gas injection pressure exceeds the AEV at day 63, a continuous gas phase begins entering the sample, and a large increase in the porefluid pressure gradient across the sample is observed as depicted by the curve t = 80 days. Once gas injection is stopped, the porefluid pressure gradients begins to decrease and equilibrate back towards the backpressure BC of 1 MPa as depicted by the decrease in porefluid pressure gradients along the length of the soil specimen at day 100 and day 120. The behaviour depicting the change in porefluid pressure gradients over time depicted by the model results in **Figure 12**(**b**) agree with our conceptualization of the experiment.

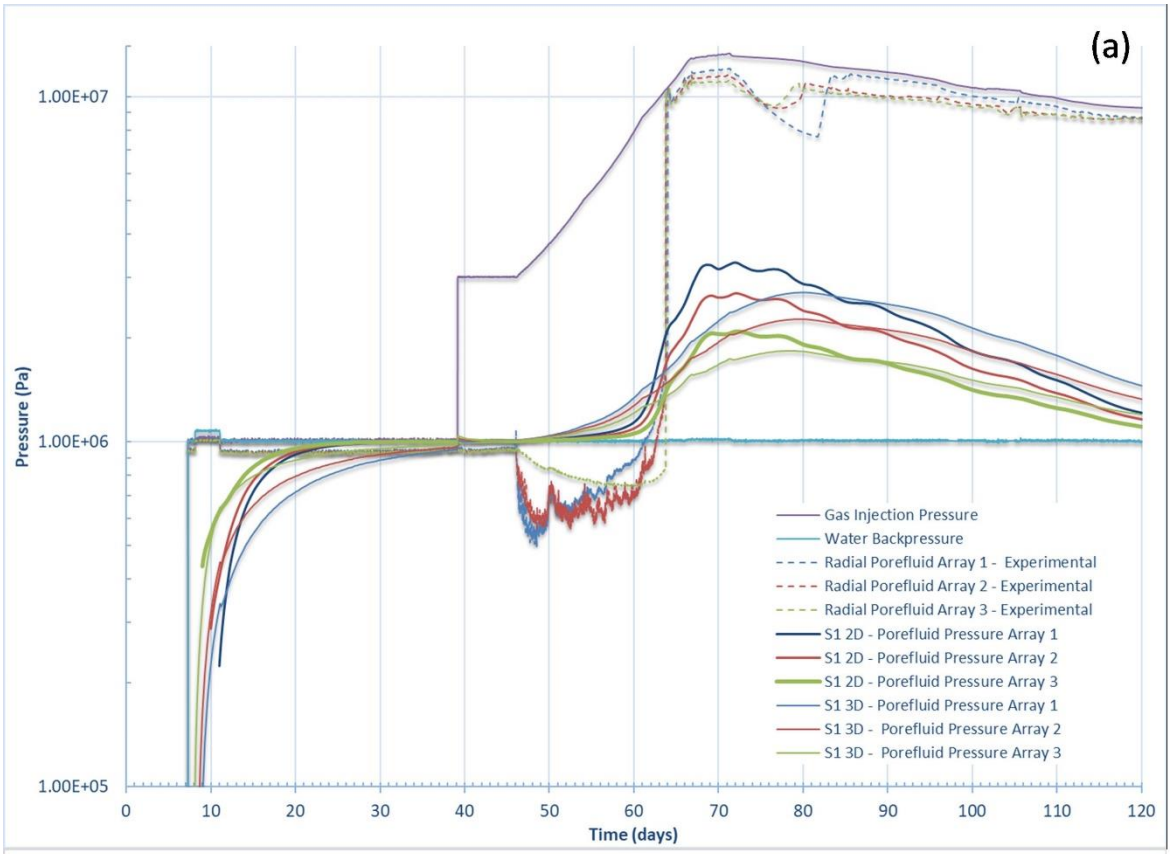
(a)
1.00E+07
1.00E+06
1.00E+05
Pressure (Pa)
0
10
20
30
40
50
60
70
80
90
100
110
120
Time (days)
Gas Injection Pressure
Water Backpressure
Radial Porefluid Array 1 - Experimental
Radial Porefluid Array 2 - Experimental
Radial Porefluid Array 3 - Experimental
S1 2D - Porefluid Pressure Array 1
S1 2D - Porefluid Pressure Array 2
S1 2D - Porefluid Pressure Array 3
S1 3D - Porefluid Pressure Array 1
S1 3D - Porefluid Pressure Array 2
S1 3D - Porefluid Pressure Array 3

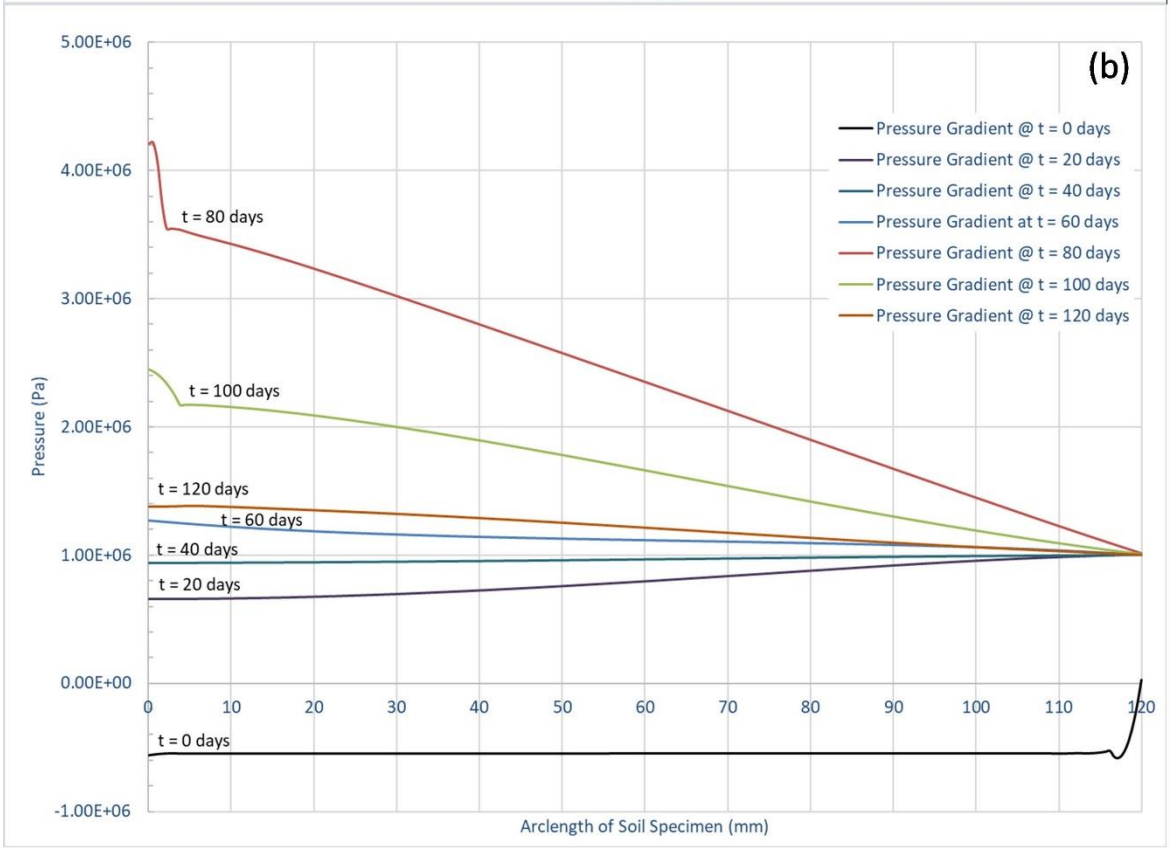
(b)
5.00E+06
4.00E+06
3.00E+06
2.00E+06
1.00E+06
0.00E+00
-1.00E+06
Pressure (Pa)
0
10
20
30
40
50
60
70
80
90
100
110
120
Arclength of Soil Specimen (mm)
Pressure Gradient @ t = 0 days
Pressure Gradient @ t = 20 days
Pressure Gradient @ t = 40 days
Pressure Gradient at t = 60 days
Pressure Gradient @ t = 80 days
Pressure Gradient @ t = 100 days
Pressure Gradient @ t = 120 days
t = 80 days
t = 100 days
t = 120 days
t = 60 days
t = 40 days
t = 20 days
t = 0 days

Figure 12. S1 Results – Porefluid pressure profiles over (a) time and (b) axial length of the specimen

For the 3D case, the total radial stresses, which are a measure of both the net normal stress acting on the solid matrix and porefluid pressure is presented in **Figure 13**. Again, we see the model able to reproduce both the shape and timing of the stress evolution acting on the radial load cell arrays. However, the magnitude could not be reproduced and was an order lower. The increase in the total radial stresses, which leads to the deviation between the experimental results and the modelled results, occurs during the initial hydration phase. This is, in part, likely a result of neglecting the effect of swelling pressure in the numerical model, a key behaviour of expansive clays. If a swelling pressure is considered in the model, then an increase in the total radial stress response being modelled during the hydration phase would be expected as well and could account for this difference.

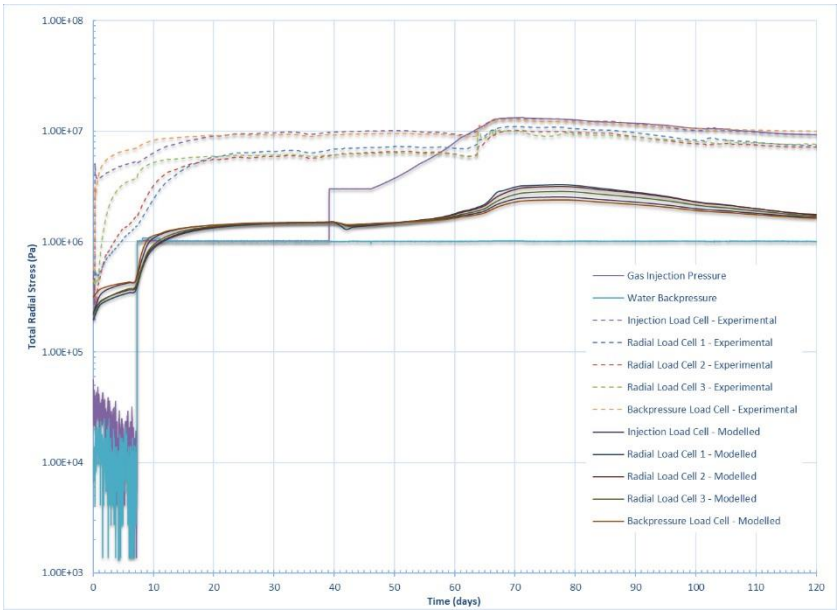

Figure 13. S1 Results – Total radial stresses over time

From the investigation of the validation scenario, S1, it was identified that improved results could be obtained if at some critical pressure, a large change in porosity, resulting in an increase in the gas permeability of between two to three orders of magnitude was introduced into the model as will be demonstrated by S11.

4.2. S2-S4: Parametric Studies

The 3D results of the parametric studies S2, S3, and S4 are provided in **Figure 14**. These results assess the contribution of advection, diffusion of gas within porewater, and the advection of dissolved gas in porewater to the flow behaviour, given the benchmark dataset available.

In **Figure 14**(**a**), the total gas inflow is broken down to the contributions from the individual mechanisms of gas migration being modelled: i) advective gas flow; ii) diffusive gas flow (diffusion of gas dissolved in porewater); and iii) advection of dissolved gas within porewater. As can be seen, gas migration is diffusion dominated until the AEV is reached, and gas migration into the sample occurs, whereby gas advection becomes the predominant transport mechanism. The results also show that advection of dissolved gas in porewater is minimal, which is to be expected as there is little movement of porewater through the system.

To demonstrate that diffusion is being adequately presented by the model, **Figure 14**(**b**) depicts the gas concentration along the length of the specimen over time. There are four distinct phases identified in the figure, and each is separated by a jump corresponding to periods when the gas injection pressure is rapidly increased requiring the system to re-establish equilibrium. The first section represents the initiation of the experiment at t = 0 days. The second phase represents the hydration period (day 7.3 to day 39), where the gas injection pressure is maintained with the water backpressure at 1 MPa. The third phase begins at the onset of gas testing on day 39, and as gas injection pressure is ramped up, so does the concentration of gas in porewater resulting in a new gradient and the system re-establishing equilibrium. The fourth phase can be identified by a decreasing concentration gradient which occurs once gas injection has stopped (day 73). These are the expected behaviours that would be observed based on the governing equations being applied in the model.

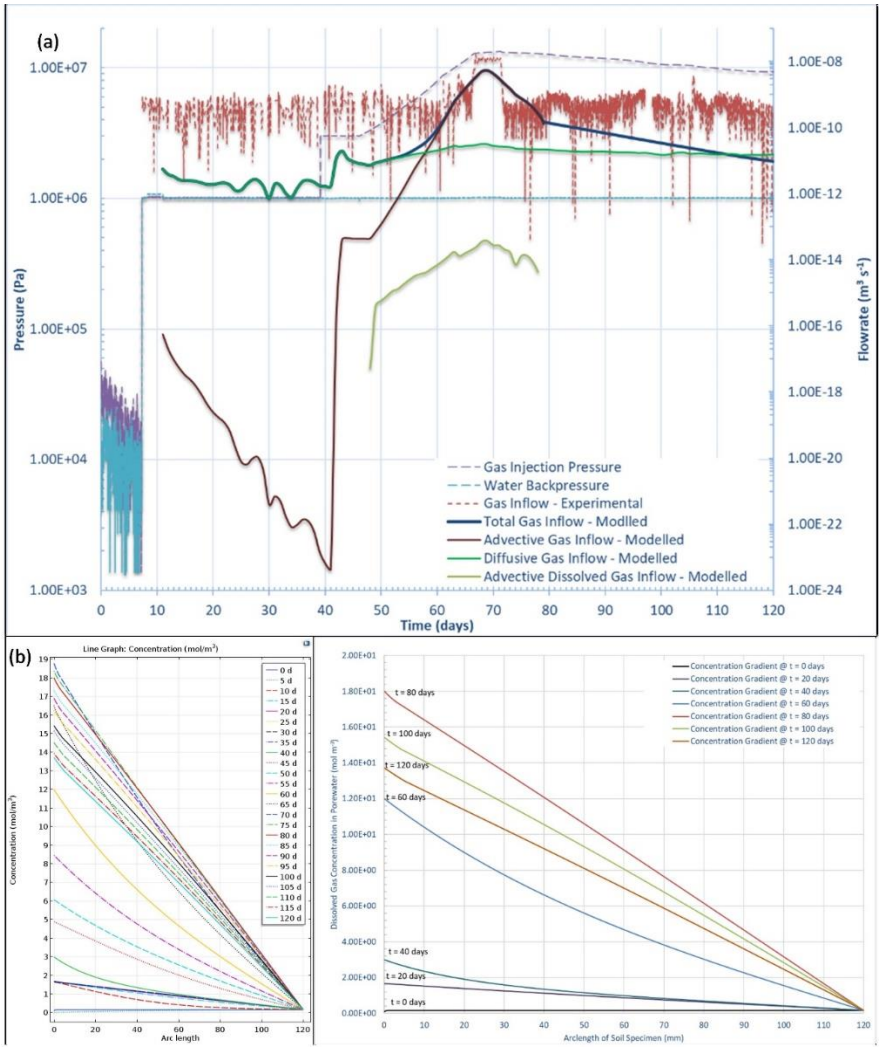

Figure 14. S2-S4 Results – (a) Contribution of advection, dissolution and diffusion to flow behaviour and (b) diffusion gradient over axial length of the soil specimen

In **Figure 15**(**a**) comparison of the porefluid profile curves for the S2, S3, and S4 scenarios are indistinguishable. This is to be expected as the porefluid pressure is a function of the pore-gas and pore-

water pressures via equation (3), and the porewater pressure is not dependent on the concentration of dissolved gas.

The results of S4 are compared to S1 in **Figure 15** (b) to see the effect of linear-elastic deformation to the flow behaviour. Although there is little contribution to flow behaviour, the HM model has smoother curves than the hydraulic models alone and could be an indication of a more stable model.

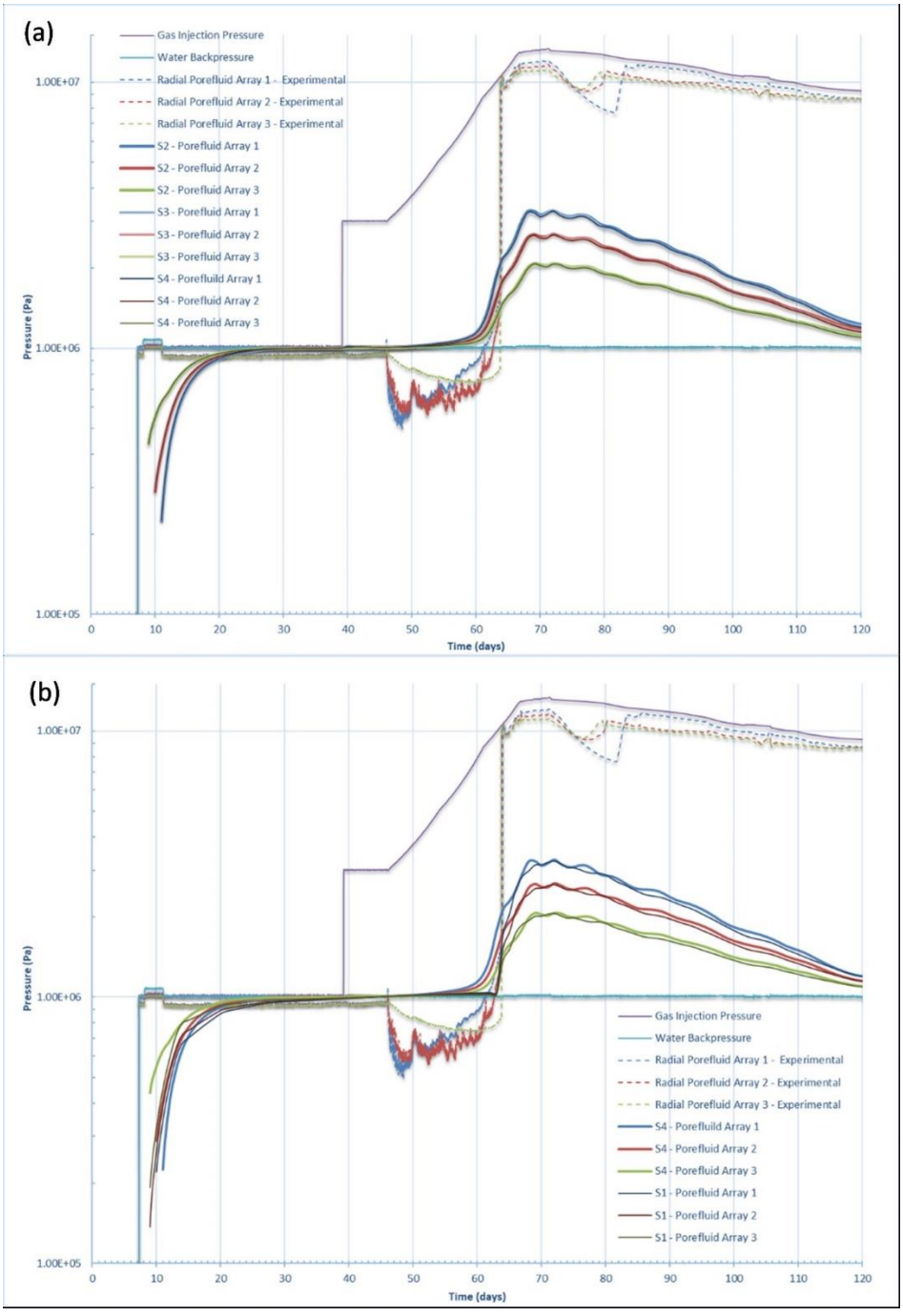

Figure 15. Contribution of (**a**) advection, dissolution and diffusion and (**b**) elastic deformation to porefluid pressure profiles

The results of the parametric studies demonstrate that for the experiment under consideration, at high gas pressures, gas flow is controlled by advection, with diffusion and elastic deformation contributing little to flow behaviour. It is also evident by the porefluid profile curves, that the mechanical deformation resulting from the inclusion of a linear-elastic model is not sufficient to result in dilatancy and self-healing of the bentonite pores. This is further illustrated by **Figure 16**, which shows small changes in porosity over time at each porefluid array. It should be noted, that as there is a constant volume boundary condition applied, the total deformation throughout the sample is in equilibrium.

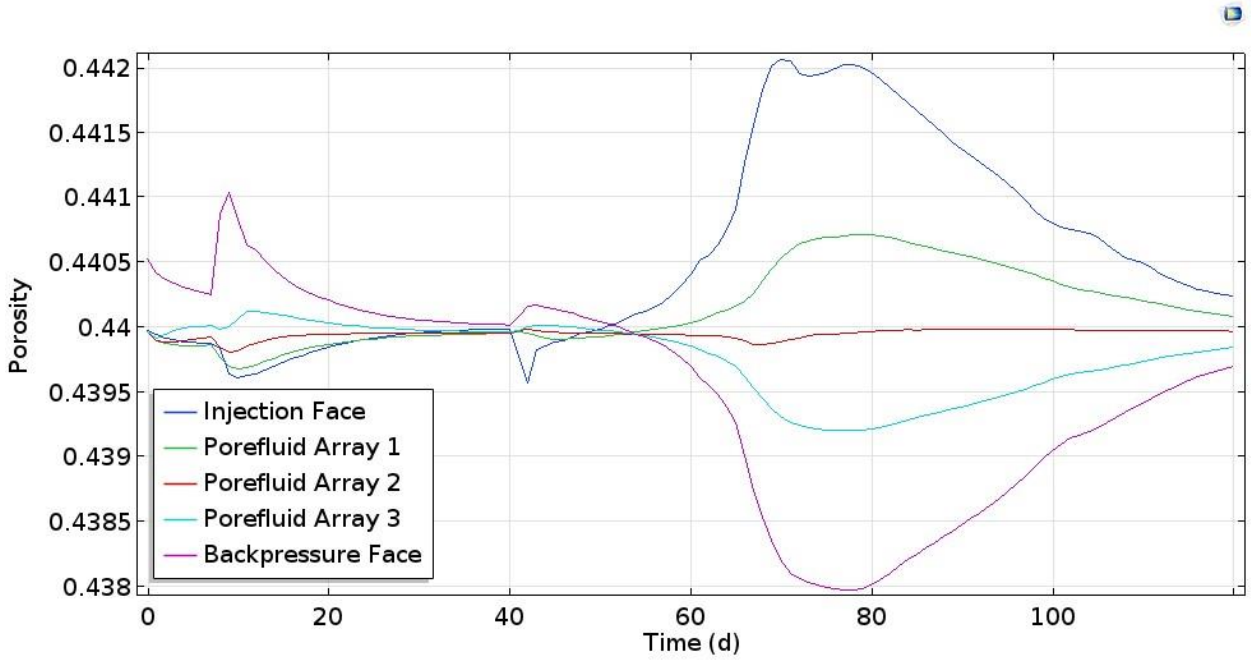

Figure 16. Change in porosity over time as a result of elastic deformation

4.3. Sensitivity Analysis

4.3.1. S5-S6: Effect of Porosity

The effect of increasing and decreasing the initial porosity on the porefluid pressure profiles are depicted in **Figure 17**(**a**) and on gas inflow in **Figure 17**(**b**). As described by equation (17) and equation (21), both the AEV (and corresponding SWCCs and relative permeability curves) and intrinsic permeability are a function of the porosity. An increase in the initial porosity to 0.48, results in both a decrease in the AEV, noted by earlier gas breakthrough, and an increase in the intrinsic permeability, as depicted by higher peak porefluid pressures. Similarly, by decreasing the initial porosity to 0.3, the required AEV for gas breakthrough is not reached by the experimental gas injection pressures. As a result, there is no gas migration into the specimen, and no change in the porefluid pressure profiles. This is as expected, providing confidence in the model.

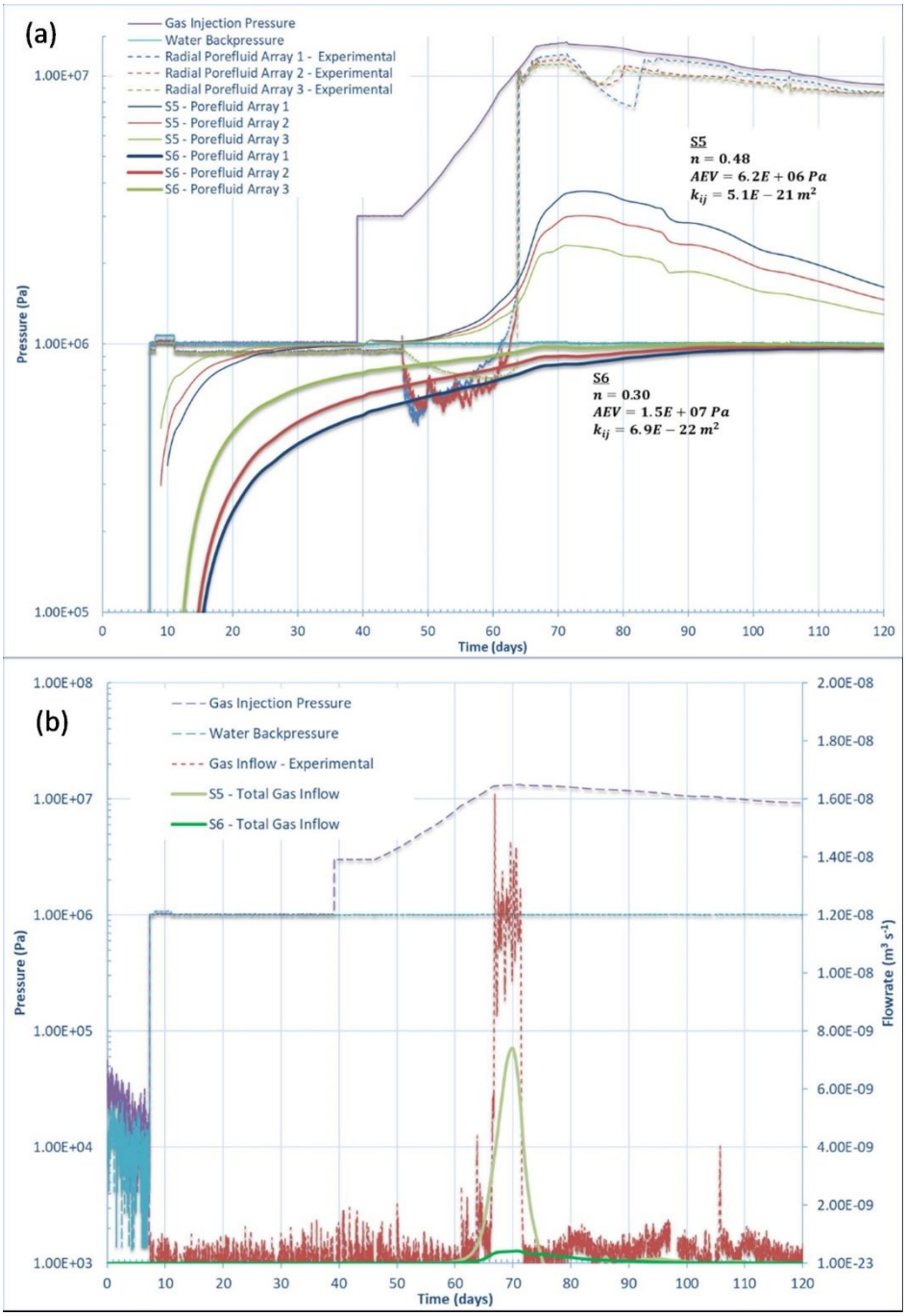

Figure 17. S5-S6 Results – Effect of changes in initial porosity on (a) porefluid pressure and (b) gas inflow

4.3.2. S7-S8: Effect of Air-Entry Value

The effect of increasing and decreasing the AEV, independent of porosity, on the porefluid pressure profiles are depicted in **Figure 18**(**a**) and on gas inflow in **Figure 18**(**b**). Since the amount of elastic deformation is small (see **Figure 16**), and therefore contributes little to changes in the AEV and intrinsic permeability, results of S7 and S8 are like those of S5 and S6. A decrease of the AEV to 5.0E+06 Pa results in earlier gas breakthrough and higher peak porefluid pressures, and an increase of the AEV to 2.0E+07 Pa, results is very little migration into the specimen.

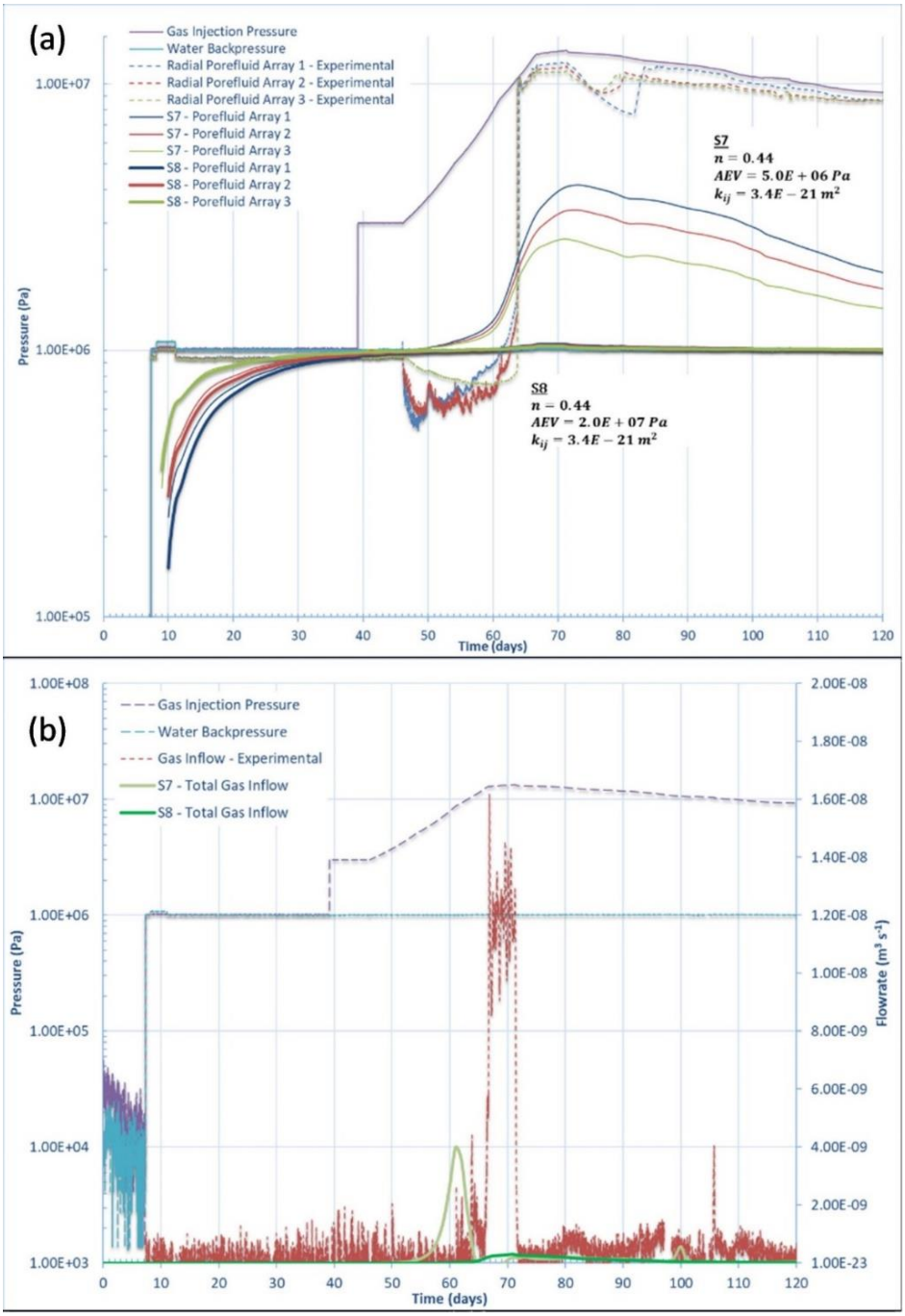

Figure 18. S7-S8 Results – Effect of changes in AEV on (a) porefluid pressure and (b) gas inflow

4.3.3. S9-S10: Effect of Intrinsic Permeability

The effect of increasing and decreasing the intrinsic permeability, k_{ij}, independent of porosity, on the porefluid pressure profiles are depicted in **Figure 19**(**a**) and on gas inflow in **Figure 19**(**b**). For the S9 simulation an increase in k_{ij} by two orders of magnitude to 10^{-20} m² shows an increase in the porefluid pressure profile once the AEV is reached, however the peak of the curve is now lower than the S1 scenario. This is to be expected as a lower porefluid pressure gradient will occur.

For the S10 scenario, a decrease of k_{ij} by over an order of magnitude to 10^{-22} m² resulted in no visible increase in the porefluid pressure profile, even when the AEV is exceeded. This is to be expected, as the experimental intrinsic permeability of 3.4E-21 m² is already low, and by decreasing it further, advective gas migration becomes so slow that once the gas pressure exceeds the AEV, there is little displacement of porewater within the experimental timeframe.

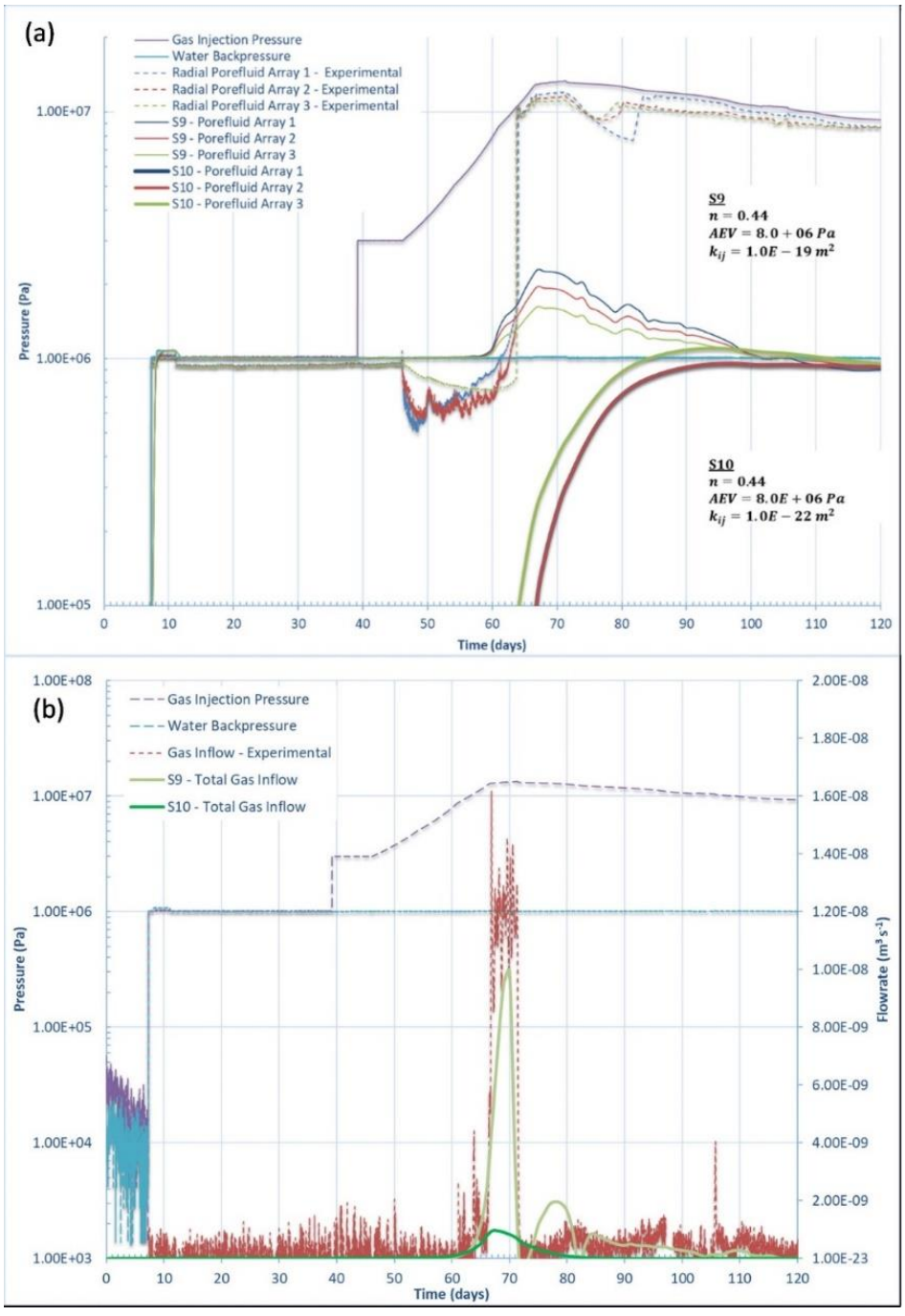

Figure 19. S9-S10 Results - Effect of changes in k_{ij} on (**a**) porefluid pressure and (**b**) gas inflow

4.3.4. S11: Effect of Damage

The parameters for the damage model presented by equations (34) to (38) are provided in **Table 8**. The compressive and tensile strengths were estimated based on information provided by Man & Martino [61], while the strains at compressive and tensile failure were calculated from the elastic modulus.

Table 8. Material properties for the Damage Model

Material	Parameter	Value
Solid Soil Matrix (Bentonite)	Compressive strength, f_c (MPa)	1
	Residual compressive strength, f_{cr} (MPa)	0.09
	Strain at compressive strength, ε_{c0}	0.0003
	Tensile strength,f_t (MPa)	-1
	Residual tensile strength, f_{tr}(MPa)	-0.09
	Strain at tensile strength, ε_{t0}	-0.0003
	Maximum permeability at maximum damage, k_{max} (m^2)	1E-18
	c, smoothing coefficient	2

The results of Scenario S11, investigating the inclusion of a damage model, are presented below. **Figure 20**, **Figure 21**, and **Figure 22** show the results for the effect of damage on the gas inflow and outflow behavior, porefluid pressure profile behavior, and total radial stresses behavior, respectively. Overall, the modelled results demonstrate much better agreement with the experimental results. Of interest is the maximum intrinsic permeability, k_{max}, which was calibrated to a value of 1E-18 m^2 in an attempt to match the peak experimental inflow.

As can depicted in **Figure 20**(**a**), considering damage, the modelled inflow is significantly higher with a peak inflow of 1.4E-9 m^3/s, and roughly 40 times higher than without damage, though it is still an order of magnitude lower than the experimental results. Also, as shown in **Figure 20**(**b**), the model was not able to reproduce gas outflow.

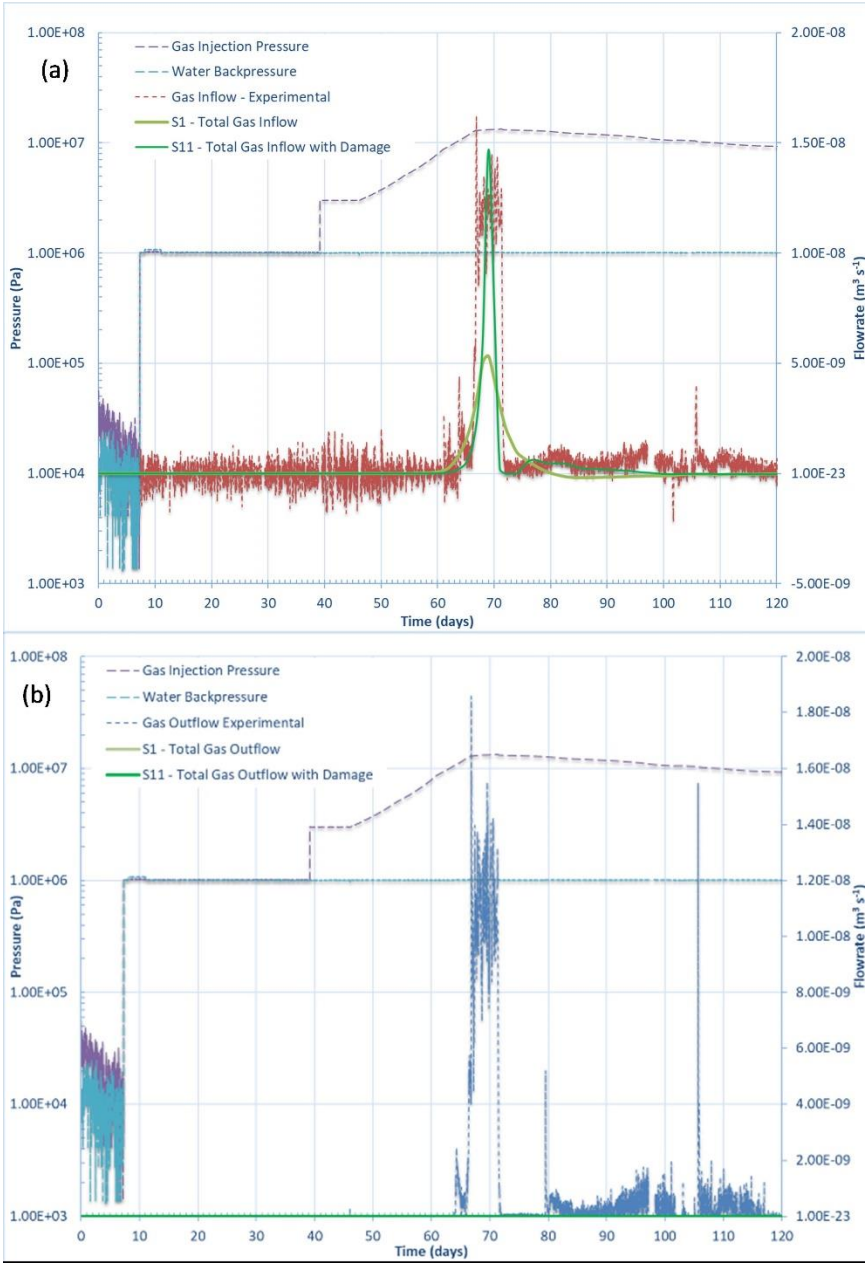

Figure 20. Effect of Damage on gas (a) inflow and (b) outflow

In **Figure 21**, the magnitude, shape and timing of the porefluid pressure profile curves are closer to the experimental results, however the full magnitude was still not realized. The total radial stress profiles are depicted in **Figure 22**, and have only improved slightly as a result of damage. **Figure 23** depicts the point of gas entry into the specimen and the migration of gas over time. Significantly increased gas flow is observed with the inclusion of the damage model, however still no preferential flow pathways representing dilation-controlled gas flow were observed.

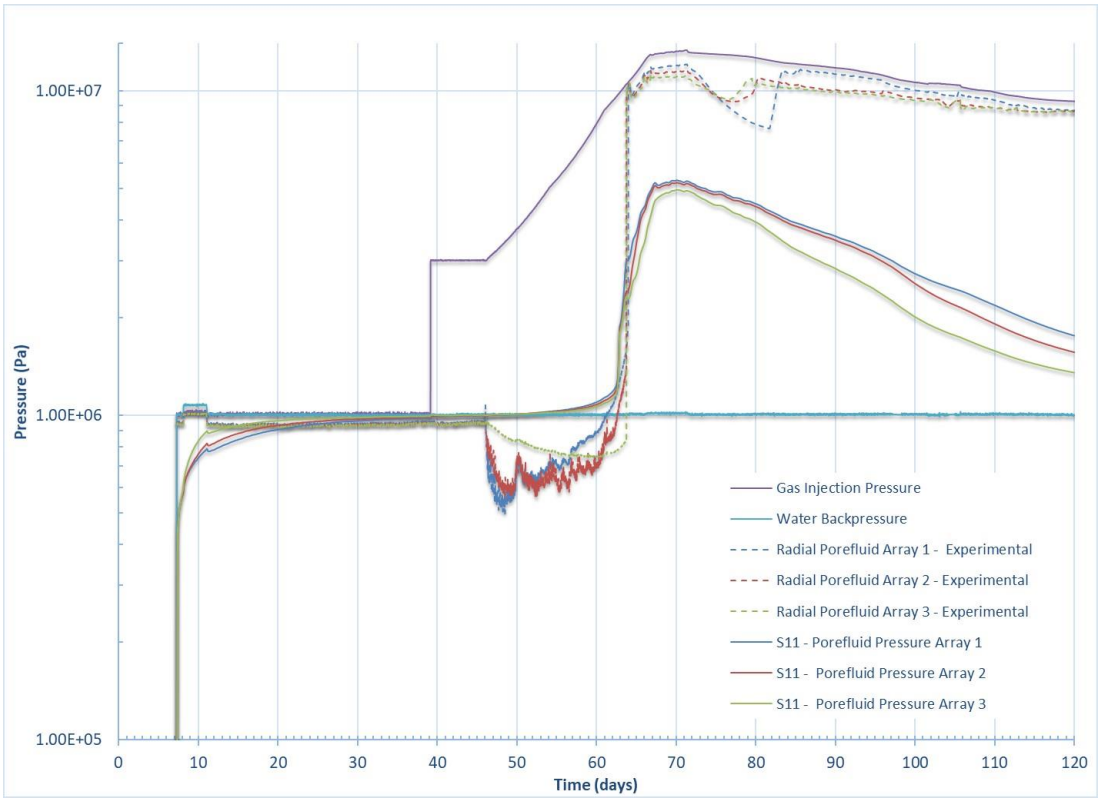

Figure 21. Effect of Damage on the porefluid pressure profiles

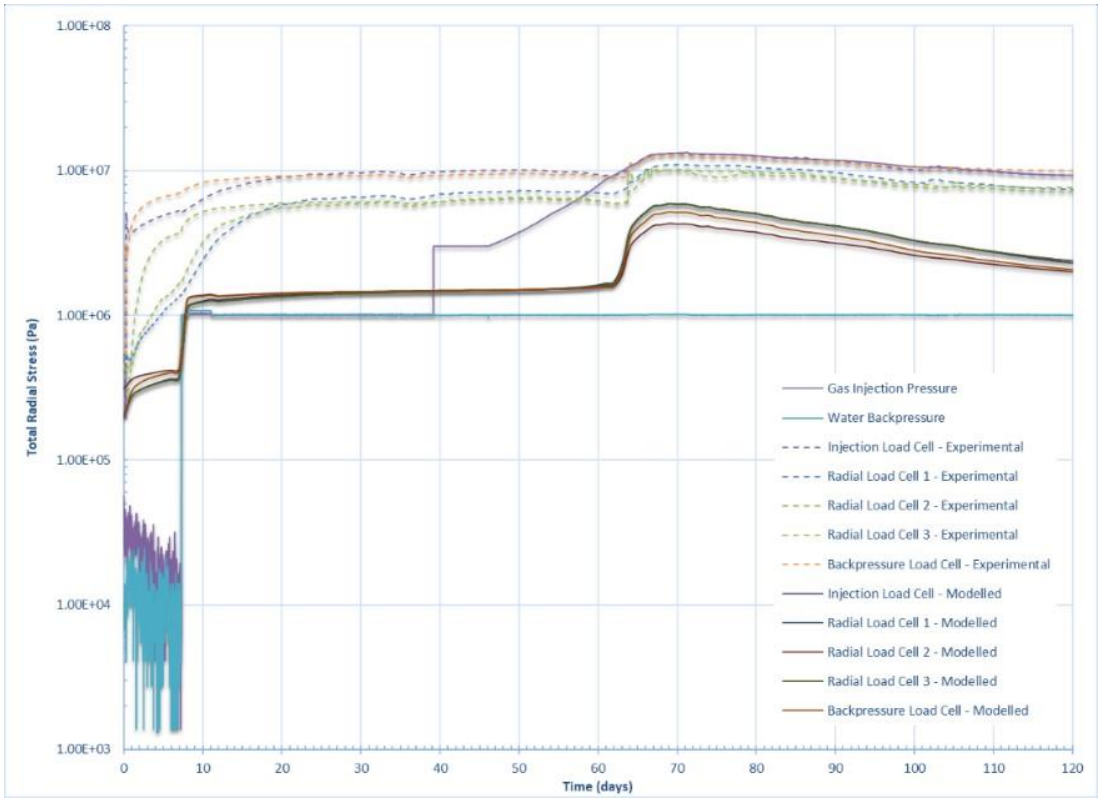

Figure 22. Effect of Damage on total radial stresses

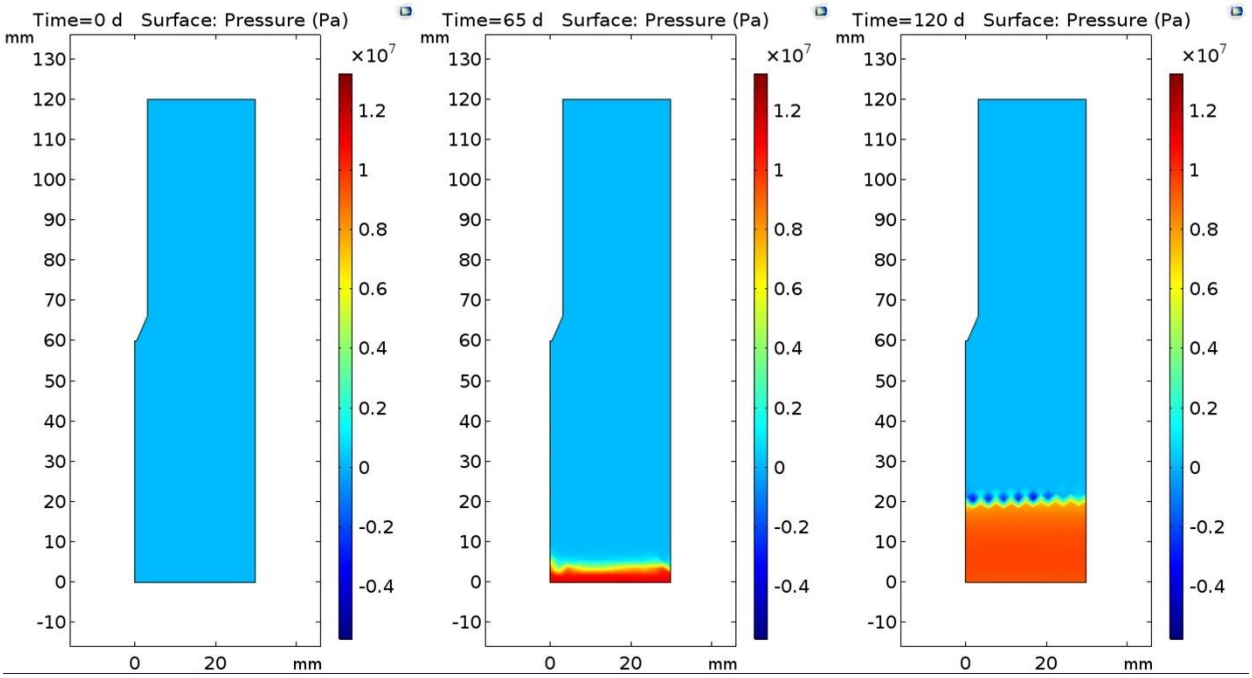

Figure 23. S11 Results – Gas migration through bentonite MX-80 sample for the 2D axisymmetric model at times (**a**) 0 days, (**b**) 65 days, and (**c**) 120 days.

Although inclusion of damage to the model provides much better agreement with the experimental results, key features of the experimental gas outflow results depicting dilatancy and self-healing were not reproduced. There is therefore still a need to investigate additional mechanisms to model dilatancy-controlled gas flow. Such mechanisms will be investigated in future studies. These will include the consideration of spatially weighted heterogeneity for porosity and a poro-elasto-plastic model to simulate flow through preferential pathways. Inclusion of a swelling stress term will also be added to investigate the swelling behaviour in expansive soils. Finally, an investigation into constitutive relations to simulate the self-healing behaviour of swelling soils will be included.

4.3.5. S12: Effect of Mesh size

A major finding of the study was the effect of mesh size on the shape of the porefluid pressure profile curves. This was initially observed when moving from a 2D-axisymetric geometry to a 3D geometry, where the number of degrees of freedom needed to solve the model significantly increases. As a result of the increased computational expense, the 3D model was not able to complete a run at higher mesh sizes, using the fully coupled, or segregated solvers in COMSOL®. To exemplify this, the number of elements and degrees of freedom for each geometry are provided in **Table 9**.

Table 9. Number of elements and degrees of freedom for 2D Axisymmetric and 3D models

Mesh Qualifier	No. of Elements	Degrees of Freedom
2D Axisymmetric HM		
Extremely Fine	6 336	83 632
Extra Fine	1 778	22 094
Finer	602	7 254

Normal	214	2,450
	3D HM	
Extra Fine	81 067	1 278 368
Finer	21 553	333 479
Normal	4 009	59 086

Figure 24 shows the effect that mesh size has on the shape of the porefluid pressure curve. In **Figure 24** results of the porefluid pressure profiles for Array 1 (blue curves) and Array 2 (red curves) with an extremely fine, finer, and normal mesh are compared. By applying a more refined mesh (i.e., solving more degrees of freedom), results in a steeper porefluid pressure curve at gas inflow and a higher peak porefluid pressure, leading to a higher resolution solution.

A similar comparison can be made between the 2D axisymmetric solution with an extremely fine mesh size and the 3D solution with a finer mesh size as depicted in **Figure 12**(**a**). Due to the computational cost of modelling in 3D this poses a number of challenges. For one, preferential flow pathways cannot be adequately modelled using a 2D axisymmetric geometry, as the microfractures cannot intersect the axis of symmetry. Therefore, in order to model dilatancy-controlled gas flow in heterogeneous specimens and propagate preferential flow pathways, it will be crucial to model in 3D. To address this current limitation, future studies will assess the use of different solvers and methods in COMSOL®, which may include the incorporation of discrete models, and identify ways to optimize the model for improved computational efficiency.

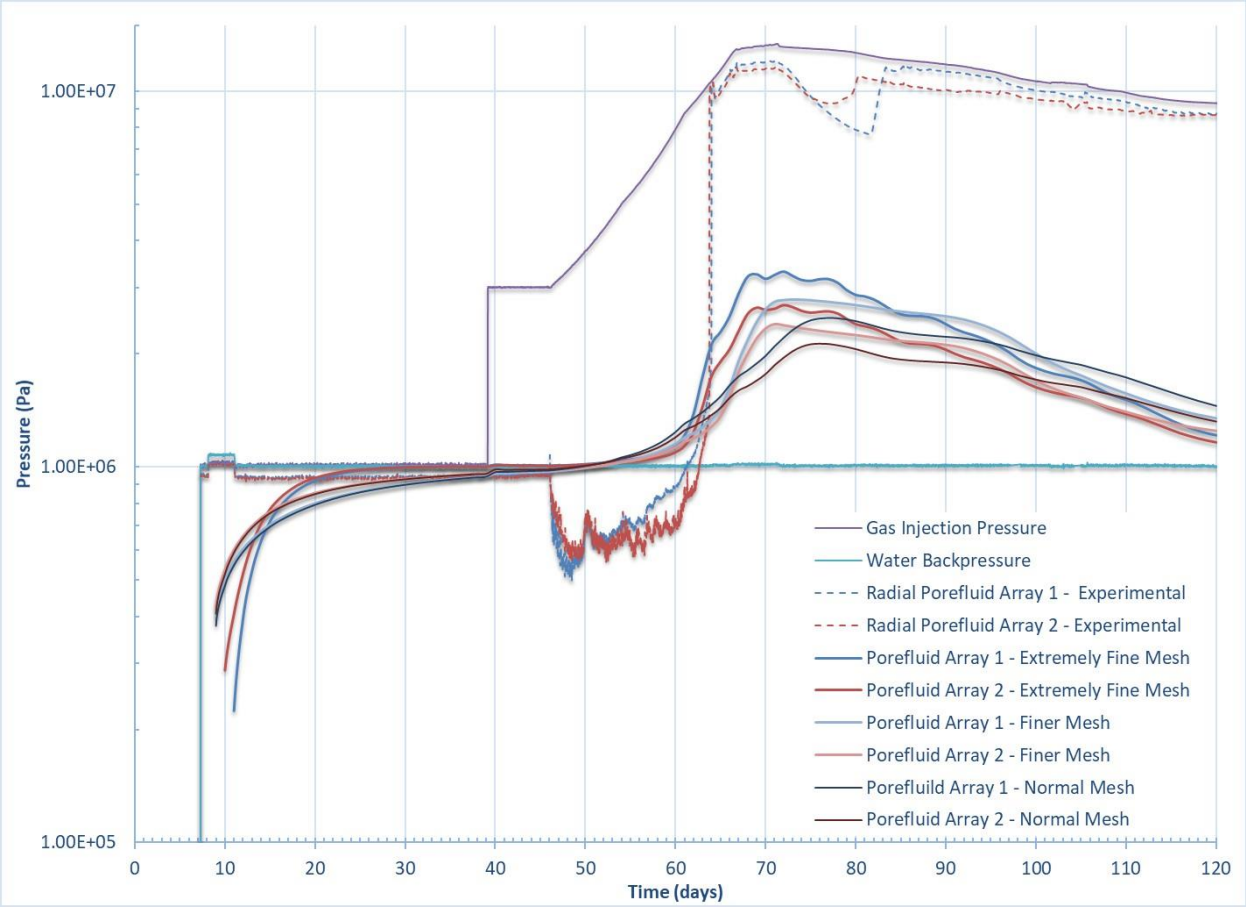

Figure 24. Effect of mesh size on porefluid pressure profiles

5. Conclusions

An important component in the design and long-term safety assessment of a DGR is the long-term performance of bentonite seals as barriers against gas migration in order to ensure the future safety to human health and the environment as a result of the exposure to these radionuclides. This paper proposes a hydro-mechanical linear poro-elastic visco-capillary mathematical model for advective-diffusive controlled two-phase flow using a Bishop's effective stress. The objective of this study was to gain insight into the key parameters influencing gas-flow behaviour in multiphase flow, and to identify whether dilation-controlled gas flow could be represented by such a model.

A validation study was conducted against experimental data from 1D flow through a saturated bentonite sample under a constant volume boundary stress condition. The experimental data demonstrated features of dilatancy-controlled gas flow. The modelled results were compared to key features of the experimental data, including the gas inflow and outflow behaviour, pore-pressure fluid behaviour, and evolution of radial stresses over the duration of the experiment. Although the model was not able to reproduce dilation-controlled gas outflow from the sample, it was able to simulate two-phase flow of water and gas through the sample, once the AEV was reached, and gas flow into the specimen was observed.

The model was able to reproduce key features of the experimental results, including both the shape and timing of changes in gas inflow, porefluid pressure, and radial stress evolution through the sample. However, the magnitude of such features was not able to be reproduced. It was identified that improved results could be obtained if at some critical pressure, a large change in porosity, resulting in an increase in the gas permeability of two to three orders of magnitude was introduced into the model.

In light of this, the effect of the inclusion of a damage model was investigated. The study confirmed that a damage mechanism calibrated to the maximum gas permeability required to match the peak experimental inflow could be successfully applied and results in much better agreement with the experimental results.

Parametric studies were performed to assess the contribution of advection, dissolution and diffusion of gas, as well as linear-elastic deformation on flow behaviour. The results of the parametric studies demonstrated that at high gas pressures, gas flow was controlled by advection, with diffusion and elastic deformation contributing little to flow behaviour. Sensitivity analysis were conducted by changing the initial porosity, permeability, and AEV of the swelling soil to test the model behaviour. In all cases the model behaved as expected.

This study provides a preliminary model for migration of gas through low-permeability swelling soils and was able to simulate two-phase flow with dissolution of gas. Further development of the model to better mimic dilation-controlled gas-flow will be addressed in subsequent studies. This model provides a basis for developing more advanced models to describe the phenomena of dilatancy-controlled gas flow.

The results of this study conclude that in order to mimic dilation, and dilatancy-controlled gas flow, additional mechanisms need to be considered within the model. Such mechanisms will be investigated in future studies. These will include the consideration of spatially weighted heterogeneity for porosity and a poro-elasto-plastic model to simulate flow through preferential pathways. Inclusion of a swelling stress term will also be added to investigate the swelling behaviour in expansive soils. Finally, an investigation into constitutive relations to simulate the self-healing behaviour of swelling soils will be addressed. [62]

CHAPTER 4: A MATHEMATICAL MODEL OF GAS AND WATER FLOW IN A SWELLING GEOMATERIAL – PART 1. VERIFICATION WITH ANALYTICAL SOLUTION

Article

A Mathematical Model of Gas and Water Flow in a Swelling Geomaterial – Part 1. Verification with Analytical Solution

Elias Ernest Dagher [1,2], Julio Ángel Infante Sedano [2] and Thanh Son Nguyen [1,2,*]

[1] Canadian Nuclear Safety Commission (CNSC), Ottawa, ON, K1P 5S9, Canada;
[2] Department of Civil Engineering, University of Ottawa, Ottawa, ON K1N 6N5, Canada; e-mail@e-mail.com
* Correspondence: son.nguyen@canada.ca

Received: 24 October 2019; Accepted: 20 December 2019; Published: 29 December 2019

Abstract: Gas generation and migration are important processes that must be considered in a safety case for a deep geological repository (DGR) for the long-term containment of radioactive waste. Expansive soils, such as bentonite-based materials, are widely considered as sealing materials. Understanding their long-term performance as barriers to mitigate gas migration is vital in the design and long-term safety assessment of a DGR. Development and the application of numerical models are key to understanding the processes involved in gas migration. This study builds upon the authors' previous work for developing a hydro-mechanical mathematical model for migration of gas through a low-permeable geomaterial based on the theoretical framework of poromechanics through the contribution of model verification. The study first derives analytical solutions for a 1D steady-state gas flow and 1D transient gas flow problem. Using the Finite Element Method, the model is used to simulate 1D flow through a confined cylindrical sample of near-saturated low-permeable soil under a constant volume boundary stress condition. Verification of the numerical model is performed by comparing the pore-gas pressure evolution and stress evolution to that of the results of the analytical solution. The results of the numerical model closely matched those of the analytical solutions. Future studies will attempt to improve upon the model complexity and investigate processes and material characteristics that can enhance gas migration in a nearly saturated swelling geomaterials.

Keywords: THMC modelling; model verification; multi-phase flow; gas migration; nuclear waste disposal; bentonite; expansive soils; swelling soils; swelling geomaterials

1. Introduction

The primary purpose of a Deep Geological Repository (DGR) for the long-term management of radioactive waste, is to contain and isolate wastes to minimize impact to the environment and radiological exposure to people. In developing a safety case for a DGR, which provides the supportive arguments that the long-term solution for the management of radioactive waste will be protective of human health and the environment over the long term, relevant features, events, and processes (FEPs), must be evaluated [17, 18]. One such process with the potential means for radiological exposure to the biosphere is the generation of radioactive gas which may migrate to the surface [19].

Gas could be generated through a number of processes including the degradation of organic matter, radioactive decay of the waste, corrosion of metals producing hydrogen gas (H_2), and the radiolysis of water producing H_2 [20, 21, 19]. If production exceeds the containment capacity of the engineered barriers or host rock, these gases could migrate through the engineered barriers and/or the host rock [22, 9]. The

preferential migration pathway of these radioactive gases, to potentially expose people and the environment to radioactivity, might be through the access and ventilation shafts, as these components are typically part of the repository design.

In recent years, a number of international projects have focused on the topics of gas generation and migration, with a focus on the impact of gas build-up and migration through an engineered barrier system (EBS) [23, 24, 4]. Expansive or swelling soils, such as bentonite-based materials, are currently the preferred choice of seal materials used for an EBS. Understanding the long-term performance of these seals as barriers against gas migration is an important factor in the design and long-term safety assessment of a DGR.

A wealth of laboratory and field-scale experimental studies have investigated gas transport processes through natural (host rock) and engineered barriers. These studies provide a wealth of evidence that suggest that at gas pressures above a critical level, there is formation of pressure-induced preferential flow pathways and dilation of the clay, resulting in increased gas flow. In addition, a number of mathematical models have been developed to simulate the gas transport processes observed through these laboratory and field scale studies with some success [33, 34, 35]. However, no studies to date have been able to determine the exact mechanisms which control gas entry, flow, and pathway sealing [25, 22, 26, 27, 28, 20, 23, 29]. Development and use of numerical models are of key importance in understanding of processes involved and in their use in long-term safety assessments.

Dagher et al. [4] developed a fully-coupled hydro-mechanical (HM) linear-elastic mathematical model for advective-diffusive visco-capillary controlled two-phase flow through geomaterials in order to model the first two transport mechanisms proposed by Marschall et al. [5]. Results from a constant volume 1-D flow experiment were used to validate the model. A number of parametric studies were investigated to assess the contribution of advection of poregas, diffusion of dissolved gas in porewater, advection of dissolved gas in porewater, and inclusion of mechanical deformation (linear elasticity) on flow behaviour with increasing gas pressures over time. Additionally, sensitivity analyses were conducted to gain an understanding of the influence of a number of soil properties on flow behaviour, such as the effect of modifying the air-entry value (AEV), intrinsic permeability, and initial porosity of the soil specimen. Finally, the study investigated the use of a linear elastic damage model to better represent the experimental results. Although the model results reproduced some of the general features noted in the experimental results, the model was unable to simulate dilatancy-controlled gas flow.

In this paper, the authors build upon previous published work by first performing a verification study of the linear poro-elastic hydro-mechanical model proposed in Dagher et al. [4]. Analytical solutions for a simplified 1D steady-state and 1D transient single-phase flow through a low permeability geomaterial problem are presented. Verification of the numerical model presented in Dagher et al. [4] is then performed by comparing the results obtained by the numerical model to the results of the analytical solutions. The model is then used to investigate the effects on gas flow of different processes and phenomena, including: i) heterogeneity within the geomaterial, ii) the Klinkenberg "slip flow" effect on gas permeability, and iii) swelling and desiccation of the geomaterial. The results of the simulation of the above factors are presented in the companion paper to this one.

This research continues to be, in part, a contribution to Task A of the current project phase of the international working group for the DEvelopment of COupled models and their VALidation against EXperiments (DECOVALEX-2019). This task, led by the British Geological Survey (BGS), further attempts to identify the physical HM mechanisms required to adequately model dilatancy-controlled gas migration.

2. Mathematical Model

2.1. Study Overview

This study expands upon the work performed by Dagher et al. [4] on the development of a mathematical model for gas migration (two-phase flow) through a low-permeable swelling geomaterial. Using the theoretical framework of poromechanics, a verification study is performed through the following:

i. derivation of analytical solutions for 1D steady-state and 1D transient single-phase gas flow (i.e., assuming immobile liquid phase) through a low-permeable geomaterial problem based on the linear poro-elastic hydromechanical mathematical model proposed in Dagher et al. [10]
ii. verification of the numerical model by comparing the results of the numerical simulations performed in COMSOL® Multiphysics® finite element method (FEM) software (Version 5.4a, COMSOL AB, Boston, US) to the results of the analytical steady-state and transient solutions.

The mathematical model follows the general formulation by Dagher et al. [4]. The applicable constitutive relations and governing equations for conservation of momentum, water mass and gas mass are presented below.

2.2. Assumptions for Poromechanical Behaviour

This paper adopts the following assumptions for the mechanical behaviour of the porous medium as presented in Dagher et al. [4]:

Bishop's modified effective stress, with a χ parameter generalized from the work of Khalili & Khabbaz [2],

linear poro-elasticity following the general framework of poromechanics.

2.2.1. Bishop's modified effective stress principle

The general form for the equation of poro-mechanics can be expressed by,

$$\sigma_{ij} = \sigma'_{ij} + \delta_{ij}\bar{p} \tag{1}$$

where σ_{ij} is total normal stress tensor acting on the soil element (Pa)

σ'_{ij} is the effective stress tensor (Pa)

δ_{ij} is the Kronecker delta (identity tensor) (adimensional) and

$\bar{p}$ is the porefluid pressure (Pa)

Many effective stress equations have been proposed to characterize the stress-state of an unsaturated soil or porous medium [1]. This paper proposes the use of Bishop's effective stress principle, which is dependent on both net normal stress and matric suction, and may be more suitable for expansive clay's, and is described by equation (2).

$$\sigma'_{ij} = (\sigma_{ij} - p_g) + \chi\delta_{ij}(p_g - p_w) \tag{2}$$

where

p_g is the poregas pressure (Pa)

p_w is the porewater pressure (Pa)

$(\sigma_{ij} - p_g)$ is the net normal stress (Pa)

$(p_g - p_w)$ is the matric suction (Pa)

χ is a parameter related to the degree of saturation of the soil (unitless)

Expanding and rearranging for σ,

$$\sigma_{ij} = \sigma'_{ij} + \delta_{ij}\left((1-\chi)p_g + \chi p_w\right) \tag{3}$$

The porefluid pressure can be defined as,

$$\bar{p} = (1-\chi)p_g + \chi p_w \tag{4}$$

Khalili and Khabbaz [2], proposed the following unique relationship for the determination of χ based on the ratio of suction over the air entry value, also termed the suction ratio,

$$\chi = \begin{cases} \left[\frac{(p_g - p_w)}{(p_g - p_w)_b}\right]^{-0.55}, \text{if } (p_g - p_w) > (p_g - p_w)_b \\ 1, \text{otherwise} \end{cases} \quad (5)$$

where $(p_g - p_w)_b$ is the air-entry value (AEV) of the soil and only applies when the matric suction > AEV [2].

2.2.2. Poro-elastic stress-strain relation

The increment of the effective stress tensor, $d\sigma'_{ij}$ is related to the increment of the total strain by the constitutive relation:

$$d\sigma'_{ij} = C_{ijkl} d\varepsilon_{kl} \quad (6)$$

where C_{ijkl} is the stiffness tensor (Pa)

ε_{kl} is the total strain tensor (adimensional)

Assuming small deformations, the total strain is related to the components of the displacement tensor as:

$$\varepsilon_{ij} = \frac{1}{2}(u_{i,j} + u_{j,i}) = \frac{1}{2}\left(\frac{\partial u_i}{\partial x_j} + \frac{\partial u_j}{\partial x_i}\right) \quad (7)$$

$$\varepsilon_{kk} = u_{k,k} = \frac{\partial u_k}{\partial x_k} \quad (8)$$

where $\varepsilon_{kk}\ (= u_{k,k} = tr\varepsilon_{ij} = \varepsilon_{vol})$ is the volumetric strain (adimensional)

$u_{i,j} = \frac{\partial u_i}{\partial x_j}$ is the spatial derivative of the displacement vector (m)

2.3. Constitutive Relations for the Hydraulic Behaviour

This paper adopts the following constitutive relations for the hydraulic behaviour as presented in Dagher et al. [4]:

- van Genuchten equation for the soil-water characteristic curve [4]
- Huang et al. [52] equation depicting the relationship between the AEV and void ratio
- Darcy's Law for two-phase flow
- Equation for the effective diffusivity for gas dissolved in water through porous media, utilizing the Millington and Quirk model to define the tortuosity as a function of the degree of saturation, S_w and the porosity, n [57]
- Pall and Moshenin et al. [56] modification to the Kozeny-Carman equation [54] for the relationship between the intrinsic permeability of water and the porosity of the soil
- Mualem's model for the relative permeabilities of gas and water [1, 4]

2.4. Governing Equations for Two-Phase Flow through a Linear Elastic Geomaterial

The governing equations as derived by Dagher et al. [4] and Nguyen and Le [1] for describing advective-diffusive visco-capillary controlled two-phase flow for a linear-elastic geomaterials are presented below.

2.4.1. Conservation of water mass

The governing equation for the conservation of water mass can be expressed by equation (9),

$$\frac{\partial}{\partial x_i}\left(\rho_w \frac{k_{ij}k_{r,w}}{\mu_w}\left(\frac{\partial p_w}{\partial x_j}+\rho_w g_j\right)\right)=-\frac{\partial(\rho_w n S_w)}{\partial t} \tag{9}$$

and solving the right-hand side, this simplifies to equation (10),

$$\frac{\partial}{\partial x_i}\left(\rho_w \frac{k_{ij}k_{r,w}}{\mu_w}\left(\frac{\partial p_w}{\partial x_j}+\rho_w g_j\right)\right)=-\rho_w\left[n\left(\frac{dS_w}{ds}\right)\frac{\partial s}{\partial t}+n\frac{S_w}{K_w}\frac{\partial p_w}{\partial t}+S_w\frac{\partial}{\partial t}\left(\frac{\partial u_k}{\partial x_k}\right)\right] \tag{10}$$

where ρ_w density of water phase (kg m^{-3})
p_w is the porewater pressure (Pa)
k_{ij} intrinsic permeability tensor of the porous medium (m^2)
$k_{r,w}$ relative permeability of the water phase (unitless)
μ_w dynamic viscosity of the water phase (Pa s or kg m^{-1} s^{-1})
g is the acceleration due to gravity (m s^{-2})
n porosity (m^3 voids · m^{-3} total)
S_w is the degree of saturation of water
s is the matric suction $(p_g - p_w)$ (Pa)
K_w is the bulk modulus of the water phase (Pa s or kg m^{-1} s^{-1})
$\frac{\partial u_k}{\partial x_k}=\varepsilon_{vol}$ is the volumetric strain (unitless)
u is the displacement (m)
t is time (s)

Note that in this study, the permeability is assumed to be isotropic, therefore k_{ij}=k, however we keep the tensorial notation in the governing equation for the sake of generalization.

2.4.2. Conservation of gas mass

The governing equation for the conservation of gas mass can be expressed by equation (11),

$$\begin{aligned}\frac{\partial\left(\rho_g\left(\frac{k_{ij}k_{r,g}}{\mu_g}\left(\frac{\partial p_g}{\partial x_j}+\rho_g g\right)+H\frac{k_{ij}k_{r,w}}{\mu_w}\left(\frac{\partial p_w}{\partial x_j}+\rho_w g\right)\right)\right)}{\partial x_i}+\frac{\partial}{\partial x_i}\left(-D_e\frac{\partial}{\partial x_k}\left(\rho_g n(HS_w)\right)\right)\\ =-\frac{\partial\left(\rho_g n(1-S_w+HS_w)\right)}{\partial t}\end{aligned} \tag{11}$$

and solving the right-hand side, this simplifies to equation (12),

$$\begin{aligned}\frac{\partial\left(\rho_g\left(\frac{k_{ij}k_{r,g}}{\mu_g}\left(\frac{\partial p_g}{\partial x_j}+\rho_g g\right)+H\frac{k_{ij}k_{r,w}}{\mu_w}\left(\frac{\partial p_w}{\partial x_j}+\rho_w g\right)\right)\right)}{\partial x_i}+\frac{\partial}{\partial x_i}\left(-D_e\frac{\partial}{\partial x_k}\left(\rho_g n(HS_w)\right)\right)\\ =-\rho_g\left[n(H-1)\left(\frac{dS_w}{ds}\right)\frac{\partial s}{\partial t}+\frac{n(1-S_w+HS_w)}{K_g}\frac{\partial p_g}{\partial t}+(1-S_w+HS_w)\frac{\partial}{\partial t}\left(\frac{\partial u_k}{\partial x_k}\right)\right]\end{aligned} \tag{12}$$

where

ρ_g density of the gas phase (kg m^{-3})
p_g is the poregas pressure (Pa)
$k_{r,g}$ relative permeability of the gas phase (unitless)
μ_g dynamic viscosity of the gas phase (Pa s or kg m^{-1} s^{-1})

H is Henry's coefficient (kg species A m^{-3} in aqueous phase kg^{-1} species A m^3 in gas phase)

D_e is the effective diffusivity of gas dissolved in water through porous media (m^2 s^{-1})

K_g is the bulk modulus of the gas phase (Pa)

It should be noted that Equation (12) does not require the assumption that the gas behaves as an ideal gas. In the derivation of the expression of gas density and bulk modulus one might need to invoke the ideal gas law or other laws that more accurately predict the gas density and compressibility at different pressures and thermal conditions.

2.4.3. Conservation of momentum (quasi-static equilibrium)

For a soil specimen in quasi-static equilibrium the total equilibrium equation for a cubical soil element can be expressed in tensor notation by equation (18).

$$\frac{\partial \sigma_{ij}}{\partial x_j} + F_{v,i} = 0 \tag{13}$$

where, σ_{ij} is the stress tensor (Pa)

$F_{v,i}$ is the volumetric body force tensor (kg m^{-2} s^{-2})

$\frac{\partial \sigma_{ij}}{\partial x_j}$ represents the change in normal and shear stresses across the soil element (kg m^{-2} s^{-2})

Substituting equation (3) into equation (13), the governing equation for the conservation of momentum for a porous geomaterial can be expressed by equation (14),

$$\frac{\partial \sigma'_{ij}}{\partial x_j} + (1-\chi)\frac{\partial p_g}{\partial x_j} + \chi\frac{\partial p_w}{\partial x_j} + F_{v,i} = 0 \tag{14}$$

For a linear poro-elastic geomaterial, applying the constitutive relations described by equations (6) through (8), the governing equation for the conservation of momentum can be expressed by equation (15),

$$G\frac{\partial^2 u_i}{\partial x_j \partial x_j} + (G+\lambda)\frac{\partial^2 u_j}{\partial x_j \partial x_i} + (1-\chi)\frac{\partial p_g}{\partial x_i} + \chi\frac{\partial p_w}{\partial x_i} + F_{v,i} = 0 \tag{15}$$

where G is the shear modulus (Pa)

λ is the Lamé constant (Pa)

3. Verification Study Analysis

3.1. Analysis Overview

Verification of the proposed mathematical model was performed by deriving analytical solutions for the 1D steady-state and 1D transient gas flow problem depicted in **Figure 1,** through the simplification of the governing equations described by equation (1) and equation (3). In the above problem, flow and deformation can occur only in the longitudinal direction x. A three-dimensional (3D) hydro-mechanical (HM) coupled multiphysics numerical model was built using the commercially available code COMSOL® Multiphysics® (COMSOL®) to numerically solve the simplified governing equations and constitutive relations described below. The analytical solution was then used to verify the numerical model in COMSOL® by comparing the numerical results to the results of the analytical solutions.

Figure 1. 1D Gas Flow through a porous medium of length, L.

The following assumptions were made for the simplification of the mathematical model:

- immobile liquid phase
- no dissolution of gas into and no diffusion gas through the porewater
- constant gas permeability
- constant gas density
- constant fluid viscosity
- constant degree of saturation of water
- role of suction ignored
- role of gravity ignored
- isothermal process
- constant volume boundary condition

It should be noted that these assumptions, as well as the downstream boundary condition set to atmospheric pressure (Figure 1) was done for simplification of the verification analysis. In a bentonite-based shaft seal design, this may be a reasonable assumption when one end of the shaft seal is exposed to surface. However, if applied to bentonite buffer surrounding the waste canister, the boundary pressure conditions would be different and would affect the fluid properties at the higher temperatures and pressures of a DGR environment.

3.2. Analytical Solutions for Two-Phase Flow through a Linear Poro-Elastic Geomaterial

3.2.1. 1D Steady-State Gas Flow Problem

Based on the above assumptions, the governing equation for the conservation of gas mass for 1D steady-state flow through a linear elastic porous medium expressed by equation (11) simplifies to the following expression,

$$\frac{d}{dx}\left(\rho_g \frac{k_g}{\mu_g}\frac{dp_g}{dx}\right) = 0 \tag{16}$$

where, k_g is the gas permeability (m^2)

Assuming an immobile water phase and ignoring the effects of gravity, the governing equation for the conservation of momentum expressed by equation (14), simplifies to the following equation for a 1D gas flow problem,

$$\frac{d\sigma'}{dx} + (1-\chi)\frac{dp_g}{dx} = 0 \tag{17}$$

Solving equation (16), the analytical solution for the pore-gas pressure and displacement as a function of distance can be expressed by,

$$p_g(x) = P_{inj} + \frac{P_{atm} - P_{inj}}{L}x \tag{18}$$

where P_{inj} is the gas injection pressure (Pa)

P_{atm} is atmospheric pressure (Pa)

L is the length of the soil specimen (m)

The displacement field along the longitudinal x-direction is given by:

$$u(x) = -\frac{\left[1-\left(\frac{2\nu^2}{1-\nu}\right)\right]}{E}(1-\chi)\frac{(P_{atm}-P_{inj})}{2}\left(\frac{x^2}{L}-x\right) \tag{19}$$

where ν is the Poisson ratio (unitless)

E is Young's Modulus (Pa)

The corresponding strain and stress can be calculated by the following expressions,

$$\varepsilon_{xx}(x) = \frac{du}{dx} = \frac{\left[1-\left(\frac{2\nu^2}{1-\nu}\right)\right]}{E}(1-\chi)(P_{atm}-P_{inj})(\frac{x}{L}-\frac{1}{2}) \tag{20}$$

$$\sigma'_{xx}(x) = (1-\chi)(P_{atm}-P_{inj})\left(\frac{x}{L}-\frac{1}{2}\right) \tag{21}$$

$$\sigma'_{yy} = \sigma'_{zz} = \left(\frac{\nu}{1-\nu}\right)\sigma'_{xx} \tag{22}$$

Detailed derivation of the analytical solution for the 1D steady-state gas flow problem is provided in Appendix A.2.

3.2.2. 1D Transient Gas Flow Problem

Based on the assumptions, the governing equation for the conservation of gas mass for 1D transient gas flow through a linear elastic porous medium expressed by equation (11) simplifies to the following,

$$\frac{d}{dx}\left(\rho_g\frac{k_g}{\mu_g}\frac{dp_g}{dx}\right) = -\frac{d\left(\rho_g n(1-S_w)\right)}{dt} \tag{23}$$

By assuming the gas density and degree of saturation remains constant in both time and space, the governing equation for the conservation of momentum expressed by equation (19) simplifies to the following,

$$\rho_g\frac{k_g}{\mu_g}\frac{d}{dx}\left(\frac{dp_g}{dx}\right) = -\rho_g(1-S_w)\frac{dn}{dt} \tag{24}$$

And solving for dn, this simplifies further to,

$$\frac{k_g}{\mu_g}\frac{d^2p_g}{dx^2} = -(1-S_w)\frac{d\varepsilon_{vol}}{dt} \tag{25}$$

Since strain is nil in the y and z directions, it can be shown from Hooke's Law that

$$\varepsilon_{vol} = \varepsilon_{xx} = \frac{du}{dx} = \frac{\left[1-\left(\frac{2\nu^2}{1-\nu}\right)\right]}{E}\sigma'_{xx} = \frac{1}{K_{1D}}\sigma'_{xx} \tag{26}$$

where $K_{1D} = \frac{E}{\left[1-\left(\frac{2\nu^2}{1-\nu}\right)\right]}$ is the Bulk Modulus (Pa).

Substituting into equation (25) and re-arranging,

$$-\frac{k_g}{\mu_g}\frac{K_{1D}}{(1-S_w)}\frac{d^2p_g}{dx^2} = \frac{d\sigma'_{xx}}{dt} \tag{27}$$

Integrating both sides of the governing equation for the conservation of momentum expressed by equation (17), and re-arranging for σ'_{xx},

$$\sigma'_{xx} = -(1-\chi)p_g + C_1 \tag{28}$$

Substituting σ'_{xx} into equation (27)

$$\frac{k_g}{\mu_g}\frac{K_{1D}}{(1-S_w)(1-\chi)}\frac{d^2p_g}{dx^2} = \frac{dp_g}{dt} \tag{29}$$

As equation (29) is analogous to the equation for transient diffusion in a plane sheet, the analytical solution as expressed by J. Crank [3] for constant surface concentrations and constant initial conditions is expressed by the following equation,

$$\begin{aligned} p_g(x,t) = P_{inj} + \left(P_{atm} - P_{inj}\right)\frac{x}{L} + \frac{2}{\pi}\sum_{n=1}^{\infty}\frac{P_{atm}\cos n\pi - P_{inj}}{n}\sin\frac{n\pi x}{L}\exp\left(-\frac{Dn^2\pi^2t}{L^2}\right) \\ + \frac{4P_0}{\pi}\sum_{m=0}^{\infty}\frac{1}{2m+1}\sin\frac{(2m+1)\pi x}{L}\exp\left(-\frac{D(2m+1)^2\pi^2t}{L^2}\right) \end{aligned} \tag{30}$$

where $D = \frac{k_g}{\mu_g}\frac{K_{1D}}{(1-S_w)(1-\chi)}$ ($m^2\ s^{-1}$)

Substituting $p_g(x,t)$ from equation (30) into equation (28) and then substituting equation (28) into equation (26) and integrating both sides, the analytical solution for the displacement can be expressed by,

$$
\begin{aligned}
u = \frac{1}{K_{1D}}(1-\chi)\frac{(P_{atm}-P_{inj})}{2}\left[x-\frac{x^2}{L}\right] \\
&+\frac{1}{K_{1D}}(1 \\
&-\chi)\frac{2}{\pi}\sum_{n=1}^{\infty}\left(\frac{P_{atm}\cos n\pi - P_{inj}}{n}\right)\exp\left(-\frac{Dn^2\pi^2 t}{L^2}\right)\left(\frac{-L}{n\pi}\right)\left(1-\frac{x}{L}+\frac{x}{L}\cos n\pi\right. \\
&\left.-\cos\frac{n\pi x}{L}\right) \\
&+\frac{1}{K_{1D}}(1 \\
&-\chi)\frac{4P_0}{\pi}\sum_{m=0}^{\infty}\exp\left(-\frac{D(2m+1)^2\pi^2 t}{L^2}\right)\left(\frac{-L}{(2m+1)^2\pi}\right)\left(1-\frac{x}{L}+\frac{x}{L}\cos(2m+1)\pi\right. \\
&\left.-\cos\frac{(2m+1)\pi x}{L}\right)
\end{aligned}
\tag{31}
$$

The strain and stress can now be calculated analytically by the following expressions,

$$
\begin{aligned}
\varepsilon_{vol} = \frac{du}{dx} = \frac{1}{K_{1D}}(1-\chi)\left(P_{atm}-P_{inj}\right)\left(\frac{1}{2}-\frac{x}{L}\right) \\
&+\frac{1}{K_{1D}}(1 \\
&-\chi)\frac{2}{\pi}\sum_{n=1}^{\infty}\left(\frac{P_{atm}\cos n\pi - P_{inj}}{n}\right)\exp\left(-\frac{Dn^2\pi^2 t}{L^2}\right)\left(\frac{1}{n\pi}-\frac{1}{n\pi}\cos n\pi - \sin\frac{n\pi x}{L}\right) \\
&+\frac{1}{K_{1D}}(1-\chi)\frac{4P_0}{\pi}\sum_{m=0}^{\infty}\frac{1}{2m+1}\exp\left(-\frac{D(2m+1)^2\pi^2 t}{L^2}\right)\left(\frac{1}{(2m+1)\pi}\right. \\
&\left.-\frac{1}{(2m+1)\pi}\cos(2m+1)\pi - \sin\frac{(2m+1)\pi x}{L}\right)
\end{aligned}
\tag{32}
$$

Detailed derivation of the analytical solution for the 1D transient gas flow problem is provided in Appendix A.3.

3.2.3. Mean Stress and Deviatoric Stress

The mean stress can be calculated by the following expression,

$$
p' = \frac{\sigma'_{11}+\sigma'_{22}+\sigma'_{33}}{3} \tag{33}
$$

The deviatoric stress can be calculated by the following expression,

$$
q' = \sqrt{3J_2} \tag{34}
$$

where,

$$
J_2 = \frac{1}{2}[(\sigma'_{11}-p')^2+(\sigma'_{22}-p')^2+(\sigma'_{33}-p')^2+2\sigma'^2_{12}+2\sigma'^2_{13}+2\sigma'^2_{23}] \tag{35}
$$

$$
q' = \sqrt{\frac{3}{2}[(\sigma'_{11}-p')^2+(\sigma'_{22}-p')^2+(\sigma'_{33}-p')^2+2\sigma'^2_{12}+2\sigma'^2_{13}+2\sigma'^2_{23}]} \tag{36}
$$

3.3. Numerical Model Description

3.3.1. Model Geometry and Mesh

For the numerical model, the geometry and mesh are presented in **Figure 2**. The numerical model consists of approximately 11,000 elements and has 162,000 degrees of freedom.

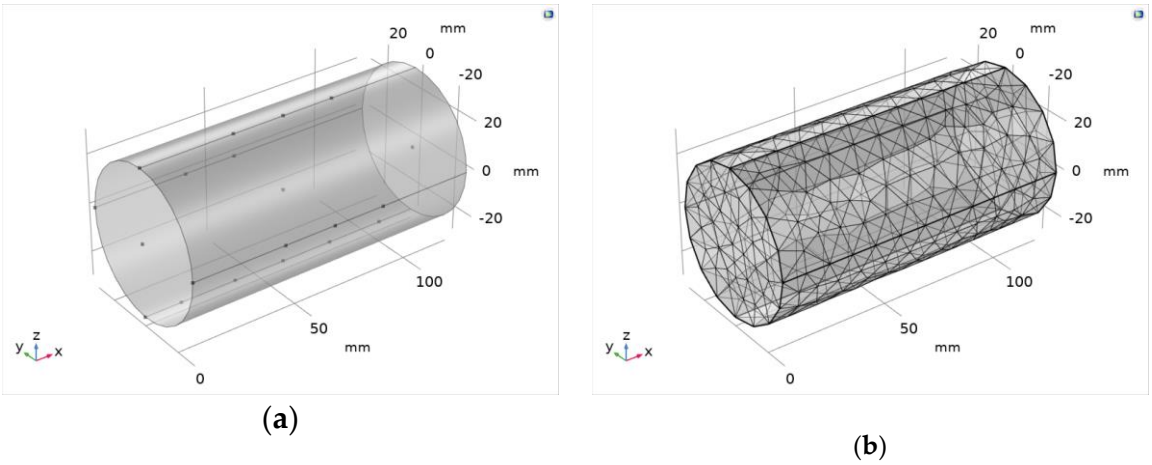

Figure 2. Verification study–numerical model (a) geometry and (b) mesh.

3.4. Results and Discussion

Verification of the numerical model results against the analytical solution for a 1D steady-state gas flow problem and a 1D transient gas flow problem are presented below. **Table 1** provides the material properties, initial conditions, and boundary conditions that were used in both the numerical model and analytical solution. The material properties correspond to those obtained experimentally from Daniels and Harrington [59] or calculated using the constitutive relations derived by Dagher et al. [4]. The initial and boundary conditions were selected based on the experimental setup of Daniels and Harrington [59], with the injection poregas pressure corresponding to the peak injection pressure observed in that experiment.

Table 1. Verification Study Parameters.

Parameter Name	Symbol	Value	Units
Length	L	0.12	m
Injection poregas pressure boundary condition	P_{inj}	1.30×10^{7}	Pa
Atmospheric gas pressure boundary condition	P_{atm}	1.01×10^{5}	Pa
Initial uniform pore-gas pressure (for transient gas flow problem)	P_0	6.55×10^{6}	Pa
Density of bentonite	ρ_b	1526	kg m^{-3}
Young's Modulus	E	3.07×10^{8}	Pa
Poisson's ratio (nu)	ν	0.4	-
Porosity	n	0.44	-
Intrinsic permeability	k_{ij}	3.40×10^{-21}	m^2
Dynamic viscosity	μ_g	2.00×10^{-5}	Pa s
Degree of saturation	S_w	0.9	-
Air-Entry-Value	AEV	1×10^{7}	Pa
Constant porewater pressure[1]	p_w	1.0×10^{6}	Pa
Relative gas permeability[1]	k_{rg}	0.03	-
Chi factor[1]	χ	0.9	-

[1]Calculated based on a degree of saturation of 0.9 and gas pressure of 1.3×10^{7} Pa.

3.4.1. Steady-State Solution

For the 1D steady-state gas flow problem, the poregas pressure and displacement in the x-direction were calculated using analytical solution presented by equations (18) and (19), respectively. The numerical and analytical results for poregas pressure and displacement over the length of the specimen is provided in **Figure 3** and **Figure 4**, respectively. The results show a near-perfect match between the simulation results of the numerical model performed in COMSOL® and the analytical solution.

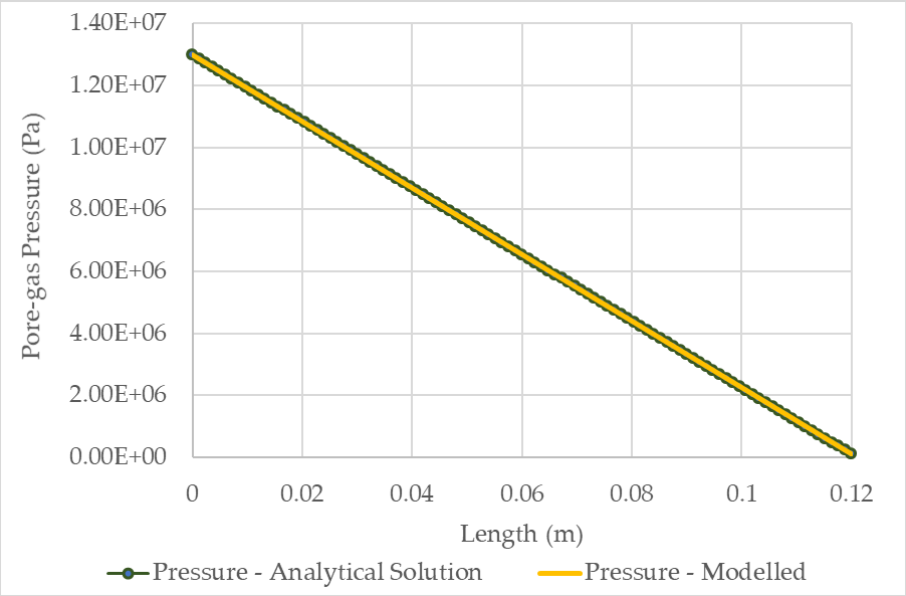

Figure 3. Verification Study - 1D steady-state solution results for poregas pressure over the length of the specimen.

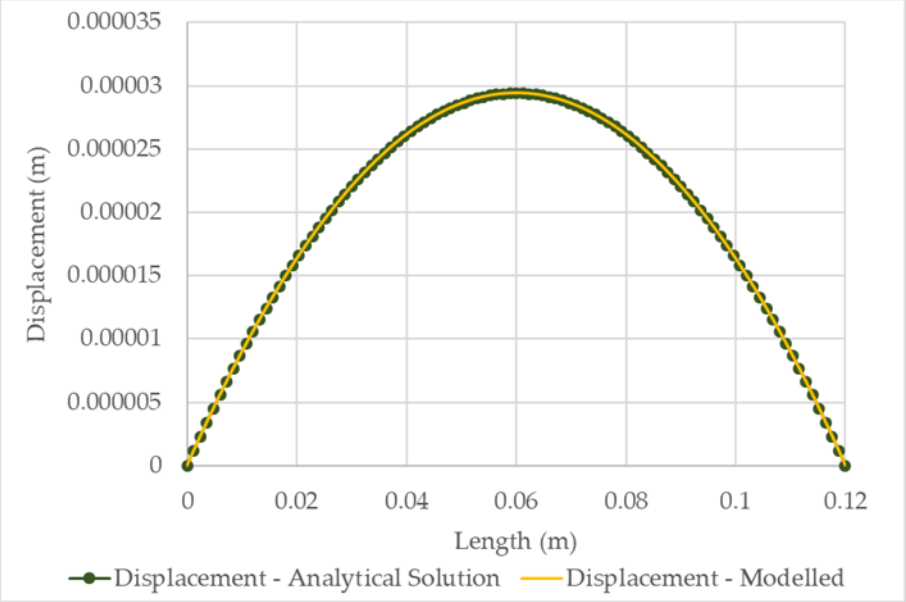

Figure 4. Verification Study - 1D steady-state solution results for displacement over the length of the specimen.

Similarly, the mean effective stress, p′, and deviatoric effective stress, q′, were calculated by first calculating the strain and resulting principal stresses described by equations (20) to (22), and then equations (33) and (36). The numerical and analytical results for mean effective stress, and deviatoric effective stress over the length of the specimen are provided in **Figure 5** and **Figure 6**, respectively. The results, also show a near-perfect match between the numerical results performed in COMSOL® and the analytical solution, thereby demonstrating verification of the numerical model being used in COMSOL®.

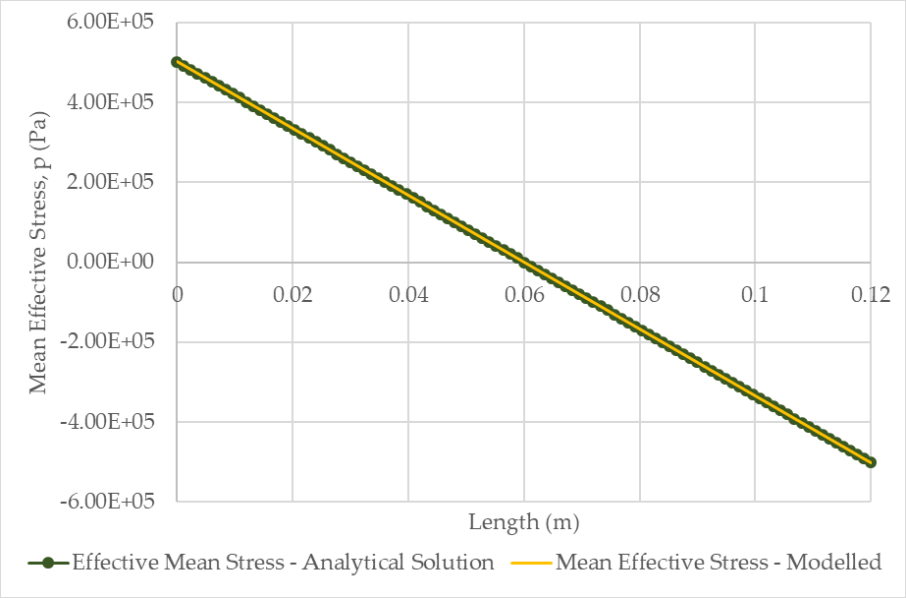

Figure 5. Verification Study - 1D steady-state solution results for mean effective stress over the length of the specimen.

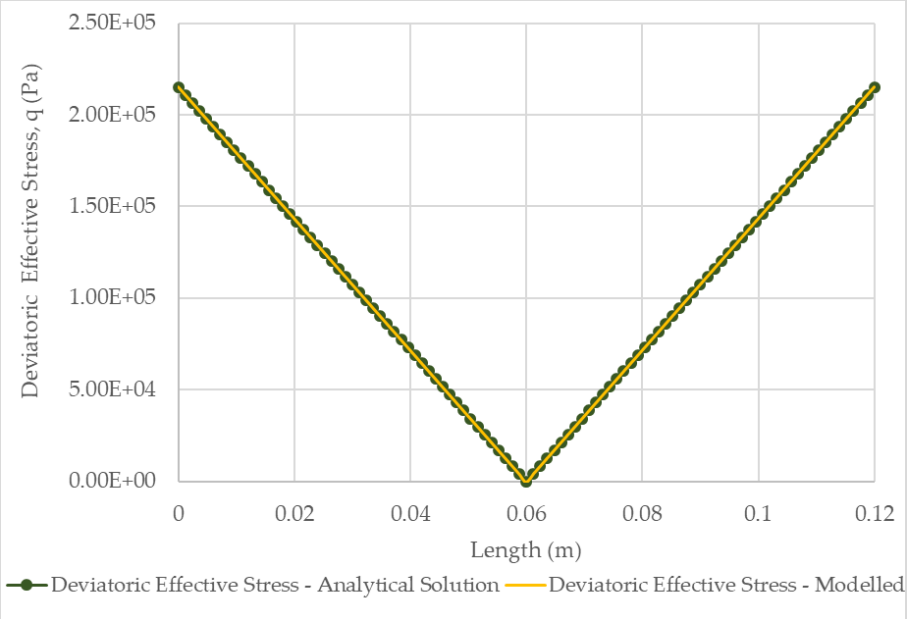

Figure 6. Verification Study - 1D steady-state solution results for deviatoric effective stress, over the length of the specimen.

3.4.2. Transient Solution

For the 1D transient gas flow problem, the poregas pressure and displacement were calculated using the analytical solution presented by equations (30) and (31). The numerical and analytical results for poregas pressure and displacement over the length of the specimen for various times are provided in **Figure 7** and **Figure 8**, respectively. The results show a near-perfect match between the simulation results of the numerical model performed in COMSOL® and the analytical solution. For the poregas pressure, there is an initial response at t = 0 s, corresponding to the sudden change in boundary conditions. Over time, the system tends towards the steady-state solution. Concurrently, as the poregas pressure increases along the column, there is a resulting increase in displacement, until steady-state is reached. Steady-state was achieved at about 5000 s, and matches the solutions provided in Section 3.4.1.

It should be noted that oscillations occurred in results obtained from both the analytical solution and numerical model at time t = 0s, and this was expected. For the analytical solution, these oscillations are due to truncation of the infinite series at n = 70 and m = 40. As these parameters tend towards infinity, if higher truncation limits were used, the oscillations would effectively dissipate. For the numerical analysis, these oscillations are an artefact of mesh size, time step, and error tolerance. Increasing mesh size, and reducing the time-step and tolerance, would help to reduce the numerical oscillations.

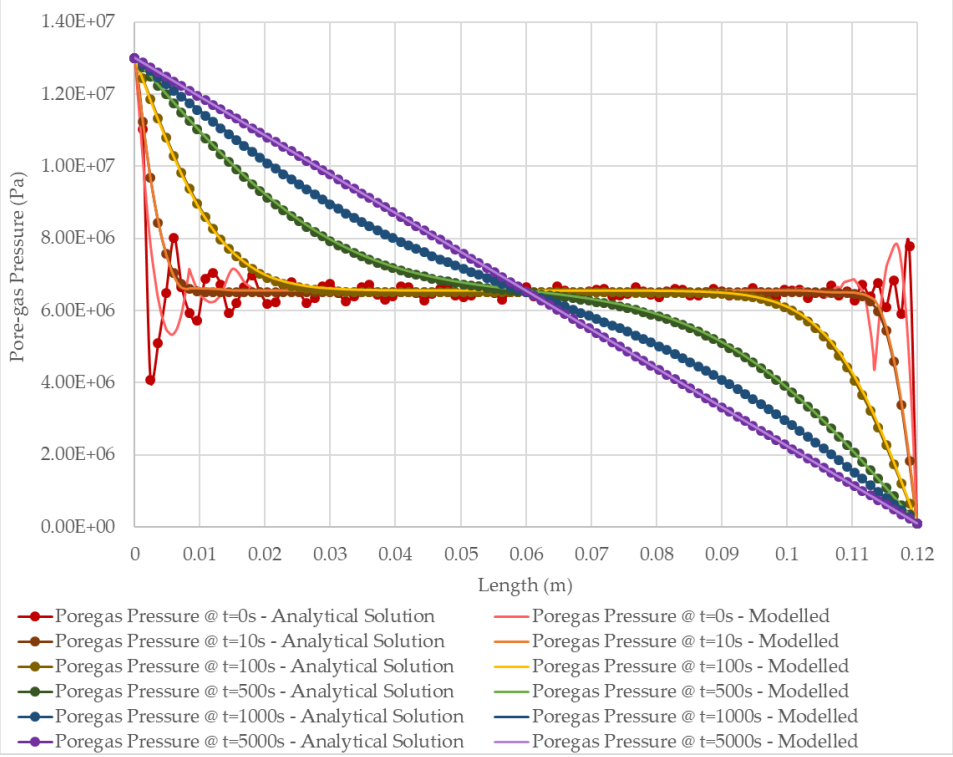

Figure 7. Verification Study - 1D transient solution results for poregas pressure and over the length of the specimen.

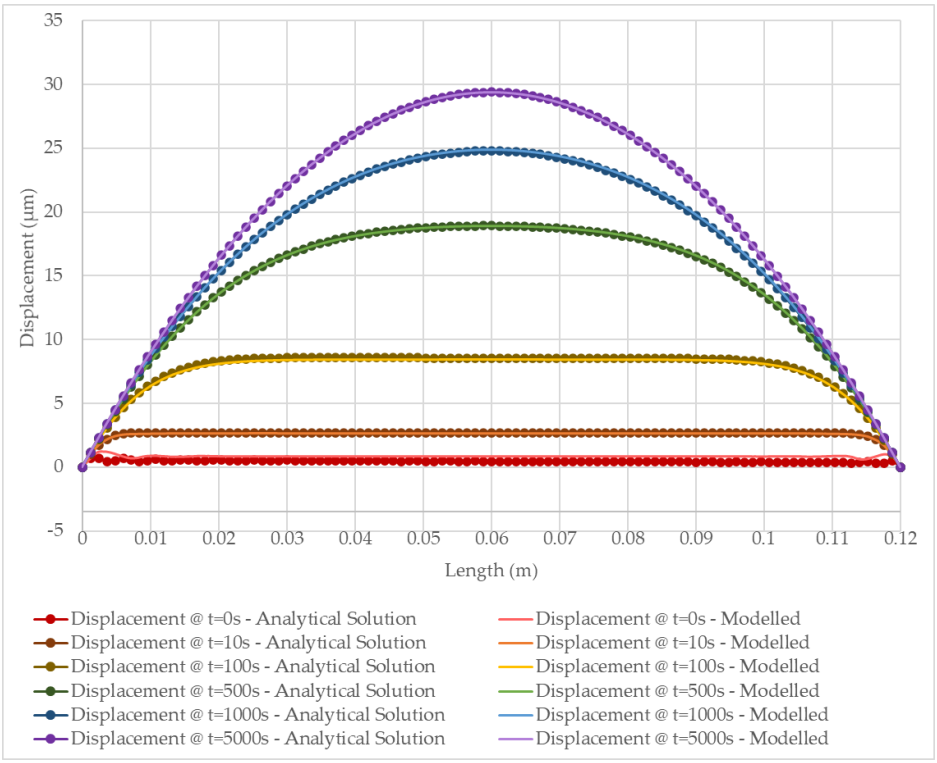

Figure 8. Verification Study - 1D transient solution results for displacement over the length of the specimen.

Similarly, the mean effective stress, p′, and deviatoric effective stress, q′, were calculated by first calculating the strain described by equation (32) and resulting principal stresses described by equations (26) and (22), and then by equations (33) and (36). The numerical and analytical results for mean effective stress, and deviatoric effective stress over the length of the specimen are provided in **Figure 9** and **Figure 10**, respectively. The results, also show a near-perfect match between the numerical results performed in COMSOL® and the analytical solution, thereby demonstrating verification of the numerical model being used in COMSOL®.

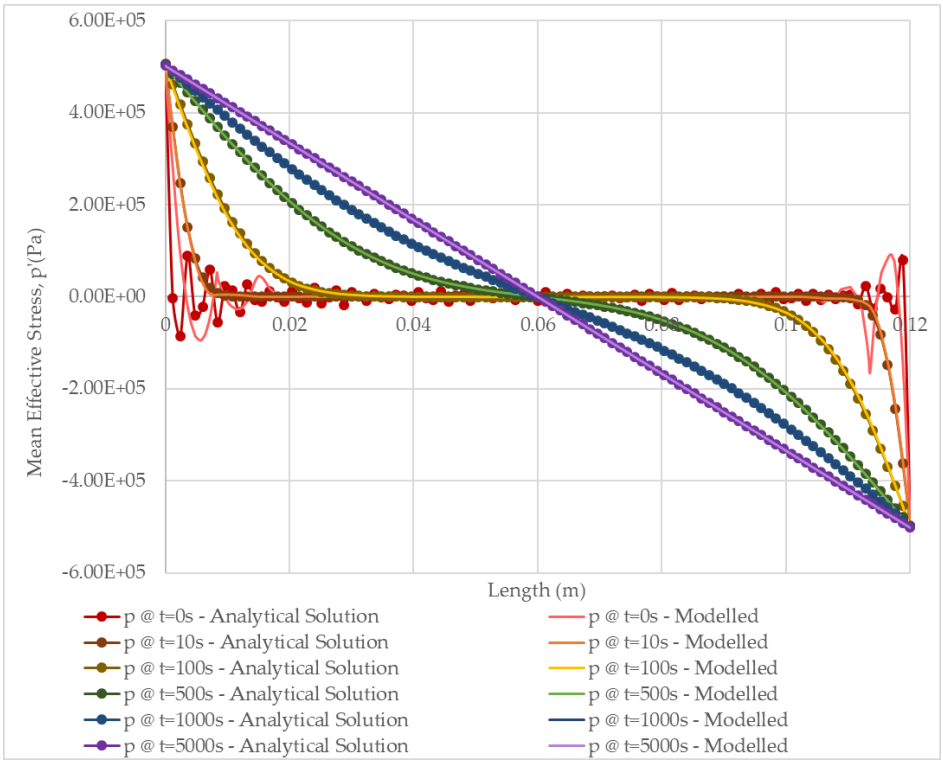

Figure 9. Verification Study - 1D transient solution results for mean effective stress over the length of the specimen.

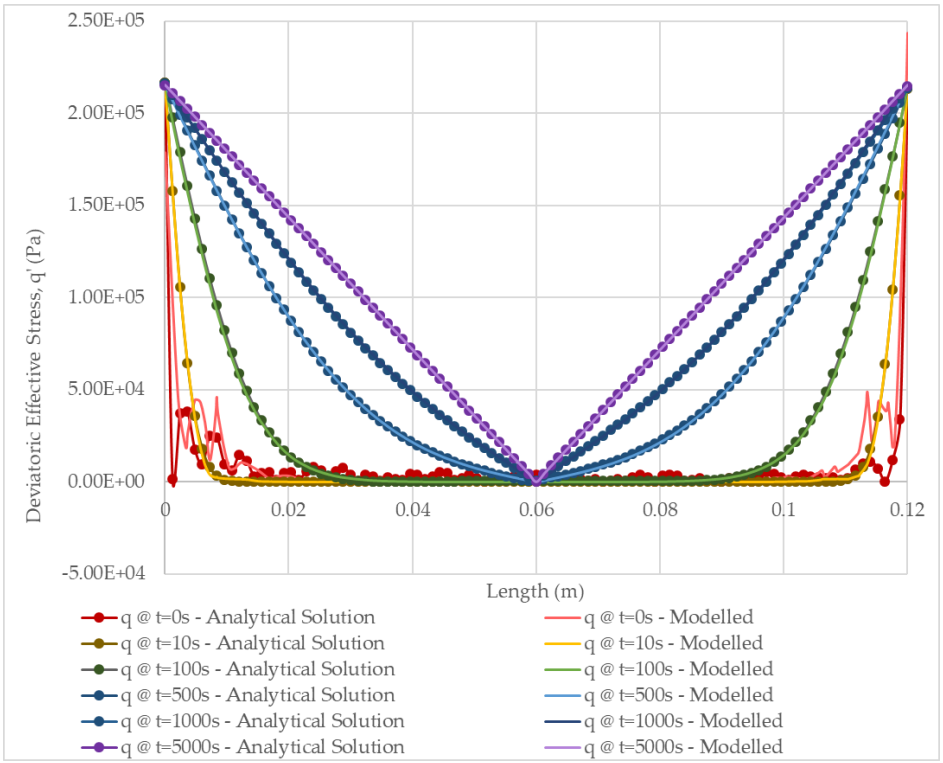

Figure 10. Verification Study - 1D transient solution results for deviatoric effective stress over the length of the specimen.

Additionally, an analysis of the p-q stress path at five different points along the specimen over time was conducted and the results are presented in **Figure 11**. Again, the numerical model results and results of the analytical solution show a close match. The analysis shows that at the center of the specimen, there is no change in stresses as expected. The analysis also shows that at the two ends, there is also no change in stresses as described by the analytical solution, however, the numerical model does show a small change in stress from 0s to t > 0s. This again can likely be attributed to the truncation of the infinite series. At distances 0.03 m and 0.09 m, the effective deviatoric stress increases linearly as a function of the effective mean stress until steady-state is reached. This is expected as a linear elastic mechanical model was adopted. It should be noted that at the injection pressure side, the mean effective stress is in tension, while at the atmospheric pressure side, the mean effective stress is in compression.

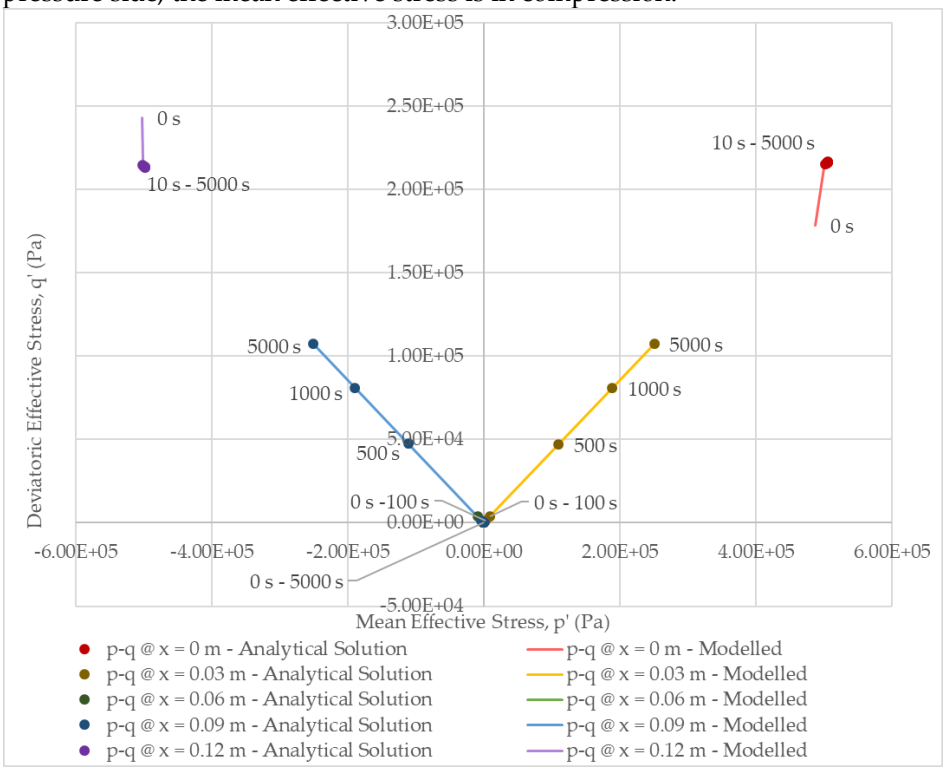

Figure 11. Verification Study - 1D transient solution results showing the p-q stress paths along the length of the soil specimen.

4. Conclusions

An important component in the design and long-term safety assessment of a DGR is the long-term performance of bentonite seals as barriers against gas migration. As gas generates from the degradation of organic waste and/or corrosion of metals, at some critical gas pressure, dilation of the bentonite could occur resulting in the creation of preferential flow pathways and a source of radionuclide exposure to people and the environment. Development and use of numerical models are of key importance in understanding of processes involved and in their use in long-term safety assessments.

In the authors previous work, a fully-coupled hydro-mechanical (HM) linear-elastic mathematical model for advective-diffusive visco-capillary controlled two-phase flow through a geomaterial was derived [4]. This study expands upon that work through the contribution of model verification. As part of this study, analytical solutions for a 1D steady-state gas flow and 1D transient gas flow problem were derived using the framework of poromechanics. Using the Finite Element Method, the numerical model was used to simulate 1D flow through a confined cylindrical sample of near-saturated low-permeable soil

under a constant volume boundary stress condition. Verification of the numerical model was performed by comparing the pore-gas pressure evolution and stress evolution to that of the results of the analytical solutions. For both the steady-state and transient problems, the poregas pressure, displacement, mean effective stress, deviatoric effective stress, and p'-q' stress path results obtained from the numerical model were compared to those of the analytical solutions. For each parameter, the results of the numerical model closely matched those of the analytical solutions, providing added confidence that the proposed mathematical model is being correctly implemented in the COMSOL® FEM software version 5.4.

Future studies will attempt to improve upon the model complexity and investigate enhanced mechanisms for two-phase flow. In the companion paper, a process simulation and enhanced two-phase flow analysis study will be conducted, whereby three enhanced mechanisms for two-phase flow will be introduced into the model. Specifically, the companion paper will look at heterogeneity, the Klinkenberg "slip flow" effect, and the effect of swelling and desiccation. An analysis of the contribution of each to flow behaviour and the potential for the formation of gas fingers will be conducted.

Author Contributions: conceptualization, Dagher and Nguyen ; methodology, Dagher and Nguyen; software, Dagher; validation, Dagher, Nguyen and Infante Sedano; formal analysis, Dagher; investigation, Dagher and Nguyen; resources, Infante Sedano; data curation, Dagher, Nguyen and Infante Sedano; writing—original draft preparation, Dagher; writing—review and editing, Nguyen and Infante Sedano; visualization, Dagher; supervision, Nguyen and Infante Sedano; project administration, Infante Sedano; funding acquisition, Infante Sedano

Funding: This work was supported by the Canadian Nuclear Safety Commission.

Acknowledgments: Decovalex (http://www.decovalex.org) is an international research project comprising participants from industry, government and academia focusing on development of understanding, models and codes in complex coupled problems in sub-surface geological and engineering applications. DECOVALEX-2019 is the current phase of the project. The authors appreciate and thank the DECOVALEX-2019 funding organizations, Andra, BGR/UFZ, CNSC, US DOE, ENSI, JAEA, IRSN, KAERI, NWMO, RWM, SÚRAO, SSM and Taipower, for their financial and technical support of the work described in this paper. The statements made in the paper are, however, solely those of the authors and do not necessarily reflect those of the funding organizations.

Conflicts of Interest: The authors declare no conflict of interest.

Appendix A. Analytical Solutions for 1-Dimensional Gas Flow in a Linear Elastic Porous Medium

A.1. Problem Statement

Derive the steady-state and transient solutions for 1D gas flow through a linear elastic porous medium of length L, fixed at both ends, $u(0,t)$ and $u(L,t) = 0$, with an initial uniform poregas pressure, $p_g(x,0) = P_0$, and with both maintained at different constant gas pressures, $p_g(0,t) = P_{inj}$ and $p_g(L,t) = P_{atm}$,

Figure A1. 1D Gas Flow through a porous medium of length, L.

The following assumptions were made for the simplification of the mathematical model:

- immobile liquid phase
- no dissolution of gas into and no diffusion gas through the porewater
- constant gas permeability
- constant gas density
- constant degree of saturation of water
- role of suction ignored
- role of gravity ignored
- isothermal process
- constant volume boundary condition

A.2. Steady-State Solution

A.2.1. Governing Equations

The governing equation for the conservation of gas mass for steady-state flow through a linear elastic porous medium can be expressed by Equation (A1),

$$\frac{d}{dx}\left(\rho_g \frac{k_g}{\mu_g}\frac{dp_g}{dx}\right) = 0 \quad \text{(A1)}$$

The governing equation for the conservation of momentum (quasi-static equilibrium) for steady-state gas-flow through a linear elastic porous medium can be expressed by Equation (A2),

$$\frac{d\sigma}{dx} = \frac{d\sigma'}{dx} + (1-\chi)\frac{dp_g}{dx} + \chi\frac{dp_w}{dx} = 0 \quad \text{(A2)}$$

Assuming an immobile water phase, this simplifies to Equation (A3),

$$\frac{d\sigma'}{dx} + (1-\chi)\frac{dp_g}{dx} = 0 \quad \text{(A3)}$$

A.2.2. Formulation of the Analytical Solution to the Conservation of Mass Equation

Re-arranging Equation (A1) and solving the double integral for p_g,

$$\rho_g \frac{k_g}{\mu_g} \int \frac{d^2 p_g}{dx^2} = \int 0 \rightarrow \frac{dp_g}{dx} = C_1 \tag{A4}$$

$$\int \frac{dp_g}{dx} = \int C_1 \rightarrow p_g = C_1 x + C_1{}' \tag{A5}$$

From our known boundary conditions, at $x = 0$, $p_g(0) = P_{inj}$ and we can solve for $C_1{}'$

$$P_{inj} = C_1(0) + C_1' \rightarrow C_1' = P_{inj} \tag{A6}$$

Substituting (A6) back into (A5) and from our known BCs at $x = L$, $p_g(L) = P_{atm}$, we can solve for C_1

$$P_{atm} = C_1(L) + P_{inj} \rightarrow C_1 = \frac{P_{atm} - P_{inj}}{L} \tag{A7}$$

Substituting Equations (A6) and (A7) into Equation (A5), the analytical solution for the governing equation for the conservation of momentum can be expressed by Equation (A8)

$$p_g(x) = P_{inj} + \frac{P_{atm} - P_{inj}}{L} x \tag{A8}$$

A.2.3. Formulation of the Analytical Solution to the Conservation of Momentum Equation

From Hooke's Law the normal principal strains and shear strains are provided in Equations (A9) to (A11), and Equations (A12) to (A14) respectively,

$$\varepsilon_{xx} = \frac{du}{dx} = \frac{1}{E}\left(\sigma'_{xx} - \nu\sigma'_{yy} - \nu\sigma'_{zz}\right) \tag{A9}$$

$$\varepsilon_{yy} = \frac{dv}{dy} = \frac{1}{E}\left(\sigma'_{yy} - \nu\sigma'_{zz} - \nu\sigma'_{xx}\right) \tag{A10}$$

$$\varepsilon_{zz} = \frac{dw}{dz} = \frac{1}{E}\left(\sigma'_{zz} - \nu\sigma'_{xx} - \nu\sigma'_{yy}\right) \tag{A11}$$

$$\varepsilon_{xy} = \frac{1}{2}\left(\frac{\partial u}{\partial y} + \frac{\partial v}{\partial x}\right) = \frac{\sigma_{xy}}{2G} \tag{A12}$$

$$\varepsilon_{yz} = \frac{1}{2}\left(\frac{\partial v}{\partial z} + \frac{\partial w}{\partial y}\right) = \frac{\sigma_{yz}}{2G} \tag{A13}$$

$$\varepsilon_{zx} = \frac{1}{2}\left(\frac{\partial w}{\partial x} + \frac{\partial u}{\partial z}\right) = \frac{\sigma_{xz}}{2G} \tag{A14}$$

For the 1D flow problem, ε_{yy} and $\varepsilon_{zz} = 0$; v and $w = 0$; and $\frac{du}{dy} = 0$ and $\frac{du}{dz} = 0$, these equations reduce to the following,

$$\varepsilon_{xx} = \frac{du}{dx} = \frac{1}{E}\left(\sigma'_{xx} - \nu\sigma'_{yy} - \nu\sigma'_{zz}\right) \tag{A15}$$

$$\frac{1}{E}\left(\sigma'_{yy} - \nu\sigma'_{zz} - \nu\sigma'_{xx}\right) = 0 \tag{A16}$$

$$\frac{1}{E}\left(\sigma'_{zz} - \nu\sigma'_{xx} - \nu\sigma'_{yy}\right) = 0 \tag{A17}$$

$$\varepsilon_{xy} = 0 \tag{A18}$$

$$\varepsilon_{yz} = 0 \tag{A19}$$

$$\varepsilon_{zx} = 0 \tag{A20}$$

Re-arranging Equations (A16) and (A17),

$$\sigma'_{xx} = \frac{1}{\nu}\sigma'_{yy} - \sigma'_{zz} \tag{A21}$$

$$\sigma'_{xx} = \frac{1}{\nu}\sigma'_{zz} - \sigma'_{yy} \tag{A22}$$

Equating Equation (A21) and Equation (A22),

$$\frac{1}{\nu}\sigma'_{yy} - \sigma'_{zz} = \frac{1}{\nu}\sigma'_{zz} - \sigma'_{yy} \tag{A23}$$

$$\frac{1}{\nu}\sigma'_{yy} + \sigma'_{yy} = \frac{1}{\nu}\sigma'_{zz} + \sigma'_{zz} \tag{A24}$$

$$\left(1 + \frac{1}{\nu}\right)\sigma'_{yy} = \left(1 + \frac{1}{\nu}\right)\sigma'_{zz} \tag{A25}$$

$$\sigma'_{yy} = \sigma'_{zz} \tag{A26}$$

Substituting Equation (A26) into Equation (A21) and re-arranging for σ_{yy} as a function of σ_{xx},

$$\sigma'_{yy} = \left(\frac{\nu}{1-\nu}\right)\sigma'_{xx} \tag{A27}$$

Substituting (A27) and (A26) into Equation (A15), we can solve for ε_{xx},

$$\varepsilon_{xx} = \frac{du}{dx} = \frac{1}{E}\left(\sigma_{xx} - 2\nu\sigma_{yy}\right) \tag{A28}$$

$$\varepsilon_{xx} = \frac{du}{dx} = \frac{1}{E}\left(\sigma_{xx} - 2\nu\left(\frac{\nu}{1-\nu}\right)\sigma_{xx}\right) \tag{A29}$$

$$\varepsilon_{xx} = \frac{du}{dx} = \frac{1}{E}\left[1 - \left(\frac{2\nu^2}{1-\nu}\right)\right]\sigma'_{xx} \tag{A30}$$

Re-arranging in terms of σ_{xx},

$$\sigma'_{xx} = \frac{E}{\left[1 - \left(\frac{2\nu^2}{1-\nu}\right)\right]}\frac{du}{dx} \tag{A31}$$

where for a 1D flow problem, it can be shown from Hooke's Law that

$$\varepsilon_{vol} = \varepsilon_{xx} = \frac{du}{dx} = \frac{\left[1 - \left(\frac{2\nu^2}{1-\nu}\right)\right]}{E}\sigma'_{xx} = \frac{1}{K_{1D}}\sigma'_{xx} = \frac{E}{\left[1 - \left(\frac{2\nu^2}{1-\nu}\right)\right]}\frac{du}{dx} \tag{A32}$$

and the Bulk modulus for 1D flow problem, K_{1D}, can be expressed as,

$$K_{1D} = \frac{E}{\left[1 - \left(\frac{2\nu^2}{1-\nu}\right)\right]} \tag{A33}$$

Substituting (A4) and (A31) into (A3) yields,

$$K_{1D}\frac{d^2u}{dx^2} + (1-\chi)\left(\frac{P_{atm} - P_{inj}}{L}\right) = 0 \tag{A34}$$

Re-arranging,

$$\frac{d^2u}{dx^2} = \frac{(1-\chi)}{K_{1D}L}\left(P_{atm} - P_{inj}\right) \tag{A35}$$

Solving the double integral,

$$\int \frac{d^2u}{dx^2} = \int \frac{(1-\chi)}{K_{1D}L}\left(P_{atm} - P_{inj}\right) \rightarrow \frac{du}{dx} = \left(\frac{(1-\chi)}{K_{1D}L}\left(P_{atm} - P_{inj}\right)x + C_2\right) \tag{A36}$$

$$\int \frac{du}{dx} = \int \left(\frac{(1-\chi)}{K_{1D}L}\left(P_{atm} - P_{inj}\right)x + C_2\right) \rightarrow u = \frac{(1-\chi)}{2K_{1D}L}\left(P_{atm} - P_{inj}\right)x^2 + C_2x + C_2{}' \tag{A37}$$

From our known BCs, at $x = 0$, $u(0) = 0$ and we can solve for $C_2{}'$

$$0 = \frac{(1-\chi)}{2K_{1D}L}\left(P_{atm} - P_{inj}\right)(0)^2 + C_2(0) + C_2{}' \rightarrow C_2{}' = 0 \tag{A38}$$

From our known BCs, $x = L$, $u(L) = 0$ and we can solve for C_2

$$0 = \frac{(1-\chi)}{2K_{1D}L}\left(P_{atm} - P_{inj}\right)(L)^2 + C_2(L) \rightarrow C_2 = -\frac{(1-\chi)}{2K_{1D}}\left(P_{atm} - P_{inj}\right) \tag{A39}$$

Substituting Equations (A38) and (A39) into Equation (A37), the analytical solution for the governing equation for the conservation of momentum can be expressed by Equation (A40) and simplified further to Equation (A41)

$$u(x) = \frac{(1-\chi)}{2K_{1D}}\left(P_{atm} - P_{inj}\right)\frac{x^2}{L} - \frac{(1-\chi)}{2K_{1D}}\left(P_{atm} - P_{inj}\right)x = -\frac{(1-\chi)}{K_{1D}}\frac{\left(P_{atm} - P_{inj}\right)}{2}\left(\frac{x^2}{L} - x\right) \tag{A40}$$

$$u(x) = \frac{1}{K_{1D}}(1-\chi)\frac{\left(P_{atm} - P_{inj}\right)}{2}\left(x - \frac{x^2}{L}\right) \tag{A41}$$

A.2.4. Final Analytical Solution

The final analytical solution for 1D steady-state gas flow through a linear elastic porous medium can be expressed by Equations (A8) and (A41),

$$p_g(x) = P_{inj} + \frac{P_{atm} - P_{inj}}{L}x \tag{A8}$$

$$u(x) = \frac{1}{K_{1D}}(1-\chi)\frac{\left(P_{atm} - P_{inj}\right)}{2}\left(x - \frac{x^2}{L}\right) \tag{A41}$$

The strain and stress can now be calculated analytically by the following expressions,

$$\varepsilon_{xx} = \frac{du}{dx} = \frac{(1-\chi)}{K_{1D}}\left(P_{atm} - P_{inj}\right)\frac{x}{L} - \frac{1}{K_{1D}}(1-\chi)\frac{\left(P_{atm} - P_{inj}\right)}{2} = \frac{1}{K_{1D}}(1-\chi)\left(P_{atm} - P_{inj}\right)\left(\frac{x}{L} - \frac{1}{2}\right) \tag{A42}$$

$$\sigma'_{xx} = K_{1D}\left(\frac{1}{K_{1D}}(1-\chi)\left(P_{atm} - P_{inj}\right)\frac{x}{L} - \frac{1}{K_{1D}}(1-\chi)\frac{\left(P_{atm} - P_{inj}\right)}{2}\right) = (1-\chi)\left(P_{atm} - P_{inj}\right)\left(\frac{x}{L} - \frac{1}{2}\right) \tag{A43}$$

$$\sigma'_{yy} = \sigma'_{zz} = \left(\frac{\nu}{1-\nu}\right)\sigma_{xx} \tag{A44}$$

A.3. Analytical Solution for 1-Dimensional Transient Gas Flow in a Linear Elastic Porous Medium

A.3.1 Governing Equations

The governing equation for the conservation of gas mass for transient (i.e., time-dependent) flow through a linear elastic porous medium can be expressed by Equation (A45),

$$\frac{d}{dx}\left(\rho_g \frac{k_g}{\mu_g}\frac{dp_g}{dx}\right) = -\frac{d\left(\rho_g n(1-S_w)\right)}{dt} \tag{A45}$$

By assuming the gas density and degree of saturation remains constant Equation (A45) simplifies to Equation (A46),

$$\rho_g \frac{k_g}{\mu_g}\frac{d}{dx}\left(\frac{dp_g}{dx}\right) = -\rho_g(1-S_w)\frac{dn}{dt} \tag{A46}$$

and solving for dn, this simplifies further to,

$$\frac{k_g}{\mu_g}\frac{d^2p_g}{dx^2} = -(1-S_w)(1-n)\frac{d\varepsilon_{vol}}{dt} \tag{A47}$$

$$-\frac{k_g}{\mu_g}\frac{1}{(1-S_w)(1-n)}\frac{d^2p_g}{dx^2} = \frac{d\varepsilon_{vol}}{dt} \tag{A48}$$

Substituting Equation (A32) into Equation (A48), yields

$$-\frac{k_g}{\mu_g}\frac{1}{(1-S_w)(1-n)}\frac{d^2p_g}{dx^2} = \frac{1}{K_{1D}}\frac{d\sigma'_{xx}}{dt} \tag{A49}$$

The governing equation for the conservation of momentum (quasi-static equilibrium) for steady-state gas-flow through a linear elastic porous medium assuming an immobile water phase was previously described by Equation (A50) as,

$$\frac{d\left(\sigma' + (1-\chi)p_g\right)}{dx} = 0 \tag{A50}$$

Integrating both sides and re-arranging for σ′,

$$\int \frac{d\left(\sigma' + (1-\chi)p_g\right)}{dx} = \int 0 \rightarrow \sigma' = -(1-\chi)p_g + C_1 \tag{A51}$$

Substituting Equation (A51) back into Equation (A49)

$$-\frac{k_g}{\mu_g}\frac{K_D}{(1-S_w)(1-n)}\frac{d^2p_g}{dx^2}=\frac{d\left(C_1-(1-\chi)p_g\right)}{dt} \tag{A52}$$

$$\frac{k_g}{\mu_g}\frac{K_D}{(1-S_w)(1-n)(1-\chi)}\frac{d^2p_g}{dx^2}=\frac{dp_g}{dt} \tag{A53}$$

where

$$D=\frac{k_g}{\mu_g}\frac{K_D}{(1-S_w)(1-n)(1-\chi)} \tag{A54}$$

A.3.2 Formulation of the Analytical Solution to the Conservation of Mass Equation

The form of Equation (A53) is analogous to that of non-steady state diffusion in a plane sheet presented in Crank [3]. The analytical solution for non-steady state diffusion in a plane sheet as derived by Crank [3] for constant surface concentrations and constant initial conditions is expressed by the following equation,

$$\begin{aligned}C(x,t)=C_1+(C_2-C_1)\frac{x}{L}+\frac{2}{\pi}\sum_{n=1}^{\infty}\frac{C_2\cos n\pi-C_1}{n}\sin\frac{n\pi x}{L}\exp\left(-\frac{Dn^2\pi^2t}{L^2}\right)\\+\frac{4C_0}{\pi}\sum_{m=0}^{\infty}\frac{1}{2m+1}\sin\frac{(2m+1)\pi x}{L}\exp\left(-\frac{D(2m+1)^2\pi^2t}{L^2}\right)\end{aligned} \tag{A55}$$

where $C(x,t)$ is the concentration at a given distance, x, and time, t, along the plane sheet
C_1 is the concentration at boundary x = 0
C_2 is the concentration at boundary x = L
C_0 is the initial uniform concentration
Considering our boundary and initial conditions provided in the problem statement.

$$\begin{aligned}p_g(x,t)=P_{inj}+\left(P_{atm}-P_{inj}\right)\frac{x}{L}+\frac{2}{\pi}\sum_{n=1}^{\infty}\frac{P_{atm}\cos n\pi-P_{inj}}{n}\sin\frac{n\pi x}{L}\exp\left(-\frac{Dn^2\pi^2t}{L^2}\right)\\+\frac{4P_0}{\pi}\sum_{m=0}^{\infty}\frac{1}{2m+1}\sin\frac{(2m+1)\pi x}{L}\exp\left(-\frac{D(2m+1)^2\pi^2t}{L^2}\right)\end{aligned} \tag{A56}$$

A.3.3 Formulation of the Analytical Solution to the Conservation of Momentum Equation

Substituting Equation (A53) into Equation (A32), the volumetric strain can be expressed as,

$$\varepsilon_{vol}=\frac{du}{dx}=C_1-\frac{1}{K_D}(1-\chi)p_g \tag{A57}$$

Integrating both sides yields,

$$\int \frac{du}{dx} = \int \left[C_1 - \frac{1}{K_D}(1-\chi)\left(P_{inj} + \left(P_{atm} - P_{inj}\right)\frac{x}{L} + \frac{2}{\pi}\sum_{n=1}^{\infty} \frac{P_{atm}\cos n\pi - P_{inj}}{n} \sin\frac{n\pi x}{L} \exp\left(-\frac{Dn^2\pi^2 t}{L^2}\right) + \frac{4P_0}{\pi}\sum_{m=0}^{\infty} \frac{1}{2m+1} \sin\frac{(2m+1)\pi x}{L} \exp\left(-\frac{D(2m+1)^2\pi^2 t}{L^2}\right)\right)\right] \tag{A58}$$

$$\int \frac{du}{dx} = \int \left[C_1 - \frac{1}{K_D}(1-\chi)P_{inj} - \frac{1}{K_D}(1-\chi)\left(P_{atm} - P_{inj}\right)\frac{x}{L} - \frac{1}{K_D}(1-\chi)\frac{2}{\pi}\sum_{n=1}^{\infty} \frac{P_{atm}\cos n\pi - P_{inj}}{n} \sin\frac{n\pi x}{L} \exp\left(-\frac{Dn^2\pi^2 t}{L^2}\right) - \frac{1}{K_D}(1 - \chi)\frac{4P_0}{\pi}\sum_{m=0}^{\infty} \frac{1}{2m+1} \sin\frac{(2m+1)\pi x}{L} \exp\left(-\frac{D(2m+1)^2\pi^2 t}{L^2}\right)\right] \tag{A59}$$

$$\begin{aligned} u &= C_1 x - \frac{1}{K_D}(1-\chi)P_{inj}x - \frac{1}{K_D}(1-\chi)\left(P_{atm} - P_{inj}\right)\frac{x^2}{2L} \\ &- \frac{1}{K_D}(1-\chi)\frac{2}{\pi}\sum_{n=1}^{\infty}\left(\frac{P_{atm}\cos n\pi - P_{inj}}{n}\right)\left(\frac{-L}{n\pi}\right)\cos\frac{n\pi x}{L}\exp\left(-\frac{Dn^2\pi^2 t}{L^2}\right) \\ &- \frac{1}{K_D}(1-\chi)\frac{4P_0}{\pi}\sum_{m=0}^{\infty}\frac{-L}{(2m+1)^2\pi}\cos\frac{(2m+1)\pi x}{L}\exp\left(-\frac{D(2m+1)^2\pi^2 t}{L^2}\right) + C_1' \end{aligned} \tag{A60}$$

From our boundary conditions $u(0,t) = 0$

$$\begin{aligned} 0 &= C_1(0) - \frac{1}{K_D}(1-\chi)P_{inj}(0) - \frac{1}{K_D}(1-\chi)\left(P_{atm} - P_{inj}\right)\frac{(0)^2}{2L} \\ &- \frac{1}{K_D}(1-\chi)\frac{2}{\pi}\sum_{n=1}^{\infty}\left(\frac{P_{atm}\cos n\pi - P_{inj}}{n}\right)\left(\frac{-L}{n\pi}\right)\cos\frac{n\pi(0)}{L}\exp\left(-\frac{Dn^2\pi^2 t}{L^2}\right) \\ &- \frac{1}{K_D}(1-\chi)\frac{4P_0}{\pi}\sum_{m=0}^{\infty}\frac{-L}{(2m+1)^2\pi}\cos\frac{(2m+1)\pi(0)}{L}\exp\left(-\frac{D(2m+1)^2\pi^2 t}{L^2}\right) \\ &+ C_1' \end{aligned} \tag{A61}$$

$$C_1' = \frac{1}{K_D}(1-\chi)\frac{2}{\pi}\sum_{n=1}^{\infty}\left(\frac{P_{atm}\cos n\pi - P_{inj}}{n}\right)\left(\frac{-L}{n\pi}\right)\exp\left(-\frac{Dn^2\pi^2 t}{L^2}\right) + \frac{1}{K_D}(1-\chi)\frac{4P_0}{\pi}\sum_{m=0}^{\infty}\frac{-L}{(2m+1)^2\pi}\exp\left(-\frac{D(2m+1)^2\pi^2 t}{L^2}\right) \tag{A62}$$

Substituting back into Equation (A60), yields,

$$
\begin{aligned}
&u \\
&= C_1 x - \frac{1}{K_D}(1-\chi)P_{inj}x - \frac{1}{K_D}(1-\chi)\left(P_{atm}-P_{inj}\right)\frac{x^2}{2L} \\
&- \frac{1}{K_D}(1-\chi)\frac{2}{\pi}\sum_{n=1}^{\infty}\left(\frac{P_{atm}\cos n\pi - P_{inj}}{n}\right)\left(\frac{-L}{n\pi}\right)\cos\frac{n\pi x}{L}\exp\left(-\frac{Dn^2\pi^2 t}{L^2}\right) \\
&+ \frac{1}{K_D}(1-\chi)\frac{2}{\pi}\sum_{n=1}^{\infty}\left(\frac{P_{atm}\cos n\pi - P_{inj}}{n}\right)\left(\frac{-L}{n\pi}\right)\exp\left(-\frac{Dn^2\pi^2 t}{L^2}\right) \\
&- \frac{1}{K_D}(1-\chi)\frac{4P_0}{\pi}\sum_{m=0}^{\infty}\frac{-L}{(2m+1)^2\pi}\cos\frac{(2m+1)\pi x}{L}\exp\left(-\frac{D(2m+1)^2\pi^2 t}{L^2}\right) \\
&+ \frac{1}{K_D}(1-\chi)\frac{4P_0}{\pi}\sum_{m=0}^{\infty}\frac{-L}{(2m+1)^2\pi}\exp\left(-\frac{D(2m+1)^2\pi^2 t}{L^2}\right)
\end{aligned}
\tag{A63}
$$

$$
\begin{aligned}
u = C_1 x &- \frac{1}{K_D}(1-\chi)\left[P_{inj}x + \left(P_{atm}-P_{inj}\right)\frac{x^2}{2L}\right] \\
&+ \frac{1}{K_D}(1 \\
&- \chi)\frac{2}{\pi}\sum_{n=1}^{\infty}\left(\frac{P_{atm}\cos n\pi - P_{inj}}{n}\right)\left(\frac{-L}{n\pi}\right)\exp\left(-\frac{Dn^2\pi^2 t}{L^2}\right)\left(1\right. \\
&\left. - \cos\frac{n\pi x}{L}\right) \\
&+ \frac{1}{K_D}(1 \\
&- \chi)\frac{4P_0}{\pi}\sum_{m=0}^{\infty}\frac{-L}{(2m+1)^2\pi}\exp\left(-\frac{D(2m+1)^2\pi^2 t}{L^2}\right)\left(1\right. \\
&\left. - \cos\frac{(2m+1)\pi x}{L}\right)
\end{aligned}
\tag{A64}
$$

From our boundary conditions $u(L,t) = 0$

$$
\begin{aligned}
0 = C_1 L &- \frac{1}{K_D}(1-\chi)\left[P_{inj}L + \left(P_{atm}-P_{inj}\right)\frac{L}{2}\right] \\
&+ \frac{1}{K_D}(1 \\
&- \chi)\frac{2}{\pi}\sum_{n=1}^{\infty}\left(\frac{P_{atm}\cos n\pi - P_{inj}}{n}\right)\left(\frac{-L}{n\pi}\right)\exp\left(-\frac{Dn^2\pi^2 t}{L^2}\right)\left(1\right. \\
&\left. - \cos\frac{n\pi(L)}{L}\right) \\
&+ \frac{1}{K_D}(1 \\
&- \chi)\frac{4P_0}{\pi}\sum_{m=0}^{\infty}\frac{-L}{(2m+1)^2\pi}\exp\left(-\frac{D(2m+1)^2\pi^2 t}{L^2}\right)\left(1\right. \\
&\left. - \cos\frac{(2m+1)\pi(L)}{L}\right)
\end{aligned}
\tag{A65}
$$

$$C_1 = \frac{1}{K_D}(1-\chi)\left[P_{inj} + \frac{\left(P_{atm} - P_{inj}\right)}{2}\right] - \frac{1}{K_D}(1 - \chi)\frac{2}{\pi}\sum_{n=1}^{\infty}\left(\frac{P_{atm}\cos n\pi - P_{inj}}{n}\right)\left(\frac{-1}{n\pi}\right)\exp\left(-\frac{Dn^2\pi^2 t}{L^2}\right)(1 - \cos n\pi) - \frac{1}{K_D}(1-\chi)\frac{4P_0}{\pi}\sum_{m=0}^{\infty}\frac{-1}{(2m+1)^2\pi}\exp\left(-\frac{D(2m+1)^2\pi^2 t}{L^2}\right)(1 - \cos(2m+1)\pi) \quad \text{(A66)}$$

Substituting back into Equation (A60)

$$u = \frac{1}{K_D}(1-\chi)\left[P_{inj} + \frac{\left(P_{atm} - P_{inj}\right)}{2} - \frac{2}{\pi}\sum_{n=1}^{\infty}\left(\frac{P_{atm}\cos n\pi - P_{inj}}{n}\right)\left(\frac{-1}{n\pi}\right)\exp\left(-\frac{Dn^2\pi^2 t}{L^2}\right)(1 - \cos n\pi) - \frac{4P_0}{\pi}\sum_{m=0}^{\infty}\frac{-1}{(2m+1)^2\pi}\exp\left(-\frac{D(2m+1)^2\pi^2 t}{L^2}\right)(1 - \cos(2m+1)\pi)\right]x - \frac{1}{K_D}(1-\chi)\left[P_{inj}x + \left(P_{atm} - P_{inj}\right)\frac{x^2}{2L}\right] + \frac{1}{K_D}(1 - \chi)\frac{2}{\pi}\sum_{n=1}^{\infty}\left(\frac{P_{atm}\cos n\pi - P_{inj}}{n}\right)\left(\frac{-L}{n\pi}\right)\exp\left(-\frac{Dn^2\pi^2 t}{L^2}\right)\left(1 - \cos\frac{n\pi x}{L}\right) + \frac{1}{K_D}(1 - \chi)\frac{4P_0}{\pi}\sum_{m=0}^{\infty}\frac{-L}{(2m+1)^2\pi}\exp\left(-\frac{D(2m+1)^2\pi^2 t}{L^2}\right)\left(1 - \cos\frac{(2m+1)\pi x}{L}\right) \quad \text{(A67)}$$

$$
\begin{aligned}
u = {} & \frac{1}{K_D}(1-\chi)\frac{(P_{atm}-P_{inj})}{2}x \\
& -\frac{1}{K_D}(1 \\
& -\chi)\frac{2}{\pi}\sum_{n=1}^{\infty}\left(\frac{P_{atm}\cos n\pi - P_{inj}}{n}\right)\left(\frac{-1}{n\pi}\right)\exp\left(-\frac{Dn^2\pi^2 t}{L^2}\right)(1 \\
& -\cos n\pi)\,x \\
& -\frac{1}{K_D}(1 \\
& -\chi)\frac{4P_0}{\pi}\sum_{m=0}^{\infty}\frac{-1}{(2m+1)^2\pi}\exp\left(-\frac{D(2m+1)^2\pi^2 t}{L^2}\right)(1 \\
& -\cos(2m+1)\pi)\,x - \frac{1}{K_D}(1-\chi)(P_{atm}-P_{inj})\frac{x^2}{2L} \\
& +\frac{1}{K_D}(1 \\
& -\chi)\frac{2}{\pi}\sum_{n=1}^{\infty}\left(\frac{P_{atm}\cos n\pi - P_{inj}}{n}\right)\left(\frac{-L}{n\pi}\right)\exp\left(-\frac{Dn^2\pi^2 t}{L^2}\right)\left(1 \\
& -\cos\frac{n\pi x}{L}\right) \\
& +\frac{1}{K_D}(1 \\
& -\chi)\frac{4P_0}{\pi}\sum_{m=0}^{\infty}\frac{-L}{(2m+1)^2\pi}\exp\left(-\frac{D(2m+1)^2\pi^2 t}{L^2}\right)\left(1 \\
& -\cos\frac{(2m+1)\pi x}{L}\right)
\end{aligned}
\tag{A68}
$$

$$
\begin{aligned}
u = {} & \frac{1}{K_D}(1-\chi)\frac{(P_{atm}-P_{inj})}{2}\left[x-\frac{x^2}{L}\right] \\
& +\frac{1}{K_D}(1 \\
& -\chi)\frac{2}{\pi}\sum_{n=1}^{\infty}\left(\frac{P_{atm}\cos n\pi - P_{inj}}{n}\right)\exp\left(-\frac{Dn^2\pi^2 t}{L^2}\right)\left(\frac{1}{n\pi}\right)(x \\
& -x\cos n\pi + L\cos\frac{n\pi x}{L} - L) \\
& +\frac{1}{K_D}(1 \\
& -\chi)\frac{4P_0}{\pi}\sum_{m=0}^{\infty}\frac{1}{(2m+1)^2\pi}\exp\left(-\frac{D(2m+1)^2\pi^2 t}{L^2}\right)\left(x \\
& -x\cos(2m+1)\pi + L\cos\frac{(2m+1)\pi x}{L} - L\right)
\end{aligned}
\tag{A69}
$$

$$
\begin{aligned}
u = \frac{1}{K_D}(1-\chi)\frac{(P_{atm}-P_{inj})}{2}\left[x-\frac{x^2}{L}\right] \\
&+\frac{1}{K_D}(1 \\
&-\chi)\frac{2}{\pi}\sum_{n=1}^{\infty}\left(\frac{P_{atm}\cos n\pi - P_{inj}}{n}\right)\exp\left(-\frac{Dn^2\pi^2 t}{L^2}\right)\left(\frac{-L}{n\pi}\right)\left(1-\frac{x}{L}\right. \\
&\left.+\frac{x}{L}\cos n\pi - \cos\frac{n\pi x}{L}\right) \\
&+\frac{1}{K_D}(1 \\
&-\chi)\frac{4P_0}{\pi}\sum_{m=0}^{\infty}\exp\left(-\frac{D(2m+1)^2\pi^2 t}{L^2}\right)\left(\frac{-L}{(2m+1)^2\pi}\right)\left(1-\frac{x}{L}\right. \\
&\left.+\frac{x}{L}\cos(2m+1)\pi - \cos\frac{(2m+1)\pi x}{L}\right)
\end{aligned}
\tag{A70}
$$

A.3.4. Final Analytical Solution

The final analytical solution for 1D transient gas flow through a linear elastic porous medium can be expressed by Equations (A56) and (A70),

$$
\begin{aligned}
p_g(x,t) = P_{inj} + (P_{atm}-P_{inj})\frac{x}{L} \\
&+\frac{2}{\pi}\sum_{n=1}^{\infty}\frac{P_{atm}\cos n\pi - P_{inj}}{n}\sin\frac{n\pi x}{L}\exp\left(-\frac{Dn^2\pi^2 t}{L^2}\right) \\
&+\frac{4P_0}{\pi}\sum_{m=0}^{\infty}\frac{1}{2m+1}\sin\frac{(2m+1)\pi x}{L}\exp\left(-\frac{D(2m+1)^2\pi^2 t}{L^2}\right)
\end{aligned}
\tag{A56}
$$

$$
\begin{aligned}
u = \frac{1}{K_D}(1-\chi)\frac{(P_{atm}-P_{inj})}{2}\left[x-\frac{x^2}{L}\right] \\
&+\frac{1}{K_D}(1 \\
&-\chi)\frac{2}{\pi}\sum_{n=1}^{\infty}\left(\frac{P_{atm}\cos n\pi - P_{inj}}{n}\right)\exp\left(-\frac{Dn^2\pi^2 t}{L^2}\right)\left(\frac{-L}{n\pi}\right)\left(1-\frac{x}{L}\right. \\
&\left.+\frac{x}{L}\cos n\pi - \cos\frac{n\pi x}{L}\right) \\
&+\frac{1}{K_D}(1 \\
&-\chi)\frac{4P_0}{\pi}\sum_{m=0}^{\infty}\exp\left(-\frac{D(2m+1)^2\pi^2 t}{L^2}\right)\left(\frac{-L}{(2m+1)^2\pi}\right)\left(1-\frac{x}{L}\right. \\
&\left.+\frac{x}{L}\cos(2m+1)\pi - \cos\frac{(2m+1)\pi x}{L}\right)
\end{aligned}
\tag{A70}
$$

The strain and stress can now be calculated analytically by the following expressions,

$$\varepsilon_{vol} = \frac{du}{dx} = \frac{1}{K_D}(1-\chi)\left(P_{atm} - P_{inj}\right)\left(\frac{1}{2} - \frac{x}{L}\right) + \frac{1}{K_D}(1 - \chi)\frac{2}{\pi}\sum_{n=1}^{\infty}\left(\frac{P_{atm}\cos n\pi - P_{inj}}{n}\right)\exp\left(-\frac{Dn^2\pi^2 t}{L^2}\right)\left(\frac{1}{n\pi} - \frac{1}{n\pi}\cos n\pi - \sin\frac{n\pi x}{L}\right) + \frac{1}{K_D}(1 - \chi)\frac{4P_0}{\pi}\sum_{m=0}^{\infty}\frac{1}{2m+1}\exp\left(-\frac{D(2m+1)^2\pi^2 t}{L^2}\right)\left(\frac{1}{(2m+1)\pi} - \frac{1}{(2m+1)\pi}\cos(2m+1)\pi - \sin\frac{(2m+1)\pi x}{L}\right) \quad \text{(A71)}$$

$$\varepsilon_{vol} = \frac{du}{dx} = \frac{1}{K_D}(1-\chi)\left(P_{atm} - P_{inj}\right)\left(\frac{1}{2} - \frac{x}{L}\right) + \frac{1}{K_D}(1 - \chi)\frac{2}{\pi}\sum_{n=1}^{\infty}\left(\frac{P_{atm}\cos n\pi - P_{inj}}{n}\right)\exp\left(-\frac{Dn^2\pi^2 t}{L^2}\right)\left(\frac{1}{n\pi}\cos n\pi - \frac{1}{n\pi} + \sin\frac{n\pi x}{L}\right) + \frac{1}{K_D}(1 - \chi)\frac{4P_0}{\pi}\sum_{m=0}^{\infty}\frac{1}{2m+1}\exp\left(-\frac{D(2m+1)^2\pi^2 t}{L^2}\right)\left(\frac{1}{(2m+1)\pi}\cos(2m+1)\pi - \frac{1}{(2m+1)\pi} + \sin\frac{(2m+1)\pi x}{L}\right) \quad \text{(A72)}$$

CHAPTER 5: A MATHEMATICAL MODEL OF GAS AND WATER FLOW IN A SWELLING GEOMATERIAL – PART 2. PROCESS SIMULATION

Article

A Mathematical Model of Gas and Water Flow in a Swelling Geomaterial – Part 2. Process Simulation

Elias Ernest Dagher [1,2], Julio Ángel Infante Sedano [2] and Thanh Son Nguyen [1,2,*]

[1] Canadian Nuclear Safety Commission (CNSC), Ottawa, ON, K1P 5S9, Canada;
[2] Department of Civil Engineering, University of Ottawa, Ottawa, ON K1N 6N5, Canada; e-mail@e-mail.com
* Correspondence: son.nguyen@canada.ca

Received: 24 October 2019; Accepted: 20 December 2019; Published: 29 December 2019

Abstract: Gases can potentially generate in a deep geological repository (DGR) for the long-term containment of radioactive waste. Natural and engineered barriers provide containment of the waste by mitigating contaminant migration. However, if gas pressures exceed the mechanical strength of these barriers, preferential flow pathways for both the gases and the porewater could form, providing a source of potential exposure to people and the environment. Expansive soils, such as bentonite-based materials, are widely considered as sealing materials. Understanding the long-term performance of these seals as barriers against gas migration is an important component in the design and long-term safety assessment of a DGR. This study proposes a hydro-mechanical mathematical model for migration of gas through a low-permeable swelling geomaterial based on the theoretical framework of poromechanics. Using the Finite Element Method, the model is used to simulate 1D flow through a confined cylindrical sample of near-saturated low-permeable soil under a constant volume boundary stress condition. The study expands upon previous work by the authors by assessing the influence of heterogeneity, the Klinkenberg "slip flow" effect, and a swelling stress on flow behavior. Based on the results, this study provides fundamental insight into a number of factors which may influence two-phase flow.

Keywords: THMC modelling; multi-phase flow; gas migration; nuclear waste disposal; bentonite; expansive soils; swelling soils; swelling geomaterials

1. Introduction

In Canada, nuclear waste has been generated and accumulated since the 1930s when the Port Radium radium mine began operating in the Northwest Territories [50]. Over the past century Canada has become a sustainable nuclear country with operating nuclear facilities across the nuclear fuel cycle all producing various forms of radioactive waste. To-date, this waste, in the form of low-, intermediate-, and high-level radioactive waste has been primarily stored on-site at nuclear power plants or in below surface radioactive waste management facilities.

In identifying a long-term solution to manage global radioactive waste, the international community, including Canada, have been evaluating the use of a Deep Geological Repository (DGR) for its long-term management. The primary purpose of a DGR is to contain and isolate wastes to minimize impact to the environment and radiological exposure to people.

In developing a safety case for a DGR to provide supportive arguments that the management of radioactive waste will be protective of human health and the environment over the long term, relevant features, events, and processes (FEPs), must be evaluated [17, 18]. One such process with the potential means for radiological exposure to the biosphere is the generation of radioactive gas which may migrate to the surface [19]. Gas could be generated through a number of processes including the degradation of

organic matter, radioactive decay of the waste, corrosion of metals producing hydrogen gas (H_2), and the radiolysis of water producing H_2 [20, 21, 19]. If production exceeds the containment capacity of the engineered barriers or host rock, these gases could migrate through the engineered barriers and/or the host rock [22, 9]. The preferential migration pathway of these radioactive gases, to potentially expose people and the environment to radioactivity, might be through the access and ventilation shafts, as these components are typically part of the repository design.

In recent years, a number of international projects have focused on the topics of gas generation and migration, with a focus on the impact of gas build-up and migration through an engineered barrier system (EBS) [23, 24, 4]. Expansive or swelling soils, such as bentonite-based materials, are currently the preferred choice of seal materials used for an EBS. Understanding the long-term performance of these seals as barriers against gas migration is an important factor in the design and long-term safety assessment of a DGR.

In 2005, Marschall et al. [5] described gas transport processes in low-permeability clay material, and their work was further investigated by Cuss et al. [20]. Marschall et al. [5] recognized that gas transport through porous media is controlled by a number of the media's hydraulic and mechanical characteristics such as the intrinsic permeability, porosity, and material strength. They identified the importance of the hydro-mechanical state of the rock or soil media (i.e., water saturation, porewater pressure, and stress state) and the gas pressure at focal points which could lead to microfracturing [5]. Marschall et al. [5] divided the basic transport mechanisms into four processes, mainly i) advective-diffusive transport of gas, ii) visco-capillary two-phase flow, iii) dilatancy-controlled gas flow and the induction of microfractures creating preferential flow pathways, and iv) gas transport along macro-fractures.

Of particular interest to this paper, is the investigation of processes and characteristics which may be contributing to dilation-controlled gas flow, resulting in an accelerated rate of gas migration in a nearly saturated geomaterial. These processes and characteristics are loosely called "enhanced mechanisms" for gas migration, since without them, the migration rate is expected to be very low. A wealth of laboratory and field-scale experimental studies have investigated gas transport processes through natural (host rock) and engineered barriers. These studies provide a wealth of evidence that suggest that at gas pressures above a critical level, there is formation of pressure-induced preferential flow pathways and dilation of the clay, resulting in increased gas flow. In addition, a number of mathematical models have been developed to simulate the gas transport processes observed through these laboratory and field scale studies with some success [33, 34, 35]. However, no studies to date have been able to determine the exact mechanisms which control gas entry, flow, and pathway sealing [25, 22, 26, 27, 28, 20, 23, 29].

Marschall et al. [5] described the primary transport mechanism of dilatancy-controlled gas flow as an important transport mechanism in clay soil or clay-rich rock with low tensile strength. Dilatancy will occur when the gas pressure reaches a reference stress level acting on the clay medium, forcing the clay particles to align in a dispersed orientation, and resulting in the formation of microfractures accompanied by an increase in plastic deformation [30]. As a result, gas flow along these microfractures will be promoted due to the increased pore space. The presence of microfractures therefore leads to an increase in the intrinsic permeability of the material and in turn results in changes in the relationship between the capillary pressure (i.e., matric suction) and degree of saturation (i.e., soil water characteristic curve (SWCC) of the material). Attributable to dilatancy-controlled gas flow, transport properties are now dependent on the stress state and state of deformation of the soil.

Other considerations when conceptualizing the physical processes taking place during two-phase flow through a porous medium is the phenomenon of viscous- or gas fingering. The phenomenon of gas fingering results from differences in the fluid viscosity of the liquid phase and of the gas phase. Sahimi et al. stated that viscous fingering would occur, when the mobility ratio, M (generally the ratio of gas and liquid viscosities), between the gas phase and the liquid phase is less than one ($M < 1$) [31]. Since movement of the gas front is faster than the liquid front this will result in a displacement front (i.e., gas front is further than the liquid front). In a porous medium the gas front may result in the formation of gas 'fingers' [31].

Several works have identified that a number of factors contribute to the effect of gas fingering. These include the displacement rate of the gas with the liquid (i.e., differences in mobility of the individual phases), the extent of heterogeneity of the porous medium and spatial variations of the porosity and permeability, the viscosity ratio between the gas and liquid, three-dimensional dispersion within the porous medium, and the aspect ratio and boundary conditions representing the narrowness of the porous medium [31, 63, 64]. Additionally, in order to numerically simulate fingering effects accurately, consideration of mesh size also plays a critical role [63]. Moortgat et al. also identified that other factors may help stabilize gas fingering, and include consideration of gravity, diffusion and capillary pressure [64].

Dagher et al. [4] developed a fully-coupled hydro-mechanical (HM) linear-elastic mathematical model for advective-diffusive visco-capillary controlled two-phase flow through geomaterials in order to model the first two transport mechanisms (i.e., advection and diffusion of dissolved gas, and visco-capillary "two-phase" flow) proposed by Marschall et al. [5]. Results from a constant volume 1-D flow experiment was used to validate the model. A number of parametric studies were investigated to assess the contribution of advection of poregas, diffusion of dissolved gas in porewater, advection of dissolved gas in porewater, and inclusion of mechanical deformation (linear elasticity) on flow behaviour with increasing gas pressures over time. Additionally, sensitivity analyses were conducted to gain an understanding of the influence of a number of soil properties on flow behaviour, such as the effect of modifying the air-entry value (AEV), intrinsic permeability, and initial porosity of the soil specimen. Finally, the study investigated the use of a linear elastic damage model to better represent the experimental results. Although the model results reproduced some of the general features noted in the experimental results, the model was unable to simulate dilatancy-controlled gas flow. The study concluded that in order to simulate dilatancy-controlled gas flow additional mechanisms need to be considered within the model. These include the use of advanced mechanism of mechanical deformation to be coupled to gas transport, consideration of heterogeneity within the soil sample to help induce preferential flow, inclusion of a swelling stress term to incorporate the swelling behaviour of expansive soils, and the incorporation of a self-healing mechanism to represent observed phenomena of experimental studies [4].

This study builds upon the authors' previous published work by investigating the use of advanced physical relationships on flow behaviour, specifically the influence of: i) heterogeneity within the geomaterial to promote preferential flow, ii) the Klinkenberg "slip flow" effect on gas permeability, and iii) a linear swelling stress to promote swelling of the geomaterial. Finally, the authors investigate the conditions that promote fingering in two-phase flow. The models are validated against experimental data from a 1D flow test. The results of this study will be used to inform the development of a more sophisticated HM model which can be used to simulate dilation-controlled gas flow in a swelling geomaterial.

This research continues to be, in part, a contribution to Task A of the current project phase of the international working group for the DEvelopment of COupled models and their VALidation against EXperiments (DECOVALEX-2019). This task, led by the British Geological Survey (BGS), further attempts to identify the physical HM mechanisms required to adequately model dilatancy-controlled gas migration.

2. Mathematical Model

2.1. Study Overview

This study expands upon the work performed by Dagher et al. [4] on the development of a mathematical model for gas migration (two-phase flow) through a low-permeable swelling geomaterial. Using the theoretical framework of poromechanics, this study provides a process simulation and analysis of enhanced processes for two-phase flow related to the inclusion of the following advanced physical relations to the HM model to investigate their effect on two-phase (water and gas) flow behaviour, specifically:

i. heterogeneity through the use of a random normal distribution of porosity,
ii. Klinkenberg "slip flow" effect for the intrinsic permeability of the gas in soil, and
iii. a swelling strain to take into account volume changes of the geomaterial with suction

The mathematical model presented in this paper follows the general formulation by Dagher et al. [4] and Nguyen and Le [1]and includes the constitutive relations for the Soil Water Characteristic Curves (SWCCs) through the application of the van Genuchten equation, and the relative permeability-saturation relationships using Mualem's Model. The applicable constitutive relations and governing equations for conservation of momentum, water mass and gas mass are also discussed in the companion paper to this one [65]. For sake of consistency, the final governing equations are also provided below along with a mathematical description of the Klinkenberg Effect and swelling strain.

2.2. Governing Equations for Two-Phase Flow through a Linear Elastic Geomaterial

2.2.1. Conservation of water mass

The governing equation for the conservation of water mass can be expressed by equation (1),

$$\frac{\partial}{\partial x_i}\left(\rho_w \frac{k_{ij,w} k_{r,w}}{\mu_w}\left(\frac{\partial p_w}{\partial x_j} + \rho_w g_j\right)\right) = -\rho_w\left[n\left(\frac{dS_w}{ds}\right)\frac{\partial s}{\partial t} + n\frac{S_w}{K_w}\frac{\partial p_w}{\partial t} + S_w\frac{\partial}{\partial t}\left(\frac{\partial u_k}{\partial x_k}\right)\right] \quad (1)$$

where ρ_w is the density of water phase (kg m^{-3})
p_w is the porewater pressure (Pa)
$k_{ij,w}$ is the intrinsic permeability tensor of water flow in the porous medium (m^2)
$k_{r,w}$ is the relative permeability of the water phase (adimensional)
μ_w is the dynamic viscosity of the water phase (Pa s or kg m^{-1} s^{-1})
g is the acceleration due to gravity (m s^{-2})
n is the porosity (m^3 voids · m^{-3} total)
S_w is the degree of saturation of water (adimensional)
s is the matric suction $(p_g - p_w)$ (Pa)
K_w is the bulk modulus of the water phase (Pa s or kg m^{-1} s^{-1})
$\frac{\partial u_k}{\partial x_k} = \varepsilon_{vol}$ is the volumetric strain (adimensional)
u is the displacement of the solid skeleton (m)
t is time (s)
Note that in this study, the permeability is assumed to be isotropic, therefore $k_{ij} = k$, however we keep the tensorial notation in the governing equation for the sake of generalization.

2.2.2. Conservation of gas mass

The governing equation for the conservation of gas mass can be expressed by equation (2),

$$\frac{\partial\left(\rho_g\left(\frac{k_{ij,g}k_{r,g}}{\mu_g}\left(\frac{\partial p_g}{\partial x_j} + \rho_g g\right) + H\frac{k_{ij}k_{rw}}{\mu_w}\left(\frac{\partial p_w}{\partial x_j} + \rho_w g\right)\right)\right)}{\partial x_i} + \frac{\partial}{\partial x_i}\left(-D_e\frac{\partial}{\partial x_k}\left(\rho_g n(HS_w)\right)\right) = -\rho_g\left[n(H-1)\left(\frac{dS_w}{ds}\right)\frac{\partial s}{\partial t} + \frac{n(1 - S_w + HS_w)}{K_g}\frac{\partial p_g}{\partial t} + (1 - S_w + HS_w)\frac{\partial}{\partial t}\left(\frac{\partial u_k}{\partial x_k}\right)\right] \quad (2)$$

where ρ_g is the density of the gas phase (kg m^{-3})
p_g is the poregas pressure (Pa)
$k_{ij,g}$ is the intrinsic permeability tensor of gas flow in the porous medium (m^2)

$k_{r,g}$ is the relative permeability of the gas phase (adimensional)
μ_g is the dynamic viscosity of the gas phase (Pa s or kg m^{-1} s^{-1})
H is Henry's coefficient (kg species A m^{-3} in aqueous phase kg^{-1} species A m^3 in gas phase)
D_e is the effective diffusivity of gas dissolved in water through porous media (m^2 s^{-1})
K_g is the bulk modulus of the gas phase (Pa)

2.2.3. Conservation of momentum (quasi-static equilibrium)

For a linear poro-elastic swelling geomaterial the governing equation for the conservation of momentum can be expressed by equation (3),

$$G\frac{\partial^2 u_i}{\partial x_j \partial x_j} + (G+\lambda)\frac{\partial^2 u_j}{\partial x_j \partial x_i} - K\beta_{sw}\frac{\partial s}{\partial x_i} + (1-\chi)\frac{\partial p_g}{\partial x_i} + \chi\frac{\partial p_w}{\partial x_i} + F_{v,i} = 0 \quad (3)$$

where G is the shear modulus (Pa)
λ is the Lamé constant (Pa)
β_{sw} is a swelling coefficient (1/Pa), as discussed in Section 2.4
K is the bulk modulus of the solid skeleton (Pa)
X is a parameter related to the degree of saturation of the soil [26]
$F_{v,i}$ is the volumetric body force tensor (kg m^{-2} s^{-2})

2.3. Intrinsic permeability and the Klinkenberg Effect "Slip Flow"

In addition to the constitutive relations for the hydraulic behavior provided in Dagher et al [4] and the companion paper to this one [65], this paper investigates the use of the Klinkenberg effect to represent a value of the intrinsic permeability of gas which is different from that of water. In this study, the intrinsic permeability tensor is assumed to be isotropic. Therefore, off-diagonal components are nil and diagonal components are equal to a value k,

$$k_{ij} = \delta_{ij} k \quad (4)$$

where δ_{ij} is the Kronecker delta (identity tensor) (adimensional)

For fine-grained expansive clays, which have very small grain-sizes less than 2 μm, and are non-uniform, Pall and Moshenin [56], proposed the following equation which is based on a volume-surface mean diameter and changing porosity to account for non-uniformity of the soil particles. This equation was applied to the author's previous model [4].

$$k_w = \frac{D_{vs}^2}{180}\frac{n^3}{(1-n)^2} \quad (5)$$

where D_{vs} is the volume-surface mean diameter (cm)

The porosity is calculated by,

$$n = n_0 + \varepsilon_{vol} \quad (6)$$

where, n_0 is the initial porosity of the porous medium (m^3 voids · m^{-3} total)

As the intrinsic permeability is not a property of the porefluid but rather a property of the geometry of the porous medium (i.e., porosity, pore shape, and pore size distribution), it is reasonable to assume that the permeability of porewater and poregas in the same soil specimen would be the same. However, a number of studies have shown that the intrinsic permeability of gas is often higher than that of water and may be related to the poregas pressure [66, 67, 68]. The Klinkenberg effect, also described as "slip flow",

has been used to conceptualize this phenomenon, whereby slip occurs between the gas molecules and the solid wall, resulting in an increase in the intrinsic permeability of gas as poregas pressure decreases [69].

Equations (7) and (8) provide the relationship between the intrinsic permeability value of water and the intrinsic permeability value of gas a function of pressure.

$$k_g = k_w\left(1 + \frac{b_{ke}}{p_g}\right) \tag{7}$$

$$b_{ke} = \frac{c_{ke}\kappa_B T}{\pi\sqrt{2}r^3} \tag{8}$$

where k_g is the intrinsic permeability value of gas (m^2)

k_w is the intrinsic permeability value of water (m^2)

b_{ke} is the Klinkenberg slip factor (Pa)

c_{ke} is a constant (adimensional)

κ_B is Boltzmann's constant ($J\ K^{-1}$)

T is the temperature (K)

r is the pore radius (m)

2.4. Swelling strain component

Using the elastic framework, the total strain can be divided into an elastic and a swelling strain component as follows:

$$\varepsilon_{kl} = \varepsilon_{ij}^{el} + \varepsilon_{ij}^{sw} \tag{9}$$

where ε_{kl} is the total strain tensor (adimensional)

ε_{ij}^{el} is the elastic strain component (adimensional)

ε_{ij}^{sw} is the swelling strain component (adimensional)

For an expansive/swelling soil, the swelling strain increment, $d\varepsilon_{ij}^{sw}$ is a function of suction, s, or the degree of saturation, S_w, whereby an increase in suction (or likewise a decrease in degree of saturation) leads to shrinkage of the geomaterial and an increase in porespace, due to the increase in volumetric strain provided by the swelling strain [70]. Assuming isotropic swelling, this can be expressed by the following equation,

$$d\varepsilon_{ij}^{sw} = \delta_{ij}\frac{\beta_{sw}}{3}ds \tag{10}$$

where β_{sw} is a swelling coefficient (1/Pa)

$s = (p_g - p_w)$ is the suction (Pa), and

To simplify the relationship between swelling strain and suction, Nasir et al. [70] proposed a linear swelling strain with a constant swelling coefficient, β_{sw}, for a bentonite-sand mixture with a relatively good fit to experimental swelling stress results.

3. Process Simulation and Enhanced Two-Phase Flow Analysis Study

3.1. Numerical Model Description

3.1.1. Overview of the Numerical Model

For the process simulation study, 3D HM coupled multiphysics numerical model was built using COMSOL® to numerically solve the governing equations and constitutive relations described in Section 2.

Using the FEM, the model is used to simulate the simultaneous migration of gas and liquid (two-phase flow) in porous media, which are coupled to the mechanical behaviour of the solid matrix.

For process testing and enhanced flow analysis study, the numerical model setup is based on laboratory experiments conducted by the BGS to simulate 1D gas flow through a saturated bentonite sample under constant volume boundary stress conditions [59]. As per the experiment, a confined cylindrical sample of near-saturated bentonite was injected on one side with helium gas with increasing gas pressures over a period of 120 days. The other side was left at a constant water backpressure throughout the duration of the experiment. Key phases of the experiment, include the hydration phase (t = 7.3 days to 39 days) where the sample was left to saturate, the gas injection phase (t = 39 days to 71 days) where gas was continuously injected into the system resulting in increasing gas pressures, and gas shut-off (t = 71 days) where the injection pump was stopped and gas pressures are allowed to dissipate naturally. The experiment was conducted under isothermal conditions at a temperature of 293.15 K. During the experiment, a number of parameters were measured including the gas inflow and outflow, the porefluid pressure at defined porefluid arrays, and the total radial stresses at radial load cell arrays. The cylindrical specimen of MX-80 bentonite had a diameter of 60 mm and a length of 120 mm. The BGS provided the experimental data that was used in the process testing and enhanced flow analysis study [59].

3.1.2. Model Geometry and Mesh

The model geometry and finite element mesh are presented in **Figure 1**(**a**) and **Figure 1**(**b**), respectively. Although the experiment attempts to simulate 1-D conditions, the actual conditions are truly 3-D due to heterogeneity of the sample, and the presence of a central injection rod inserted at the outlet face. This central injection rod is not used in this experiment. Therefore, the FE mesh, as shown in **Figure 1**(**b**) is 3D, consisting of approximately 11,000 elements.

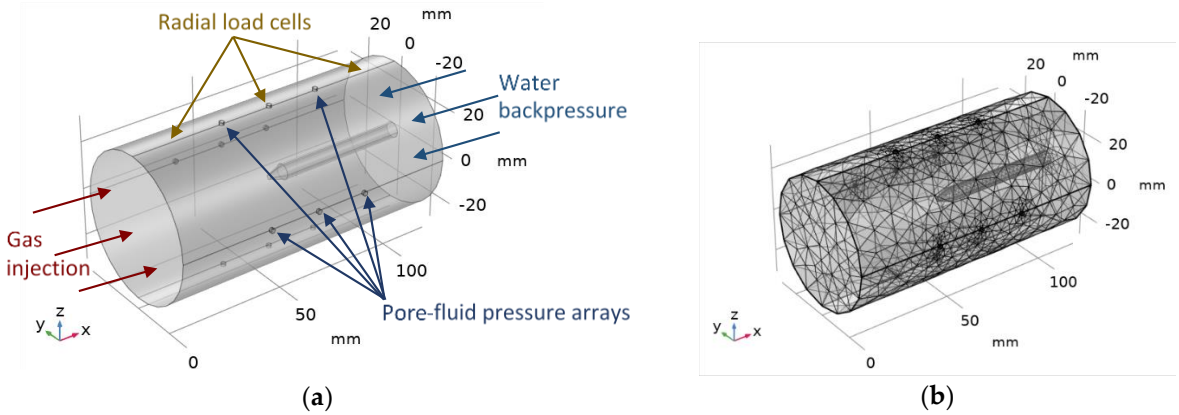

Figure 1. Process Simulation Study - Numerical Model (**a**) Geometry and (**b**) Meshing.

3.1.3. Material Properties

Material properties for the solid bentonite MX-80 soil matrix, helium gas and water are provided in **Table 1** and were adopted from Dagher et al. [4]. In the proposed numerical model, the expression for the density of gas, ρ_g, and bulk modulus, K_g, provided in Table 1, were derived from the ideal gas law, as described in Dagher et al. [4]. As the behavior of gases at high pressures deviate from that of an ideal gas, this presents an over-simplification. In light of this, future work will consider applying a correction factor to these expressions.

Table 1. Material properties of the solid soil matrix and gas and liquid phases.

Material	Parameter Name	Symbol [units]	Value
Solid Soil Matrix (MX-80 Bentonite)	Young's Modulus	E_b [MPa]	307
	Poisson's ratio	ν [-]	0.4
	Initial Porosity	n [-]	0.44
	Intrinsic permeability of water	k_w [m^2]	3.4×10^{-21}
	Dry density	ρ_d [kg m^{-3}]	1560
	Saturated degree of saturation	$S_{w_{sat}}$ [-]	1
	Residual degree of saturation	S_{w_r} [-]	0.05
	Bulk Modulus of bentonite	K_b [Pa]	5.0×10^8
	Volume-surface mean diameter	D_{vs} [m]	1.50×10^{-9}
	Pore radius	r [m]	1.50×10^{-8}
	Tortuosity [57, 4]	τ [-]	$n^{\frac{1}{3}} S_w^{\frac{7}{3}}$
Gas (Helium)	Density of helium	ρ_g[kg m^{-3}]	$p_g \frac{M}{RT}$ (1)
	Dynamic viscosity of helium @ 293.15 K	μ_g [Pa s]	2.0×10^{-5}
	Bulk Modulus of helium	K_g [Pa]	p_g (1)
	Henry's Coefficient for dissolution of helium in water	H	0.0091
	Diffusivity of helium in water	D_f [m^2 s^{-1}]	6.29×10^{-9}
	Diameter of helium gas particle	d_{he} [m]	1.0×10^{-10}
Liquid (Water)	Density of water	ρ_w [kg m^{-3}]	1×10^3
	Dynamic Viscosity @ 293.15 K	μ_w [Pa s]	0.001
	Bulk Modulus of water	K_w [Pa]	2.2×10^9

(1) As a simplification to the model, the density of gas and bulk modulus are derived from the ideal gas law, as described in Dagher et al. [11].

3.1.4. Initial Value Condition

The initial conditions at t = 0 across the domain are provided in **Table 2**. The initial conditions assume an initial pore gas pressure equal to atmospheric within the bentonite sample and a 96% degree of water saturation.

Table 2. 1D Flow Case - Initial Value Conditions.

Parameter Name	Parameter	Initial Value Condition
Initial poregas pressure	$p_{g_{initial}}$	1.01×10^5 Pa
Initial degree of saturation	$S_{w_{initial}}$	0.96
Initial suction (from SWCC)	$s_{initial}$	5.95×10^6 Pa
Initial porewater pressure	$p_{w_{initial}}$	-5.85×10^6 Pa
Initial displacement field	u_i	0 m
Initial stress	$\sigma_{0_{xx}} = \sigma_{0_{yy}} = \sigma_{0_{zz}}$	0.45×10^6 Pa
Initial gas concentration in porewater @STP	C_{g,H_2O}	0.073 mol m^{-3}
Initial AEV	AEV	1×10^7 Pa

*AEV: air-entry value; SWCC: soil water characteristic curves; STP: standard temperature and pressure.

3.1.5. Boundary Conditions

The hydraulic and mechanical boundary conditions (BC) for gas transport, water transport, and momentum transport are provided below.

3.1.5.1. Gas Conservation BCs

For gas transport, a no flow Neumann BC, $\frac{\partial p_g}{\partial x_i} = 0$, was set at the radial boundaries. Dirichlet BCs were set at a specified gas injection pressure, P_{inj}, for the front-face boundary, and atmospheric pressure, P_{atm}, at the back-face boundary.

For the concentration of gas in porewater, $C_{g,\,H_2O}$, the Ideal Gas Law was assumed,

$$p_g V = nRT \tag{11}$$

$$p_g V = \frac{m_g}{M} RT \tag{12}$$

Re-arranging,

$$\frac{m_g}{V} = \rho_g = p_g \frac{M}{RT} \tag{13}$$

where p_g is the poregas pressure (Pa)

Assuming instantaneous dissolution, the concentration of gas in the porewater can be calculated by multiplying equation (13) by Henry's coefficient, H, and the portion of water in a unit volume, nS_w

$$C_{g,\,H_2O} = \rho_g H(nS_w) \tag{14}$$

where $C_{g,\,H_2O}$ is the concentration of gas in water (kg gas m^{-3} water)

3.1.5.2. Water Conservation BCs

For water transport, Dirichlet BCs were set at a value equal to the water backpressure at the back-face boundary as well as at the radial porefluid arrays. This is a change from the BCs applied at the radial porefluid arrays in the previous study by the authors [4], which assumed no water flow through the radial porefluid arrays. This change in radial porefluid BC allows for increased hydration during the hydration period which ran from t = 7.3 days to 39 days, and is more representative of the experiment [4]. A no flow Neumann BC, $\frac{\partial p_w}{\partial x_i} = 0$, was set at the front face boundary and along the radial boundaries.

3.1.5.3. Momentum Conservation BCs

For the momentum conservation equation, a roller constraint was applied along the upper, lower, and radial boundaries to represent a condition whereby the boundary is free to move in the tangential direction, but is fixed in the normal direction, simulating an overall constant volume condition, as per the experimental set-up.

The gas injection pressure and water backpressure Dirichlet BCs were imported from the experimental data provided by BGS and have been calculated from the previously described theory plotted in **Figure 2**(**a**), while the concentration of dissolved gas BCs have been plotted in **Figure 2**(**b**).

(a)

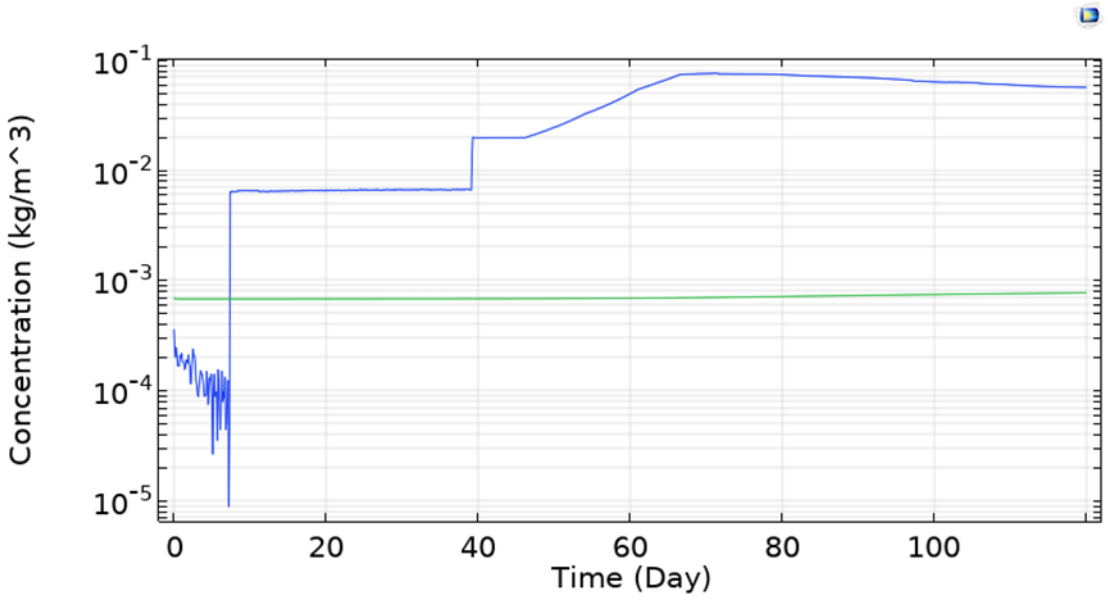

(b)

Figure 2. Dirichlet Boundary Conditions for the (**a**) lower gas injection pressure and upper water backpressure (**b**) lower and upper gas concentrations in porewater.

3.2. Modelling Approach

In this study the simulation of a number of study scenarios were performed with increasing model complexity, in order to gain an understanding of the contribution of heterogeneity, the Klinkenberg "slip flow" effect, and the inclusion of a linear swelling strain on two-phase flow. The results of each simulation were compared to the experimental results and the effect of each on flow behaviour analyzed [59]. **Table 3**summarizes the simulations which were run and values of key model parameters. It should be noted that these model parameters were selected based on calibrating the model to best match the experimental results while maintaining numerical stability and convergence.

Table 3. Process Simulation and Enhanced Two-Phase Flow Analysis Study Scenarios.

Scenario Number	Purpose	Description[1]	Initial Porosity Distribution (mean ± sd)	Coefficient of Klinkenberg Effect, $\mathbf{c_{ke}}$ (-)	Initial Average Intrinsic Permeability of Water, $\mathbf{k_w}$ (m^2)
S0	Single-Phase Flow Case	Single Phase	0.44	0	3.4×10^{-21}
S1	Base Case Scenario	Base Case	0.44	0	3.4×10^{-21}
S2	Test if heterogeneity alone could influence preferential flow pathways or the formation of gas fingers	Introduce H	0.44 ± 0.06	0	3.4×10^{-21}
S3	Test if Klinkenberg effect could influence preferential flow pathways and contribute to gas fingering	Introduce K	0.44	1×10^{8}	3.4×10^{-21}

S4	Test effect of both heterogeneity and Klinkenberg effect to development of preferential flow pathways	H, K	0.44 ± 0.06	1×10^{8}	3.4×10^{-21}
S5	Test if Klinkenberg effect contributes to reducing number and size of gas fingers	H and ↑ k_w	0.44 ± 0.06	0	5.0×10^{-19}
S6	Test effect of linear swelling on total stress evolution	H, K, S	0.44 ± 0.06	1×10^{8}	3.4×10^{-21}

[1]H – Heterogeneity, K – Klinkenberg effect, S – Swelling

Additionally, a special study, S0, utilizes the simplified single-phase flow model that was used in the verification of the numerical model [65]. This scenario was included to assess the difference in increasing model complexity from a single-phase model, to a two-phase flow model. This model is identical to that of the base case, S1, but was simplified to be consistent with the verification study through the following assumptions:

- immobile liquid phase
- no dissolution of gas into and no diffusion gas through the porewater
- constant gas permeability
- constant gas density
- constant degree of saturation of water
- role of suction ignored
- role of gravity ignored
- isothermal process
- constant volume boundary condition

For this process simulation study, the simplified single-phase flow model applies the same material properties used in the verification study [65], but now applies boundary conditions and initial conditions that were described above. As per the assumptions, the material properties for the parameters used for scenario S0 remain constant through the model run, and are presented in **Table 4**. The van Genuchten equations for the SWCC and AEV are provided in the authors' original paper [65].

Table 4. Process S0 - Parameters.

Parameter Name	Symbol	Value	Units
Length	L	0.12	m
Density of bentonite	ρ_b	1526	kg m^{-3}
Young's Modulus	E	3.07×10^{8}	Pa
Poisson's ratio (nu)	ν	0.4	-
Porosity	n	0.44	-
Intrinsic permeability	k_w	3.40×10^{-21}	m^2
Dynamic viscosity	μ_g	2.00×10^{-5}	Pa s
Degree of saturation	S_w	0.9	-
Air-Entry-Value	AEV	1×10^{7}	Pa
Constant porewater pressure[1]	p_w	1.0×10^{6}	Pa
Relative gas permeability[1]	k_{rg}	0.03	-
Chi factor[1]	χ	0.9	-

[1]Calculated based on a degree of saturation of 0.9 and gas pressure of 1.3×10^{7} Pa corresponding peak experimental injection pressure by Daniels and Harrington [59].

3.3. Implementation of Enhanced Mechanisms for Two-Phase Flow

3.3.1. Introduction of Heterogeneity

Heterogeneity was introduced into the simulated sample by spatially applying a random normal distribution to the initial porosity material property with a mean porosity set at the experimentally determined value of 0.44 and applying a standard deviation of 0.06. There is no spatial correlation in heterogeneity intended with this approach. The application of this method to generate heterogeneity is not based on any experimental literature, and is applied in this study in an attempt to trigger the generation of preferential flow pathways by the given models. A standard deviation of 0.06 was selected, as it provided the largest degree of heterogeneity while maintaining model stability. The initial porosity distribution within the bentonite sample is depicted in **Figure 3**, while **Figure 4** provides the XZ-plane cross section of the initial porosity distribution.

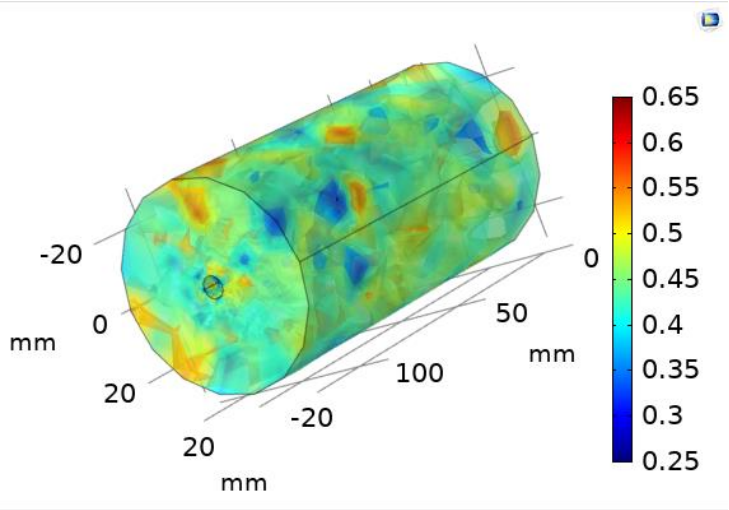

Figure 3. Heterogeneity introduced through random normal distribution of initial porosity.

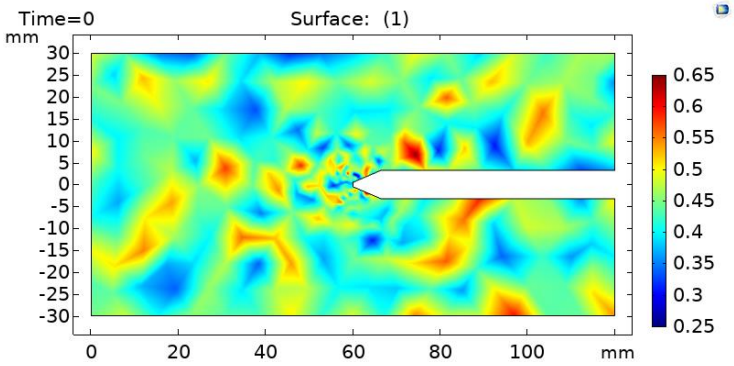

Figure 4. Cross-section of initial porosity distribution.

3.3.2. Klinkenberg "Slip Flow" Effect – Intrinsic Permeability of Gas

A number of studies have attempted to empirically estimate the Klinkenberg slip factor [71] [72], and have proposed the following empirical equation for the slip factor as a function of the intrinsic permeability of water,

$$b_{ke} = 0.251 k_w^{-0.36} \quad (12)$$

Based on the experimental intrinsic permeability of water in this study, k_w (3.4×10^{-21} m^2), Figure 5 shows the relationship between poregas pressure and intrinsic permeability using a Klinkenberg slip factor

based on Equations (7) and (8) with a constant of, $c = 1.0 \times 10^8$ and $c = 1.0 \times 10^4$, as well as using Equation (15) to empirically solve for the slip factor. As depicted by the figure, the intrinsic permeability of the gas increases significantly with a decrease in poregas pressure, and as poregas pressures increase, the intrinsic permeability of the gas approaches that of water. As there is little information in literature regarding the slip factor for helium in bentonite clays, in order to assess whether the Klinkenberg effect could provide a significant role in matching key features of the experimental results, a constant, $c = 1.0 \times 10^8$, was used for the Klinkenberg effect. A value of $c = 1.0 \times 10^4$, which matches that of the empirical equation, would not provide the significant change in permeability needed to obtain complete breakthrough into the sample.

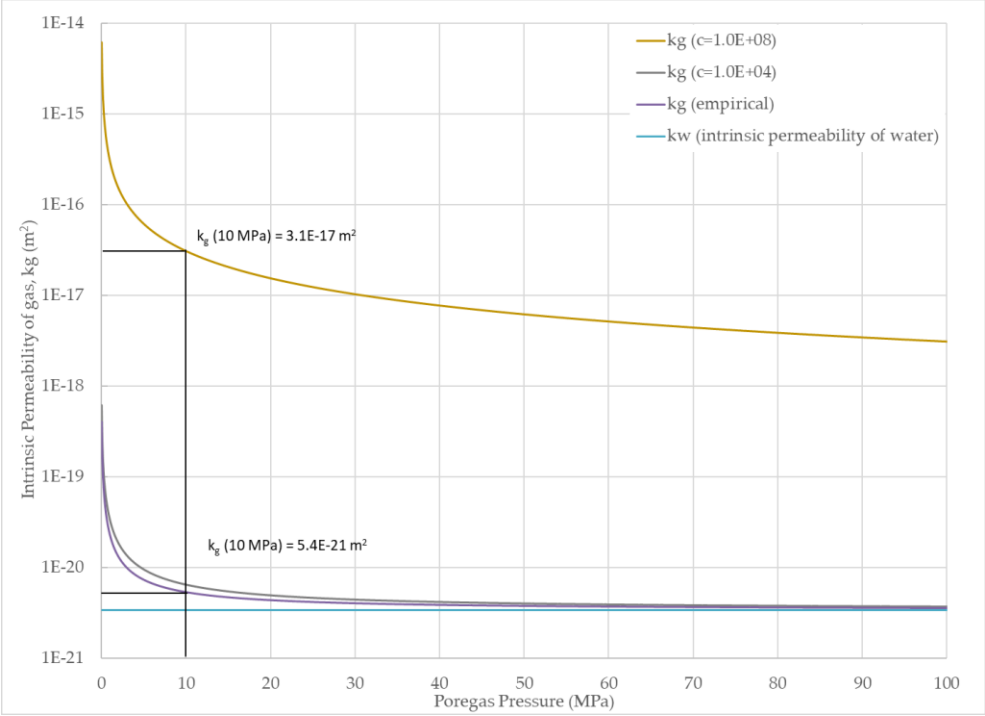

Figure 5. Klinkenberg Effect - Intrinsic permeability of gas as a function poregas pressure, k_g

3.3.3. Coefficient of Swelling Strain

This study applied a swelling coefficient β_{sw} [1/Pa] of 1×10^{-9}. This coefficient was initially informed by that obtained by Nasir et al. [70] and calibrated to best match the experimental data while maintaining numerical stability and convergence.

3.4. Results and Discussion

In this section, the compression-positive sign convention is used for stress components and pressures.

The results of the 1D flow process simulation and enhanced two-phase flow analysis study are presented below. For each study scenario the following results are discussed:

1. poregas pressure evolution through the specimen
2. gas inflow/outflow
3. gas storage in the system
4. total stress evolution

The experimental results provided for comparison were discussed in Daniels & Harrington [59] and in Dagher et al. [4] and are not discussed in detail in this paper. This paper focuses on the contribution of each enhanced flow mechanism to flow behavior.

3.4.1. Poregas Pressure Evolution through the Specimen

Poregas pressure profiles over time for the central cross section (XZ-plane) are depicted in **Figure 6** for S0, and **Figure 7**(**a**) to **Figure 7**(**g**) for S1 to S6. For the single-phase flow case depicted by **Figure 6,** the poregas pressure migration results follow a uniform gradient. This differs from the transient pore-pressure results provided in the companion paper [65], which demonstrate a non-linear kinked shape following a sudden increase in injection pressure, until steady-state is reached. However, in the companion paper, at these same poregas pressures (10 MPa), steady-state is reached in approximately 1.5 hours. In this study, our timescale is in days. Therefore it is expected that transient response is very fast, and equilibrium is reached quickly.

For the base case scenario S1 representing the linear elastic advective-diffusive visco-capillary two-phase flow model represented in **Figure 7**(**a**), the results match those first published in Dagher et al. [4], whereby once the AEV is exceeded (at 69 days), there is gas breakthrough into the sample followed by a slow moving uniform gas flow through the specimen. The advective poregas front only travels roughly 5% through the sample.

Results of S2 are provided by **Figure 7**(**b**), and show that once heterogeneity is introduced, the poregas front travels slightly further than the base case, and is no longer uniform, with the formation of small gas fingers.

Figure 7(**c**) shows the results of S3, once the Klinkenberg "slip flow" effect has been introduced. With a fairly large coefficient of the Klinkenberg effect of 1×10^{8}, significantly increased gas migration into the sample and complete gas breakthrough are experienced. Up to 68 days, a relatively uniform gas front advances into the sample, however as the front approaches the central rod, its shape becomes concave. As poregas moves forward, there is increased resistance to gas migration as a result of increased porewater pressure buildup around the central rod. This results in a lag in the poregas migration front which is more pronounced closer to the center of the specimen. Once past the central rod, the poregas front returns to uniformity. It should be noted, that with the introduction of slip flow, there is some migration of poregas at low gas injection pressures, however the predominant breakthrough of gas into the sample occurs once the AEV has been reached. One notable observation in the evolution of poregas migration, is that the Klinkenberg effect tends to saturate the gas in the bentonite specimen, and does not aid in the formation of distinct preferential flow pathways.

The results of S4, which introduce both the Klinkenberg effect and heterogeneity are presented in **Figure 7**(**d**). Characteristics of the results for both S2 and S3 can be seen, whereby the introduction of heterogeneity provides the formation of small fingers, with the poregas now travelling quickly through the specimen. In fact, with the inclusion of heterogeneity, the poregas front migrated further relative to S3. One particular item to note, is that even with increased flow through the system relative to S2, the size of the fingers remains small and subtle, not large and distinct as the authors originally anticipated. Any fingers, which do form, eventually shrink and disappear. This may be due to a number of factors which could be physical, such as the presence of suction and diffusion, which aid in impeding the fingering capacity, or numerical and related to the method applied to introducing heterogeneity within the sample and to the mesh size.

In order to test whether Klinkenberg slip flow plays a role in mitigating the formation of gas fingers, the model is run using a much higher initial permeability of 5×10^{-19} m^2 compared to that provided experimentally of 3.4×10^{-21} m^2. These results are provided for S5 in **Figure 7**(**e**). The results did not show an increase in the number or extent of gas fingers in comparison to S4, thereby demonstrating that the Klinkenberg effect may not play a large role in stabilizing the formation of gas fingers.

Finally, the effect of introducing a linear swelling strain is provided by S6 as depicted in **Figure 7**(**f**). In comparison to S4, the presence of swelling does not result in a noticeable difference in the time it takes for the poregas migration front to travel through the sample. However, once gas shut-off occurs (at day 71)

the presence of swelling in S6 appears to stabilize or reduce the effect of fingering in comparison to S4. Additionally, at day 75, an odd point of low gas pressure is exhibited. This is not a numerical figment, but a result of fingering that occurred around a spot of low permeability, and corresponds to that same point of low permeability present in **Figure 4**.

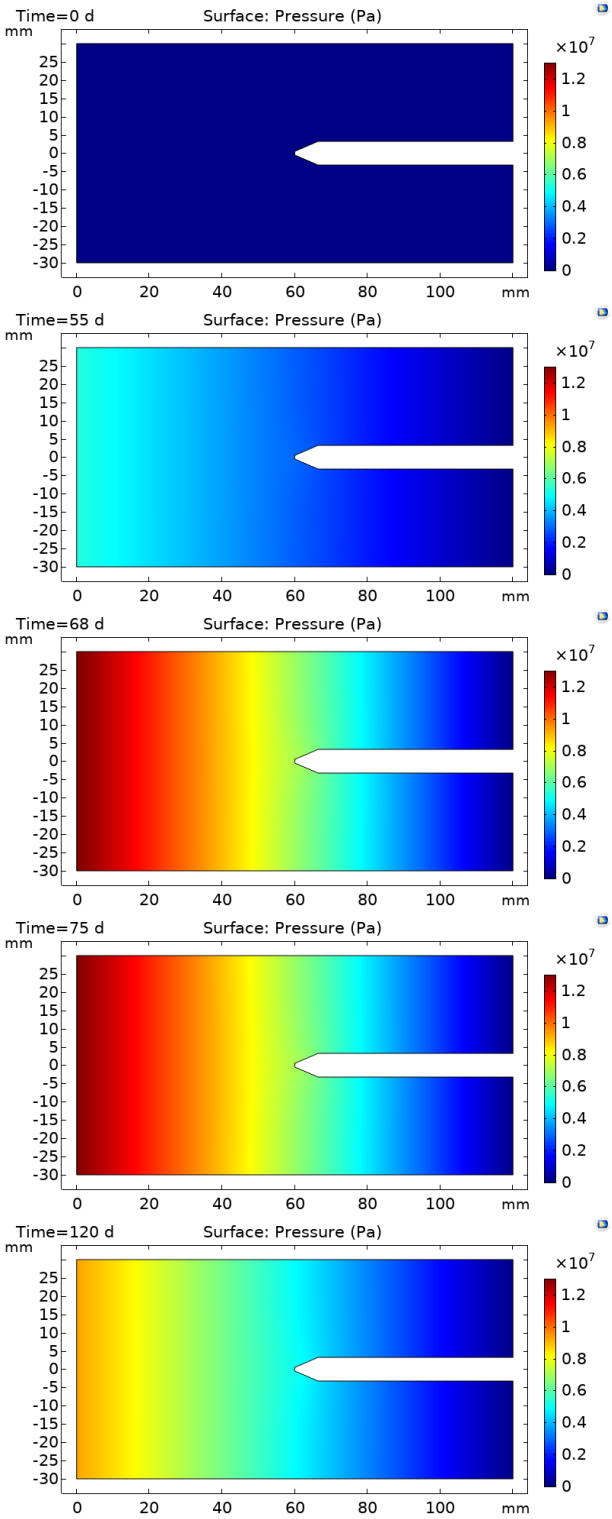

Figure 6. 1D Flow Case Results: Pore-gas pressure at t=0, 55, 68, 75, and 120 days for S0.

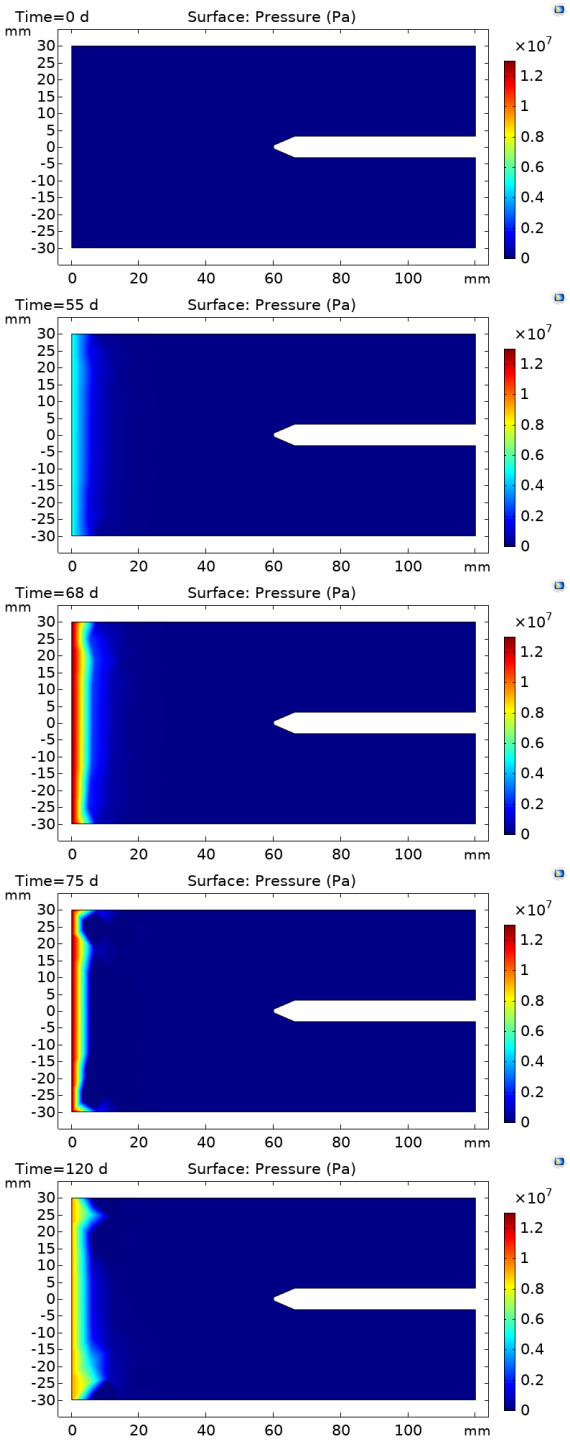
Time=0 d
Surface: Pressure (Pa)
Time=55 d
Surface: Pressure (Pa)
Time=68 d
Surface: Pressure (Pa)
Time=75 d
Surface: Pressure (Pa)
Time=120 d
Surface: Pressure (Pa)
mm
×10^7
1.2
1
0.8
0.6
0.4
0.2
0
0 20 40 60 80 100 mm

S1(**a**)

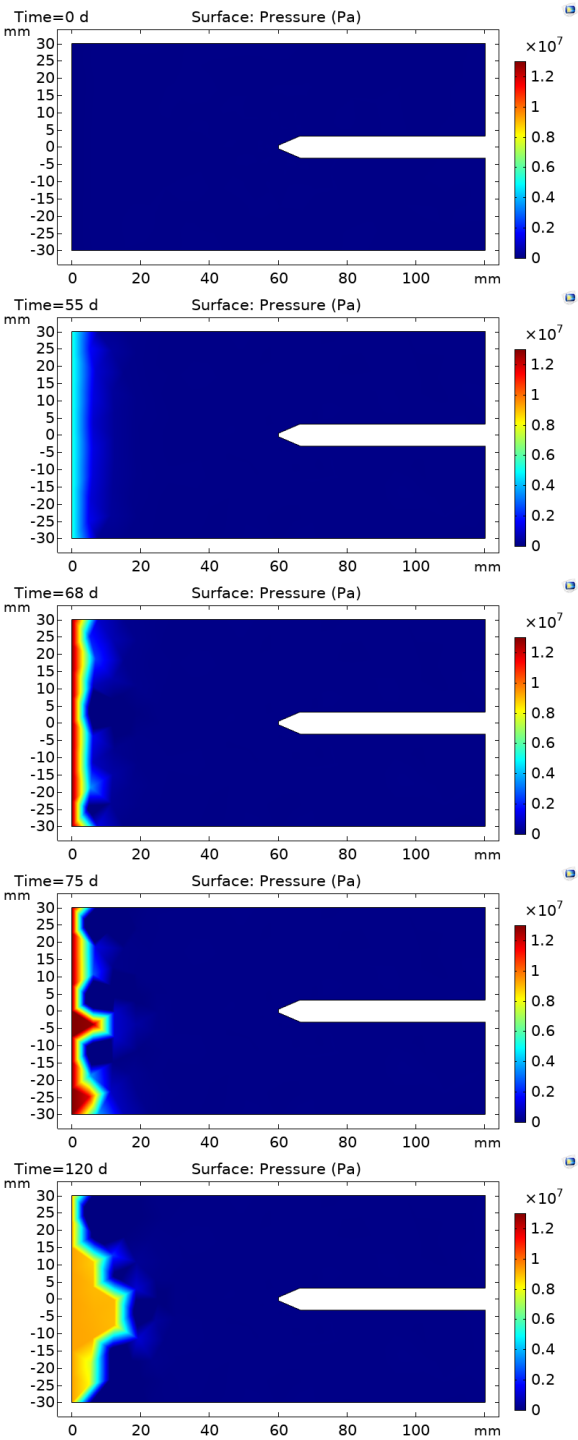
Time=0 d
Surface: Pressure (Pa)
Time=55 d
Surface: Pressure (Pa)
Time=68 d
Surface: Pressure (Pa)
Time=75 d
Surface: Pressure (Pa)
Time=120 d
Surface: Pressure (Pa)
mm
×10^7
1.2
1
0.8
0.6
0.4
0.2
0
0 20 40 60 80 100 mm

S2(**b**)

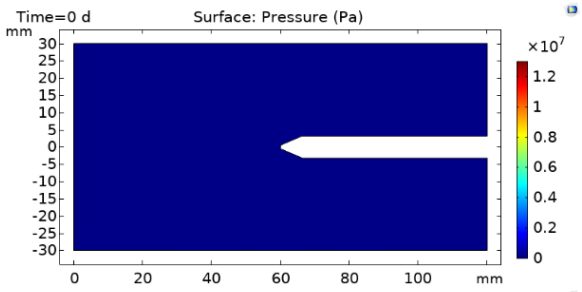
Time=0 d
Surface: Pressure (Pa)
mm
×10^7
1.2
1
0.8
0.6
0.4
0.2
0
30
25
20
15
10
5
0
-5
-10
-15
-20
-25
-30
0
20
40
60
80
100
mm

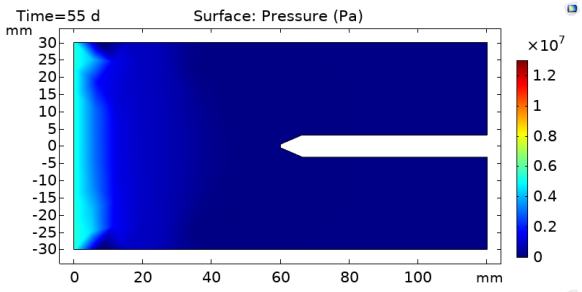
Time=55 d
Surface: Pressure (Pa)
mm
×10^7
1.2
1
0.8
0.6
0.4
0.2
0
30
25
20
15
10
5
0
-5
-10
-15
-20
-25
-30
0
20
40
60
80
100
mm

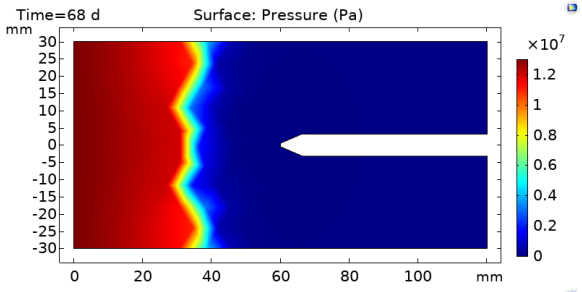
Time=68 d
Surface: Pressure (Pa)
mm
×10^7
1.2
1
0.8
0.6
0.4
0.2
0
30
25
20
15
10
5
0
-5
-10
-15
-20
-25
-30
0
20
40
60
80
100
mm

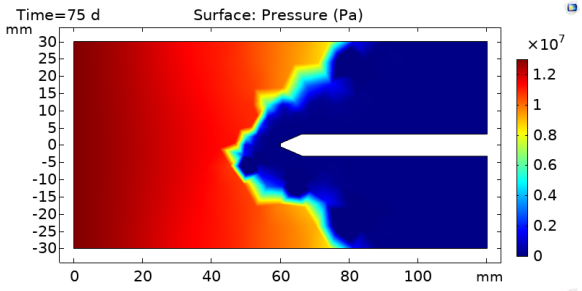
Time=75 d
Surface: Pressure (Pa)
mm
×10^7
1.2
1
0.8
0.6
0.4
0.2
0
30
25
20
15
10
5
0
-5
-10
-15
-20
-25
-30
0
20
40
60
80
100
mm

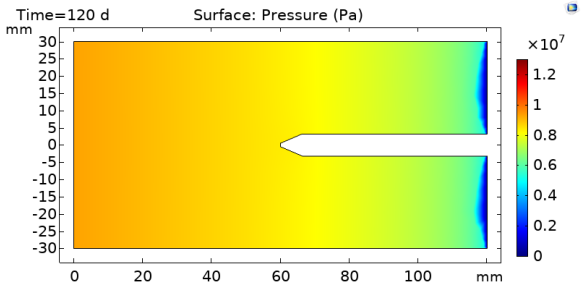
Time=120 d
Surface: Pressure (Pa)
mm
×10^7
1.2
1
0.8
0.6
0.4
0.2
0
30
25
20
15
10
5
0
-5
-10
-15
-20
-25
-30
0
20
40
60
80
100
mm

S3(**c**)

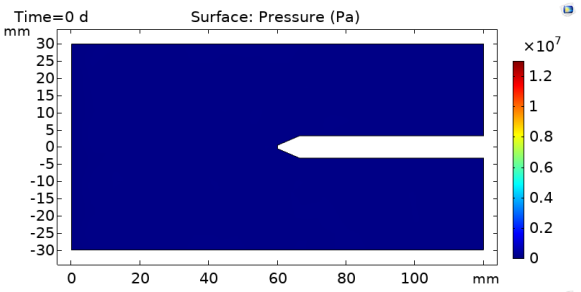
Time=0 d
Surface: Pressure (Pa)
mm
×10^7
1.2
1
0.8
0.6
0.4
0.2
0
30
25
20
15
10
5
0
-5
-10
-15
-20
-25
-30
0
20
40
60
80
100
mm

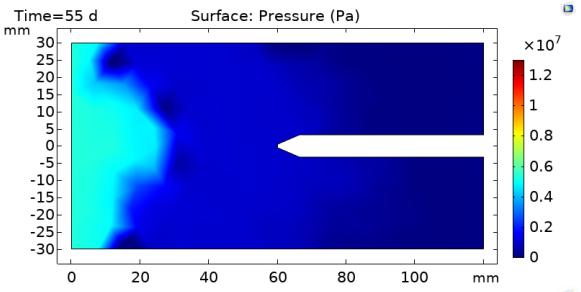
Time=55 d
Surface: Pressure (Pa)
mm
×10^7
1.2
1
0.8
0.6
0.4
0.2
0
30
25
20
15
10
5
0
-5
-10
-15
-20
-25
-30
0
20
40
60
80
100
mm

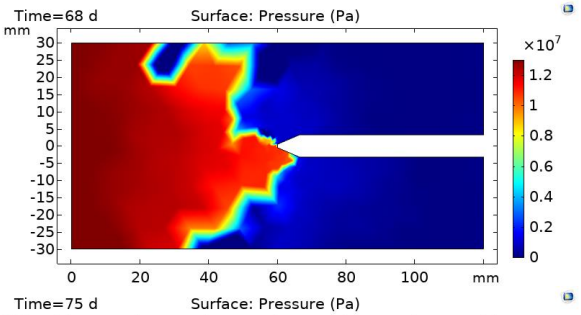
Time=68 d
Surface: Pressure (Pa)
mm
×10^7
1.2
1
0.8
0.6
0.4
0.2
0
30
25
20
15
10
5
0
-5
-10
-15
-20
-25
-30
0
20
40
60
80
100
mm

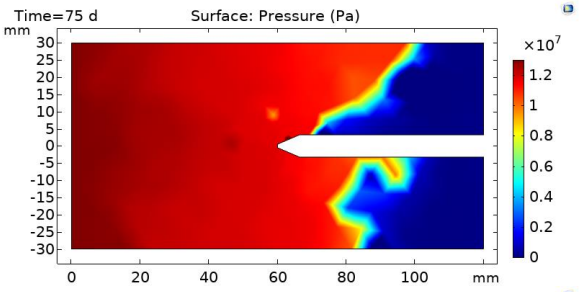
Time=75 d
Surface: Pressure (Pa)
mm
×10^7
1.2
1
0.8
0.6
0.4
0.2
0
30
25
20
15
10
5
0
-5
-10
-15
-20
-25
-30
0
20
40
60
80
100
mm

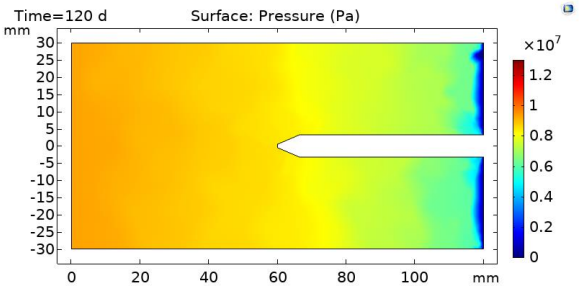
Time=120 d
Surface: Pressure (Pa)
mm
×10^7
1.2
1
0.8
0.6
0.4
0.2
0
30
25
20
15
10
5
0
-5
-10
-15
-20
-25
-30
0
20
40
60
80
100
mm

S4(**d**)

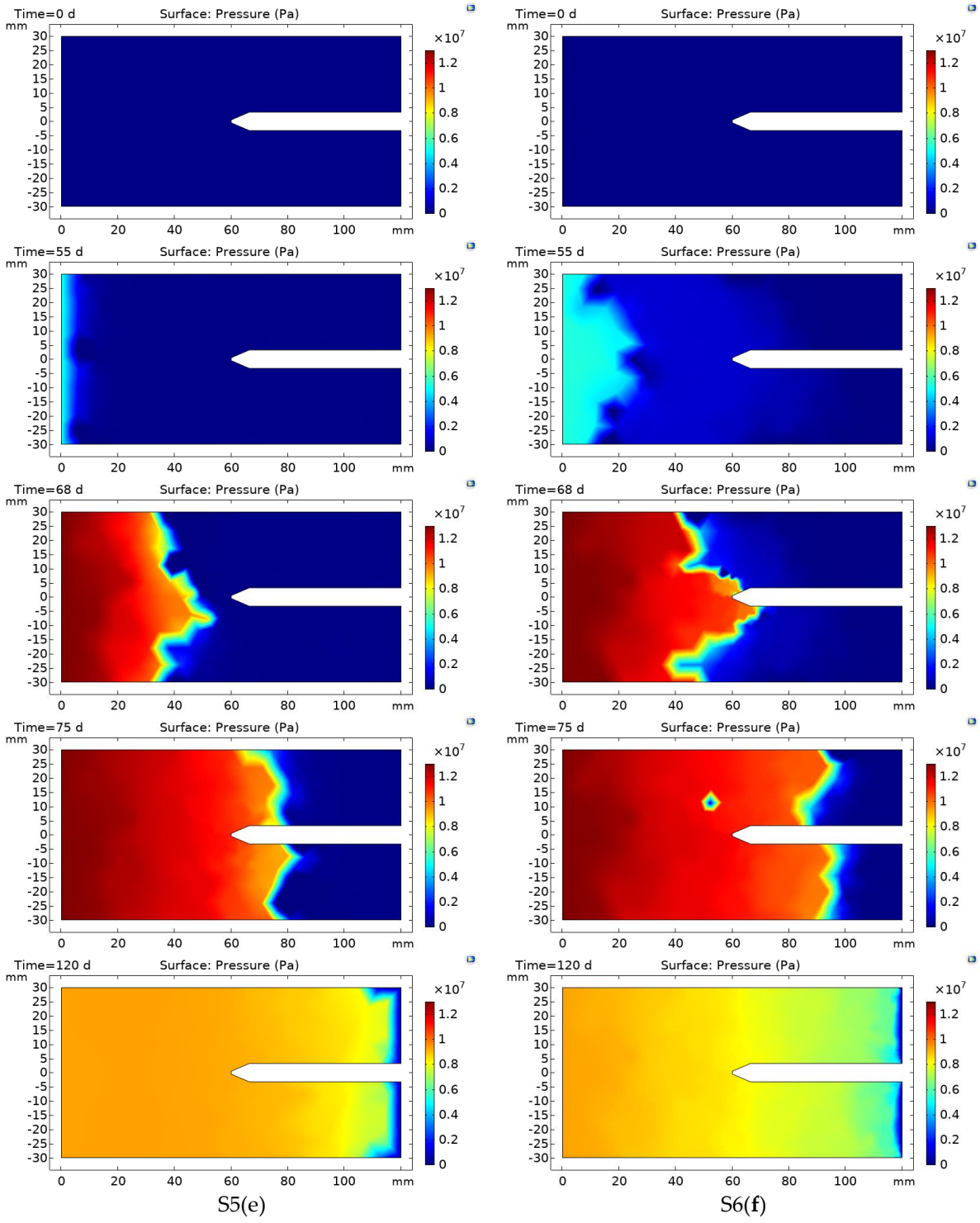

Figure 7. 1D Flow Case Results: Pore-gas pressure at t=0, 55, 68, 75, and 120 days for (**a**) S1; (**b**) S2; (**c**) S3; (**d**) S4; (**e**)S5; and (**f**) S6.

3.4.2. Gas Inflow and Outflow

Total gas inflow and outflow profiles over time for the experimental data as well as for each study scenario are depicted in **Figures 8–10**. The experimental gas inflow shows a steep rise in gas into the sample

when the injection pressure exceeds the AEV of 1×10^7 Pa (at 63 days). This is followed by chaotic inflow behavior and then a sudden drop in inflow, which corresponds to shut-off of the experimental injection pump (at 71 days). A similar behavior is exhibited for the experimental gas outflow, whereby gas flow out of the sample occurs almost immediately following gas flow into the sample, followed by a period of chaotic flow behavior and the occurrence of several sudden bursts of outflow near the end of the experimental run. The authors interpreted this as the almost immediate formation of microfractures and the propagation of preferential flow pathways.

Figure 8 depicts the modelled inflow and outflow curves for the single-phase flow scenario, S0. **Figure 8**(**a**) shows that the modelled gas inflow is not able to match the shape, timing, or magnitude of the experimental inflow curve. However, the inflow curve responds almost immediately to the injection pressure boundary condition with no rebound curve at each large change in injection pressure. This similar behavior is observed at the outflow in **Figure 8**(**b**), with a magnitude several of orders lower compared to the inflow, corresponding to the poregas pressure at outflow. These results are expected and are due to the very low constant gas permeability applied to the model (of the order of 10^{-22} m^2).

Figure 9(**a**) depicts the modelled inflow curves for scenarios S1, S2 and S3. The curve representing the base case was capable of capturing the general shape and timing of gas breakthrough into the bentonite specimen, but was unable to capture the peak magnitude of the inflow, nor the sporadic inflow behavior during the period where gas was flowing into the sample. For S2, introducing heterogeneity results in slightly early breakthrough and slightly higher inflow compared to the base case. This is likely a result of the presence of areas within the injection face with larger pore sizes and consequently localized areas with lower AEVs, resulting in earlier breakthrough into the sample. For S3, when the Klinkenberg effect is introduced there is a chaotic inflow behavior observed which is similar to that of the experimental data. However, the model is unable to match the inflow magnitude, and shows that inflow continues to occur even after the injection pump was stopped (i.e., day 71). The reason for this can be attributed to the Klinkenberg "slip flow" factors being applied. At approximately 63 days, once the AEV has been reached and airflow into the sample begins, the gas permeability corresponding to a poregas pressure of 10 MPa is approximately 3.1×10^{-17} m^2 (see **Figure 5**). Once gas injection has been shut-off at day 71, the residual poregas pressure still remains above the AEV, and increases exponentially as the poregas injection pressures decrease. **Figure 9**(**b**) depicts gas outflow curves. No outflow was observed for the base case or when applying heterogeneity to the sample. However, when the Klinkenberg effect was applied, a rapid increase in gas outflow was observed at approximately 88 days, and continued with a steady declining outflow. This is due to the lag time it takes for the poregas migration front to completely flow through the sample (i.e., complete breakthrough). This modelled outflow behavior was not observed experimentally, and is more representative of a plug flow behavior as opposed to dilation-controlled outflow as indicated by the experimental data.

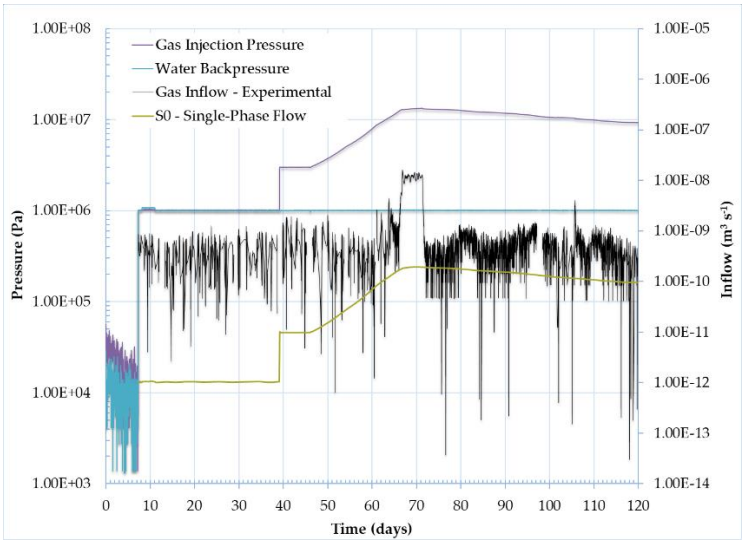

(**a**)

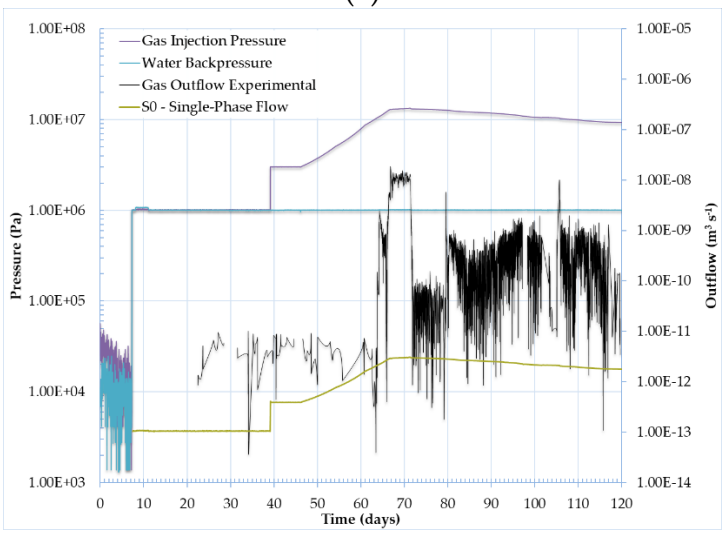

(**b**)

Figure 8. Results of (**a**) gas inflow and (**b**) gas outflow for S0.

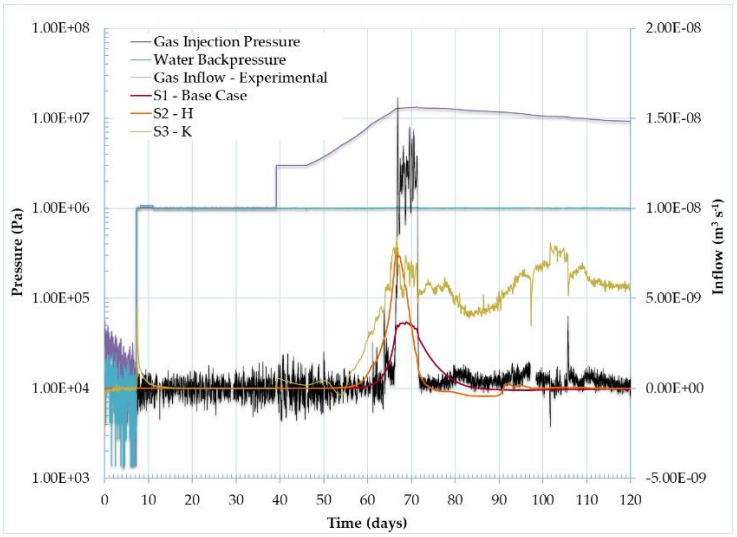

(**a**)

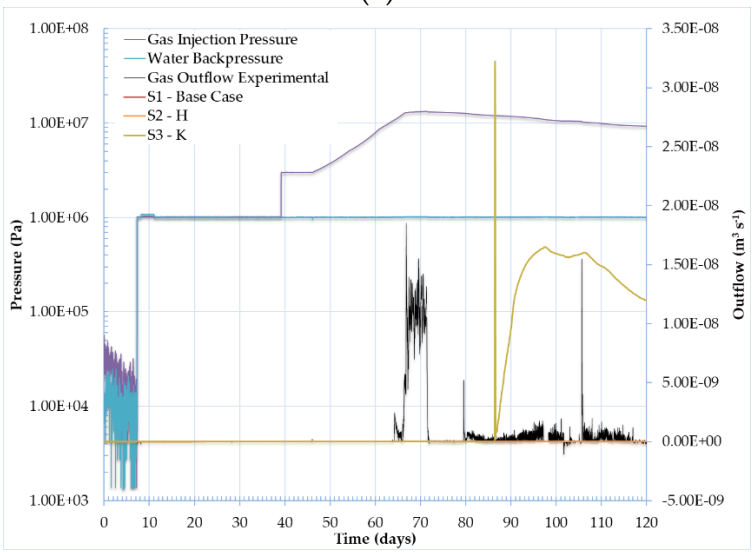

(**b**)

Figure 9. Results of (**a**) gas inflow and (**b**) gas outflow for S1, S2 and S3.

Figure 10(**a**) depicts the modelled inflow curves for scenarios S4, S5 and S6. For S4, where both heterogeneity and the Klinkenberg effect were applied, the results show significantly higher gas inflow and a similar chaotic behaviour when compared to the results of S3. A noticeable difference between the modelled results and the experimental results, is that following gas shut-off, there is an even larger increase in gas inflow between 78 and 95 days. As with S3, this is likely attributed to increasing gas permeability as the residual injection gas pressures decrease while remaining above the AEV. The effect is even more pronounced as slip flow is now occurring along more localized pathways due to the presence of heterogeneity. When assessing the S4 outflow curve depicted in **Figure 10**(**b**), outflow now occurs at around 69 days and matches the same shape and timing of the modelled inflow curve, without the chaotic behavior. This may be due to flow stabilization occurring during migration through the sample as a result of suction and diffusion. Another unusual observation, is that the magnitude of outflow under the presence of heterogeneity is roughly 2.5 times higher than that of the inflow curve. This could only be attributed to

a rapid increase in gas permeability throughout the sample which occurs as a result of a decrease in poregas pressures during shut-off, leading to rapid outflow and desaturation of the sample.

For S5, when the Klinkenberg effect is restricted in the model, and a much higher average initial intrinsic permeability of water is applied, the inflow profile more closely resembles that of the experimental data, with some chaotic behavior, although not as sporadic as when Klinkenberg slip flow is present. However, following gas shut-off, the results of S5 do not result in a sharp decrease as observed experimentally, indicating that other mechanisms controlling the gas entry into the sample are occurring, such as damage or plasticity. For S5, complete gas breakthrough occurs at 90 days, but the outflow behavior is not representative of the experimental data.

For scenario S6 when a linear swelling strain is present, the inflow curves match the general shape and timing of that of S4 (without swelling), but reach a slightly higher peak inflow at 68 days when breakthrough into the sample first occurs. In comparison to S4, the peak inflow following gas shut-off achieved numerically at 104 days, is reduced in the instance of linear swelling. This is expected by the model as a decrease in suction at the injection interface due to the decrease in poregas injection pressure, would result in a decrease in the volumetric strain and corresponding porosity and gas permeability. This results in less flow into the sample. This effect is also observed in the outflow.

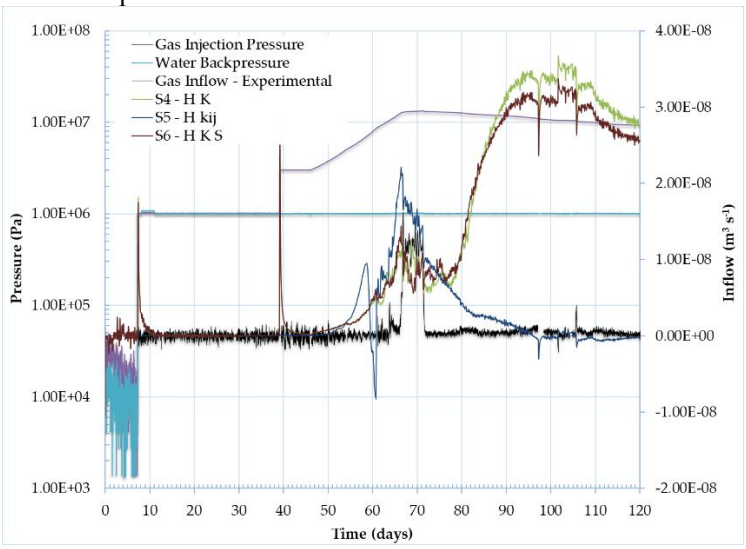

(**a**)

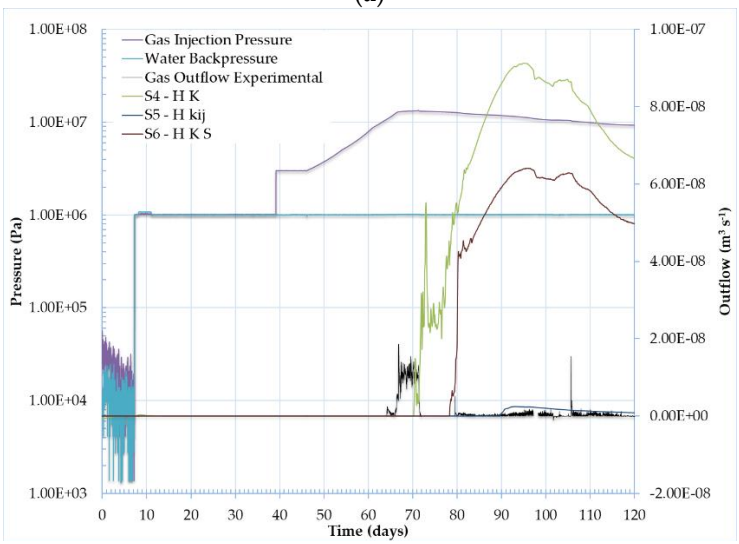

(**b**)

Figure 10. Results of (**a**) gas inflow and (**b**) gas outflow for S4, S5 and S6.

None of the modelled simulations were able to reproduce the experimental inflow and outflow well. This suggests that the role of AEV, and the presence of heterogeneity, slip flow, and reduction in porosity with increasing suction as result of a swelling strain, cannot fully describe breakthrough through the system. Although the presence of heterogeneity and slip flow contributed to some preferential flow and chaotic inflow behavior, in order to obtain a sharp and rapid increase in flow as observed experimentally, some other HM-coupled mechanism is needed to promote the rapid increase and decrease of flow into the system.

3.4.3. Gas Storage in the System

An important part of this process simulation study is a comparison of the modelled results to the experimental volume of gas stored in the system over time (i.e., inflow minus outflow). It is expected that dilation-controlled gas flow and the formation of preferential flow pathways would result in minimal gas storage within the system. This was observed by the experimental inflow and outflow results whereby the majority of gas entering the system almost immediately exited the system, with several delayed bursts of outflow (at ~80 days and ~116 days) attributed to pathway sealing and the creation of new pathways. This was a key feature of the experimental inflow and outflow results originally noted by the experimenters [59]. This feature of the experimental results can be observed by a comparison of the experimental inflow and outflow (black lines) presented in **Figure 9**(**a**) and **Figure 9**(**b**), respectively.

Figure 11displays the experimental volume of gas storage in the system and volume of gas stored for each model scenario. The experimental results show little gas storage within the soil specimen with approximately 0.002 m^3 of gas stored in the system at 120 days. The results of S0 show a large increase in volume of gas stored. Although flow into the sample was low, due to the high-pressure gradient, and constant permeability, continuous gas migration occurred through the sample resulting in large volume of gas stored in comparison to the experimental data.

As for the two-phase flow models, the results of S1 and S2 match the experimental values quite well, however this is likely only a coincidence as in both these cases (S1 and S2) gas flowed into the sample with no advective gas outflow occurring.

For S3, the Klinkenberg effect results in a small volume of gas entering the system at lower gas pressures. Once the AEV is reached, the amount of gas stored in the system increases significantly. Once gas shut-off occurs, there is a desaturation of the gas as it flows out of the system. This behavior is in-line with what was visually depicted in **Figure 7**(**c**) to (**h**)**.** When both heterogeneity and slip flow are present, there is an even earlier increase in gas stored within the system, followed by a longer period of gas desaturation. Introduction of a swelling strain in S6 and S7 did not significantly affect the volume of gas stored. The inclusion of the Klinkenberg effect provides a large deviation from the behavior observed experimentally, supporting the notion that inclusion of the Klinkenberg effect results in more plug flow like behavior, as opposed to the formation of more discrete preferential flow pathways. These results reinforce the conclusion that additional mechanisms of mechanical deformation are required to initiate dilation-controlled gas flow and the formation of discrete preferential flow pathways.

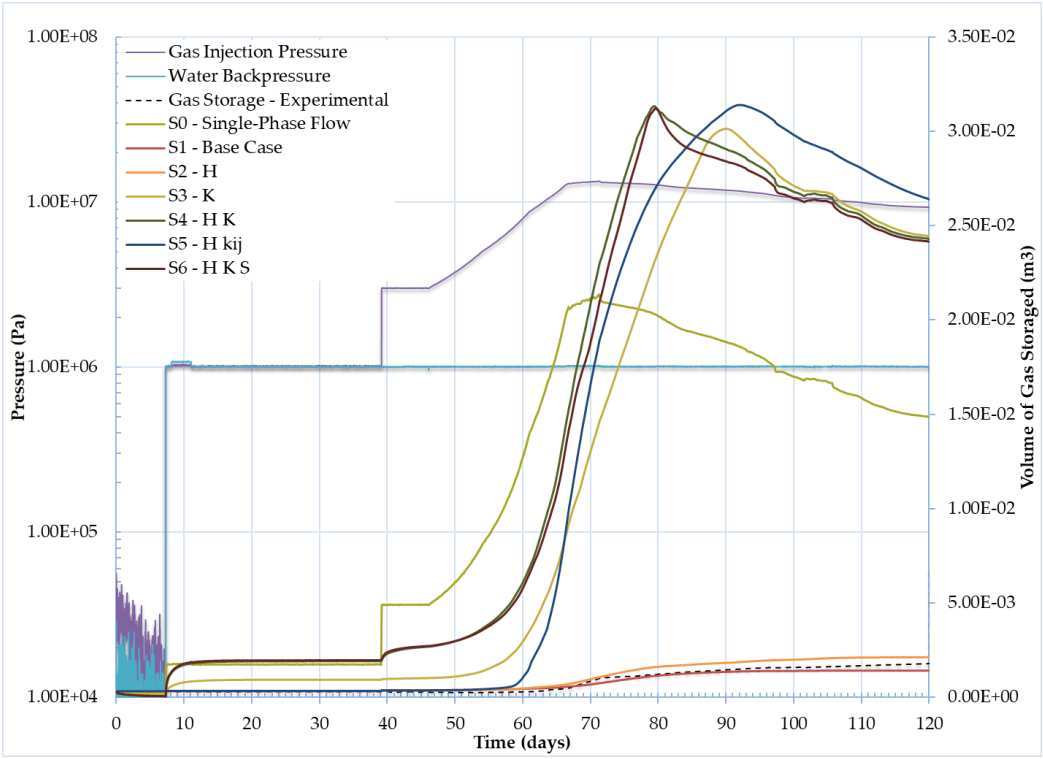

Figure 11. Volume of Gas Stored for S1-S6.

3.4.4. Evolution of Total Stresses

The total stress evolution as measured by the injection load cell, radial load cells, and backpressure load cell, are presented in **Figure 12**. The experimental results depict an initial large increase in total stress during the hydration phase (t = 7.3 days to 39 days) followed by stabilization of the stresses. Once the injection pressure exceeds the AEV (t = 63 days), there is another rapid increase in total stresses until gas injection ceases. In their previous work, the authors were not able to replicate the magnitude of the total stress evolution within the hydration phase, and attributed this, in part, to neglecting the effect of swelling pressure in the mathematical model, a key behavior of expansive clays. Three key attributes are assessed within this study to attempt to replicate the total stress evolution observed experimentally: (i) modified BCs to allow for additional hydration of the sample from the radial porefluid arrays, (ii) Klinkenberg effect leading to increased gas flow through the system, and (iii) the application of a swelling strain to simulate swelling of the clay.

Figure 12(**a**) provides the total stress evolution for the single-phase flow case, S0. The results show a minor stress response with increasing injection gas pressures when compared to the experimental data. This is to be expected, as the single-phase flow model only considers changes in pore-fluid pressure associated with an increase in pore-gas pressure at a constant $\chi = 0.9$ and ignores the porefluid pressure associated with the immobile water phase.

Figure 12(**b**) provides the total stress evolution for the base case, S1. The results show much better agreement of the total stress evolution during the hydration phase in comparison to the authors previous work [4], being able to capture the shape, timing, and magnitude of the stress evolution. This is evidently a direct result of the change in BCs that was applied in this study. However, S1 is not capable of simulating the total stress response observed following breakthrough into the sample.

Figure 12(**c**) provides the total stress evolution for S2. The results are similar to that of S1, but with a larger spread between the total stress curves due to the introduced heterogeneity. During the hydration

phase the total stress profiles at the axial load cells (i.e., injection load cell and backpressure load cell) do not increase to the same magnitude as the experimental data, although the total radial stresses are captured fairly well. This may be due to increased heterogeneity at the injection and backpressure fronts during installation of the specimen. Again, S2 is not capable of simulating the total stress response observed following breakthrough.

The results of introducing "slip flow" are provided in **Figure 12**(**d**). For S3, when the Klinkenberg effect is introduced, the modelled results following breakthrough capture the experimental behavior very well, with a steep increase in total stress at both the axial and radial load cells, followed by a subtle tail off once injection has stopped. This increase in total stress is due to achieving complete breakthrough through the sample. The model does have difficulties reaching the maximum total stresses recorded experimentally at the injection and backpressure load cells, however there is reasonably good agreement.

Figure 12(**e**) shows the stress evolution for S4. When heterogeneity and Klinkenberg effect are both introduced, the model is able to achieve a higher separation of stress curves and match the range of peak total stresses recorded experimentally, although still not quite able to match the total axial stresses exhibited during the initial hydration period. Furthermore, a deeper analysis of the stress evolution at each individual load cell array shows an overprediction of total stress at radial load cell 1 (RLC1), and an underprediction at the backpressure load cell (BLC). However, this may be due to the specific random distribution of heterogeneity applied in our model. If multiple iterations of the model were run using different randomly generated porosity distributions, the total stress evolution behavior exhibited experimentally by the individual load cell arrays may be realized by the model.

Figure 12(**f**) shows the stress evolution for S5, whereby the initial intrinsic permeability was set two orders of magnitude higher than that measured experimentally in order to observe the effect on flow behavior. For this scenario, the results show a much greater increase in total stresses from t = 0 days to t = 7.3 days, followed by fairly stable stress curves throughout the remainder of the simulation. Of particular note, is that there is minimal stress response during breakthrough. These results, when compared to the experimental results, support the notion that the Klinkenberg effect may play an important role in the gradual stress response of the system.

The results of S6 is provided in **Figure 12**(**g**). The introduction of a swelling strain provides a larger separation between the total stress curves. It also reduces the total stresses on the system in comparison to S4, with the exception of a peak total stress observed once gas breakthrough into the sample followed by a rapid decrease. This behavior in total stress under the presence of a swelling is expected, as an increase in gas pressure results in an increase in suction and decrease in volumetric strain. In our process simulation study this is most evident at the peak at RLC1, whereby once the AEV is reached there is a rapid increase in total stress in the system. Following gas shut-off there is an even steeper decline. It should be noted, that this behavior is not observed experimentally, although use of a non-linear swelling strain may lead to a better fit.

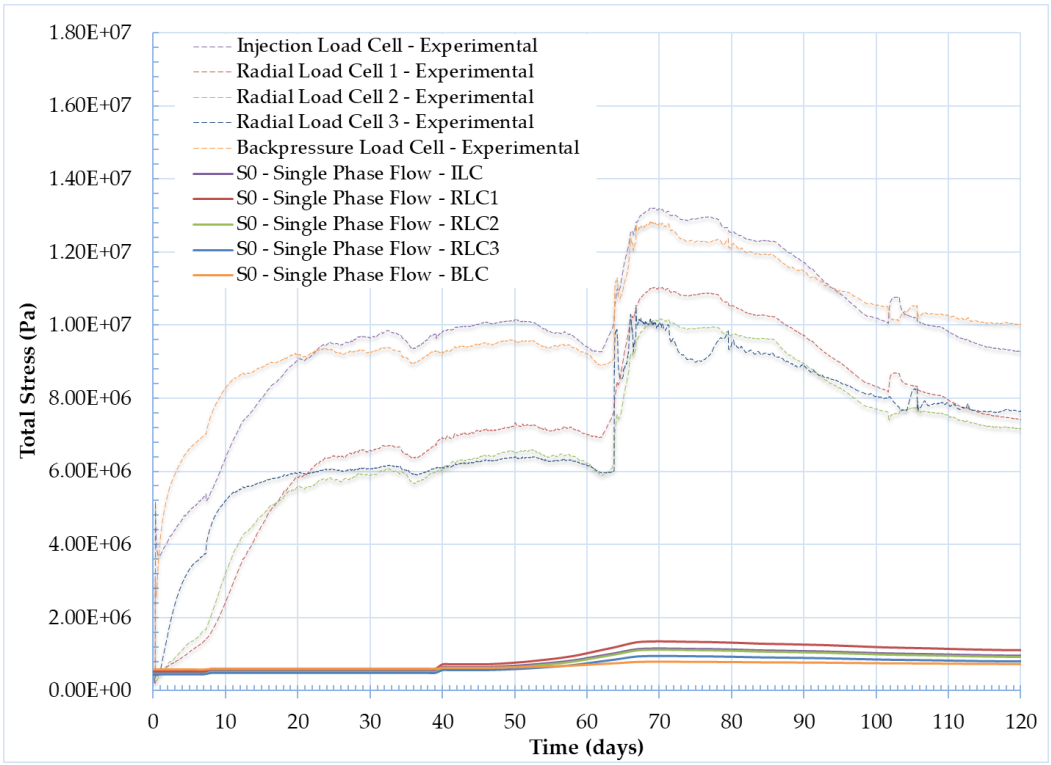
Injection Load Cell - Experimental
Radial Load Cell 1 - Experimental
Radial Load Cell 2 - Experimental
Radial Load Cell 3 - Experimental
Backpressure Load Cell - Experimental
S0 - Single Phase Flow - ILC
S0 - Single Phase Flow - RLC1
S0 - Single Phase Flow - RLC2
S0 - Single Phase Flow - RLC3
S0 - Single Phase Flow - BLC
Total Stress (Pa)
1.80E+07
1.60E+07
1.40E+07
1.20E+07
1.00E+07
8.00E+06
6.00E+06
4.00E+06
2.00E+06
0.00E+00
0
10
20
30
40
50
60
70
80
90
100
110
120
Time (days)

S0(**a**)

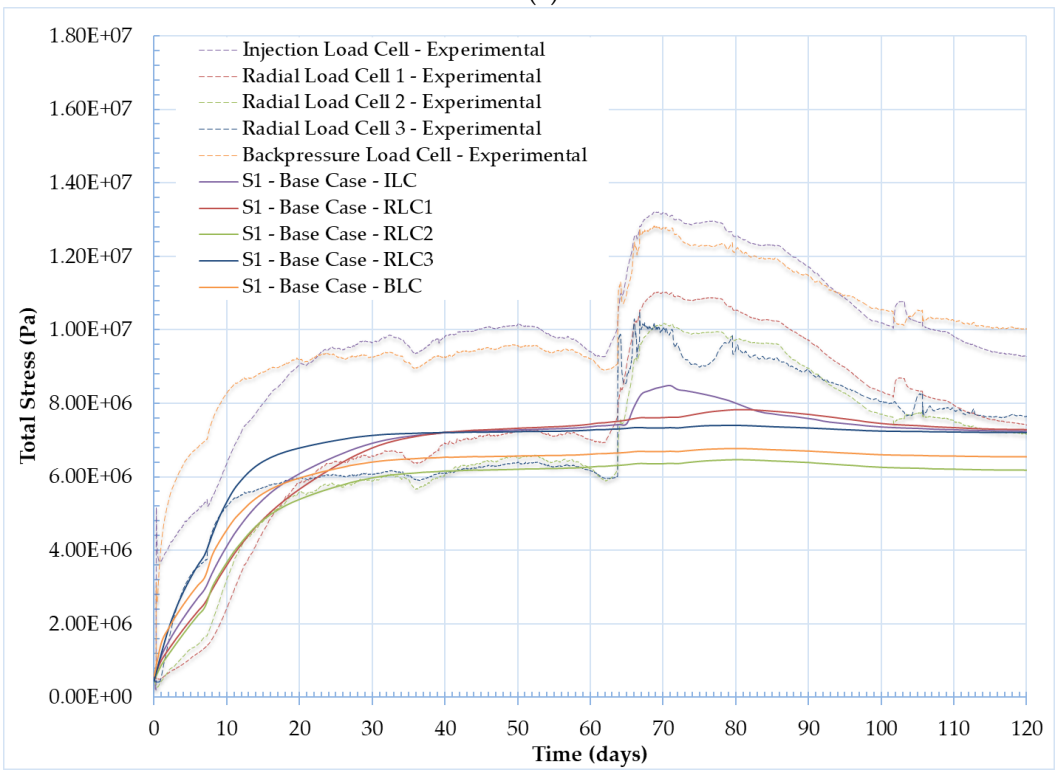
Injection Load Cell - Experimental
Radial Load Cell 1 - Experimental
Radial Load Cell 2 - Experimental
Radial Load Cell 3 - Experimental
Backpressure Load Cell - Experimental
S1 - Base Case - ILC
S1 - Base Case - RLC1
S1 - Base Case - RLC2
S1 - Base Case - RLC3
S1 - Base Case - BLC
Total Stress (Pa)
1.80E+07
1.60E+07
1.40E+07
1.20E+07
1.00E+07
8.00E+06
6.00E+06
4.00E+06
2.00E+06
0.00E+00
0
10
20
30
40
50
60
70
80
90
100
110
120
Time (days)

S1(**b**)

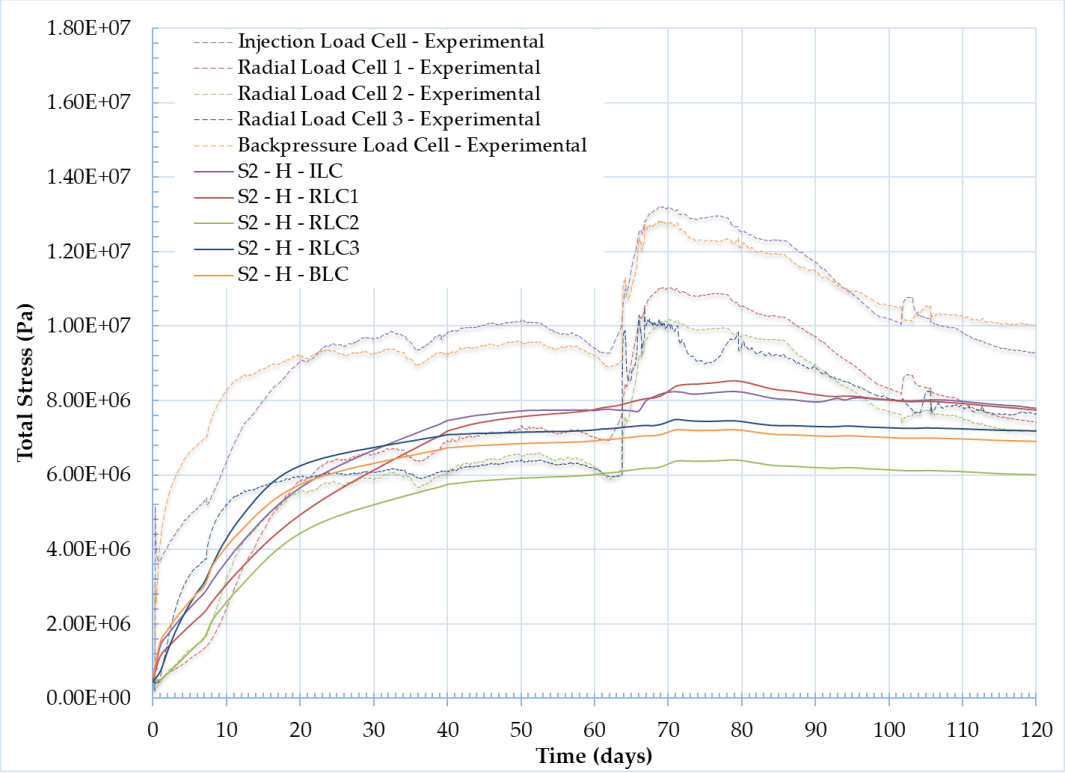
Injection Load Cell - Experimental
Radial Load Cell 1 - Experimental
Radial Load Cell 2 - Experimental
Radial Load Cell 3 - Experimental
Backpressure Load Cell - Experimental
S2 - H - ILC
S2 - H - RLC1
S2 - H - RLC2
S2 - H - RLC3
S2 - H - BLC
Total Stress (Pa)
1.80E+07
1.60E+07
1.40E+07
1.20E+07
1.00E+07
8.00E+06
6.00E+06
4.00E+06
2.00E+06
0.00E+00
0
10
20
30
40
50
60
70
80
90
100
110
120
Time (days)

S2(**c**)

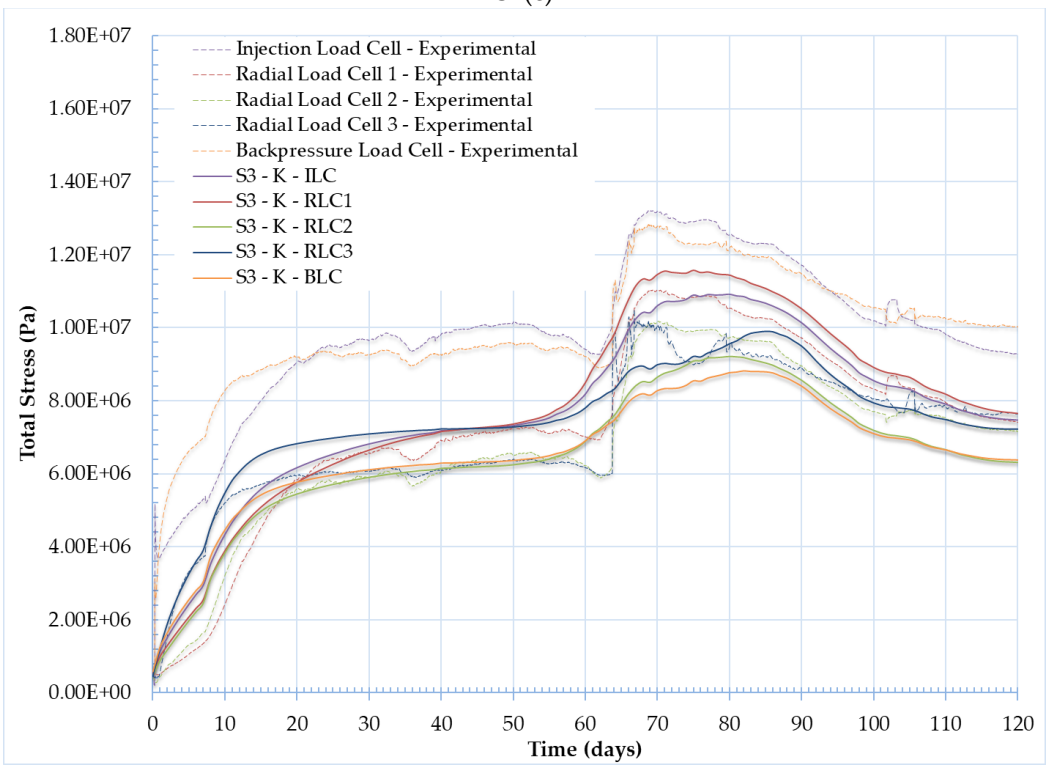
Injection Load Cell - Experimental
Radial Load Cell 1 - Experimental
Radial Load Cell 2 - Experimental
Radial Load Cell 3 - Experimental
Backpressure Load Cell - Experimental
S3 - K - ILC
S3 - K - RLC1
S3 - K - RLC2
S3 - K - RLC3
S3 - K - BLC
Total Stress (Pa)
1.80E+07
1.60E+07
1.40E+07
1.20E+07
1.00E+07
8.00E+06
6.00E+06
4.00E+06
2.00E+06
0.00E+00
0
10
20
30
40
50
60
70
80
90
100
110
120
Time (days)

S3(**d**)

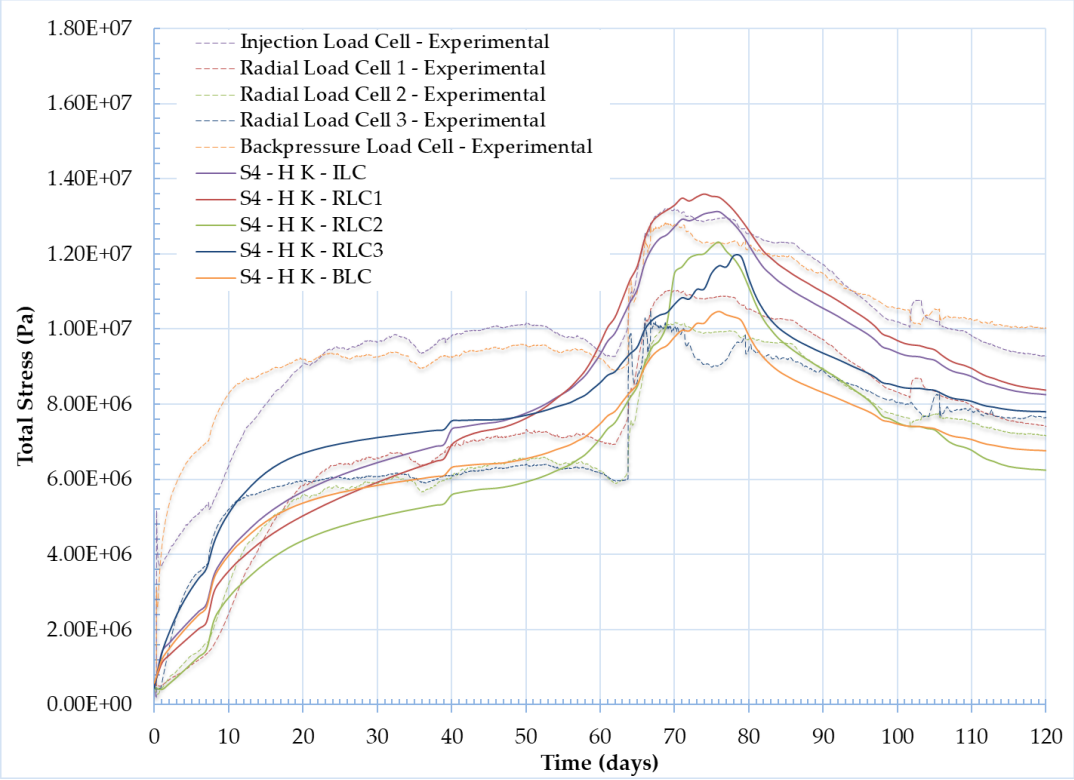
Injection Load Cell - Experimental
Radial Load Cell 1 - Experimental
Radial Load Cell 2 - Experimental
Radial Load Cell 3 - Experimental
Backpressure Load Cell - Experimental
S4 - H K - ILC
S4 - H K - RLC1
S4 - H K - RLC2
S4 - H K - RLC3
S4 - H K - BLC
Total Stress (Pa)
1.80E+07
1.60E+07
1.40E+07
1.20E+07
1.00E+07
8.00E+06
6.00E+06
4.00E+06
2.00E+06
0.00E+00
0
10
20
30
40
50
60
70
80
90
100
110
120
Time (days)

S4(e)

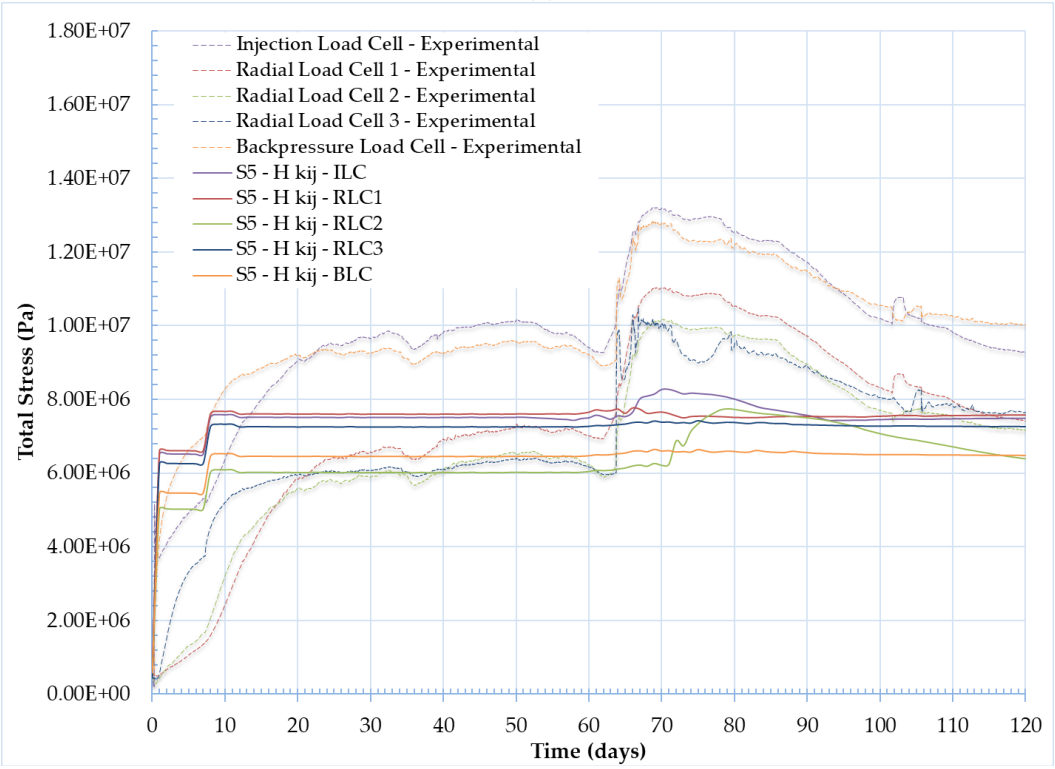
Injection Load Cell - Experimental
Radial Load Cell 1 - Experimental
Radial Load Cell 2 - Experimental
Radial Load Cell 3 - Experimental
Backpressure Load Cell - Experimental
S5 - H kij - ILC
S5 - H kij - RLC1
S5 - H kij - RLC2
S5 - H kij - RLC3
S5 - H kij - BLC
Total Stress (Pa)
1.80E+07
1.60E+07
1.40E+07
1.20E+07
1.00E+07
8.00E+06
6.00E+06
4.00E+06
2.00E+06
0.00E+00
0
10
20
30
40
50
60
70
80
90
100
110
120
Time (days)

S5(f)

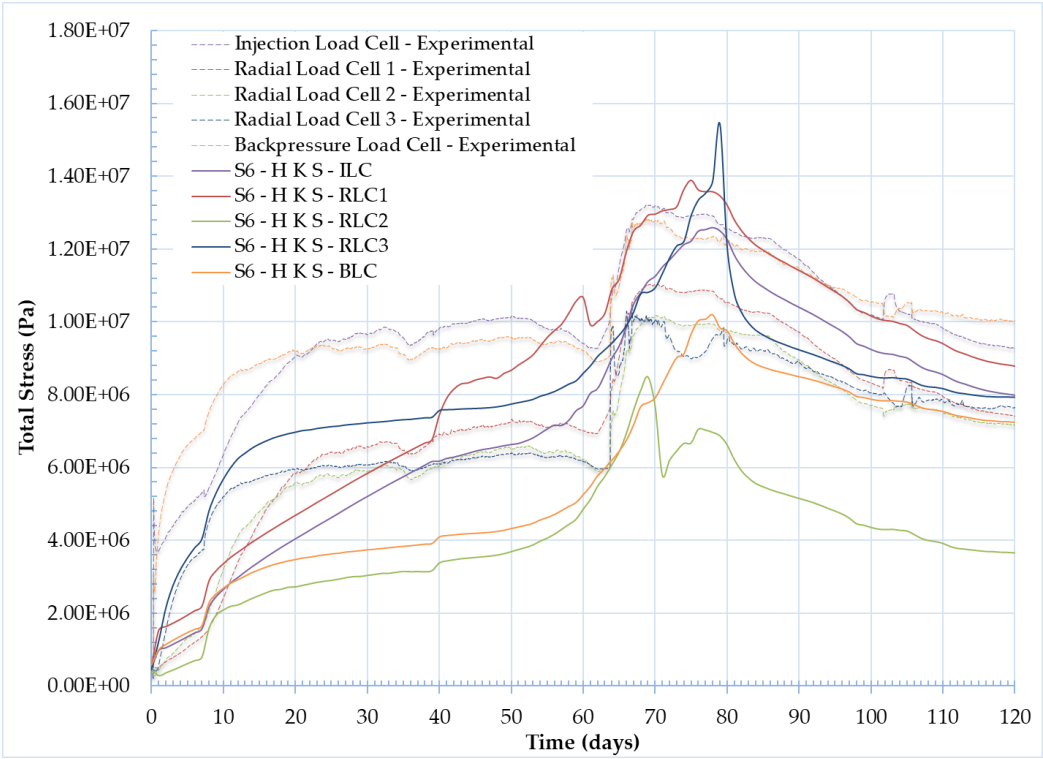

S6(**g**)

Figure 12. Total stress evolution over time for (**a**) S0; (**b**) S1; (**c**) S2; (**d**) S3; (**e**) S4; (**f**) S5; and (**g**) S6.

In light of these results, more work is needed to better fit the total stress evolution during the hydration period. This may be through re-evaluating the initial degree of saturation of the specimen, the initial hydration provided by the experiment and additional calibration of the non-linear swelling stress parameters.

3.5. Additional Factors

3.5.1. Mesh Dependency, Time Stepping, and Relative Tolerance

Based on the results of this study, it was identified that a number of numerical factors play a significant role in the numerical modelling of two-phase flow. These factors include the output time step selected in COMSOL®, mesh size and relative tolerance.

During the numerical analysis, an output time step of 0.1 Day was set in COMSOL® in order to capture the chaotic peak behavior observed by the experimental results. During the model runs, when a higher output time step of 1 Day was applied, the model results were not able to capture the full oscillations well. Output time steps of 0.01 Day were also performed, and although the results provided even greater resolution of the chaos observed, in order to balance computational time and the resolution needed to capture main features of the experimental data, it was determined that an output time step of 0.1 Day was adequate. It should be noted that COMSOL® applies an effective time step smaller than, but based on the user defined time step.

For each model run, a user defined optimum relative tolerance had to be set in order to reach convergence. The selected relative tolerance had to be set low enough to minimize the relative error that could be generated by the numerical model, while simultaneously allowing for enough buffer to converge in areas with dynamic changes in poregas pressure.

3.5.2. Extent of heterogeneity

It should be noted that the authors originally modelled small heterogeneities within the bentonite sample considering a mean porosity distribution of 0.44 with a standard deviation of 0.01. However, when small heterogeneities were applied there were very little impacts to model results. Based on the proposed models, if heterogeneity is to play a large role in preferential flow, larger heterogeneities within the bentonite sample would be required. Further work investigating the extent of heterogeneity in swelling clays is required.

4. Discussion and Conclusions

An important component in the design and long-term safety assessment of a DGR is the long-term performance of bentonite seals as barriers against gas migration. As gas generates from the degradation of organic waste and/or corrosion of metals, at some critical gas pressure, dilation of the bentonite could occur resulting in the creation of preferential flow pathways and a source of radionuclide exposure to people and the environment.

In an attempt to understand the physical mechanisms associated with dilation and two-phase flow in a swelling geomaterial, this study provides a number of improvements to the HM mathematical model originally proposed by Dagher et al. [4]. A process simulation and enhanced two-phase flow analysis study was conducted. Three enhanced mechanisms for two-phase flow were introduced into the model, specifically, heterogeneity, the Klinkenberg "slip flow" effect, and a linear swelling stress. An analysis of the contribution of each to flow behaviour and the potential for the formation of gas fingers was conducted for a swelling geomaterial.

The analysis was performed by comparing results of a number of study scenarios against experimental data from a 1D flow test through a saturated bentonite sample under a constant volume boundary stress condition. The modelled results were compared to key features of the experimental data, including the gas inflow and outflow, volume of gas stored in the system, and evolution of total axial and radial stresses. Although the models were not able to reproduce dilation-controlled gas flow, substantial insight into enhanced model features was obtained.

The results show that heterogeneity may play a role in supporting the development of localization and preferential flow, however the introduction of heterogeneity alone to the linear elastic model is not enough to trigger preferential flow, and other advanced processes are required to generate preferential flow and exasperate dilation.

Introduction of the Klinkenberg "slip flow" effect significantly increased gas permeability and migration through the system. It also promoted the notable chaotic behavior in both gas inflow and outflow observed by the experimental results. However, key model features including sharp changes in inflow rate could not be achieved by the Klinkenberg effect. When coupled with heterogeneity, the model accurately simulated the total stresses evolution observed by the experimental results, a stark improvement from the authors previous work. However, the Klinkenberg "slip flow" effect, may not provide as much of a contribution to gas migration through preferential flow pathways, as the authors had initially hypothesized. When looking at the volume of gas stored in the system, the experimental results showed expected behavior of preferential flow whereby gas flowing into the sample follows discrete pathways resulting in nearly immediate gas outflow and little gas storage within the sample. The model results on the other hand, demonstrated a plug flow behavior, whereby saturation of the bentonite sample was observed. This suggests that although the Klinkenberg effect may play a role in two-phase flow, it cannot be used to explain the rapid increase in permeability and the formation of preferential flow pathways, as the effect tends to saturate the sample.

Introduction of a swelling strain played a minor role in the shape and timing of gas inflow, gas outflow, and volume of gas stored within the system. Its presence did improve each of the results slightly.

Investigation into the use of a non-linear swelling, however, may provide better agreement with the experimental data.

With respect to the investigation into the formation of gas fingers, as discussed above, a number of physical conditions are required in order to simulate viscous fingering. These included differences in viscosity of both fluids, heterogeneity in the porosity and permeability of the geomaterial, and a very fine mesh. Our modelling results were able to produce gas fingers. This was a result of differences in viscosities of each fluid (helium and water) considered within their own transport equations (Darcy's law), the inclusion of heterogeneity in pore size, and the selected mesh size. The results showed that the extent of gas fingering was more strongly related to changes in permeability within the soil specimen than size of the mesh. Additionally, when fingering was present, the size of the gas fingers were short and their formation short lived, likely as the effect of gravity, diffusion and suction did in fact hinder formation of long discrete fingers, as had been identified by previous studies on gas fingering [64].

The results of this paper support the conclusion that other highly coupled HM mechanisms must be at play. In light of this, future studies will assess the contribution of several types of stress-strain relationships on flow behavior, including damage and poro-elastoplasticity.

The results of this study conclude that in order to mimic dilation, and dilatancy-controlled gas flow, additional considerations to the stress-strain behaviour is required. Future studies will look at the effects of different stress-strain constitutive models on flow behaviour. These will include a detailed assessment of the coupling between flow and stress state triggered by mechanical damage and plasticity. Future studies will also investigate the application of strain-localization and channeling in an attempt to simulate dilatancy-controlled gas flow and exasperate dilation and creation of preferential flow paths. Finally, multiple model iterations of randomly normally- distributed initial porosities will be assessed in an attempt to define, through a probabilistic assessment, the chaotic nature of dilation pathways.

Author Contributions:

Conceptualization, Dagher and Nguyen; methodology, Dagher and Nguyen; software, Dagher; validation, Dagher, Nguyen and Infante Sedano; formal analysis, Dagher; investigation, Dagher and Nguyen; resources, Infante Sedano; data curation, Dagher, Nguyen and Infante Sedano; writing—original draft preparation, Dagher; writing—review and editing, Nguyen and Infante Sedano; visualization, Dagher; supervision, Nguyen and Infante Sedano; project administration, Infante Sedano; funding acquisition, Infante Sedano

Funding: This work was supported by the Canadian Nuclear Safety Commission.

Acknowledgments: Decovalex (http://www.decovalex.org) is an international research project comprising participants from industry, government and academia focusing on development of understanding, models and codes in complex coupled problems in sub-surface geological and engineering applications. DECOVALEX-2019 is the current phase of the project. The authors appreciate and thank the DECOVALEX-2019 funding organizations, Andra, BGR/UFZ, CNSC, US DOE, ENSI, JAEA, IRSN, KAERI, NWMO, RWM, SÚRAO, SSM and Taipower, for their financial and technical support of the work described in this paper. The statements made in the paper are, however, solely those of the authors and do not necessarily reflect those of the funding organizations.

Conflicts of Interest: The authors declare no conflict of interest.

CHAPTER 6: INFLUENCE OF STRESS-STRAIN BEHAVIOUR AND DAMAGE ON GAS TRANSPORT IN A SWELLING GEOMATERIAL

Article

Influence of Stress-Strain Behaviour and Damage on Gas Transport in a Swelling Geomaterial

Elias Ernest Dagher [1,2], Julio Ángel Infante Sedano [2] and Thanh Son Nguyen [1,2*]

[1] Canadian Nuclear Safety Commission (CNSC), Ottawa, ON, K1P 5S9, Canada;
[2] Department of Civil Engineering, University of Ottawa, Ottawa, ON K1N 6N5, Canada; e-mail@e-mail.com
* Correspondence: son.nguyen@canada.ca

Received: date; Accepted: date; Published: date

Special Publication of International Journal of Rock Mechanics and Mining Sciences – Submission

Abstract: In a deep geological repository (DGR) for the long-term containment of radioactive waste, gases could be generated through a number of processes. If gas production exceeds the containment capacity of the engineered barriers or host rock, the gases could migrate through these barriers and potentially expose people and the environment to radioactivity. Expansive soils, such as bentonite-based materials, are currently the preferred choice of seal materials. Understanding the long-term performance of these seals as barriers against gas migration is an important component in the design and long-term safety assessment of a DGR. This study proposes a mathematical hydro-mechanical (HM) model for migration of gas (two-phase flow) through a low-permeable heterogeneous swelling geomaterial. It is based on the theoretical framework of poromechanics, applies Darcy's Law for both the porewater and poregas, and incorporates a modified Bishop's effective stress principle. The study expands upon previous work by the authors, by assessing three stress-strain constitutive models in an attempt to simulate dilatancy-controlled gas flow; i) an enhanced elastic damage model, ii) a local elastoplastic model with damage, and iii) a non-local elastoplastic model with damage. Using the Finite Element Method (FEM), the models were used to simulate 1D and 3D flow through a low-permeable swelling soil. The results were validated against experimental results found in the current literature for a confined cylindrical sample of near-saturated bentonite under a constant volume condition. This study provides fundamental insight into the highly coupled nature of multi-phase flow to the stress state of the material. Future work should expand the model to assess methods of localization to generate flow through preferential pathways.

Keywords: THMC modelling; multi-phase flow; gas migration; nuclear waste disposal; bentonite, expansive soils, swelling soils, swelling geomaterials, plasticity, localization

1. Introduction

In Canada, nuclear waste has been generating and accumulating since the 1930s when the Port Radium radium mine began operating in the Northwest Territories [50]. Since then Canada has become a sustainable nuclear country with operating nuclear facilities across the nuclear fuel cycle all producing various forms of radioactive waste. To-date, this waste, in the form of low-, intermediate-, and high-level radioactive waste has been primarily stored on the site of nuclear power plants or in below surface radioactive waste management facilities.

Canada and the international community, have been investigating disposal of the waste in a Deep Geological Repository (DGR) for its long-term management. The primary purpose of a DGR is to contain

and isolate wastes to minimize impact to the environment and radiological exposure to people. To adequately develop a safety case for a DGR, consideration must be given to the relevant features, events, and processes (FEPs), and their impact on the primary objectives of a DGR [17, 18]. One such process with the potential means for radiological exposure to the biosphere is the generation of radioactive gas which may migrate to the surface [19]. Gas could be generated through a number of processes including the degradation of organic matter, radioactive decay of the waste, corrosion of metals producing hydrogen gas (H_2), and the radiolysis of water producing H_2 [20, 21, 19]. If production exceeds the containment capacity of the engineered barriers or host rock, the gases could migrate through these engineered barriers and/or the host rock [22, 9]. The preferential migration pathway of these radioactive gases, to potentially expose people and the environment to radioactivity, might be through the access and ventilation shafts; as these components are typically part of the repository design.

In recent years, a number of international projects have focused on the topics of gas generation and migration, with a focus on the impact of gas build-up and migration through an engineered barrier system (EBS) [23, 24, 4]. Expansive or swelling soils, such as bentonite-based materials, are currently the preferred choice of seal materials used for an EBS. Understanding the long-term performance of these seals as barriers against gas migration is an important component in the design and long-term safety assessment of a DGR.

An investigation of the gas transport processes in low-permeability clay material was described by Marschall et al. [5], and further investigated by Cuss et al. [20]. Marschall et al. [5] recognized that gas transport through porous media is controlled by a number of the media's hydraulic and mechanical characteristics such as the intrinsic permeability, porosity, and material strength. They identified the importance of the hydro-mechanical state of the rock or soil media (i.e., water saturation, porewater pressure, and stress state) and the gas pressure at focal points which could lead to microfracturing [5]. Marschall et al. [5] divided the basic transport mechanisms into four processes, mainly i) advective-diffusive transport of dissolved gas, ii) visco-capillary two-phase flow (of poregas and porewater), iii) dilatancy-controlled gas flow and the induction of microfractures creating preferential flow pathways, and iv) gas transport along macro-fractures. At low gas pressure, advective-diffusive processes are solely responsible for gas transport. In that first flow regime, deformation of the soil skeleton is minimal and the influence of the mechanical process on the gas flow process could be neglected. When the gas pressure increases, the other processes will in turn contribute to gas migration. Of particular interest to this paper, is the investigation into the highly coupled hydromechanical processes involved in dilatancy-controlled gas flow. A wealth of laboratory and field-scale experimental studies have investigated gas transport processes through natural (host rock) and engineered barriers. These studies have provided considerable evidence suggesting that gas flow at gas pressures above a reference level is accompanied by the creation of pressure-induced preferential pathways and dilation of the clay, yet have not been able to determine the exact mechanisms which control gas entry, flow, and pathway sealing [25, 22, 26, 27, 28, 20, 23, 29]. In addition, a number of mathematical models have tried to simulate the gas transport processes observed through these laboratory and field scale studies without success [33, 34, 35].

Marschall et al. [5], described the primary transport mechanism of dilatancy-controlled gas flow as an important transport mechanism in clay soil or clay-rich rock with low tensile-strength. Dilatancy will occur when the gas pressure reaches a reference stress level acting on the clay medium, forcing the clay particles to align in a dispersed orientation, and resulting in the formation of microfractures accompanied by an increase in plastic deformation [30]. As a result, gas flow along these microfractures will be promoted due to the increased pore space. The presence of microfractures therefore leads to an increase in the intrinsic permeability of the material and in turn results in changes in the relationship between the capillary pressure (i.e., matric suction) and degree of saturation (i.e., from the soil-water characteristic curves of the material). As a result of dilatancy-controlled gas flow, transport properties are now dependent on the stress-state and state of deformation of the soil.

In this paper, we apply the Critical State Theory (CST) in order to simulate the stress-strain response of expansive soils and assess the influence of the soil mechanical behaviour on gas migration. According to the CST, the stress-strain response consists of three regimes: i) an elastic regime (elastic/reversible deformation), ii) a plastic regime (plastic/irreversible deformation), and iii) the critical state where shear distortion increases without any increase in stress, i.e. the soil behaves like a frictional fluid [30].

Figure 1 illustrates the authors' conceptualization of the potential stress path evolution of a soil when injected with gas. **Figure 1**(**a**) shows the stress paths taken by two points in a confined (no overall volume change) sample of swelling geomaterial being injected with gas. Near the injection point, the porefluid pressure increases, leading to a decrease in the effective mean stress and resulting in a stress path that crosses the critical state line (CSL) and eventually reaches the initial yield surface. This stress path is characterized by strain softening and dilation. For points away from the injection point, the sample will go through a series of strain-hardening plastic deformations before ultimately reaching the CSL. However, consideration to capillary pressure or suction may also impact the mode of mechanical deformation. With an increase in suction, the CSL and yield surface may shift to the left as depicted by **Figur**e 1(**b)**. Near the injection point, the stress path is characterized by dilation and strain softening. In addition, depending on the magnitude of suction, an increase in poregas pressure could result in the stress path crossing the deviatoric stress axis, resulting in tensile effective mean stress.

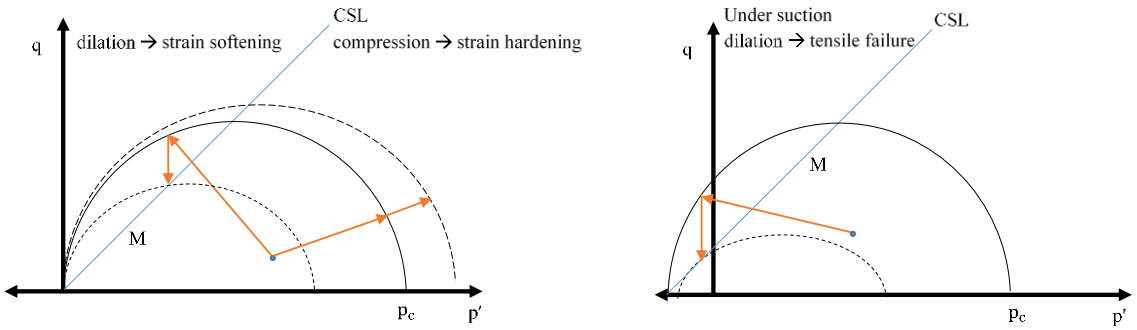

Figure 1. p'-q stress path response of a highly compacted soil specimen (p' is the effective mean stress; q is the deviatoric stress).

Dagher et al. [4] developed a fully-coupled, hydro-mechanical linear-elastic mathematical model for advective-diffusive visco-capillary controlled two-phase flow through geomaterials in order to model the first two transport mechanisms proposed by Marschall et al. [5]. Results from a 1-dimensional flow constant volume boundary condition experiment was used to validate the model. A number of parametric studies were investigated to assess the contribution of advection of poregas, diffusion of dissolved gas in porewater, advection of dissolved gas in porewater, and inclusion of mechanical deformation (linear elasticity) on flow behaviour with increasing gas pressures over time. Additionally, sensitivity analysis were conducted to gain an understanding of the influence of a number of soil properties on flow behaviour, such as the effect of modifying the air-entry value (AEV), intrinsic permeability, and initial porosity of the soil specimen. Finally, the study investigated the use of a linear elastic damage model to better represent the experimental results.

Although the model results reproduced some of the general features noted in the experimental results, the model was not able to simulate dilatancy-controlled gas flow. The study concluded that in order to promote dilatancy-controlled gas flow additional mechanisms need to be considered within the model. These include the use of advanced stress-strain models to be coupled to gas transport, consideration of heterogeneity within the soil sample to help induce preferential flow, inclusion of a swelling stress term to

incorporate the swelling behaviour of expansive soils, and the incorporation of a self-healing mechanism to represent observed phenomena of experimental studies [4].

Subsequent work by the authors included both verification of the numerical model proposed in the original work [73], as well as an investigation into the effects of enhanced processes for two-phase flow, including the application of heterogeneity, the Klinkenberg "slip flow" effect, and swelling of the geomaterial [74]. In the enhanced two-phase flow analysis, the study results were compared to the same experimental dataset provided in the authors original work for 1D gas flow through a saturated bentonite sample under constant volume boundary condition. The results showed significant improvement to the inflow and outflow behaviour and the total stress evolution throughout the system, however these processes resulted in a plug flow behaviour as opposed to preferential flow behaviour observed by the experimental data. The primary conclusions of this study were that although heterogeneity, slip flow and a swelling stress may play a role in the development of preferential flow pathways, other mechanisms of mechanical deformation are required in order to generate dilatancy and more localized flow.

This study builds upon the work done by Dagher et al. [4, 73, 74] by investigating the use of three distinct stress-strain constitutive models and their influence on two-phase flow behaviour. Specifically, this study investigates the use of an enhanced elastic damage model with self-healing behaviour, an elastoplastic model with damage, and a non-local elastoplastic model with damage. Additionally, these models incorporate the supplementary processes of two-phase flow investigated by Dagher et al. [74], including heterogeneity of the geomaterial, the Klinkenberg "slip flow" effect, and a swelling stress to promote swelling of the geomaterial. The models are validated against experimental data from a 1D flow test and a 3D spherical flow test.

This research continues to be, in part, a contribution to Task A of the current project phase of the international working group for the DEvelopment of COupled models and their VALidation against EXperiments (DECOVALEX-2019). This task, led by the British Geological Survey (BGS), further attempts to identify the physical HM mechanisms required to adequately model dilatancy-controlled gas migration.

2. Mathematical Model

2.1. Study Overview

This study proposes and compares three different hydro-mechanical (HM) models to describe the migration of gas (two-phase flow) through a low-permeability expansive soil using the theoretical framework of poromechanics:

1. Elastic damage (ED) model with self-healing
2. Elastoplastic (EPD) model with damage utilizing a modified extended Barcelona Basic Model (xBBM)
3. Non-local elastoplastic (NLPD) model with damage utilizing xBBM

Each model follows the general formulation by Dagher et al. [4] with the addition of the following features discussed in Dagher et al. [74]:

- Incorporation of material heterogeneity, through the use of a random normal distribution of porosity,
- Consideration of the Klinkenberg "slip flow" effect for the intrinsic permeability of the gas in soil, k_{ij_g}; and
- Incorporation of a swelling stress, σ_{sw}.

In the case of the EPD and NLPD models, material defects have instead been introduced, in order to assess their impact in promoting plastic deformation, and is discussed further in Section 3.6.2.

The mathematical model presented in this paper follows the general formulation by Dagher et al. [4, 74] and Nguyen and Le [1] and includes the constitutive relations for the Soil Water Characteristic Curves (SWCCs) through the application of the van Genuchten equation, and the relative permeability-saturation

relationships using Mualem's Model. The applicable constitutive relations and governing equations for conservation of momentum, water mass and gas mass are discussed below.

2.2. Effective Stress Principle and Constitutive Relations for the Mechanical Behaviour

2.2.1. Bishop's modified effective stress principle

In this work, a modified form for the Bishop's effective stress is adopted,

$$\sigma_{ij} = \sigma'_{ij} + \delta_{ij}\bar{p} \tag{1}$$

where σ_{ij} is total stress tensor (Pa)

σ'_{ij} is the effective stress tensor (Pa) and

$\bar{p}$ is the porefluid pressure (Pa), which is a weighted average of the gas and water pressures as discussed next.

Many effective stress equations have been proposed to characterize the stress-state of an unsaturated soil or porous media [1]. This paper proposes the use of Bishop's effective stress principle, which is dependent on both net normal stress and matric suction, and may be more suitable for expansive clay's, and is described by equation (2).

$$\sigma'_{ij} = (\sigma_{ij} - p_g) + \chi\delta_{ij}(p_g - p_w) \tag{2}$$

where

p_g is the poregas pressure (Pa)

p_w is the porewater pressure (Pa)

$(\sigma_{ij} - p_g)$ is the net normal stress (Pa)

$(p_g - p_w)$ is the matric suction (Pa)

δ_{ij} is the Kronecker delta (identity tensor) (adimensional)

χ is a parameter related to the degree of saturation of the soil (unitless)

Expanding and rearranging for σ_{ij},

$$\sigma_{ij} = \sigma'_{ij} + \delta_{ij}\left((1-\chi)p_g + \chi p_w\right) \tag{3}$$

The porefluid pressure can be defined as,

$$\bar{p_f} = (1-\chi)p_g + \chi p_w \tag{4}$$

where $\bar{p}_f$ is the porefluid pressure (Pa).

In this work, the authors adopted Khalili and Khabbaz [2] unified relationship for the determination of χ based on the ratio of suction over the air entry value, also termed the suction ratio,

$$\chi = \begin{cases} \left[\dfrac{(p_g - p_w)}{(p_g - p_w)_b}\right]^{-0.55}, \text{if } (p_g - p_w) > (p_g - p_w)_b \\ 1, \text{otherwise} \end{cases} \tag{5}$$

where $(p_g - p_w)_b$ is the air-entry value (AEV) of the soil and only applies when the matric suction > AEV [2].

2.2.2. Elastoplastic stress-strain relation with the consideration of swelling

The increment of effective stress tensor, $d\sigma'_{ij}$ is related to the increment of the total strain by the constitutive relation:

$$d\sigma'_{ij} = C_{ijkl} d\varepsilon_{kl} \quad (6)$$

where C_{ijkl} is the stiffness tensor (Pa)

Assuming small deformations, the total strain is related to the components of the displacement vector as:

$$\varepsilon_{ij} = \frac{1}{2}\left(u_{i,j} + u_{j,i}\right) = \frac{1}{2}\left(\frac{\partial u_i}{\partial x_j} + \frac{\partial u_j}{\partial x_i}\right) \quad (7)$$

$$\varepsilon_{kk} = u_{k,k} = \frac{\partial u_k}{\partial x_k} \quad (8)$$

Using the elastoplasticity framework, we divide the total strain into an elastic, a plastic component. In addition a swelling component is also considered as follows:

$$\varepsilon_{kl} = \varepsilon_{ij}^{el} + \varepsilon_{ij}^{pl} + \varepsilon_{ij}^{sw} \quad (9)$$

where ε_{kl} is the total strain tensor

ε_{ij}^{el} is the elastic strain component

ε_{ij}^{pl} is the plastic strain component

ε_{ij}^{sw} is the swelling strain component

Swelling strain component

For an expansive/swelling soil, the swelling strain increment, $d\varepsilon_{ij}^{sw}$, is a function of suction, s, or the degree of saturation, S_w, whereby an increase in suction (or likewise a decrease in degree of saturation) results in a decrease in the swelling strain [70]. Assuming isotropic swelling, this can be expressed by the following equation,

$$d\varepsilon_{ij}^{sw} = \delta_{ij} \frac{\beta_{sw}}{3} ds \quad (10)$$

where β_{sw} is a swelling coefficient (1/Pa)

$s = (p_g - p_w)$ is the suction (Pa), and

Although unpublished, Nguyen and Barnichon [75], presented a non-linear relationship for swelling strain, by considering the state surface equation presented by Lloret and Alonso [76]. Nguyen and Barnichon [75] were successful in simulating SEALEX in-situ swelling tests under controlled suction by applying a swelling coefficient as a function of the void ratio, e, the mean effective stress σ'_m, and suction, s, as follows,

$$\beta_{sw} = \frac{1}{1+e} \frac{B + C \log\left(\frac{-\sigma'_m + p_{ref}}{p_{ref}}\right)}{s + s_{ref}} \quad (11)$$

where e is the void ratio (adimensional)

B and C are fitting parameters describing the range in magnitude of the volumetric strain (adimensional)

σ'_m is the mean effective stress

p_{ref} is a reference pressure (Pa)

s_{ref} is a reference suction (Pa), influencing the rate of change in volumetric strain with suction

2.2.3. Extended Barcelona Basic Model for an unsaturated poro-elastoplastic soil

In order to determine plastic strain, the authors adopted the Barcelona Basic Model which is an extension of the classical Cam Clay Model [77] for unsaturated soils. The Barcelona Basic Model was developed by Alonso et al. [78]. In this work, the authors apply a variation of the extended BBM (xBBM) proposed by Pedroso & Farias in order to allow the simulation of elastoplastic behaviour during cycles of both mechanical and hydraulic loading [79].

In the xBBM two yield surfaces are defined, f_1 and f_2, which are expressed as functions of the following stress-state variables

$$p' = \frac{tr(\sigma)}{3} = \frac{\sigma_{kk}}{3} = \sigma'_m \tag{12}$$

$$q = \sqrt{\frac{3}{2} dev(\sigma_{ij}) : dev(\sigma_{ji})} \tag{13}$$

$$\boldsymbol{\sigma}_D = dev(\sigma_{ij}) = \sigma_{ij} - \frac{\sigma_{kk}}{3}\delta_{ij} \tag{14}$$

where p' is the mean effective stress (Pa)

q is the deviatoric stress (Pa)

$\boldsymbol{\sigma}_D$ is the deviatoric stress tensor (Pa)

The first yield surface, f_1, is dependent on the value of yield stress also termed consolidation pressure for saturated conditions, p_c, which is also a hardening parameter:

$$f_1(p', q, s, p_{cs}) = \frac{q^2}{(p' + p_s)} - M(\theta)^2(p_{cs} - p') + \frac{C_{xbbm}}{(p' + p_s)} = 0 \tag{15}$$

where $M(\theta)$ is the slope of the critical state line as a function of the Lode angle, θ, and angle of internal friction, ϕ (unitless)

p_s is the tensile strength attributed to suction (Pa), and

p_{cs} is the consolidation pressure at current suction (Pa)

C_{xbbm} is an additional term to the original BBM (Pa^2)

The second yield surface, f_2, is dependent on the maximum historic suction value, s_y (i.e., hardening parameter of the suction increase yield curve).

$$f_2(s, s_y) = s - s_y = 0 \tag{16}$$

where s_y is the suction yield value at current suction (Pa)

C_{xbbm} is an additional term proposed by Pedroso & Farias [79] to the original BBM to overcome problems at the intersections between the loading-collapse (LC) surface and the suction-increase (SI) surface.

$$C_{xbbm}(s, s_y) = p_{ref}^2 * \left(e^{\frac{b_{xbbm}(s - s_y)}{p_{ref}}} - e^{-\frac{b_{xbbm} s_y}{p_{ref}}} \right) \tag{17}$$

where p_{ref} is a reference pressure corresponding to a reference void ratio e_{ref} on the e vs ln(p) curve (Pa)

b_{xbbm} (unitless) is a constant that controls the smoothness of the LC/SI transition.

Flow rules

For small plastic strains, the plastic strain tensor increment is defined as,

$$d\varepsilon_{ij}^{pl} = \lambda_p \frac{\partial Q_p}{\partial \sigma_{ij}} \tag{18}$$

where λ_p is the plastic (consistency) multiplier, and

Q_p is the plastic potential.

The xBBM applies an associated flow rule whereby $Q_p = f_1$ Through some simplification the volumetric plastic strain tensor increment can be described by

$$d\varepsilon_v^{pl} = \text{trace}\left(d\varepsilon_{ij}^{pl}\right) \tag{19}$$

where $d\varepsilon_v^{pl}$ is the volumetric plastic strain rate (adimensional)

Likewise, the effective plastic strain rate, $d\varepsilon_{epe}$, is based on the plastic shear components and can be described by,

$$d\varepsilon_{epe} = \sqrt{\frac{2}{3}\text{dev}\left(d\varepsilon_{ij}^{pl}\right) : \text{dev}\left(d\varepsilon_{ji}^{pl}\right)} \tag{20}$$

where $d\varepsilon_{epe}$ is the effective plastic strain rate (adimensional)

Slope of the Critical State Line (CSL)

In the original BBM model, the slope of the CSL was provided by M_{cs},

$$M_{cs} = \frac{6\sin\phi}{3 - \sin\phi} \tag{21}$$

The slope of the CSL has been modified in the xBBM to account for a broader range of friction angles that guarantee convexity [80, 81, 79]. The slope of the CSL can be obtained by

$$M(\theta) = M_{cs}\left[\frac{2\omega}{1 + \omega - (1 - \omega)\sin(2\theta)}\right]^{\frac{1}{4}} \tag{22}$$

where

$$\omega = \left(\frac{3 - \sin\phi}{3 + \sin\phi}\right)^4 \tag{23}$$

In COMSOL® the Lode angle, θ, is calculated as

$$\theta = \frac{1}{3}\arctan\left(\frac{3\sqrt{3}}{2} \cdot \frac{J_3(\varepsilon_{ij})}{J_2(\varepsilon_{ij})^{\frac{3}{2}}}\right) \tag{24}$$

where $J_2(\varepsilon_{ij})$ and $J_3(\varepsilon_{ij})$ are the second and third invariants of the strain deviator tensor, $\text{dev}(\varepsilon_{ij})$, respectively.

Relationship between tensile strength and suction

The increase in tensile strength as a function of suction, p_s, can be calculated by,

$$p_s = k_s s \tag{25}$$

where k_s is the parameter describing the increase in tensile strength with matric suction

Yield stress and hardening laws

The yield stress or consolidation pressure at current suction, p_{cs}, associated with the yield surface, f_1, is given by the following expression,

$$p_{cs} = p_{ref}\left(\frac{p_c}{p_{ref}}\right)^{\frac{\lambda_0-\kappa_s}{\lambda_s-\kappa_s}} \tag{26}$$

where p_{cs} is yield stress or consolidation pressure at current suction (Pa)

p_c is the yield stress or consolidation pressure under saturated conditions (Pa)

p_{ref} is the reference pressure (Pa)

λ_0 is the compression index (slope of the virgin isotropic consolidation line) at saturation (adimensional)

λ_s is the compression index (slope of the virgin isotropic consolidation line) at current suction (adimensional)

κ_s is the swelling index (slope of the rebound-reloading line) at current suction (adimensional)

The consolidation pressure under saturated conditions, p_c, is given by the following expression

$$p_c = p_{c,0} + dp_c \tag{27}$$

where $p_{c,0}$ is the initial consolidation pressure [Pa] and

dp_c is the consolidation pressure rate [Pa]

The hardening law associated with the yield surface, f_1 is described by the change in the consolidation pressure, dp_c, as a function of the change in volumetric plastic strain, $d\varepsilon_v^{pl}$, expressed as follows,

$$dp_c = \frac{1+e_{ref}}{\lambda_0-\kappa_s}p_c d\varepsilon_v^{pl} \tag{28}$$

The compression index at current suction, λ_s can be calculated from the following expression,

$$\lambda_s = \lambda_0\left[(1-r)e^{-\beta s} + r\right] \tag{29}$$

where r is the parameter defining the maximum soil stiffness

β is the parameter controlling the rate of soil stiffness increase with suction

Nasir et al. [70] adopted the following expression from Alonso et al. [82] to determine the swelling index at current suction, κ_s,

$$\kappa_s = \kappa_0(1-\alpha_\kappa s) \tag{30}$$

where κ_0 is the swelling index at saturation (unitless)

α_κ is a parameter describing the change in κ_s with suction

The yield value at current suction associated with the yield surface, f_2, is given by the following expression,

$$s_y = s_{y0} + ds_y \tag{31}$$

where s_{y0} is the initial yield value at current suction

ds_y is the change in yield value at current suction (Pa).

The hardening law associated with the yield surface, f_2, is described by the change in the yield value at current suction, ds_y, as a function of the change in volumetric plastic strain, $d\varepsilon_v^{pl}$, expressed as follows,

$$ds_y = \frac{1+e_{ref}}{\lambda_s-\kappa_s}\left(s_y + p_{atm}\right)d\varepsilon_v^{pl} \tag{32}$$

where p_{atm}, is the atmospheric pressure (Pa).

Non-linear elastic soil model

A non-linear elastic soil model has been incorporated into the xBBM poro-elastoplasticity model where the Bulk Modulus, K_b, is given by the expression

$$K_b = B_{el} p_{ref} e^{-B_{el}\varepsilon_v^{el}} \tag{33}$$

$$B_{el} = \frac{1 + e_{ref}}{\kappa_s} \tag{34}$$

where K_b is the Bulk Modulus (Pa)
ε_v^{el} is the elastic volumetric strain (adimensional)
The Shear Modulus, G_s, is given by the expression,

$$G_b = \frac{3K_b(1-2\nu)}{2(1-\nu)} \tag{35}$$

where G_b is the Shear Modulus (Pa) and
ν is Poisson's Ratio (adimensional)
The void ratio, e, can be calculated via

$$e = e_{ref} - (\lambda_s - \kappa_s)\ln\left(\frac{p_{cs}}{p_{c,0}}\right) - \kappa_s\left(\frac{1+e_{ref}}{\kappa_s}\right)\varepsilon_v^{el} \tag{36}$$

2.2.4. Non-local plasticity

It is well known when modelling plasticity using continuum models, that the strain-softening constitutive law will cause loss of ellipticity of the governing differential equations, and result in the localization of plastic deformation into a zero volume zone [83, 84, 85]. This may result in what appears to be a number of singular cracks which do not coalesce. However, in reality, the initiation of fractures, and their coalescence and interconnection maybe determined by nonlocal homogenization and energy release from a finite volume surrounding the microcrack. This may be a result of heterogeneity of the soil microstructure, the interaction between microcracks, and the natural statistical distribution of microcracks within the specimen [83]. Consideration of non-local plasticity removes this smearing by interpolating the plastic deformation over a zone of influence defined by a characteristic length,l_c. This zone of influence can be physically interpreted as the area by which these sharp cracks or shear bands diffuse into the surrounding domain.

For the NLPD model, the loss of ellipticity is handled through the defining of a non-local plastic strain which is solved through the Helmholtz equation [83],

$$\bar{\gamma} - l_c^2\nabla^2\bar{\gamma} = \varepsilon_v^{pl} \tag{37}$$

where $\bar{\gamma}$ is the nonlocal equivalent plastic strain (adminensional)
l_c^2 is a defined characteristic length (m), and
ε_v^{pl} is the volumetric plastic strain (adimensional),
and a homogeneous Neumann boundary condition:

$$\frac{\partial\bar{\gamma}}{\partial\mathbf{n}} = 0 \tag{38}$$

where **n** is the vector normal to the boundary.

In order to smoothen the integrated effect, a linear weighting function is used.

$$\varepsilon_{nlp} = m\varepsilon_v^{pl} + (1 - m)\bar{\gamma} \tag{39}$$

where ε_{nlp} is the plastic strain measure incorporating non-local plastic strain (adimensional), and m is a linear weighing parameter (adimensional).

Integrating equation (28), the consolidation pressure at saturation, p_c, can be calculated as a function of the plastic strain measure, ε_{nlp},

$$p_c = p_{c0} e^{\left(-\frac{\varepsilon_{nlp}}{\lambda_{i0} - \kappa_{i0}}\right)} \tag{40}$$

2.3. Constitutive Relations for the Hydraulic Behaviour

This paper adopts the following constitutive relations for the hydraulic behaviour presented in Dagher et al. [4, 74]:

- van Genuchten equation for the SWCC [4]
- Huang et al. [52] equation depicting the relationship between the Air-Entry Value (AEV) and void ratio
- Darcy's Law for two-phase flow
- Equation for the effective diffusivity for gas dissolved in water through porous media, utilizing the Millington and Quirk model to define the tortuosity as a function of the degree of saturation, S_w and the porosity, n, [57]
- Pall and Moshenin et al. [56] modification to the Kozeny-Carman equation [54] for the relationship between the intrinsic permeability of water and the porosity of the soil
- Mualem's model for the relative permeabilities of gas and water [1]
- Klinkenberg Effect [69]

2.3.1. Intrinsic permeability of gas, the Klinkenberg Effect "Slip Flow"

As with the author's previous work [74] this paper incorporates the use of the Klinkenberg effect to represent a value of the intrinsic permeability of gas which is different from that of water. In this study, the intrinsic permeability tensor is assumed to be isotropic. Therefore, off-diagonal components are nil and diagonal components are equal to a value k,

$$k_{ij} = \delta_{ij} k \tag{41}$$

For expansive clays, which have small particles, Pall and Moshenin [56], proposed the following equation which is based on a volume-surface mea diameter and changing porosity to account for non-uniformity of the soil particles. This equation was applied to the author's previous model [4].

$$k_w = \frac{D_{vs}^2}{180} \frac{n^3}{(1 - n)^2} \tag{42}$$

where k_w is the intrinsic permeability of water (m^2) and
D_{vs} is the volume-surface mean diameter (m)
The porosity is calculated by,

$$n = n_0 + \varepsilon_{vol} \tag{43}$$

where, n_0 is the initial porosity of the porous medium (m^3 voids · m^{-3} total)

As the intrinsic permeability is not a property of the porefluid but rather a property of the geometry of the porous medium (i.e., porosity, pore shape, and pore size distribution), it seems reasonable to assume

that the permeability of porewater and poregas in the same soil specimen would be the same. However, a number of studies have shown that the intrinsic permeability of gas is often higher than that of water and may be related to the poregas pressure [66, 67, 68]. The Klinkenberg effect, also described as "slip flow", has been used to conceptualize this phenomenon, whereby slip occurs between the gas molecules and the contact with the solid particles, resulting in an increase in the intrinsic permeability of gas as poregas pressure decreases [69].

Equations (44) and (45) provide the relationship between the intrinsic permeability value of water and the intrinsic permeability value of gas a function of pressure.

$$k_g = k_w\left(1 + \frac{b_{ke}}{p_g}\right) \tag{44}$$

$$b_{ke} = \frac{c_{ke}\kappa_B T}{\pi\sqrt{2}r^3} \tag{45}$$

where k_g is the intrinsic permeability value of gas (m^2)
b_{ke} is the Klinkenberg slip factor (Pa)
c_{ke} is a constant (adimensional)
κ_B is Boltzmann's constant ($J\ K^{-1}$)
T is the temperature (K)
r is the pore radius (m)

2.4. Constitutive Relations for Damage

This study considers the use of two separate models for damage described below.

2.4.1. ED Model - Damage Model

Damage applied in the ED model has been introduced based on that developed by Tang et al. [58] and adopted by Fall et al. [35], whereby an element under tension or compression will experience damage, D ($0 < D < 1$), when the stress of the element satisfies the strength criterion, and the element begins to fail. Failure results in a decrease in the elastic modulus and an increase in the intrinsic permeability, as expressed in this paper by equations (46) and (47), respectively,

$$E_D = E_{UD}(1 - D^c) \tag{46}$$

where D is the damage (unitless)
E_{UD} is the Young's modulus before damage (Pa)
E_D is the Young's modulus after damage (Pa)

$$k_w = k_{UD} + k_D \tag{47}$$

where k_w is the water permeability at any given time (m^2)
k_{UD} is the permeability before damage (m^2) and is expressed by equation (42)
k_D is the increase in permeability as a result of damage (m^2) and can be expressed by equation (48)

$$k_D = D^c(k_{max} - k_{UD}) \tag{48}$$

where k_{max} (m^2) is the maximum permeability obtained when $D = 1$
c is a smoothing coefficient (unitless) and may be calibrated anywhere from 2 to 20 depending on the mesh size and the rate of increase in damage
k_{max} and c, are determined through model calibration.
The damage component consists of tensile damage and compressive damage components where,

$$D_{ED} = D_t + D_c \tag{49}$$

where D_{ED} is the total damage (adimensional)

D_t is the tensile damage (adimensional)

D_c is the compressive damage (adimensional)

Tensile damage, D_t, occurs when the absolute value of the first principal strain exceeds the absolute value of the strain at the material tensile strength, while compressive damage, D_c, occurs when the absolute value of the third principal strain exceeds the absolute value of the strain at the material compressive strength. The criterion for D_t in multi-axial tension is expressed by equation (50), while the criterion for D_c in multi-axial compression is expressed by equation (51):

$$D_t = \begin{cases} 0 & \varepsilon \le \varepsilon_{t0} \\ 1 - \dfrac{f_{tr}}{E_0 \varepsilon} & \varepsilon_{t0} \le \varepsilon \le \varepsilon_{tu} \\ 1 & \varepsilon \ge \varepsilon_{tu} \end{cases} \tag{50}$$

$$D_c = \begin{cases} 0 & \varepsilon_{c0} \le \varepsilon \\ 1 - \dfrac{f_{cr}}{E_0 \varepsilon} & \varepsilon \le \varepsilon_{c0} \end{cases} \tag{51}$$

where ε is the strain (unitless)

ε_{tu} is the tensile strain corresponding to a complete material failure

ε_{t0} is the tensile strain corresponding to the point of tensile strength

ε_{c0} is the compressive strain corresponding to the compressive strength

f_{tr} is the residual tensile strength (Pa)

f_{cr} is the residual compressive strength (Pa)

Note for equation (50) and (51) the sign convention for both stress and strain is positive for tension and negative for compression.

2.4.2. Damage Model for Plastic Models

Damage in the plastic models is assumed to be a function of the effective plastic strain rate, ε_{epe}, and is expressed by equations (52),

$$D_{pl} = 1 - e^{(-b'\varepsilon_{epe})^{c'}} \tag{52}$$

where D_{pl} is the total damage applied in the plastic (EPD/NLPD) models (adimensional)

b' is an empirical coefficient (adminesional)

c' is an empirical coefficient (adminesional)

The damage effect on the bulk modulus is described by the following equation.

$$K_D = K_{UD}(1 - D^c) \tag{53}$$

K_{UD} is the Bulk modulus before damage (Pa)

K_D is the Bulk modulus after damage (Pa)

It's effect on intrinsic permeability is the same as that described by equations (47) and (48).

2.5. Governing Equations

2.5.1. Conservation of momentum (quasi-static equilibrium)

The quasi-static equilibrium equation in tensor notation can be written as:

$$\frac{\partial \sigma_{ij}}{\partial x_j} + F_{v,i} = 0 \tag{54}$$

where, σ_{ij} is the total stress tensor (Pa)
$F_{v,i}$ is the volumetric body force tensor (kg m^{-2} s^{-2})
$\frac{\partial \sigma_{ij}}{\partial x_j}$ represents the change in normal and shear stresses across the soil element (kg m^{-2} s^{-2})

Linear poro-elastic swelling soil material

For a linear poro-elastic swelling soil material (applied in the ED model), the governing equation for the conservation of momentum can be expressed by equation (55),

$$G\frac{\partial^2 u_i}{\partial x_j \partial x_j} + (G+\lambda)\frac{\partial^2 u_j}{\partial x_j \partial x_i} - K\beta_{sw}\frac{\partial s}{\partial x_i} + \alpha_B(1-\chi)\frac{\partial p_g}{\partial x_i} + \chi\frac{\partial p_w}{\partial x_i} + F_{v,i} = 0 \tag{55}$$

where G is the shear modulus (Pa)
λ is the Lamé constant (Pa)

Non-linear poro-elastoplastic swelling soil material

For a non-linear poro-elastoplastic swelling soil material (applied in the EPD and NLPD models), the governing equation for the conservation of momentum can be expressed by equation (56),

$$\frac{1}{2}C_{ijkl}^{el,pl}\left(\frac{\partial^2 u_i}{\partial x_j \partial x_j} + \frac{\partial u_j}{\partial x_i \partial x_j}\right) - K\beta_{sw}\frac{\partial s}{\partial x_i} + \alpha_B(1-\chi)\frac{\partial p_g}{\partial x_i} + \chi\frac{\partial p_w}{\partial x_i} + F_{v,i} = 0 \tag{56}$$

2.5.2. Conservation of water mass

The governing equation for the conservation of water mass can be expressed by equation (57),

$$\frac{\partial}{\partial x_i}\left(\rho_w \frac{k_{ij}k_{r,w}}{\mu_w}\left(\frac{\partial p_w}{\partial x_j} + \rho_w g_j\right)\right) = -\frac{\partial(\rho_w n S_w)}{\partial t} \tag{57}$$

and solving the right-hand side, this simplifies to equation (58),

$$\frac{\partial}{\partial x_i}\left(\rho_w \frac{k_{ij}k_{r,w}}{\mu_w}\left(\frac{\partial p_w}{\partial x_j} + \rho_w g_j\right)\right) = -\rho_w\left[n\left(\frac{dS_w}{ds}\right)\frac{\partial s}{\partial t} + n\frac{S_w}{K_w}\frac{\partial p_w}{\partial t} + S_w\frac{\partial}{\partial t}\left(\frac{\partial u_k}{\partial x_k}\right)\right] \tag{58}$$

where ρ_w density of water phase (kg m^{-3})
p_w is the porewater pressure (Pa)
k_{ij} intrinsic permeability tensor of the porous medium (m^2)
$k_{r,w}$ relative permeability of the water phase (adimensional)
μ_w dynamic viscosity of the water phase (Pa s or kg m^{-1} s^{-1})
g is the acceleration due to gravity (m s^{-2})
n porosity (m^3 voids · m^{-3} total)
S_w is the degree of saturation of water (adimensional)
s is the matric suction $(p_g - p_w)$ (Pa)
K_w is the bulk modulus of the water phase (Pa s or kg m^{-1} s^{-1})
$\frac{\partial u_k}{\partial x_k} = \varepsilon_{vol}$ is the volumetric strain (adimensional)
u is the displacement (m)

t is time (s)

Note that in this study, the permeability is assumed to be isotropic, therefore $k_{ij} = k$, however we keep the tensorial notation in the governing equation for the sake of generalization.

2.5.3. Conservation of gas mass

The governing equation for the conservation of gas mass can be expressed by equation (59),

$$\frac{\partial\left(\rho_g\left(\frac{k_{ij}k_{r,g}}{\mu_g}\left(\frac{\partial p_g}{\partial x_j}+\rho_g g\right)+H\frac{k_{ij}k_{r,w}}{\mu_w}\left(\frac{\partial p_w}{\partial x_j}+\rho_w g\right)\right)\right)}{\partial x_i}+\frac{\partial}{\partial x_i}\left(-D_e\frac{\partial}{\partial x_k}\left(\rho_g n(HS_w)\right)\right) = -\frac{\partial\left(\rho_g n(1-S_w+HS_w)\right)}{\partial t} \quad (59)$$

and solving the right-hand side, this simplifies to equation (60),

$$\frac{\partial\left(\rho_g\left(\frac{k_{ij}k_{r,g}}{\mu_g}\left(\frac{\partial p_g}{\partial x_j}+\rho_g g\right)+H\frac{k_{ij}k_{r,w}}{\mu_w}\left(\frac{\partial p_w}{\partial x_j}+\rho_w g\right)\right)\right)}{\partial x_i}+\frac{\partial}{\partial x_i}\left(-D_e\frac{\partial}{\partial x_k}\left(\rho_g n(HS_w)\right)\right) = -\rho_g\left[n(H-1)\left(\frac{dS_w}{ds}\right)\frac{\partial s}{\partial t}+\frac{n(1-S_w+HS_w)}{K_g}\frac{\partial p_g}{\partial t} + (1-S_w+HS_w)\frac{\partial}{\partial t}\left(\frac{\partial u_k}{\partial x_k}\right)\right] \quad (60)$$

where ρ_g density of the gas phase (kg m^{-3})
p_g is the poregas pressure (Pa)
$k_{r,g}$ relative permeability of the gas phase (adimentional)
μ_g dynamic viscosity of the gas phase (Pa s or kg m^{-1} s^{-1})
H is Henry's coefficient (kg species A m^{-3} in aqueous phase kg^{-1} species A m^3 in gas phase)
D_e is the effective diffusivity of gas dissolved in water through porous media (m^2 s^{-1})
K_g is the bulk modulus of the gas phase (Pa)

It should be noted that equation (60) does not require the assumption that the gas behaves as an ideal gas. In the derivation of the expression of gas density and bulk modulus one might need to invoke the ideal gas law or other laws that more accurately predict the gas density and compressibility at different pressures and thermal conditions.

3. Numerical Model

3.1. Overview of the Numerical Models

The ED, EPD, and NLPD models described above were each applied to simulate two flow cases. The two flow cases were based on two laboratory experiments conducted by the British Geological Survey (BGS) to assess i) one-dimensional (1D) flow and ii) three-dimensional (3D) spherical flow through a saturated bentonite sample under constant volume boundary stress conditions [59, 62].

For each flow case, a 3D time-dependent (i.e., transient) hydro-mechanical (HM) coupled multiphysics numerical model was developed. The models simulate the simultaneous migration of gas and liquid (two-phase flow) in porous media, which are coupled to the mechanical behaviour of the solid matrix using the finite element method (FEM). The commercially available code COMSOL Multiphysics® (COMSOL®) was used to numerically solve the governing equations of the model. The results of the numerical models were

validated against the experimental results [59, 62]. Additionally, for each flow case, the results obtained using each of the models were compared.

3.2. Material Properties

Material properties for the solid bentonite MX-80 soil matrix, helium gas and water are provided in **Table 1** and were adopted from Dagher et al. [4]. As the same bentonite material was used for both the 1D and 3D spherical flow cases, the same material properties of bentonite were applied to both 1D and 3D spherical flow cases.

As the behavior of gases at high pressures and temperatures deviate from that of an ideal gas, a compressibility factor for helium, Z, was applied to the ideal gas law in the derivation of the expression for the density of gas, ρ_g, and bulk modulus, K_g, as described in Dagher et al. [4]. At the experimental temperature of 293.15 K and with maximum injection pressures reaching approximately 13 MPa, there is little deviation from an ideal gas [86]. In light of this, a factor of $Z = 1$ was applied and acceptable.

Table 1. Material properties of the solid soil matrix and gas and liquid phases

	Parameter Name	Symbol [units]	Value
Solid Soil Matrix (MX-80 Bentonite)	Young's modulus	E [MPa]	307
	Poisson's ratio	ν [-]	0.4
	Porosity	n [-]	0.44
	Intrinsic permeability	k_{ij_w} [m²]	3.4×10^{-21}
	Dry density	ρ_d [kg m^{-3}]	1560
	Saturated degree of saturation	$S_{w_{sat}}$ [-]	1
	Residual degree of Saturation	S_{w_r} [-]	0.05
	Bulk Modulus of bentonite	K_b [Pa]	5.1E+08
	Volume-surface mean diameter	D_{vs} [m]	1.50E-09
	Pore radius	r [m]	1.50E-08
	Tortuosity [4] [57]	τ [-]	$n^{\frac{1}{3}}S_w^{\frac{7}{3}}$
Gas (Helium)	Density of helium	ρ_g[kg m^{-3}]	$p_g\frac{M_{He_1}}{ZRT}$
	Compressibility factor for helium	Z [-]	1^2
	Dynamic Viscosity of helium @ 293.15 K	μ_g [Pa s]	2.0E-05
	Bulk Modulus of helium	K_g [Pa]	p_g
	Henry's Coefficient for dissolution of helium in water	H	0.0091
	Diffusivity of helium in water	D_f [m² s^{-1}]	6.29E-9
	Diameter of helium gas particle	d_{he} [m]	1.0E-10
Liquid (Water)	Density of water	ρ_w [kg m^{-3}]	2.2E+09
	Dynamic Viscosity @ 293.15 K	μ_w [Pa s]	0.001

	Bulk Modulus of water	K_w [Pa]	2.2E+09

[1]to account for the non-ideal nature of gases at high pressures and lower temperatures, a compressibility factor has been considered for the density of helium.

[2]A compressibility factor of 1 has been selected for helium as it is reasonable to assume it behaves as close to an ideal gas below pressures of 13 [MPa] at 293.15 K [86].

3.3. Validation Study 1: 1D Flow Case

3.3.1. Description of the Experiment

For the 1D flow case, helium gas was injected at one end of a confined cylindrical sample of near-saturated bentonite for a period of 120 days, and moves primarily along the x-axis. The other side was left at a constant water backpressure throughout the duration of the experiment [40].

Three key phases of the experiment include, (i) the hydration phase (t = 7.3 days to 39 days), where the sample was left to saturate, (ii) the gas injection phase (t = 39 days to 71 days), where gas was continuously injected into the system resulting in increasing gas pressures, and (iii) gas shut-off (t = 71 days), where the injection pump was stopped and gas pressures were allowed to dissipate naturally (refer to **Figure 4**). The experiment was conducted under isothermal conditions at a temperature of 293.15 K.

During the experiment, a number of parameters were measured including the gas inflow and outflow, the porefluid pressure at defined porefluid arrays, and the total radial stresses at radial load cell arrays. The cylindrical specimen of MX-80 bentonite had a diameter of 60 mm and a length of 120 mm. **Table 2** provides the location of the monitoring sensors within the specimen.

Table 2. Location of the porefluid arrays in the experimental setup and in the numerical model

Sensor name	Measurement Type	Axial distance from front-face (mm)
Injection load cell	Total stress	0
Radial load cell 1	Total stress	15.2
Radial load cell 2	Total stress	60
Radial load cell 3	Total stress	104.8
Backpressure load cell	Total stress	120
Radial porewater array 1	Porefluid pressure	38.6
Radial porewater array 2	Porefluid pressure	60
Radial porewater array 3	Porefluid pressure	81.4
Central filter (Middle)	Porefluid pressure	60

The BGS provided the experimental data that was used in the model validation [40]. For the numerical models, the 3D geometry and meshing are presented in **Figure 2**.

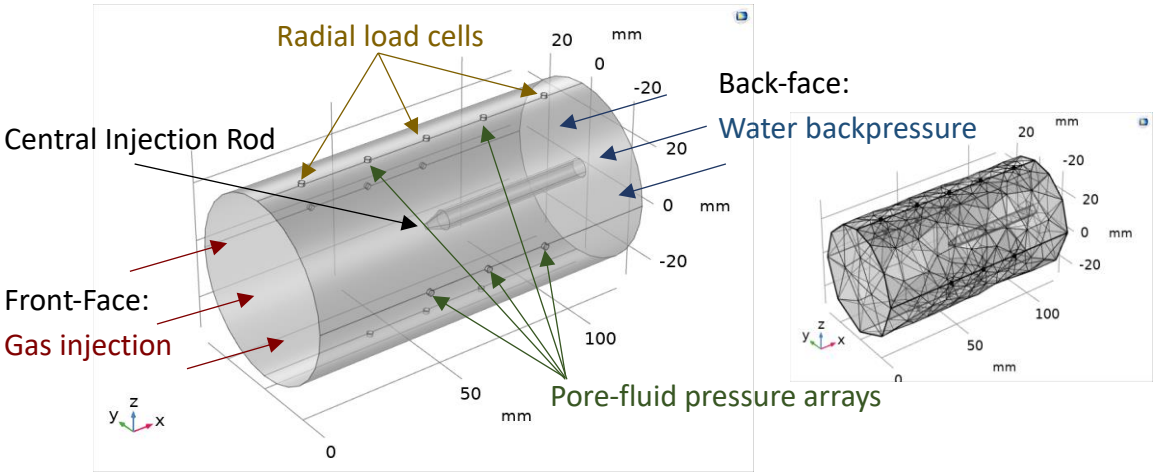

Figure 2. 1D Flow Case – 3D Geometry and Meshing

3.3.2. Initial Value Conditions

The initial conditions at t = 0 days across the domain are provided in **Table 3**, and are based on experimental data provided by BGS [40]. It should be noted that the bentonite sample was not fully saturated upon the start of the experiment but underwent a hydration phase which began on t = 7.3 days and ended on t = 39 days. Thereby an initial degree of saturation, $S_{w,inital}$, measured at approximately 0.96 was used as the initial condition. This is important as the numerical model assumes a continuous gas-phase throughout the specimen and does not account for entrapment of gas within the pore space.

Table 3. 1D Flow Case - Initial Value Conditions

Parameter Name	Parameter	Initial Value Condition
Initial poregas pressure	$p_{g_{initial}}$	1.01E+05 Pa
Initial degree of saturation	$S_{w_{initial}}$	0.96
Initial suction (from SWCC)	$s_{initial}$	5.0E+06 Pa
Initial porewater pressure	$p_{w_{initial}}$	-4.89E+06 Pa
Initial displacement field	u_i	0 m
Initial stress	$\sigma_{0_{xx}} = \sigma_{0_{yy}} = \sigma_{0_{zz}}$	-4.5E+05 Pa
Initial gas concentration in porewater @STP	C_{g,H_2O}	0.073 mol m-3

3.3.3. Boundary Conditions

The hydraulic and mechanical boundary conditions (BC) for gas transport, water transport, and momentum conservation are summarized in **Table 4**.

Table 4. 1D Flow Case - Boundary Conditions

Boundary	Gas Conservation BCs	Water Conservation BCs	Momentum Conservation BCs
Front-Face	Dirichlet BC: $p_g = p_{g,inj}(t)$[1]	No flow Neumann BC: $\frac{\partial p_w}{\partial x_i} = 0$	Roller constraint[3]
Back-Face	Dirichlet BC: $p_g = p_{w,bp}(t)$[1,2]	Dirichlet BC: $p_w = p_{w,bp}(t)$[1]	
Radial Pore-fluid Arrays			
Load Cell Arrays	No flow Neumann BC:	No flow Neumann BC:	
All Other Boundaries			

Central Injection Rod	$\frac{\partial p_g}{\partial x_i} = 0$	$\frac{\partial p_w}{\partial x_i} = 0$

[1]gas injection pressure and water backpressure BCs were imported from measured data plotted in **Figure 3.**

[2]gas pressure set at water backpressure to ensure zero suction at these boundaries, as they are maintained under saturated conditions.

[3]boundary is free to move in tangential direction, but fixed in normal direction, simulating a constant volume condition.

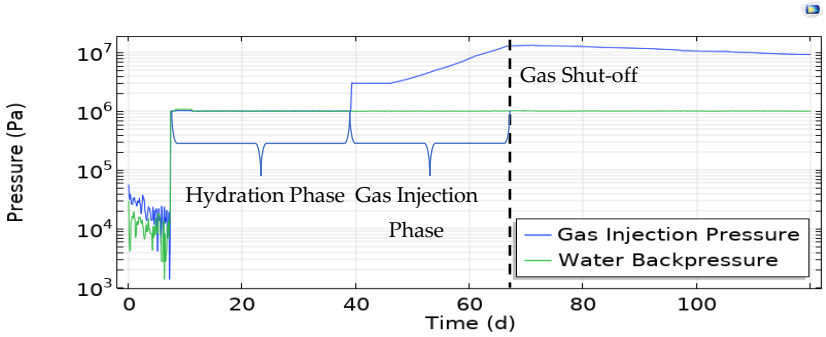

Figure 3. Dirichlet BCs for the gas injection pressure and water backpressures from data provided by BGS [40]

For the concentration of gas in porewater, C_{g,H_2O}, Dirichlet BCs were applied to the front-face, back-face and radial porefluid arrays as a function of the poregas pressure and based on the Ideal Gas Law with consideration of a compressibility factor, as follows:

$$\rho_g = p_g \frac{M}{ZRT} \tag{32}$$

Assuming instantaneous dissolution, the concentration of gas in the porewater can be calculated by multiplying equation (32) by Henry's coefficient, H, and the portion of water in a unit cell, nS_w

$$C_{g,H_2O} = \rho_g H(nS_w) \tag{33}$$

3.4. Validation Study 2: 3D Spherical Flow Case

3.4.1. Description of the Experiment

For the 3D spherical flow case, helium gas was injected, through a central injection rod, into a confined cylindrical sample of near-saturated bentonite over a period of 100 days (day 735 to day 835 day). Each end of the sample was left at a constant water backpressure of 1 [MPa] for the duration of the experiment. Radial porefluid arrays located along the column were also maintained at this backpressure of 1 [MPa].

There are two main phases observed in the experiment. The first phase is the gas injection phase from 735 days to 772 days. During this period three rapid dips in the injection pressure are observed and can be linked to periods of rapid gas influx to the sample. At day 772 gas injection was shutoff and like the 1D Flow case, the gas pressure was left to dissipate naturally (refer to **Figure 5**). The experiment was conducted under isothermal conditions at a temperature of 293.15 K. During the experiment, a number of parameters where measured including the gas inflow at the central injection rod, gas outflow at the porefluid arrays, the total axial stresses at axial load cell arrays, and the total radial stresses at radial load cell arrays. As with the 1D flow case, the cylindrical specimen of MX-80 bentonite had a diameter of 60 mm and a length of 120 mm. The location of the monitoring sensors within the specimen are the same as those in **Table 2**.

The BGS provided the experimental data that was used in the model validation [41]. For the 3D spherical flow case the 3D geometry and meshing applied to the models are presented in **Figure 4**.

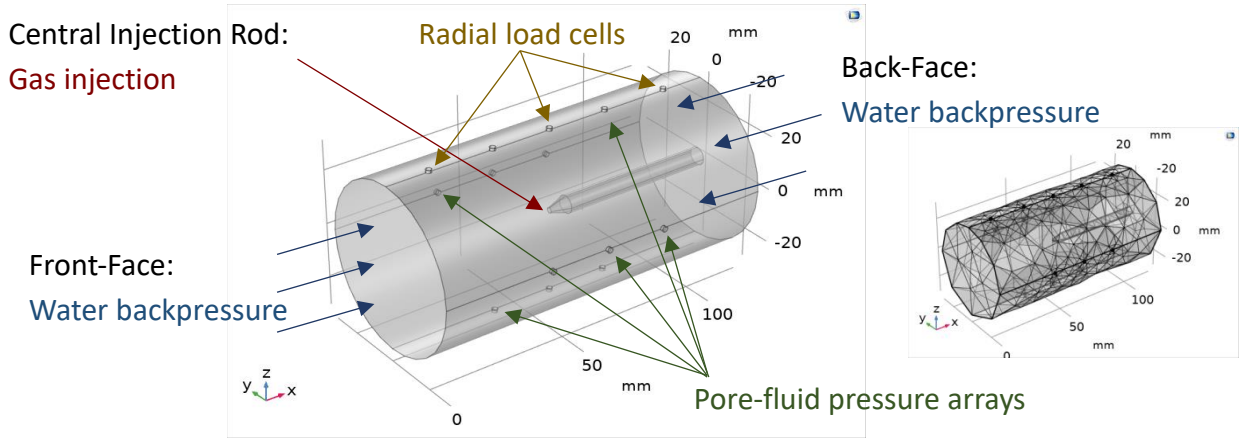

Figure 4. 3D Spherical Flow Case – 3D Geometry and Meshing

3.4.2. Initial Value Conditions

The initial conditions at t = 735 days across the domain are provided in **Table 5,** and are based on experimental data provided by BGS [41].

Table 5. 3D Spherical Flow Case - Initial Value Conditions

Parameter Name	Parameter	Initial Value Condition
Initial porewater pressure	$p_{w_{initial}}$	1.0E+06 Pa
Initial degree of saturation	$S_{w_{initial}}$	0.995
Initial suction (from SWCC)	$s_{initial}$	0 Pa (ED Model) 3.0E+06 Pa (Plastic Models)[1]
Initial poregas pressure	$p_{g_{initial}}$	1.0E+06 Pa
Initial displacement field	u_i	0 m
Initial stress	$\sigma_{0_{xx}} = \sigma_{0_{yy}} = \sigma_{0_{zz}}$	-6.5E+06 Pa (ED Model) -6.0E+05 Pa (Plastic Models)[1]
Initial gas concentration in porewater @STP	C_{g,H_2O}	$\rho_g H(nS_w)$

[1]For the EPD and NLPD Models, the initial stress has been adjusted so that it falls within the yield envelope.

3.4.3. Boundary Conditions

The hydraulic and mechanical boundary conditions (BC) for gas transport, water transport, and momentum conservation are summarized in **Table 6**.

Table 6: 3D Spherical Flow Case - Boundary Conditions

Boundary	Gas Conservation BCs	Water Conservation BCs	Momentum Conservation BCs
Central Injection Rod Face	Dirichlet BC: $p_g = p_{g,inj}(t)$[1]	No flow Neumann BC: $\frac{\partial p_w}{\partial x_i} = 0$	Roller constraint[3]
Front-Face	Dirichlet BC: $p_g = p_w = 1$ MPa[2]	Dirichlet BC: $p_w = 1$ MPa	
Back-Face			
Radial Pore-fluid Arrays			
Load Cell Arrays	No flow Neumann BC: $\frac{\partial p_g}{\partial x_i} = 0$	No flow Neumann BC: $\frac{\partial p_w}{\partial x_i} = 0$	
All Other Boundaries			

[1]gas injection pressure was imported from measured data plotted in **Figure 5.**

[2]gas pressure set at water backpressure to ensure zero suction at these boundaries, as they are maintained under saturated conditions.
[3]boundary is free to move in tangential direction, but fixed in normal direction, simulating a constant volume condition.

As with the methodology presented in the 1D flow case, for the concentration of gas in porewater, C_{g,H_2O}, BCs were applied to the central gas injection rod as a function of the gas injection pressure and to the front-face, back-face, and radial porefluid array boundaries as a function of the water backpressure.

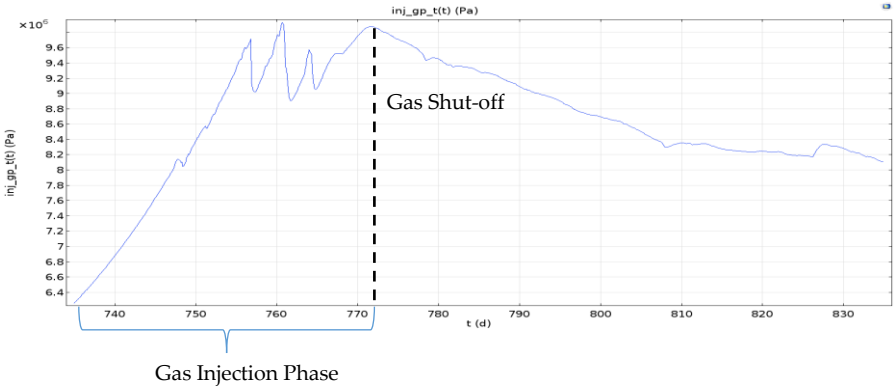

Figure 5. Dirichlet BC for the gas injection pressure of dissolved gas in porewater at the central injection rod

3.5. Modelling Approach and Calibration Parameters

In this study, the simulation of each model was performed in order to understand the contribution of the mechanical deformation and damage produced by each on flow behaviour. The results of each simulation were compared to the experimental results and the effect of each on flow behaviour analyzed [40] [41]. **Table 7** provides a list of the study scenarios along with values of key model parameters. It should be noted that these model parameters were selected based on calibrating the model to best match the experimental inflow. Additionally, calibration parameters specific to the ED model are provided in **Table 8**, while the calibration parameters specific to the EPD and NLPD models are provided in **Table 9**. Calibration parameters for the xBBM applied to both the EPD and NLPD models are provided in **Table 10**. As the same bentonite material was used for both the 1D and 3D spherical flow cases, the same calibrated values are applied to both flow cases. This helps to provide confidence in the general application of the model, and remove potential for curve-fitting which may skew the results.

It should be noted that these model parameters were selected based on calibrating the model to best match the experimental results while maintaining numerical stability and convergence. For the ED damage model, the strain and tensile/compressive material strength values are calibrated so that the modelled inflow represents the experimental inflow.

A number of model improvements from the author's previous work [23] have also been incorporated. These include a better calibrated AEV, a more reasonable coefficient of the Klinkenberg effect, use of a non-linear swelling strain, and more representative boundary conditions.

Table 7. Validation Study Scenarios

Scenario Number	Mechanical Model	Description	Initial Porosity Distribution (mean ± sd)	Coefficient of Klinkenberg Effect, c_{ke}	Initial AEV (Pa)
S1	ED Model	Enhanced Damage Model	0.44 ± 0.06	1E+05	8.0E+06
S2	EPD Model	Local Plastic Model with Damage	0.44	1E+04	8.0E+06
S3	NLPD Model	Non-Local Plastic Model with Damage	0.44	1E+04	8.0E+06

Table 8. ED Model specific calibration parameters

Calibrated Model	Parameter Name	Symbol [units]	Value
ED Damage Model	Maximum intrinsic permeability	k_{max} [m²]	5.0E-18
	Damage weighting parameter	ξ	2.5
	Damage smoothing coefficient	c [-]	2
	Compressive strength	f_c [MPa]	1[1]
	Residual compressive strength	f_{cr} [MPa]	0.09[2]
	Strain at compressive strength	ε_{c0}	0.0005
	Tensile strength	f_t [MPa]	-1[1]
	Residual tensile strength	f_{tr}[MPa]	-0.09[2]
	Strain at tensile strength	ε_{t0}	-0.0005

[1]The magnitude of compressive and tensile material strength were first estimated by experimental data provided in Man and Martino [43], then calibrated to the gas inflow.
[2]The residual tensile and compressive strengths of the material were set at a fraction of the absolute material strengths initially based on work by Tang et al. [39] then calibrated to the gas inflow.

Table 9. EPD and NLPD Model specific calibration parameters

Calibrated Model	Parameter Name	Symbol [units]	Value
EPD Damage Model	Maximum intrinsic permeability	k_{max} [m²]	1.0E-19
	Coefficient of Damage 1	b′	25
	Coefficient of Damage 2	c′	1
NLPD Damage Model	Maximum intrinsic permeability	k_{max} [m²]	5.0E-19
	Coefficient of Damage 1	b′	25
	Coefficient of Damage 2	c′	3
NLPD Model Non-local plasticity	Characteristic length	l_c^2 [m]	5E-4
	Weighting factor	m	0.3

Table 10. EPD and NLPD Model - Extended Barcelona Basic Model calibration parameters

Calibrated Model	Parameter Name	Symbol [units]	Value
Extended BBM	Consolidation pressure at saturation	p_{c0} [MPa]	2.0
	Reference pressure	p_{ref} [MPa]	7.5
	Reference void ratio	e_{ref}	0.79
	Compression Index at saturation	λ_{p0}	0.15
	Swelling Index at saturation	κ_{p0}	0.026[1]
	Parameter describing the change in κ_s with suction	α_κ [1/MPa]	0.0001
	Parameter defining the maximum soil stiffness	r_B	0.8
	Parameter controlling the rate of increase of soil stiffness with suction	β_B [1/MPa]	50
	Initial yield at suction	s_{y0} [MPa]	1
	Dimensionless smoothing parameter	b_B	0
	Parameter describing the increase in tensile strength with suction	k_s	0.1
	Angle of internal friction at saturation	ϕ[rad]	0.225

[1]calculated to match experimental Bulk Modulus of 510 MPa at p_{ref} and e_{ref}

Table 11 lists the fitting parameters for the van Genuchten-Mualem model SWCCs and relative permeability curve corresponding to the initial mean porosity of n = 0.44. Values for the van Genuchten SWCC fitting parameters were assessed from literature taking the calculated dry density of MX-80

bentonite [61, 39, 62, 37]. The van Genuchten equations for the SWCCs and Mualem model for relative permeability curves are provided in the authors' original paper [11].

Table 11. van Genuchten-Mualem SWCC and relative permeability function fitting parameters

Parameter	Value
SWCC fitting parameter, a' (1/m)	0.0005 [11]
SWCC fitting parameter, n'	2.04 [61]
SWCC fitting parameter, m'	0.51 [61]
Relative permeability function fitting parameter, L'	1 [11]

3.6. Implementation of Advanced Mechanisms for Two-Phase Flow

3.6.1. Introduction of Heterogeneity

Heterogeneity applied to Hydraulic Properties

Heterogeneity was introduced into the simulated sample for the ED model by spatially applying a random normal distribution to the initial porosity material property with a mean porosity set at the experimentally determined value of 0.44 and applying a standard deviation. For the ED model a standard deviation of 0.06 was applied to the initial porosity. This value of the standard deviation was set to promote a large range of initial porosities (heterogeneity) within the specimen, while maintaining numerical stability and convergence. The heterogeneity field is mesh dependent, as a unique value of porosity is given to each node, based on its spatial location which aligns with a randomly generated normal distribution table of porosities. There is no spatial correlation in heterogeneity intended with this approach. The initial porosity distribution within the bentonite sample is depicted in **Figure 6(a),** while **Figure 6(b)** provides the XZ-plane cross section of the initial porosity distribution.

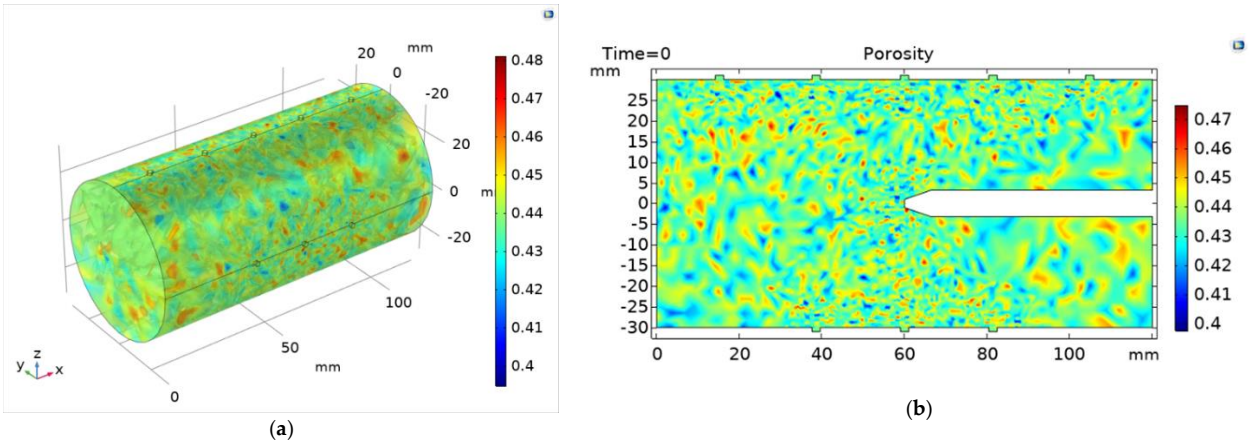

(**a**) (**b**)

Figure 6. Heterogeneity introduced through random normal distribution of initial porosity in the (a) 3D model and (b) XZ-plane cross section.

3.6.2. Introduction of a Material Defect

For the EPD and NLPD models, material defects were introduced at both the center of the point of injection and at the opposite facing end of the specimen in order to attempt to facilitate a preferential damage zone. The material defects were introduced by setting the initial consolidation pressure at saturation to a value of 1.5 MPa to test if preferential flow could be generated through these defects. **Figure**

7 provides the XZ-plane cross section of the sample depicting the location of the defects in initial consolidation pressure.

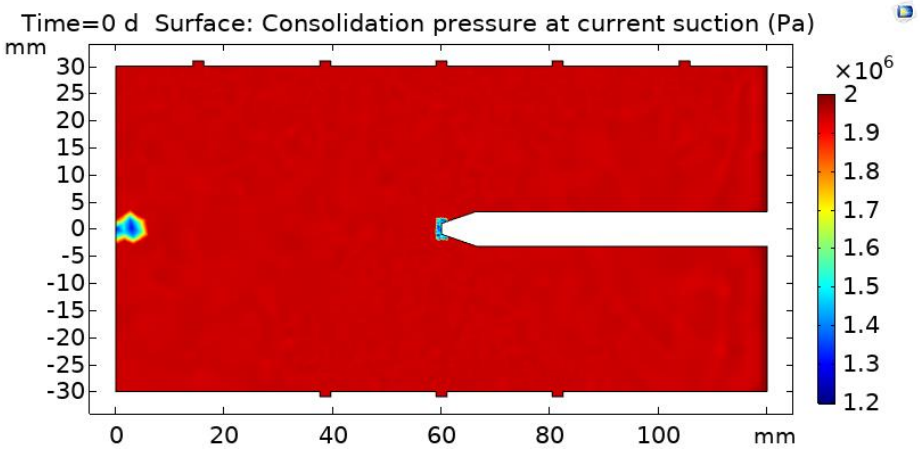

Figure 7. Cross-section of material showing defects in initial consolidation pressure.

3.6.3. Klinkenberg Effect - Intrinsic Permeability of Gas

A number of studies have attempted to empirically estimate the Klinkenberg slip factor [71] [72], and have proposed the following empirical equation for the slip factor as a function of the intrinsic permeability of water,

$$b_{ke} = 0.251 k_w^{-0.36} \tag{65}$$

Based on the experimental intrinsic permeability of water in this study, k_w (3.4E-21 m^2), **Figure 8** shows the relationship between poregas pressure and intrinsic permeability using a Klinkenberg slip factor based on equation (44) and equation (45) with a constant of, c = 1.0E+05 and c = 1.0E+04, as well as using equation (65) to empirically solve for the slip factor. As depicted by the figure, the intrinsic permeability of the gas increases significantly with a decrease in poregas pressure, and as poregas pressures increase the intrinsic permeability of the gas approaches that of water. In this study, a more realistic slip factor of c = 1.0E+05 was applied to the ED and EPD models, than in the author's previous work [74] in order to complement the increase in permeability due to damage and in order to provide the significant change in permeability needed to obtain complete breakthrough into the sample. A coefficient of the Klinkenberg effect of c = 1.0E+04 was applied to the NLPD model to ensure convergence.

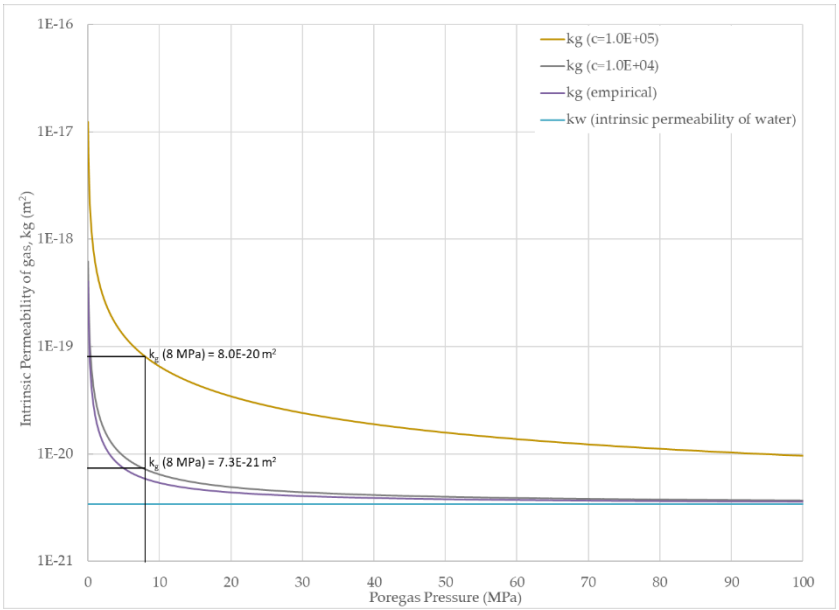

Figure 8. Klinkenberg Effect - Intrinsic permeability of gas as a function poregas pressure, k_g

3.6.4. Coefficient of a Swelling Stress

Figure 9 shows curves for the coefficient of a swelling strain as a function of suction, applied for a linear swelling strain and for three different mean effective stresses at our initial void ratio, e = 0.78, applied for a non-linear swelling strain, as per equation (11).

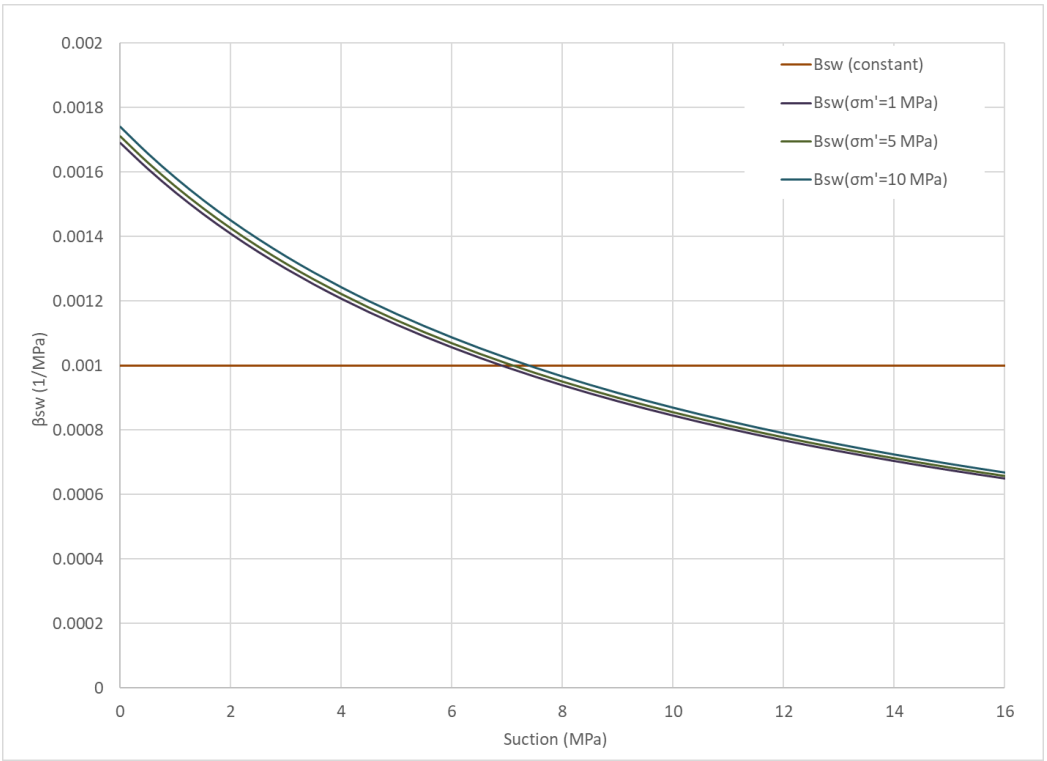

Figure 9. Swelling coefficient as a function of suction

It should be noted that the shape of the curve described by equation (11) is reliant on the selected calibration parameters. **Table 12** provides the calibration parameters for the linear and non-linear swelling strain. These values were initially informed by those obtained in studies by Nasir et al. [70] and Nguyen and Barnichon [75] for the linear and non-linear swelling strain, respectively. Calibration parameters for the reference pressure, $p_{ref,sw}$, and reference suction, $s_{ref,sw}$, were selected based on increasing the swelling potential, while maintaining numerical stability and convergence.

Table 12. Coefficient of swelling strain calibration parameters

Calibrated Model	Parameter Name	Symbol [units]	Value
Linear Swelling Strain	Swelling Coefficient	β_{sw}[1] [1/Pa]	1E-9
Non-linear Swelling Strain	Reference pressure	$p_{ref,sw}$ [MPa]	25
	Reference suction	$s_{ref,sw}$ [MPa]	10
	Fitting parameter	B[2]	0.03
	Fitting parameter	C[2]	-0.01

[1] adopted from [70]

[2] adopted from [75]

3.6.5. Damage Curve – Plastic Models

Figure 10 shows the damage curve as a function of the effective plastic strain, as per equation (52), for calibrated coefficients of damage applied in the EPD and NLPD models, respectively (see **Table 8**). It should be noted, that based on model calibration, the damage curve formed by the damage coefficients applied to the NLPD model (see **Table 8**) allows for increased damage at lower plastic strains than for the damage curve applied to the EPD model.

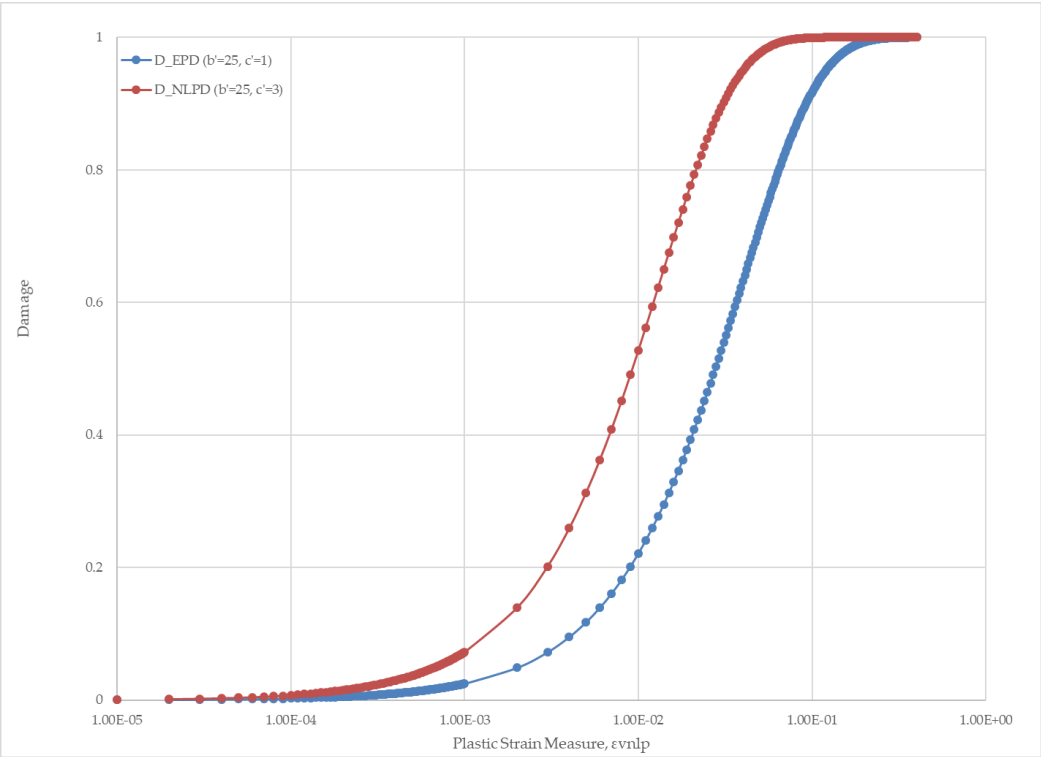

Figure 10. Damage as a function of plastic strain measure.

4. Results and Discussion

In this section, the following sign convention is used: i) strain components and volumetric deformations are positive for expansion and negative for contraction; and ii) stress components and pressures are positive for compression and negative for tension.

4.1. Validation Study 1: 1D Flow Case

The results of the 1D flow validation study are presented below. For each study scenario corresponding to a different mechanical model (i.e., ED, EPD, NLPD), the following results are discussed:

1. migration of poregas and extent of damage over time
2. gas inflow/outflow
3. gas storage in the system
4. evolution of total stresses over time
5. p-q stress path analysis

The experimental results provided for comparison were discussed in Daniels & Harrington [59] and in Dagher et al. [4] and are not discussed in detail in this paper.

4.1.1. Migration of poregas pressure and extent of damage

Poregas migration profiles over time for the central cross section (XZ-plane) of each study scenario are depicted in **Figure 11**, **Figure 12**, and **Figure 13**.

Poregas pressure results for the ED model is presented in **Figure 11**(**a**) with the damage presented in **Figure 11**(**b**). The results show that once the AEV is exceeded (day 68), there is gas breakthrough into the sample and migration through the sample. The distance travelled by the poregas front is facilitated by the propagation of damage. As the model was calibrated in order to match inflow curves, this leads to an

advective poregas front which travels approximately half-way through the sample and does not reach complete breakthrough.

It should be noted, that there is damage forming around the tip of the injection rod, and around the radial porefluid pressure and load cell arrays (see **Figure 2**), which do not correspond to the active poregas migration front. The formation of this damage is expected as the porefluid (mainly porewater) pre-existing within the sample is displaced (i.e., pushed forward) by the moving poregas front. This increases in porefluid pressure along the specimen, results in an increase in the total stresses and damage around the areas of protrusion and intrusions.

As identified previously by the authors [74], some gas fingers do form under the presence of heterogeneity and slip flow, however even with the introduction of damage, these distinct fingers do not remain and eventually seal, as indicated at day 68 days and day 75.

Of particular note is the presence of self-sealing behavior provided by the damage model. As gas is injected into the sample, at a given position along the poregas migration front, the poregas pressure will increase, resulting in an increase in both suction and the overall porefluid pressure as per equation (4). The porefluid pressure will continue to increase until the first and third principle strains exceed the strain at their tensile and compressive material strengths, respectively, leading to the onset of damage. Once damage is triggered, the corresponding decrease in elastic modulus and increase in permeability allows for further migration of the poregas, and a release in porefluid pressure at this point. This decrease in poregas pressure corresponds to a decrease in the local suction and an increase in the overall degree of water saturation, allowing for the material to swell and self-heal, while damage propagates forward along the migration front. This is facilitated in the model by the decrease in first and third principle strains to a point where damage no longer exists. As this model is purely elastic, the formation of this damage is a completely reversible process. In **Figure 11**(**b**) this self-sealing behavior is observed by a reduction in damage, and in areas where damage has completely dissipated.

In the case of the EPD model, **Figure 12**(**a**) and **Figure 12**(**b**) show the poregas pressure migration and damage evolution over time. The poregas migration front does not travel as far as that of the ED model, however as depicted in **Figure 12**(**b**), localized damage does form, increasing the mobility of poregas. There seems to be shear bands forming, creating channeling of flow. Unfortunately, it is not possible to accentuate further the jump in permeability associated with these shear bands, while maintaining numerical stability an convergence. This shear-banding may also be influenced by mesh size.

Figure 13(**a**) **and Figure 13**(**b**) shows the poregas pressure evolution and damage evolution for the NLPD model, where the change in consolidation pressure is a function of the non-local plastic strain measure, and damage is a function of the effective plastic strain. The results show increased gas flow within the system as observed by a farther poregas migration front when compared to the EPD model. This is likely due to the larger zone of influence in the plasticity model, which appears to have smoothed or spread out the areas of plastic deformation, and is evident by smoother damage zones depicted in **Figure 13**(**b**). Similar to the EPD model, discrete pathways, though smoother, are still visible, demonstrating evidence of channeling and preferential flow.

Figure 13(**b**) shows the damage evolution over time. In this case, the characteristic length, l_c, influences the size of the localized damaged zone. Once the AEV is reached the damage zone becomes more pronounced at the point of injection and damage propagates forward, but dissipates further away from the injection point. Unlike the ED model, it is evident that there is no self-healing behavior provided by the EPD and NLPD model. This is due to the use of the effective plastic strain in our damage model, and therefore damage is purely a function of irreversible deformation.

Figure 14 illustrates the evolution of the consolidation pressure over-time. As can be observed, there is a reduction in the consolidation pressure downstream of the side of injection prior to gas flow into the sample, characteristic of strain softening as a result of dilation of the clay. Once the AEV is reached, the consolidation pressure at the point of injection begins to increase with an increase suction, as the poregas

migrates through the specimen. This sheds light onto the dissipation of damage that was observed in **Figure 13**(**b**). As suction is increased, the yield stress increases, making it more difficult for plastic deformation and damage to propagate through the soil.

Regarding the introduction of a material defect (in consolidation pressure) at the point of injection and at the central injection rod, the authors anticipated that their inclusion would promote a preferential flow pathway between the two material defects. In **Figure 12**, this was observed to not be the case. The authors also ran these simulations without the inclusion of the material defects, and the presence of the material defects do not have a significant impact on the results.

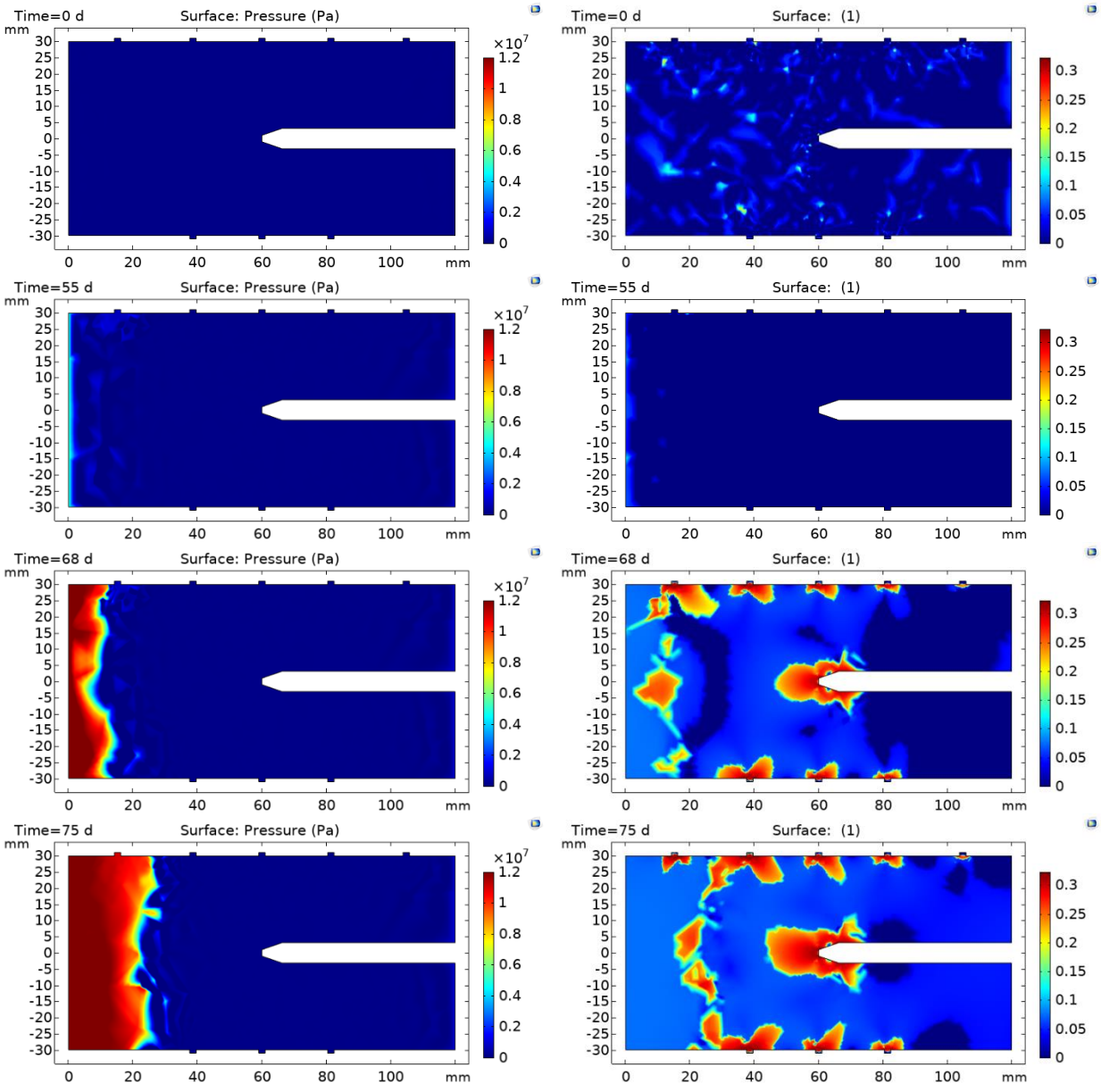

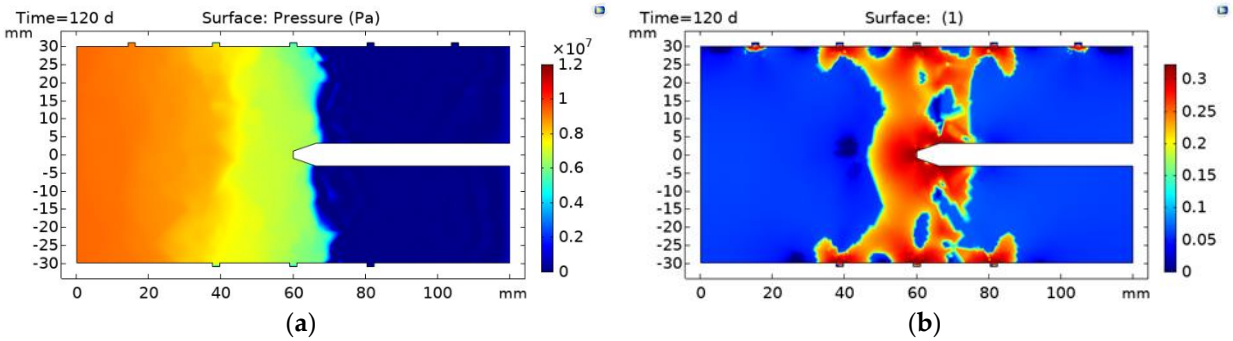

Figure 11. 1D Flow Case – ED model results for (**a**) poregas pressure and (**b**) damage at t=0, 55, 69, 75, and 120 days

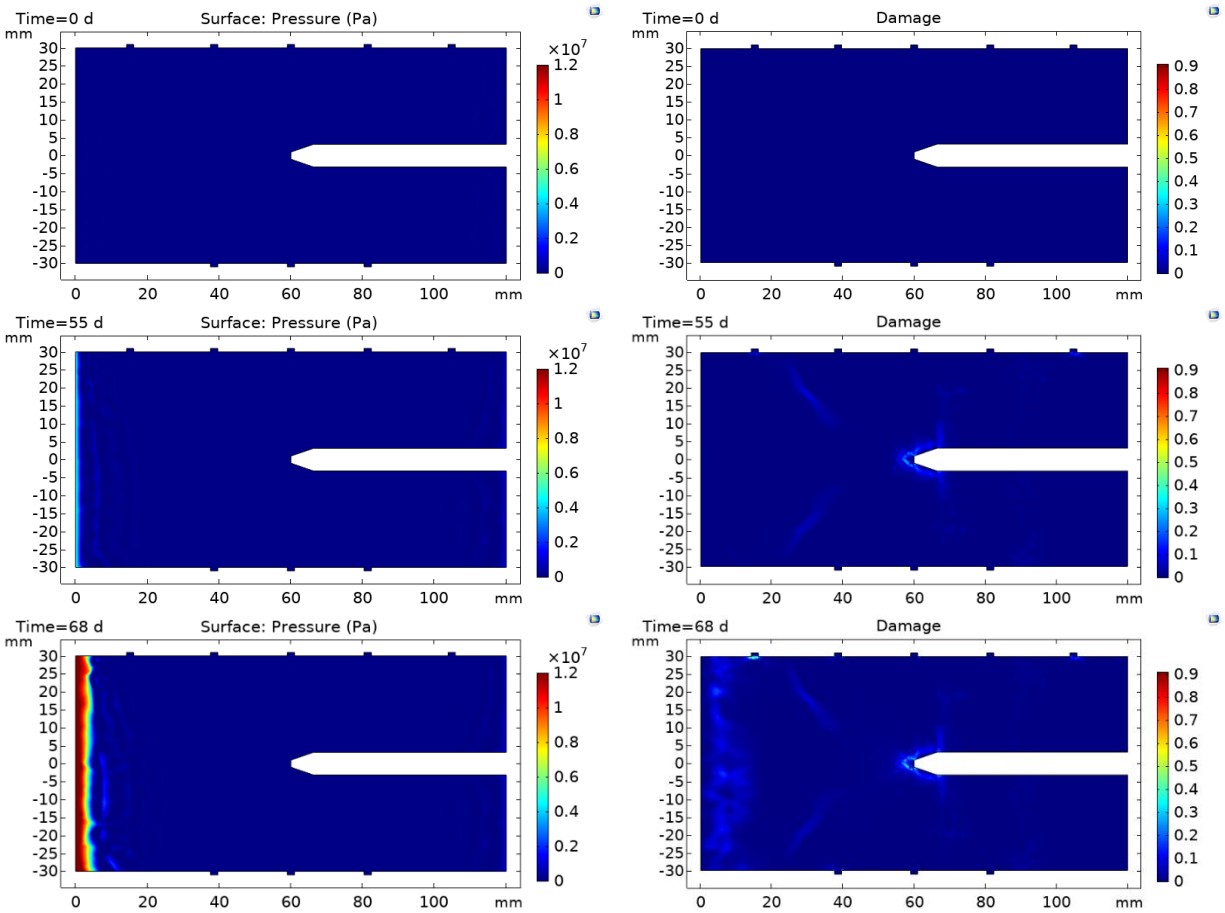

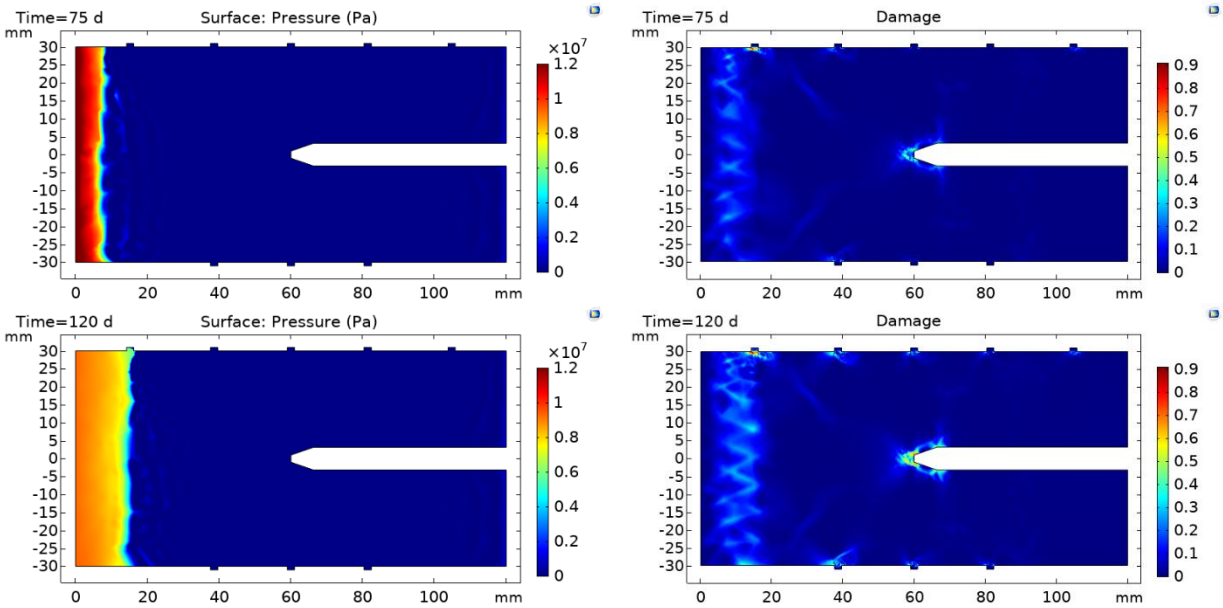

Figure 12. 1D Flow Case – EPD model results for poregas pressure at t=0, 55, 68, 75, and 120 days

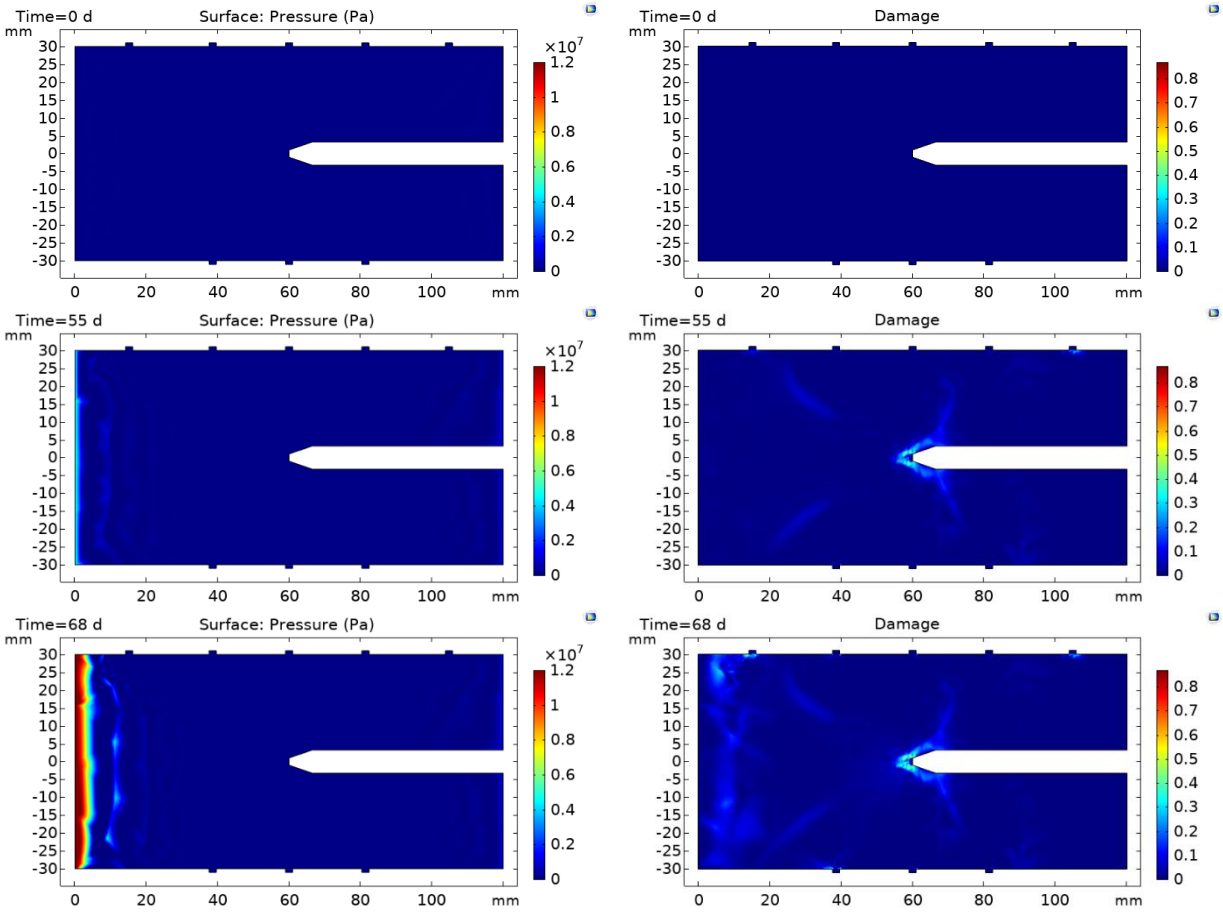

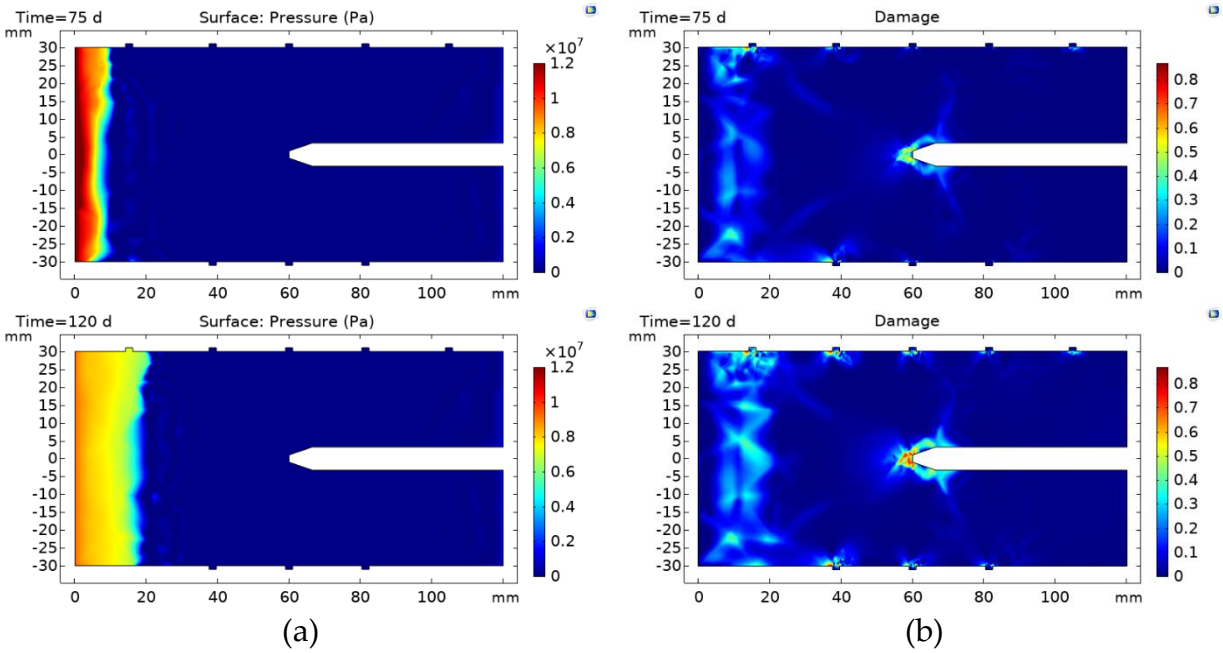

Figure 13. 1D Flow Case – NLPD model results for (**a**) poregas pressure and (**b**) damage at t=0, 55, 68, 75, and 120 days

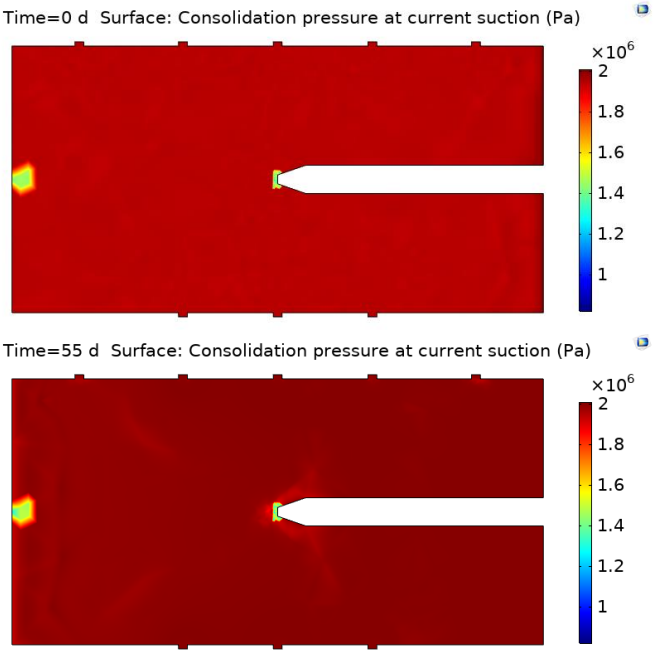

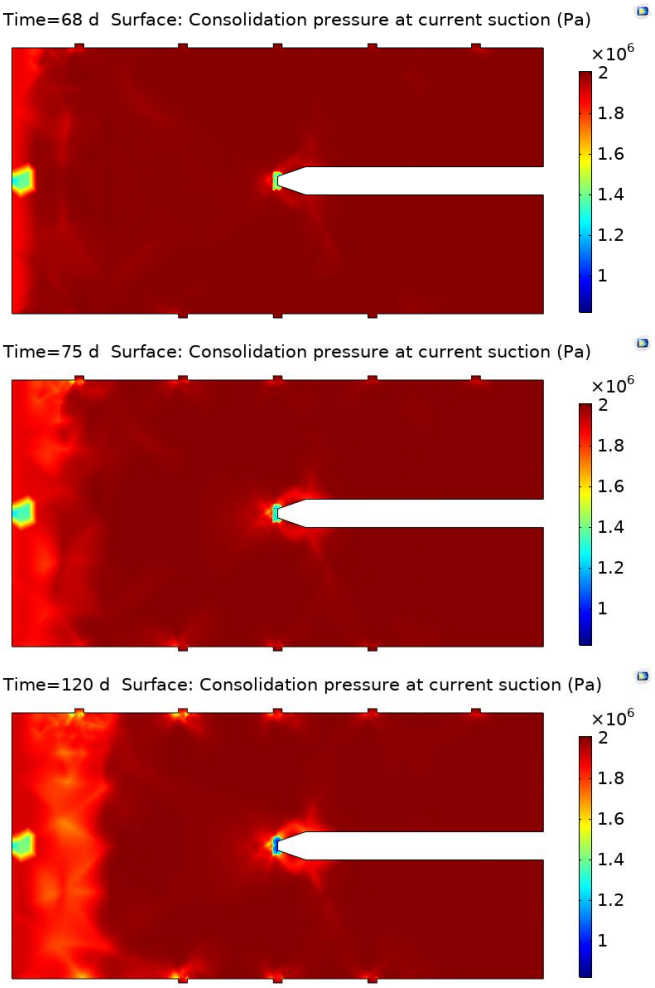

Figure 14. 1D Flow Case – NLPD model results for consolidation pressure at t=0, 55, 68, 75, and 120 days

4.1.2. Gas inflow and outflow

Gas inflow and outflow profiles over time for the experimental data and for each mechanical model assessed are depicted in **Figure 15**(**a**) and **Figure 15**(**b**), respectively.

As can be seen in **Figure 15**(**a**), the ED model is very well capable of predicting the gas inflow behavior, from the rapid inflow that occurs at around 63 days, to the sudden gas shut-off which occurs at 71 days. The timing of gas inflow is specifically related to the selected value of the principal strain at tensile failure ($\varepsilon_{t0} = 0.0006$) and the principal strain at compressive failure ($\varepsilon_{c0} = -0.0006$), which initiates the onset of damage. The large change in magnitude of gas inflow is entirely related to the magnitude of the first and third principle strains (unique to the ED model), and the calibrated value of the maximum permeability, k_{max}. Moreover, the ED model is also capable of reproducing the chaotic inflow behaviour observed experimentally. The observed "chaotic" peaks are associated with equation (50) and equation (51), and correspond to the point at which the first and third principle strains exceed the principal strain at tensile failure and the principal strain and compressive failure, respectively

However as depicted by **Figure 11**, damage simulated by the ED model does not propagate through the entire sample and as a result, complete gas breakthrough and advective gas outflow in the sample is not observed. Additional calibration may resolve this, however when there are sudden large changes in

permeability (i.e., several orders of magnitude) due to damage, the model fails to converge, and this has limited the use of damage for achieving complete breakthrough.

The inflow and outflow gas curves for the EPD model somewhat captures the shape and timing of inflow, but not the maximum inflow. Furthermore, complete gas breakthrough does not occur, and no outflow was measured.

Once non-local plasticity is introduced, gas inflows are much higher than that of the EPD model, and is due to the presence and coalescence of damage (see **Figure 13**). Again, the shape and timing of gas inflow are similar to the experimental results (with two inflow peaks being observed), although the gas inflow does not drop dramatically with gas shut-off. The model is also not able to achieve the peak inflow observed experimentally, and thus, no outflow is observed.

It is important to note that the calibrated maximum permeability, k_{max}, is much higher for the ED model than the EPD and NLPD models, and this is one significant contributor to the difference in the inflow and outflows achieved. For plastic models, the rapid increase in damage being concentrated in high damage zones, leads to numerical instability, which limits how high the maximum permeability can be set. As a result, the plasticity models do not achieve the same flow through the system as the ED model is capable of achieving. Ideally, if this numerical instability could be overcome, the plastic models would be capable of achieving enhanced flow through channeling, as damage is more concentrated in narrower zones than in the ED model.

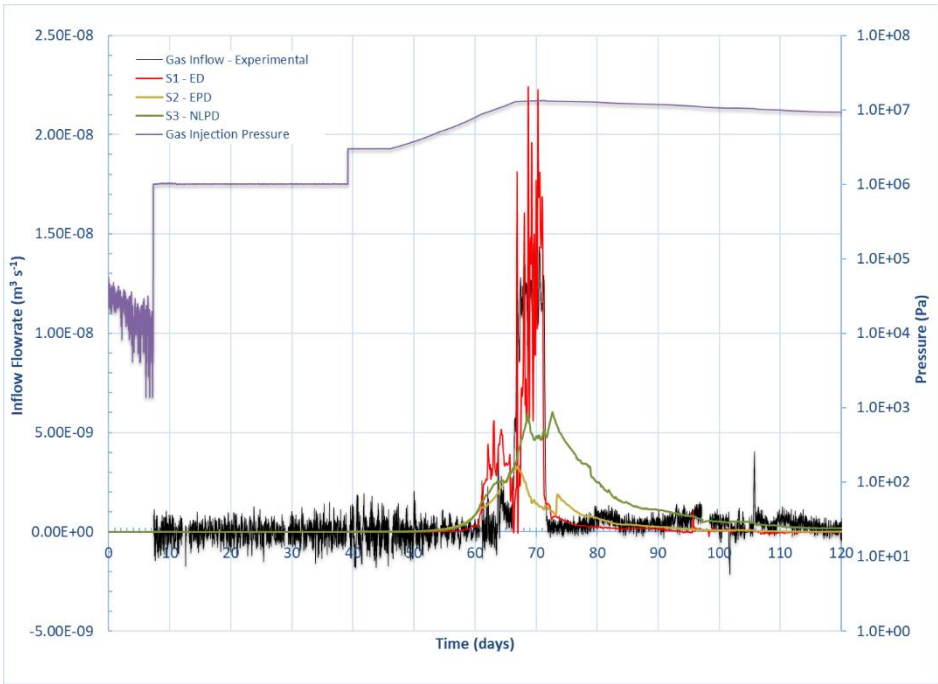

(**a**)

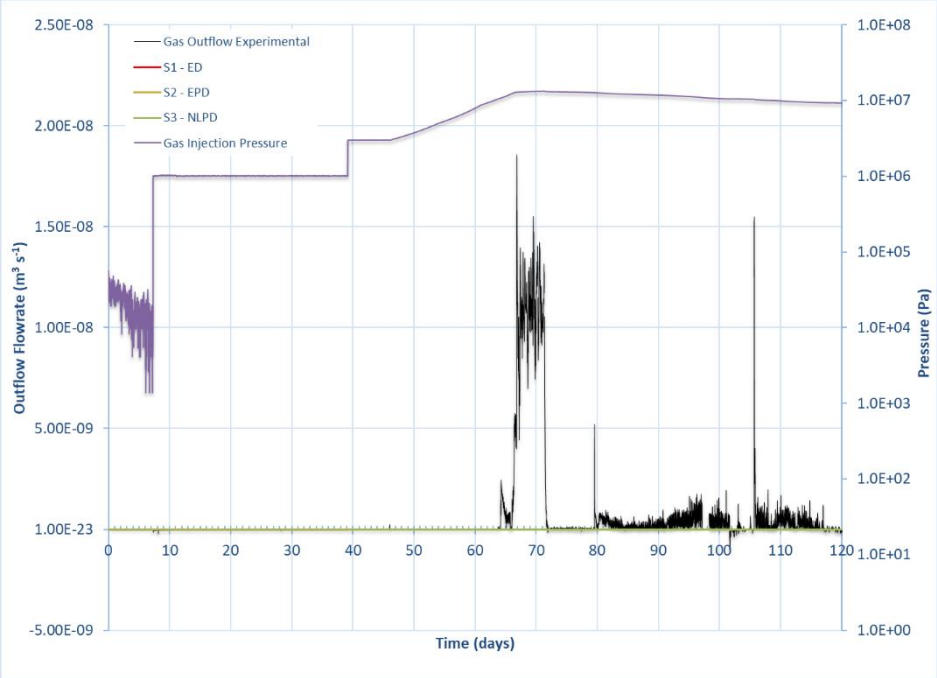

(**b**)

Figure 15. 1D Flow Case Results: (**a**) gas inflow and (**b**) gas outflow profiles over time

4.1.3. Gas storage in the system

An important part of this validation study is a comparison of the modelled results to the experimental volume of gas stored in the system over time. It is expected that dilatancy-controlled gas flow and the formation of preferential flow pathways would result in minimal gas storage within the system. This was eluded to by the experimental inflow and outflow observed in both the 1D and 3D spherical flow cases, whereby gas entering the system almost immediately exited the system [59, 62].

Figure 16. displays the volume of gas stored in the system over time, measured experimentally and for each model scenario. The experimental results show minimal gas storage within the soil specimen. All three model show significantly more gas stored in the sample, and this is a result of the plug flow behavior exhibited, whereby the simulated sample is being saturated with gas. For the ED model, although the gas inflow curves matched, the volume of gas stored in the sample is much higher than that observed in the experimental results, and is because there was little outflow observed by the model (no gas exited the system). For the EPD model, the results are closer to experimental, however this is to be expected as there was little inflow to the system to begin with and no outflow. This was similarly observed with the elastic model presented in the authors previous work [74]. The NLPD model provides slightly higher volume of gas stored, due to the increased flow into the system.

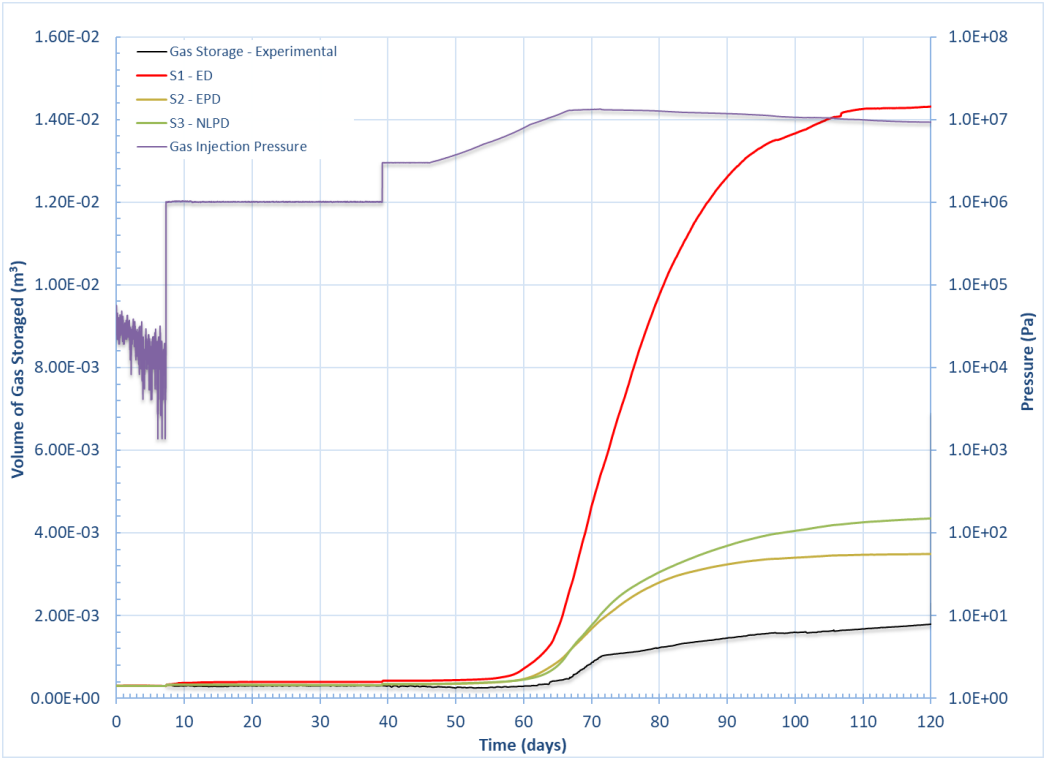

Figure 16. 1D Flow Case Results: Volume of gas stored

4.1.4. Evolution of total stresses

The results of the total stress evolution simulated by each of the models and measured experimentally at the injection load cell, radial load cells, and backpressure load cell, are presented in **Figure 17**, **Figure 18**, and **Figure 19** for the 1D flow case. Where the modelled inflow results provided by the ED model matched reasonably well with the experimental data, the total stress evolution does not, as depicted in **Figure 17**. There is some agreement with the shape and timing of the curves, particularly at load cells ILC and RLC1, but the magnitude of stresses is not realized. As discussed in the authors' previous works [11, 23], the reason the total stresses remain stable at the load cells located further down (i.e., RLC2, RLC3, and BLC), is likely due to the poregas migration front not reaching these load cell arrays. Without the increase in porefluid pressure provided by the increase in poregas pressure, there is little change in the total stress. Small oscillations are also present following gas inflow and are likely numerical.

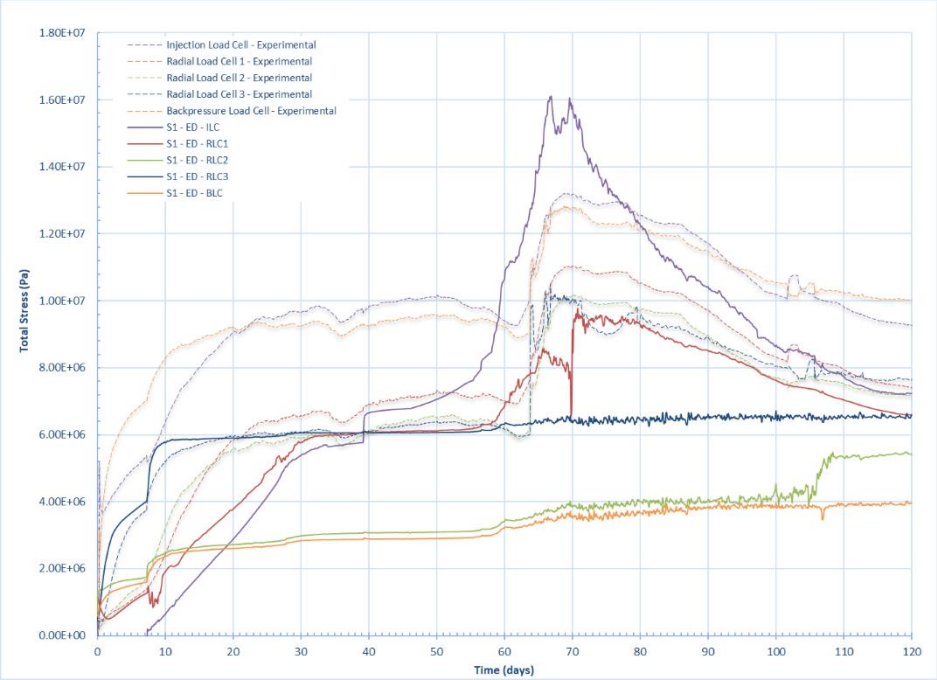

Figure 17. 1D Flow Case – ED Model -Total stress evolution over time

Total stress evolution results for the EPD model are presented in **Figure 18**. Similar to what was observed for the linear elastic model tested in the authors previous work, although the shape and timing of the stress evolution is captured at several simulated load cells, the EPD model is also not capable of reproducing the overall large increase in stresses observed experimentally. This is again attributed to low gas mobility within the simulated soil specimen.

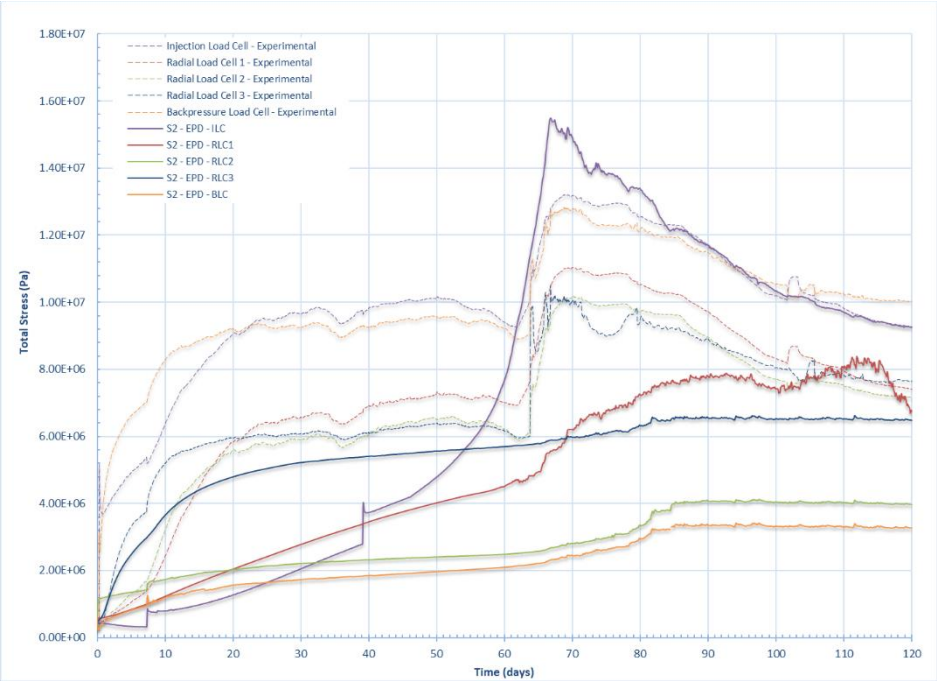

Figure 18. 1D Flow Case – EPD Model -Total stress evolution over time

For the NLPD model results presented in **Figure 19**, the total stress evolution fares better than the EPD model, being able to capture total stress evolution during the hydration phase generally well. Once the AEV is exceeded and inflow does occur, there is a jump in porefluid pressure and resulting total stress, with the injection load cell array and closer radial load cell arrays 1 and 2 experiencing a larger increase than the other two. The magnitude of this total stress increase is related to the extent of poregas migration, and if complete breakthrough had been achieved, it is reasonably expected that the results would much more closely agree.

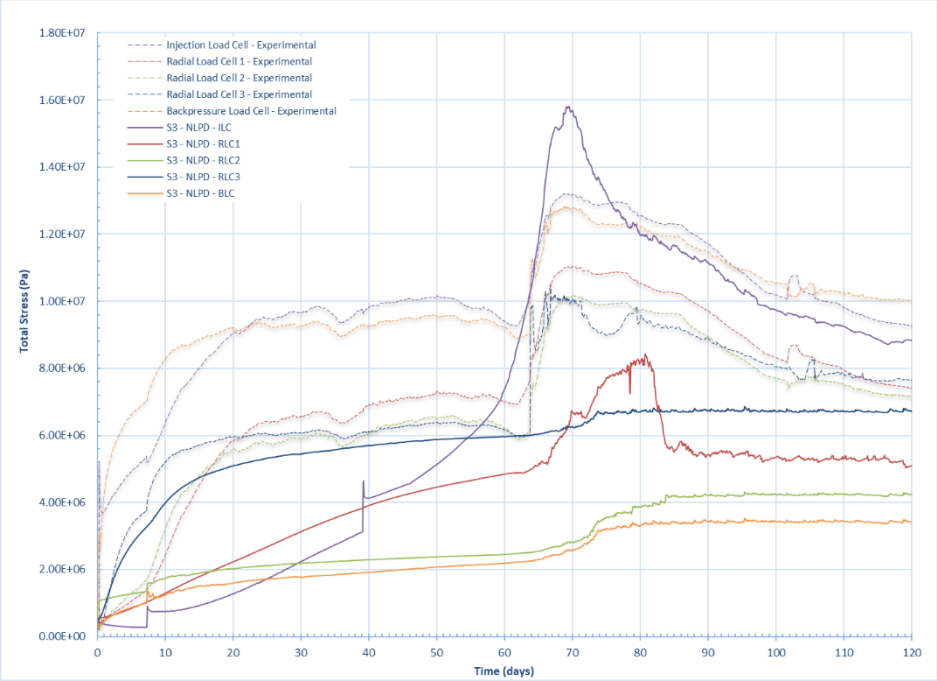

Figure 19. 1D Flow Case - NLPD Model -Total stress evolution over time

4.1.5. Stress path analysis

For each study scenario, an analysis of the p-q stress path at two points along the specimen over time was conducted and the results are presented in **Figure 20**, **Figure 21** and **Figure 22** for the ED, EPD and NLPD models, respectively. The first point is located near the injection point (x = 5 mm, y = 0 mm, z = 0 mm), while the second point is located near the center of the specimen (x = 64 mm, y = 0 mm, z = -13 mm). For the EPD and NLPD models, the xBBM yield surface at different suctions have also been plotted in the figures to support stress path analysis in p-q-s space.

For the ED model, as presented in **Figure 20**, the stress path at the injection end (i.e., x = 5 mm) is initially in tension and remains in tension. As the porefluid pressure increases with time, the deviatoric stress increases linearly as a function of the mean effective stress. This increase in deviatoric stress continues until gas injection shut-off, when the mean effective stress decreases following the same path in reverse. As an elastic model is being used, this reversal is expected. The figure also shows that the decrease in mean effective stress is associated with an increase in suction. An important finding of this study, is that the damage that occurs along the poregas migration front, and as depicted by the stress path (red curve) in **Figure 15**, is a result of tensile failure. For this reason, tensile damage contributes primarily to poregas flow.

The stress point near the central injection rod (i.e., x = 64 mm) is initially in elastic compression, as there is an increase in deviatoric stress with an increase mean effective stress. This is consistent with the results discussed in the authors' previous work for a 1D single phase gas flow case [73], whereby closer to

the injection rod, the specimen is in tension, while further away, the specimen is in compression. Once the poregas migration front reaches the stress point (at day 100), the stress path increases in tension. This is further supported by the increase in suction from 0 MPa to a 5.5 MPa by day 120.

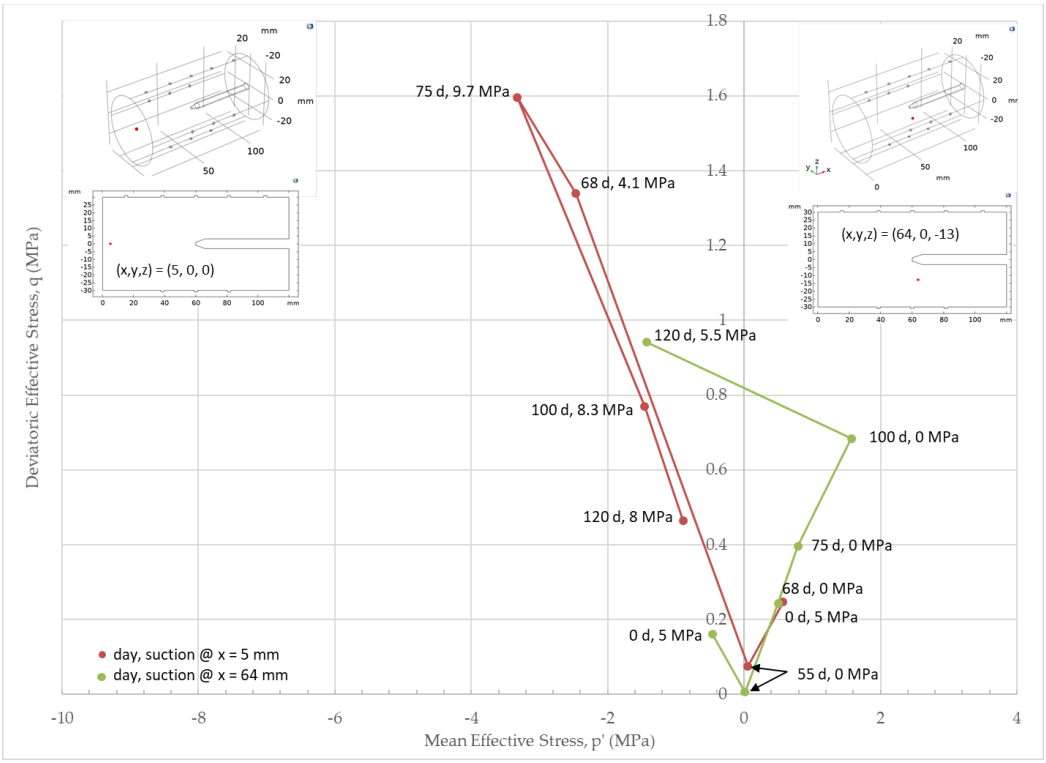

Figure 20. 1D Flow Case - ED Model – Stress path analysis

For the EPD model, the results of the stress path analyses conducted near the point of injection is presented in **Figure 21**(**a**), and near the central rod, presented in **Figure 21**(**b**). In **Figure 21**(**a**), at time t = 0 d, the initial effective mean stress is at -0.45 MPa and under a suction of 5.0 MPa, and is consistent with our initial conditions. During the hydration phase, the point undergoes elastic compression moving linearly in a positive direction along the p' axis, while suction continues to decrease. At approximately day 60, the suction value has dropped to approximately 1.3 MPa. Following gas injection into the sample, there is an increase in the displacement of water being pushed forward by the entering poregas. This results in some compressive strain, likely contributed to the increase in swelling strain, as the pore space becomes saturated and suction is reduced to 0. Noting that the critical-state line is suction-dependent, the stress path then moves in tension, until approximately day 66, when it approaches the yield surface for a suction of 0 MPa, triggering plastic dilation. During dilation, the deviatoric stress decreases with a decrease in mean effective stress (due to the expansion of the clay). Between day 67 and day 70, the stress path moves in elastic tension, until it again approaches the yield surface at a suction of 2.9 MPa, triggering a second larger period of dilation. Meanwhile, as poregas pressure continues to increase, the yield surface continues to expand due to the rapid increase in suction. At approximately day 72, the suction has increased to 6.4 MPa, and the stress path now continues in elastic tension.

The p-q stress path for the point near the center of the specimen is presented in **Figure 21**(**b**). As anticipated, since the point is located on the second half of the specimen, the stress path moves in compression. There is also a notable decrease in suction as this part of the specimen is being hydrated, and

the poregas pressure does not migrate to this point of the sample. Again, as with the ED model, there is only a small change in stress-state, due to the poregas migration front not reaching this point.

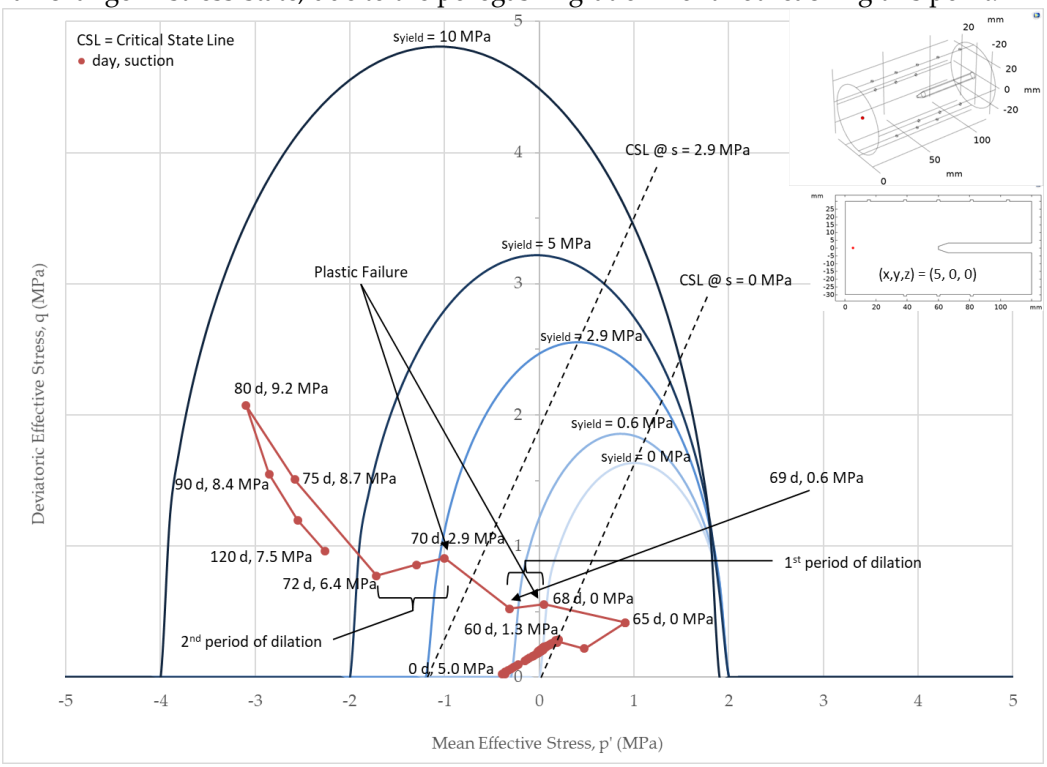

(a)

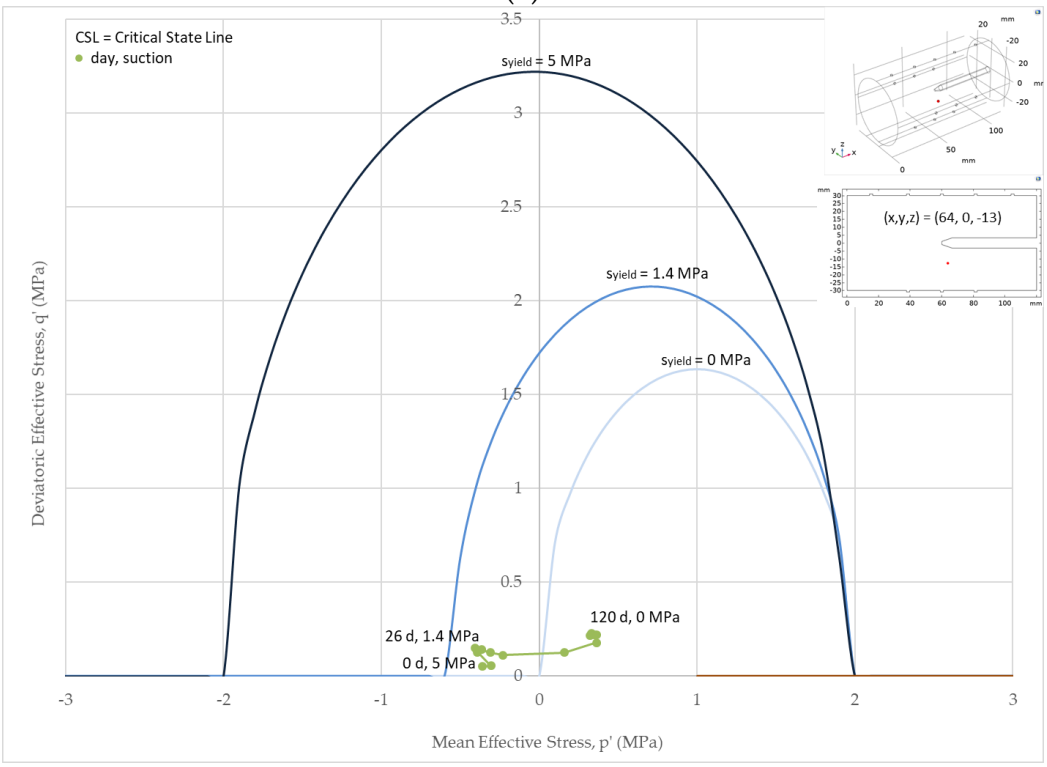

(b)

Figure 24. 1D Flow Case: EPD Model – Stress path analysis at (**a**) point of injection and (**b**) center of specimen

The stress paths taken by the results for the NLPD model presented in **Figure 22**(**a**) and **Figure 22**(**b**) near the point of injection and near the central rod, are very similar to the stress paths observed for the EPD model. With changes in mean effective stress and suction, the critical state line is reached several times, resulting in plastic dilation and strain-softening, followed by strain hardening (due to suction increase), until the critical-state line is reached again.

The NLPD model follows the same general stress path, first moving in elastic compression during the hydration phase, until a suction of 0 MPa is reached and the sample becomes saturated. Once gas is injected into the sample, the deviatoric effective stress increases with an increase in effective mean stress, and the stress path very quickly intersects the yield surface at a suction 0 MPa, resulting in plastic dilation. Once the poregas migration front reaches a horizontal distance of 5 mm, the value of suction increases rapidly and the yield surface expands, as the mean effective stress continues to increase in elastic tension. At day 69, there is a second period of plastic dilation and strain softening. As the suction continues to increase, the stress moves again in elastic tension, however in the NLPD model, there is a third period of plastic dilation which occurs at day 72. At day 74 the suction has rapidly increased further and the stress-state remains in elastic tension until approximately day 83, when the mean effective stress begins to decrease in elastic compression, indicative of the gas shut-off and the corresponding drop in poregas pressure.

For the point near the center of the specimen in **Figure 22**(**b**), the stress state remains in elastic compression as expected, as the stress path does not intersect with the yield surface at given values of suction. Again, deformations are small, as the poregas migration front has not yet reached the center of the specimen. Some differences are expected as a result of the use of the non-local plasticity, which can be seen by some differences in the stress path over time.

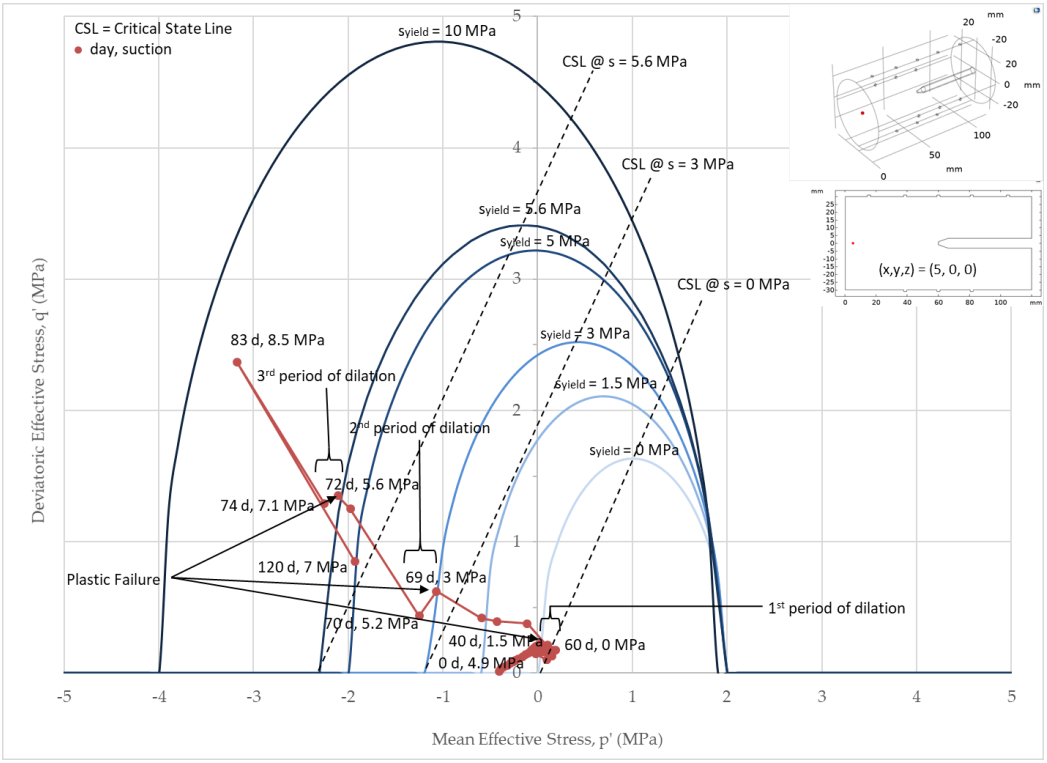

(a)

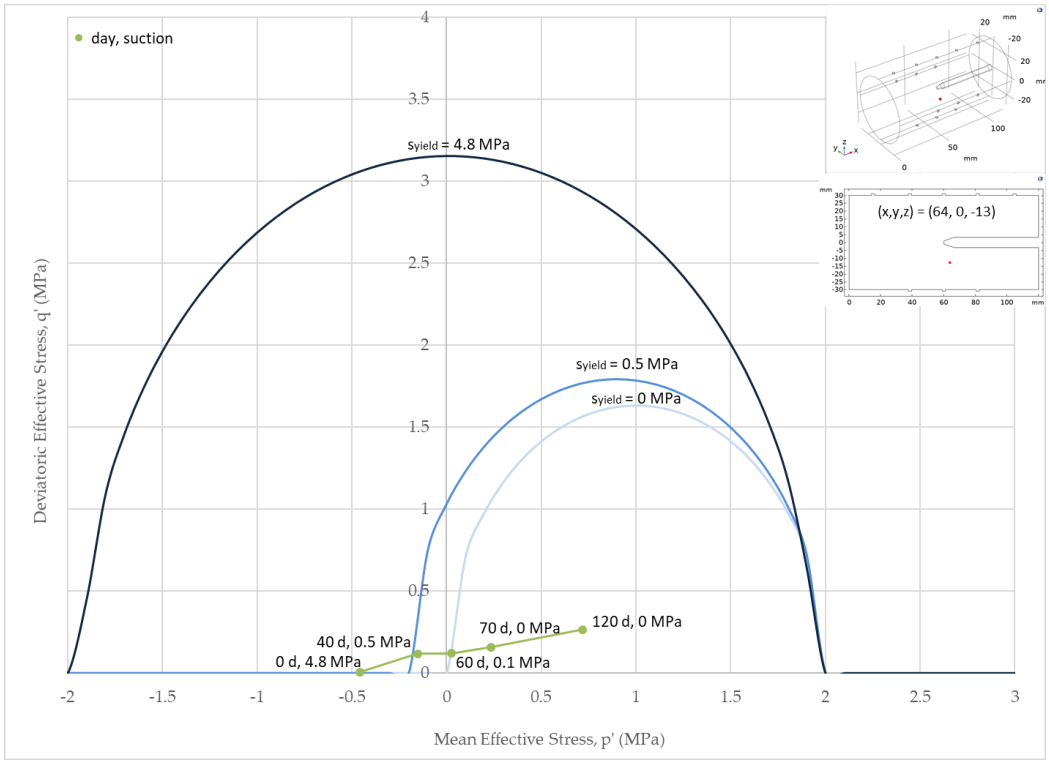

(b)

Figure 22. 1D Flow Case: NLPD Model – Stress path analysis at (**a**) point of injection and (**b**) center of specimen

4.2. Validation Study 2: 3D Spherical Flow Case

The results of the 3D spherical flow validation study are presented below. For each study scenario corresponding to a different mechanical model (i.e., ED, EPD, NLPD), the following results are discussed:

1. migration of poregas through the specimen over time
2. gas inflow/outflow
3. gas storage in the system
4. evolution of total stresses over time
5. p-q stress path analysis

The experimental results provided for comparison were discussed in Harrington et al. [62] and are not discussed in detail in this paper.

4.2.1. Migration of poregas pressure and extent of damage

Poregas migration profiles over time for the central cross section (XZ-plane) of each study scenario are depicted in **Figure 23**, **Figure 24**, and **Figure 25**. Poregas pressure results for the ED model are presented in **Figure 23**(**a**) with the damage presented in **Figure 23**(**b**). The results show that the onset of damage begins to occur before the AEV is reached (which occurs on day 747). Damage can be seen propagating spherically outward before it reaches the radial walls, and then continues to propagate towards each end of the specimen, when complete gas breakthrough is realized. The self-sealing behavior implemented through the damage model is very evident in **Figure 23**(**b**). As damage propagates the bentonite self-seals behind it. An interesting phenomenon can be observed at day 755, when where the presence of damaged zones and discrete undamaged bands can be seen, indicating the formation of preferential flow pathways.

It should be re-iterated that four processes and characteristics were central to achieving this breakthrough, and they were the AEV, the strains at material failure, the enhanced flow provided by the Klinkenberg effect, and the presence of material heterogeneity.

In the case of the EPD model, **Figure 24**(**a**) shows poregas pressure results over time. As with the 1D flow case, there is little poregas migration observed, even with the presence of damage. As with the 1D flow case, this is attributed to the damage model calibration parameters (**Table 8**), and specifically the calibrated maximum permeability, which could not be increased further while maintaining numerical stability and convergence. Of particular note in **Figure 24**(**b**), is that the extent of damage associated with strain softening, appears singular, and as a result does not propagate, further reinforcing the use of a non-local plastic model.

This is further investigated in **Figure 25**, which displays the volumetric plastic strain at day 835. Zones of localized plastic strain can be seen throughout the specimen, and these zones do not coalesce or connect throughout the sample. As a result, these zones remain isolated and damage is not able to propagate throughout allowing for the formation of distinct migration pathways. These singular features observed when introducing plasticity were anticipated as described earlier. For this reason, this study assesses the use of a non-local plastic model.

Figure 26(**a**) and **Figure 26**(**b**) show the poregas pressure evolution and damage evolution when a non-local plasticity model with damage has been applied. As with the 1D flow case, when applied to the 3D spherical flow, the non-local plastic model was able to achieve larger zones of damage and more significant gas flow, when compared to the local plastic model. This capability comes from the non-local smoothing of the effective plastic strain over the region defined by the characteristic length, allowing for higher calibrated damage coefficients to be applied, while maintaining numerical stability and convergence.

Figure 27 shows the change in consolidation pressure over time, which provides some insight that the plastic model is being implemented correctly. **Figure 27** shows that as the degree of suction increases, the consolidation pressure and corresponding yield stress increases, as would be expected. This is also evident from the stress path analysis described in Section 4.2.5. Also evident from **Figure 27**, and consistent with **Figure 14** in the 1D flow case, the presence of a material defect (represented by a lower consolidation pressure) does not influence the zone of damage or help promote gas flow. This is due to the stress path taken as described in Section 5.2.5.

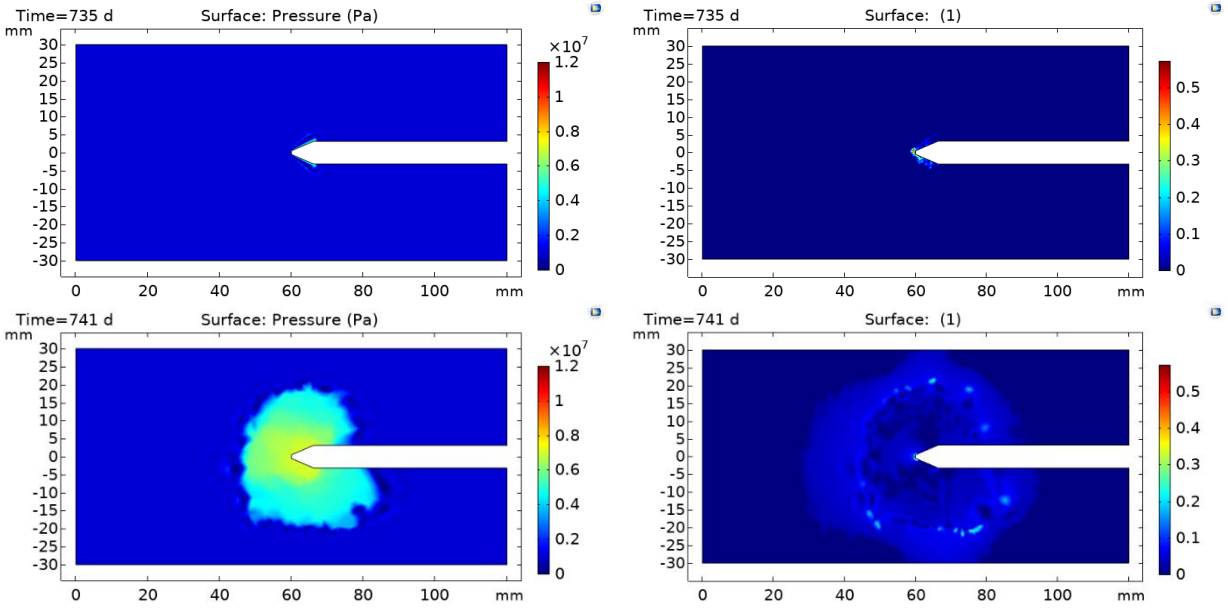

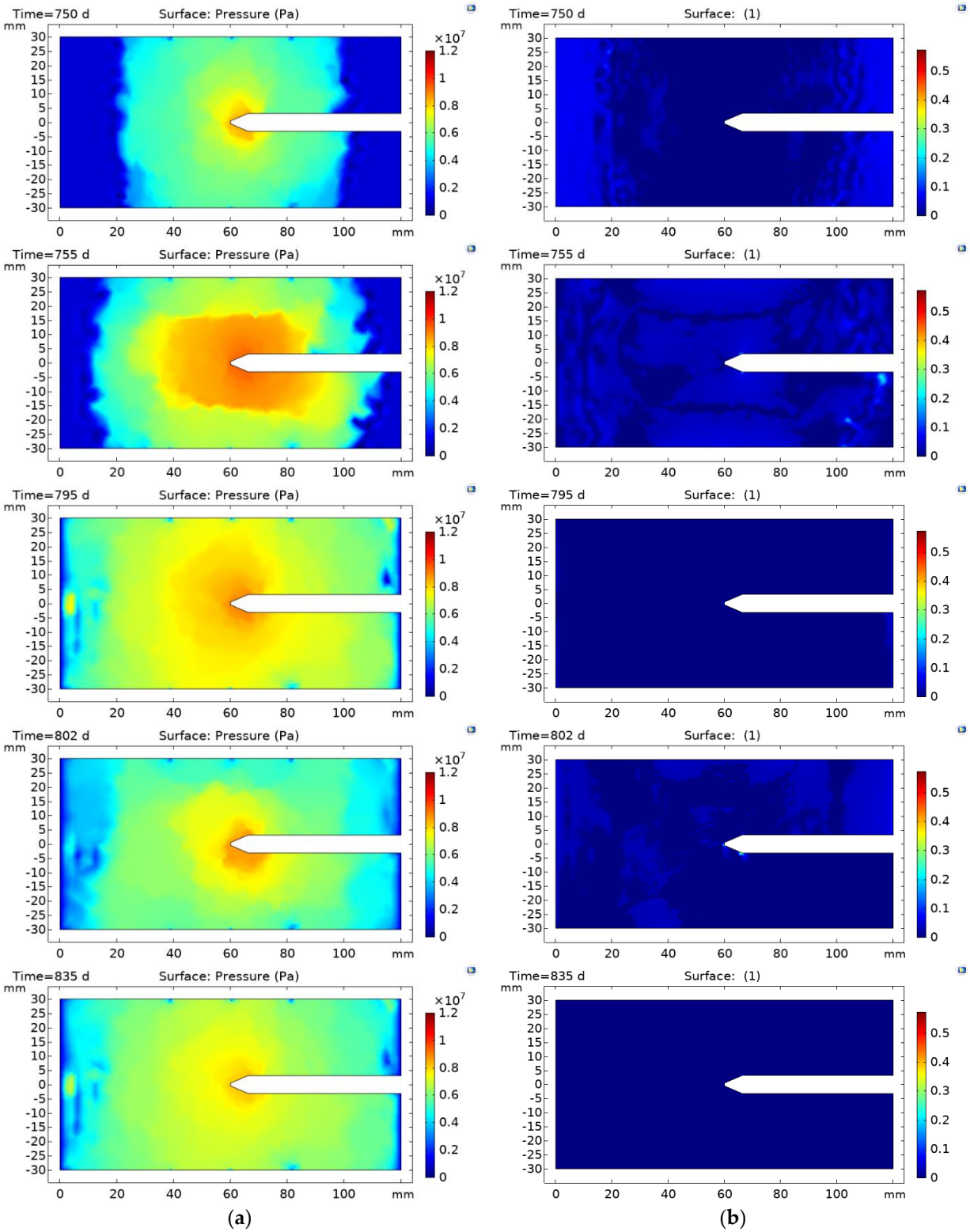

Figure 23. 1D Flow Case – ED model results for (**a**) poregas pressure and (**b**) damage at t=735, 741, 750, 755, 795, 802, and 835 days

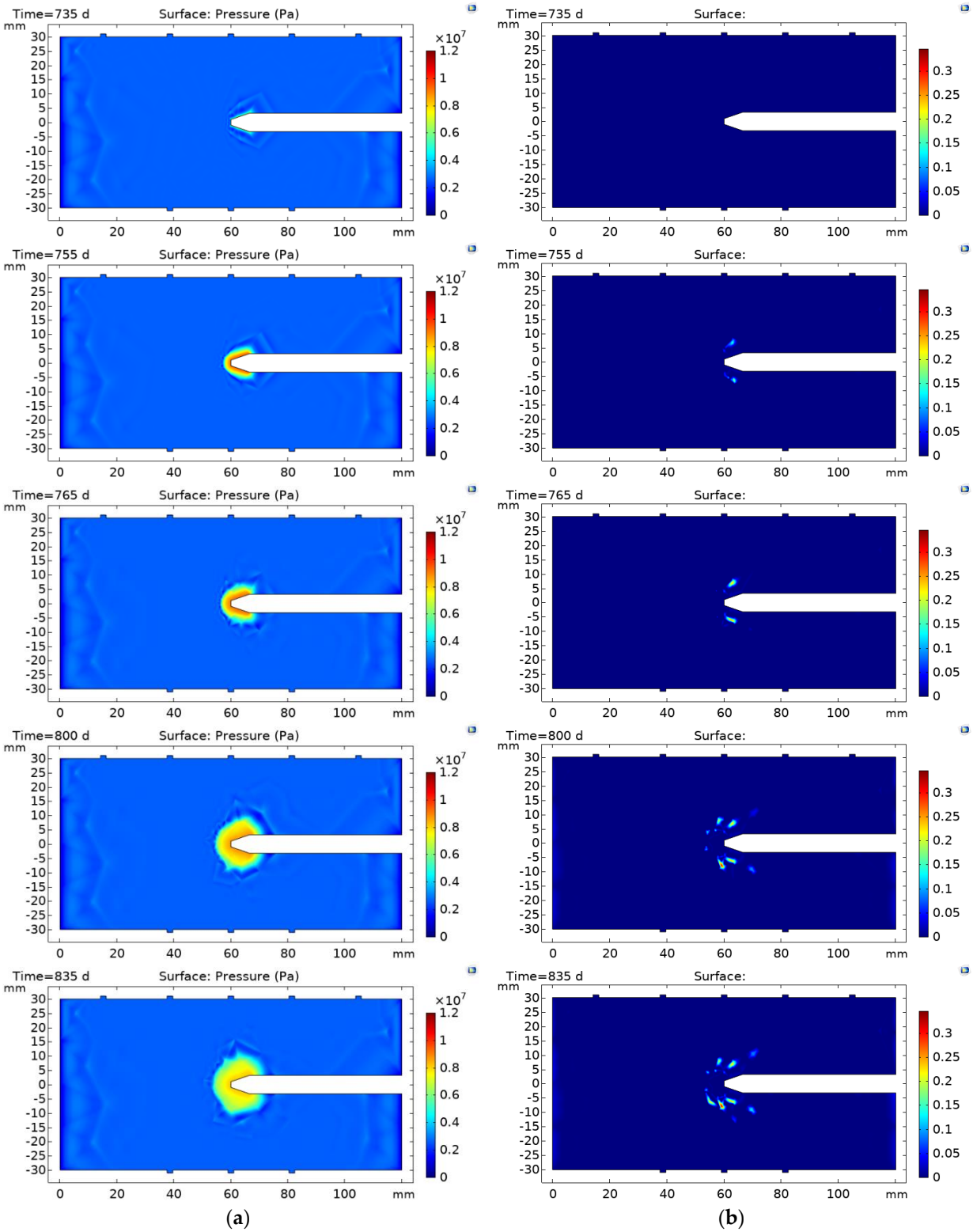

Figure 24. 1D Flow Case – EPD model results for (**a**) poregas pressure and (**b**) consolidation pressure at t=735, 755, 765, 800 and 835 days

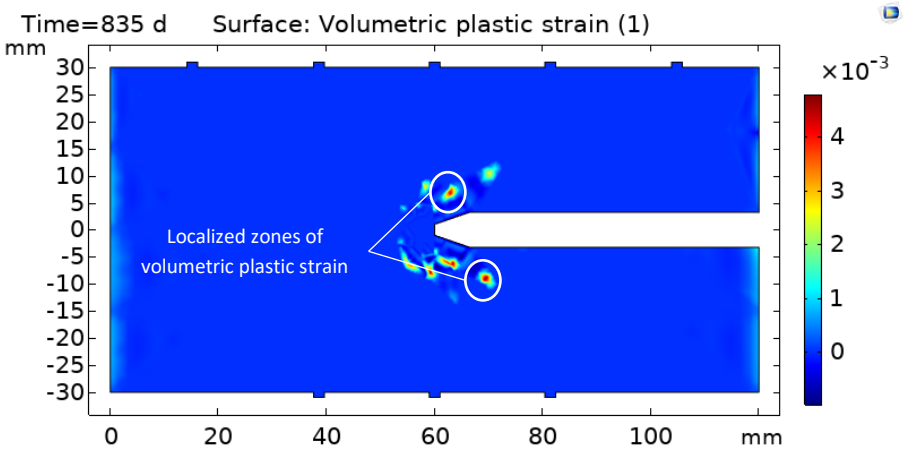

Figure 25. 3D Spherical Flow Case – EPD model – Plastic Volumetric Strain at t=835 days

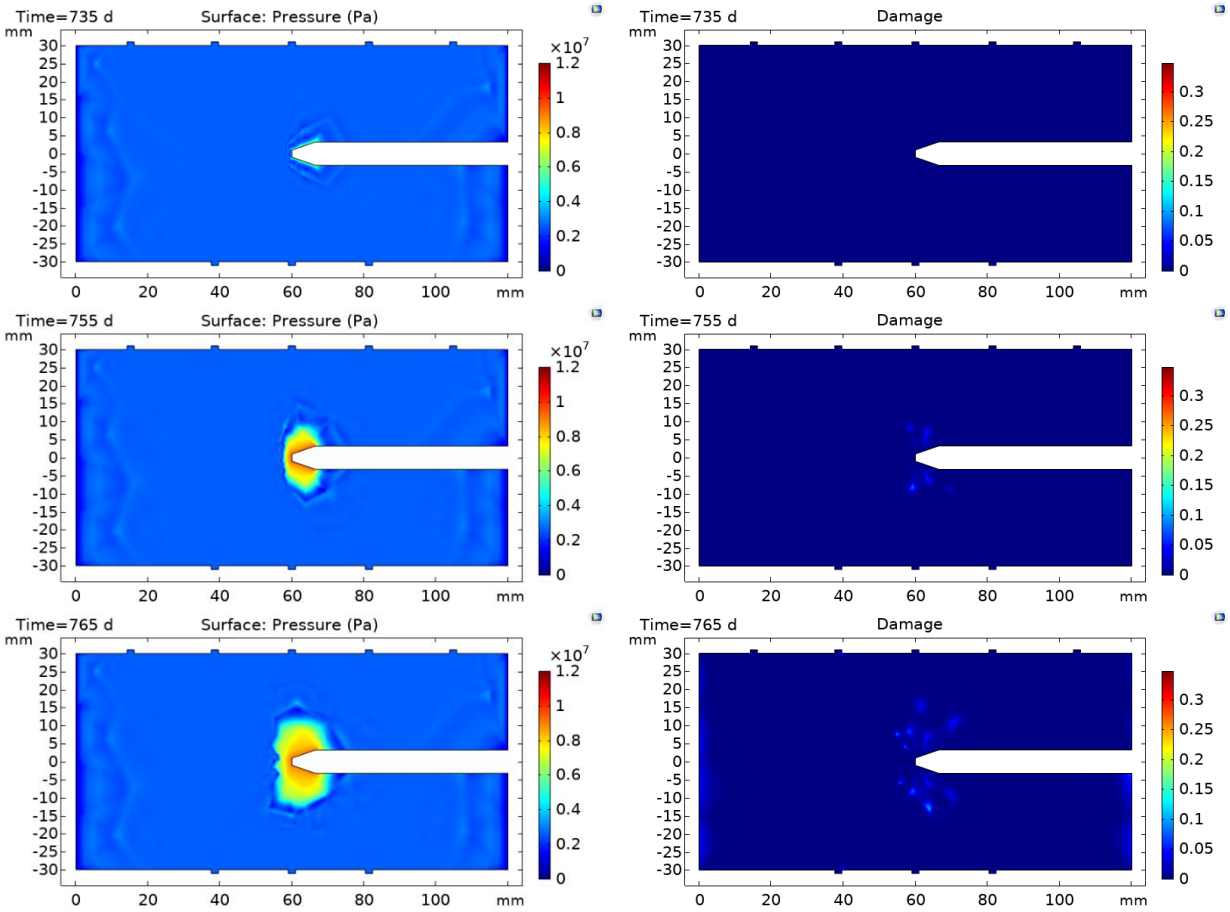

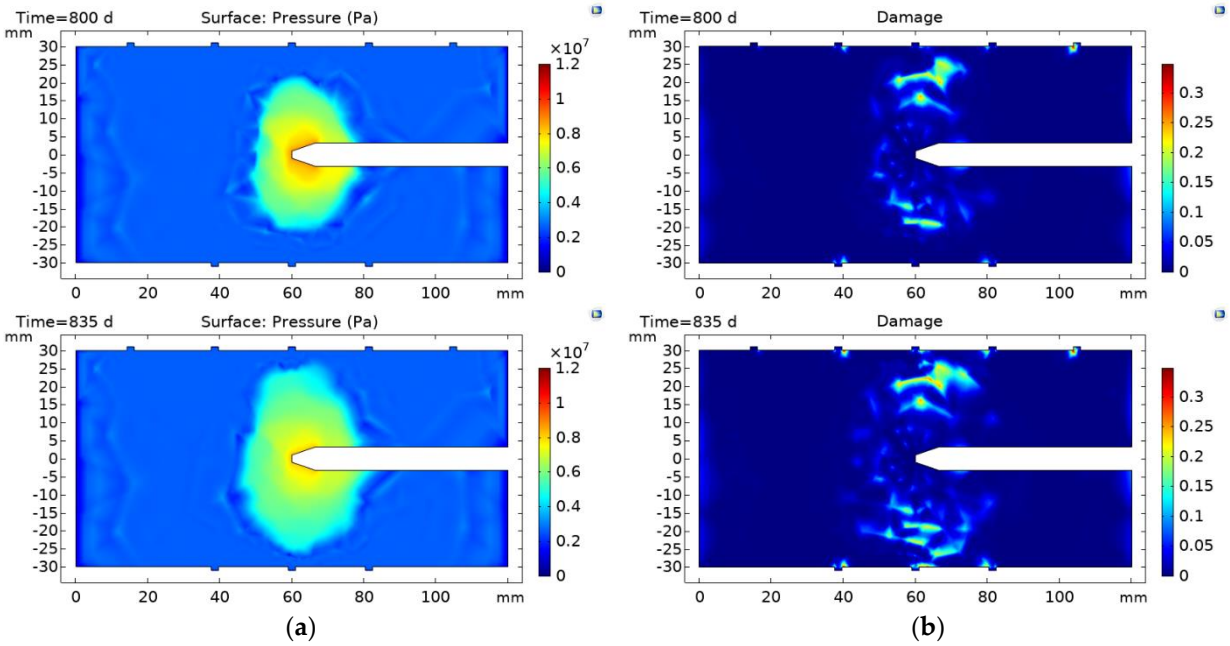

Figure 26. 3D Spherical Flow Case – S3 NLPD model results for (**a**) poregas pressure and (**b**) damage at t=735, 755, 765, 800 and 835 days

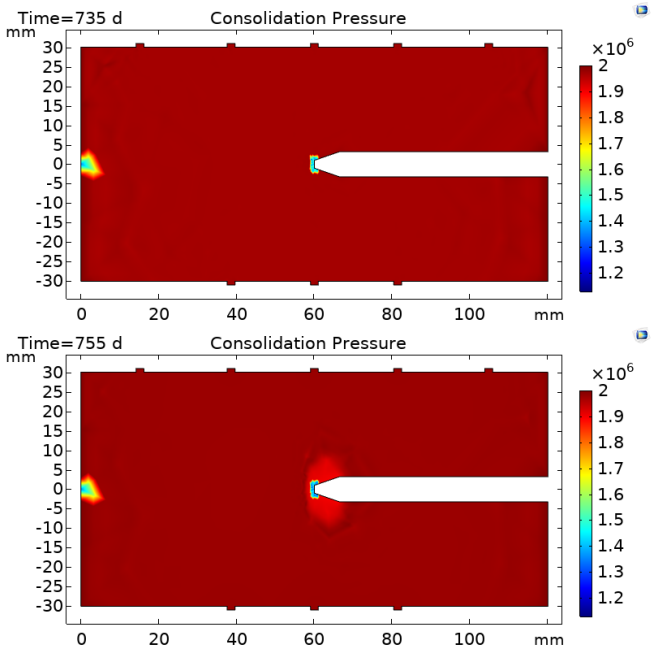

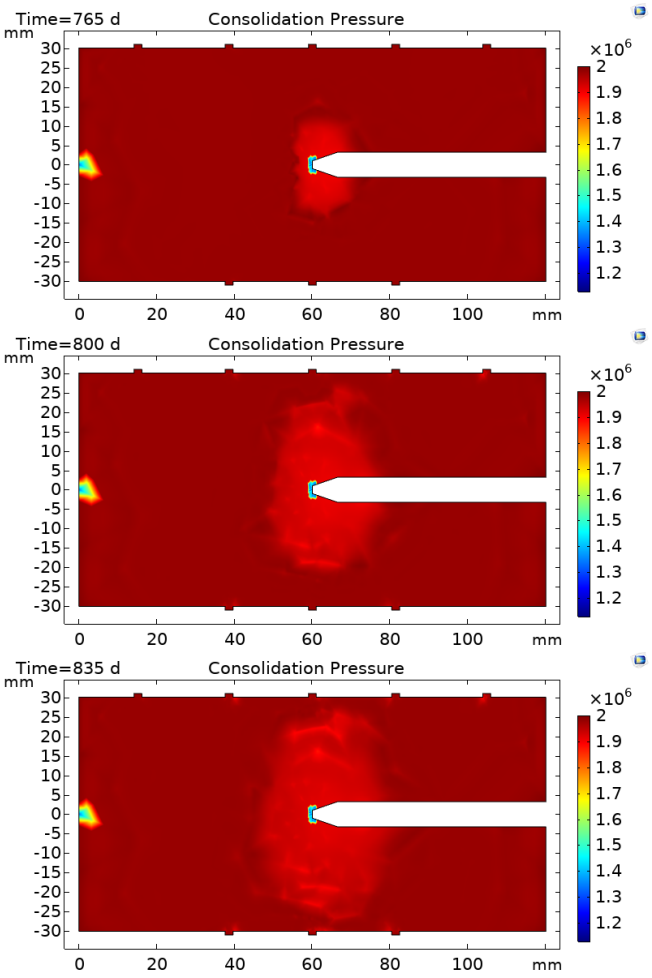

Figure 27. 3D Spherical Flow Case – S3 NLPD model results for consolidation pressure at t = 735, 755, 765, 800, and 835 days

4.2.2. Gas inflow and outflow

Gas inflow and outflow profiles over time for the experimental data and for each mechanical model assessed are depicted in **Figure 28**(**a**) and **Figure 28**(**b**), respectively.

As can be seen in **Figure 28**(**a**), the ED model is very well capable of predicting the gas inflow behavior. The model correctly simulated the shape, timing, and magnitude of the rapid inflow that occurs at $t = 757$ days and 761 days (observed by the inflow peaks). These peaks align with the dips in experimental injection pressure, associated with rapid flux into the sample. The model was also able to represent the decrease in inflow following gas shut-off at day 772. Moreover, as with the 1D flow case, the chaotic inflow behaviour was also reproduced, which provides some confidence in the general application of the model to represent two-phase flow.

Unlike the 1D flow case, for the 3D spherical flow case the authors were able to simulate total gas outflow as depicted in **Figure 28**(**b**). Total gas outflow was calculated by adding the sum of outflow from each of the radial porefluid pressure arrays as well as both ends of the specimen. There is some agreement between the shape and timing of modelled and experimental outflow at the onset of outflow, however the magnitude could not be captured. Additionally, there is a large burst of outflow which occurs between 795 days and 805 days. This was not observed experimentally, and could be a result of some of the stored gas taking a longer preferential flow path. This burst of outflow also visually aligns with the damage which

was triggered at day 802 as depicted in **Figure 23**(**b**). It is hypothesized that if a probabilistic analysis was conducted, whereby repeated model runs using a different orientation of spatially randomly distributed material heterogeneity in hydraulic properties were applied, the experimental results may fall within the distribution. It should be noted that experimental data of gas outflow from each of the radial porefluid pressure arrays exists. In addition to probabilistic analysis, future analysis should explore in more detail the magnitude of gas outflow from the individual porefluid pressure arrays.

The EPD model results were not able to match gas inflow or achieve any measurable gas outflow. Although there was inflow as depicted by **Figure 28**(**a**), the flow rate was at the order of 1E-10 m^3/s, significantly lower than what was exhibited experimentally. As discussed earlier, this is expected due to the limited plasticity and damage obtained by the local plastic model. As for the NLPD model, even with more extensive plasticity and damage facilitated by the non-local plastic model, the magnitude of gas inflow and outflow were not realized. However, the NLPD model results are promising and may be improved with further model calibration and optimization, in particular with the use a function that would allow a more significant increase in permeability with damage while ensuring numerical convergence.

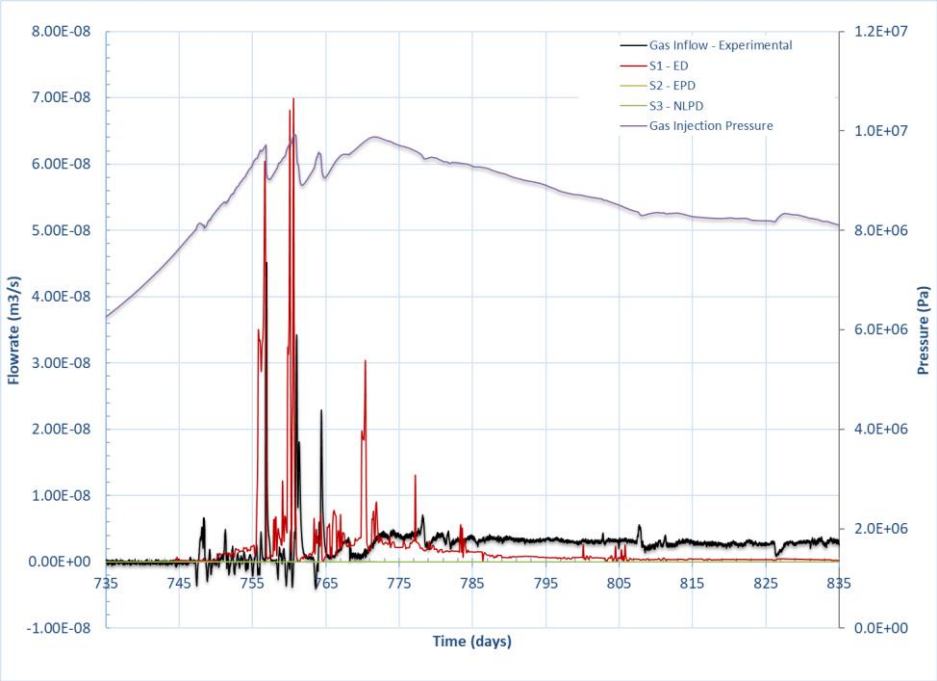

(**a**)

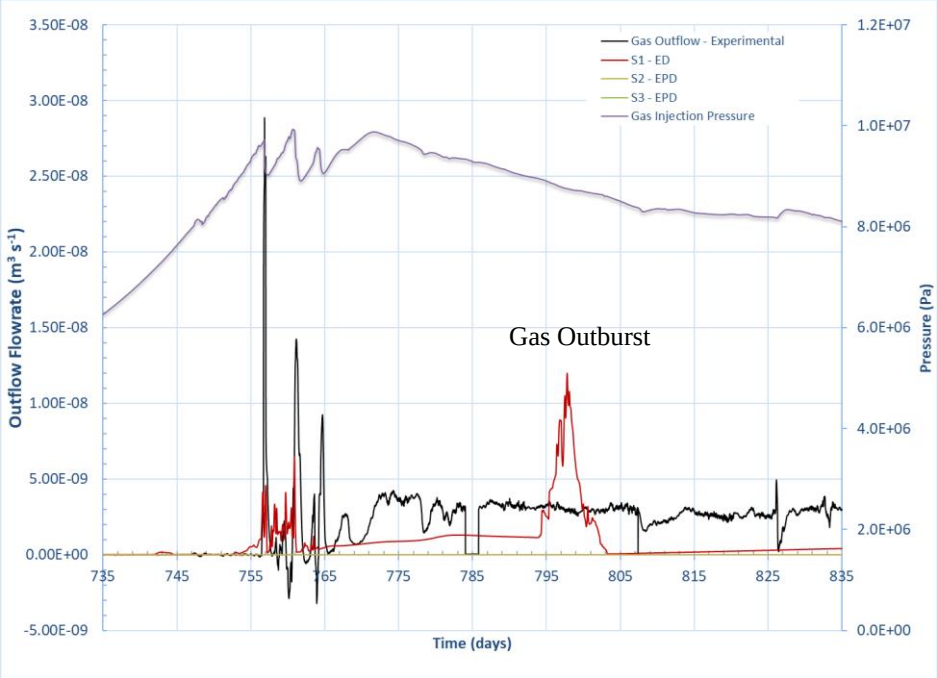

(**b**)

Figure 28. 3D Spherical Flow Case Results: (**a**) gas inflow and (**b**) gas outflow profiles over time

4.2.3. Gas storage in the system

The modelled results of volume of gas stored within the simulated specimen fare better than those observed for the 1D flow case. As demonstrated in **Figure 29**, for the ED model, there is very close agreement between the modelled and experimental results. Of particular note, is that following gas shut-off, the volume of gas stored observed experimentally remains larger than that modelled, until the large burst of outflow occurs. This corresponds well with the difference between the areas under the outflow and inflow curves.

As there was little gas flow into the sample using the EPD model, it is not surprising that there was almost no gas storage within the specimen. In comparison to the EPD model, there was a larger volume of gas stored within the specimen when the NLPD model was applied, and this corresponds to the increased gas flow into the system provided by the non-local plastic model.

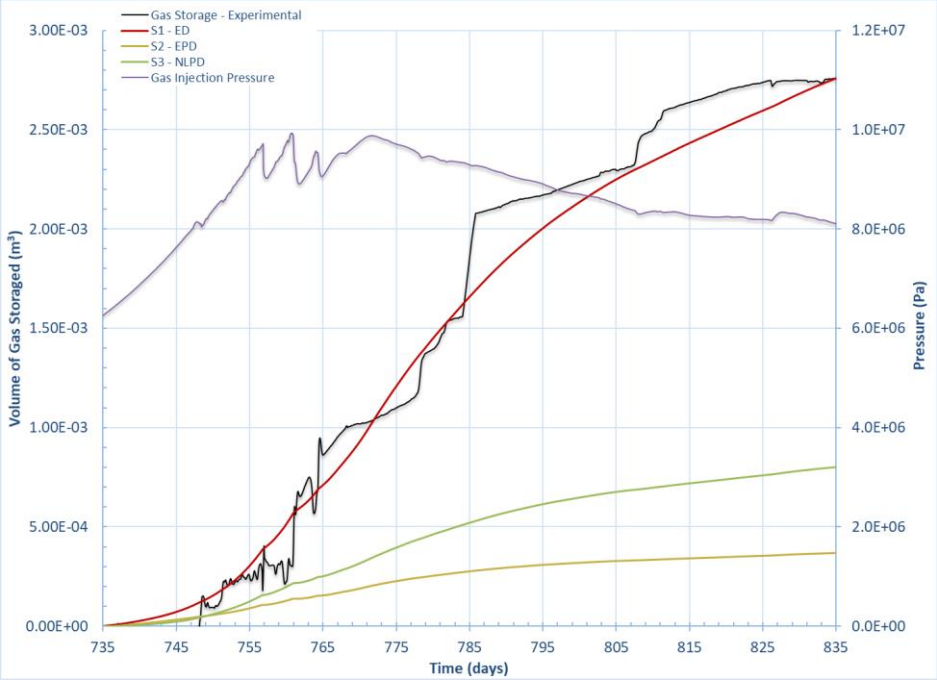

Figure 29. 3D Spherical Flow Case Results: Volume of gas stored

4.2.4. Evolution of total stresses

The results of the total stress evolution simulated by each of the models and measured experimentally at the injection load cell, radial load cells, and backpressure load cell, are presented in **Figure 30**, **Figure 31**, and **Figure 32**.

Figure 30 presents the results of the ED model, which shows good agreement with the experimental results. Although not perfect, at each of the load cell arrays, the modelled results are capable of capturing the initial dip, sharp rise in total stress, chaotic behavior during breakthrough, and tail period following gas shut-off. The model results are not quite able to capture the magnitude of decrease in total stress during dissipation of the gas following gas shut-off. Also, the timing of the drop in total stress occurs around 802 days, which again corresponds to the period of burst outflow. This corroborates that, from 765 days to 795 days, there is a continued evolution of poregas pressure buildup within the system following gas shut-off, and that this is released once gas pressures increase and damage is again triggered.

The total stress evolution results for the EPD model are depicted in **Figure 31**. The results show little change in total stresses. As with the 1D flow case, this is due to little poregas migration through the sample. Results for the NLPD model are presented in **Figure 32**. The results are slightly better than those of the EPD model, due to the increased gas flow in the system provided by the non-local plastic model, although still not representative of the experimental data.

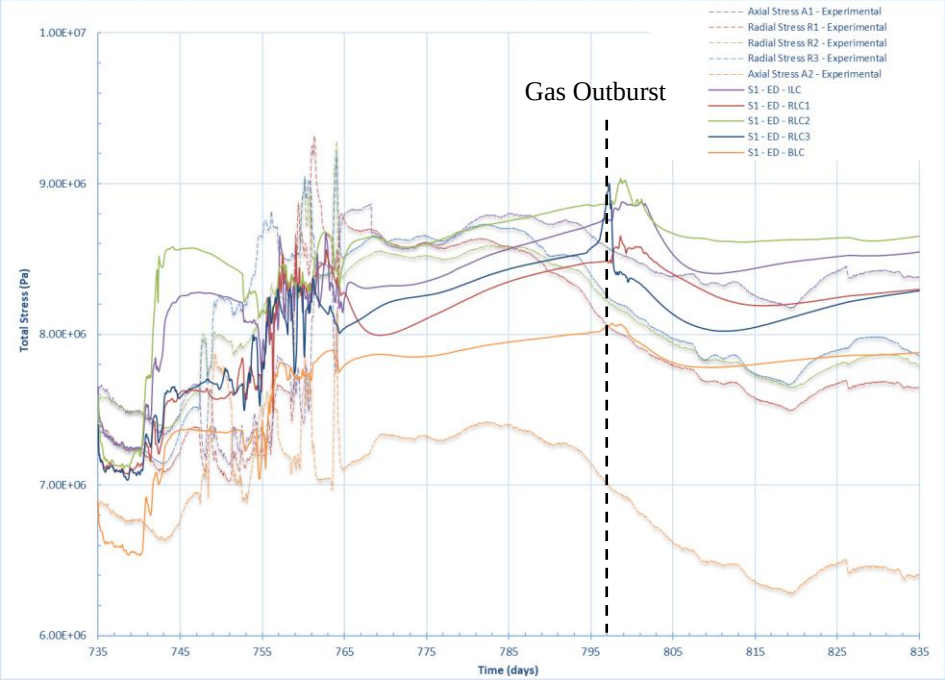

Figure 30. 3D Spherical Flow Case: ED Model – Total stress evolution over time

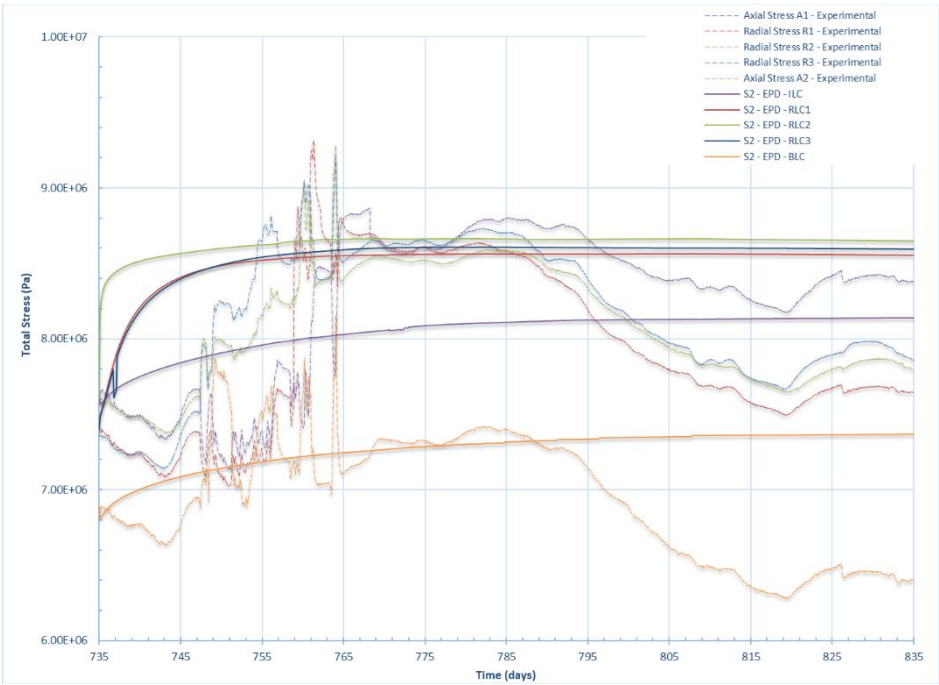

Figure 31. 3D Spherical Flow Case: EPD Model – Total stress evolution over time

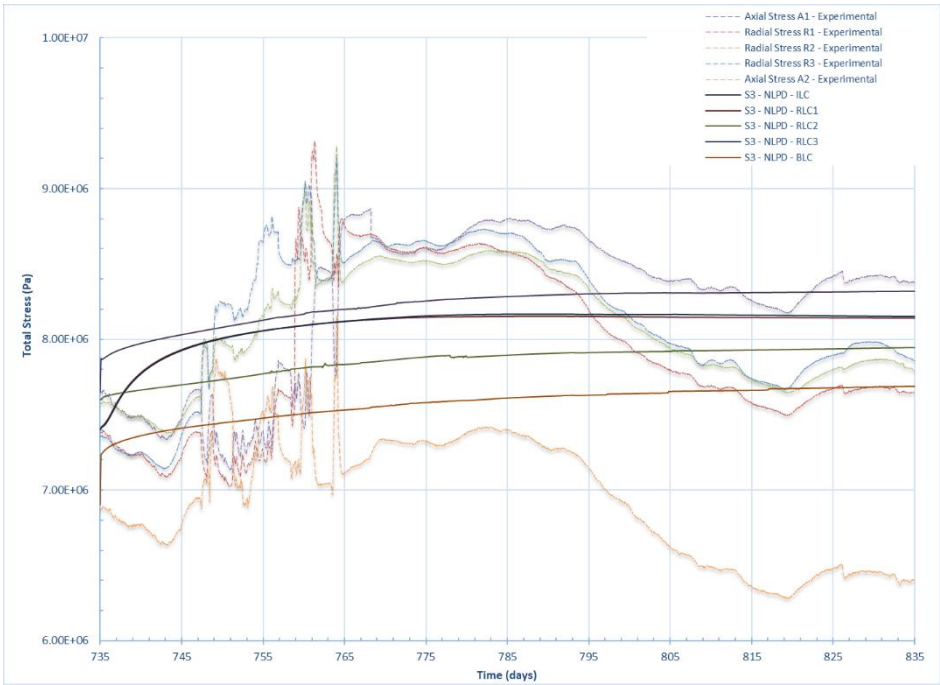

Figure 32. 3D Spherical Flow Case: NLPD Model – Total stress evolution over time

4.2.5. Stress path analysis

For each study scenario, an analysis of the p-q stress path at two points along the specimen over time was conducted and the results are presented in **Figure 33**, **Figure 34**, and **Figure 35** for the ED, EPD and NLPD models, respectively. The first point is located near the central injection rod (x = 60 mm, y = 0 mm, z = -8 mm) and was selected to correspond to the zone of significant plastic strain identified in **Figure 25**. The second point is located near the front axial end of the specimen opposite the injection rod (x = 5 mm, y = 0 mm, z = 0 mm). For the EPD and NLPD models, the xBBM yield surface at different suctions have also been plotted on the figures to assist in the p-q-s stress path analyses.

The stress path analysis for the ED model is presented in **Figure 33**(**a**) at a point near the central injection rod, and in **Figure 33**(**b**) at the point near the front axial end. The initial stress state is at -6.5 MPa and at a suction of 0 MPa, which is in-line with the initial conditions for the ED model. As with the results of the 1D flow case presented in **Figure 20**, near the point of gas injection, the stress point is initially in tension and remains in tension as the mean effective stress decreases with an increase in porepressure. At day 745, there is a significant decrease in the deviatoric stress, which in fact corresponds to the period of self-sealing of the bentonite which is observed between day 745 and day 755 (see **Figure 23**(**b**)). As discussed earlier, the self-sealing behavior is a result of the reduction in damage, which is associated with the magnitude of the principle strains. However, even though there is no more damage, poregas continues to migrate slowly through the sample, and the mean effective stress continues to decrease, but with a decrease in deviatoric stress. At day 750 damage is triggered for a second time at the stress point, and the deviatoric stress again increases with a decrease in mean effective stress, until day 760, when the damage has again self-sealed and inflows into the system have been reduced. Here, the soil does not follow the same stress path that was initially taken. This is hypothesized to be due to porefluid pressure changes being smaller between day 750 and day 760 (suction increase of 2.1 MPa), than between day 735 and day 745 (suction increase of 5.2 MPa). The stress path then moves in elastic compression until day 790 when there is a jump in deviatoric stress and slight increase in mean effective stress, indicating a desaturation of gas in the system. This period corresponds to the outburst of gas as evident in **Figure 28**(**b**). Following gas

outburst, damage is reduced again, and the bentonite exhibits a second self-sealing, as the deviatoric stresses subside.

The stress path near the front-facing axial end of the specimen is depicted in **Figure 33**(**b**). As expected, and consistent with the author's previous work [73], from day 735 to day 740, the stress state is in elastic compression, the opposite behavior as that near the point of injection. The stress path then becomes somewhat chaotic between day 740 and day 750. This may be due to onset and persistence of damage at the axial ends during this period as depicted in **Figure 23**(**b**). Once damage is triggered at day 742, there is a significant increase in deviatoric stress, until day 745, where the deviatoric stress decreases again until day 755. It should be noted that during this period the specimen remains saturated (i.e., zero suction). At day 755, the poregas front reaches this point and begins to migrate through. The stress path then mimics the same path observed in **Figure 33**(**a**) (i.e., at the point near injection).

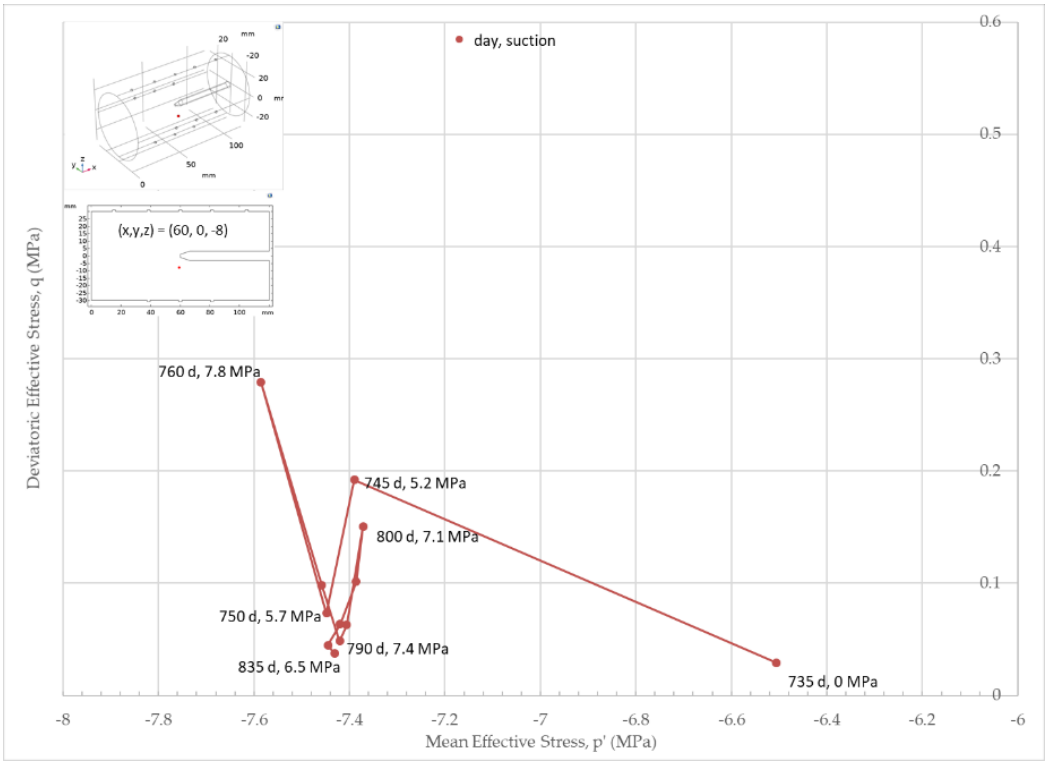

(a)

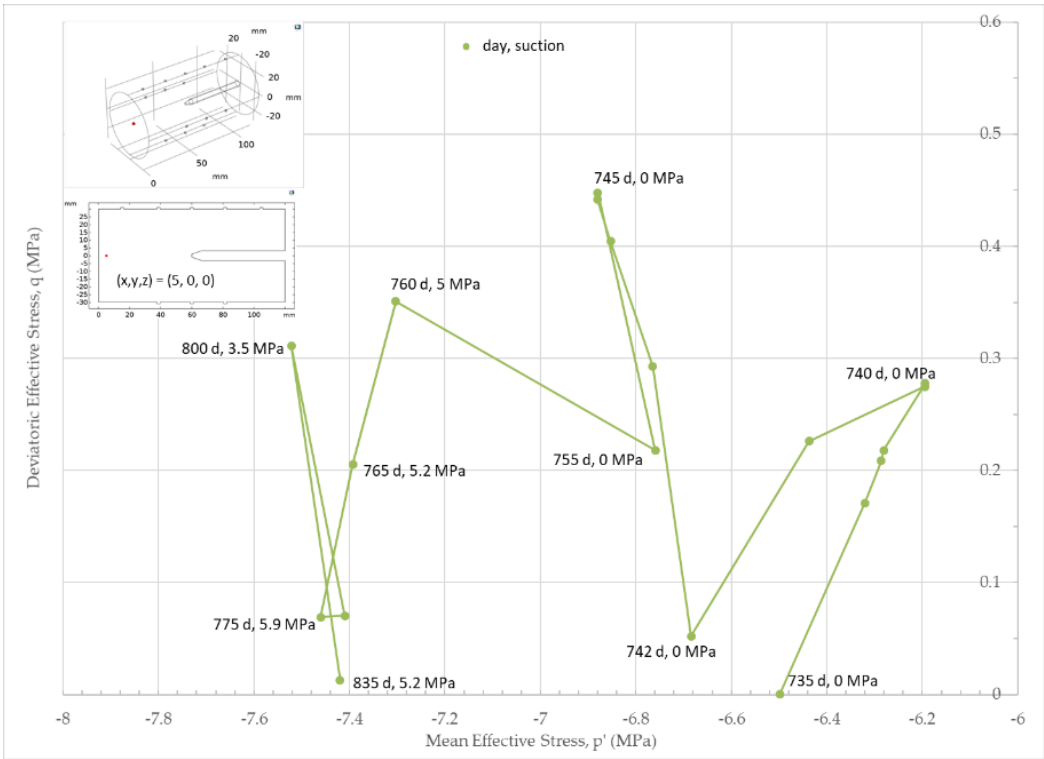

(b)

Figure 33. 3D Spherical Flow Case: ED Model – Stress path analysis

For the EPD model, the results of the stress path analyses conducted near the point of injection is presented in **Figure 34**(**a**). At time t = 735 d, the initial stress state is at -0.6 MPa and under a suction of 3.0 MPa, and is consistent with our initial conditions. It should be noted that in order to ensure the stress point begins within the yield envelope, the initial conditions for the plasticity models were adjusted (see **Table 5**). The stress point is initially under elastic compression moving linearly in a positive direction along the p' axis, while suction continues to decrease, along with the yield surface. At approximately day 766, the stress path intersects the yield surface at a suction of 1.1 MPa, causing an extended period of dilation and strain-softening as the yield surface continues to decreases with a decrease in suction. This decrease in suction is again likely due to the displacement of the waterfront caused by migration of gas into the sample at the injection point. At day 775 the poregas begins to migrate past this location and the stress point returns back within the yield envelop as suction begins to increase. The stress path then continues in elastic tension until day 835.

Figure 34(**b**) depicts the stress path taken by the stress point near the front axial end. There is very little change in stress state at this location, due to the little poregas migration promoted by the EPD model. One particular feature to be noted is that as porewater is being displaced from the central injection rod towards the boundaries of the specimen, the value of suction at the front axial end decreases.

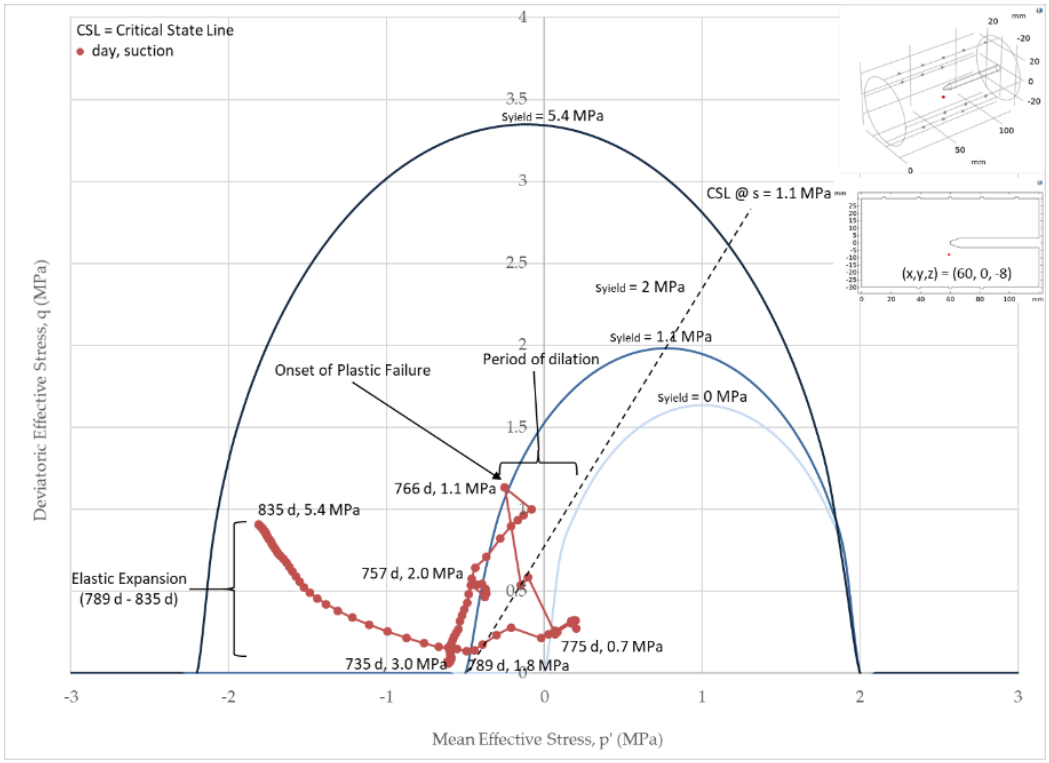

(a)

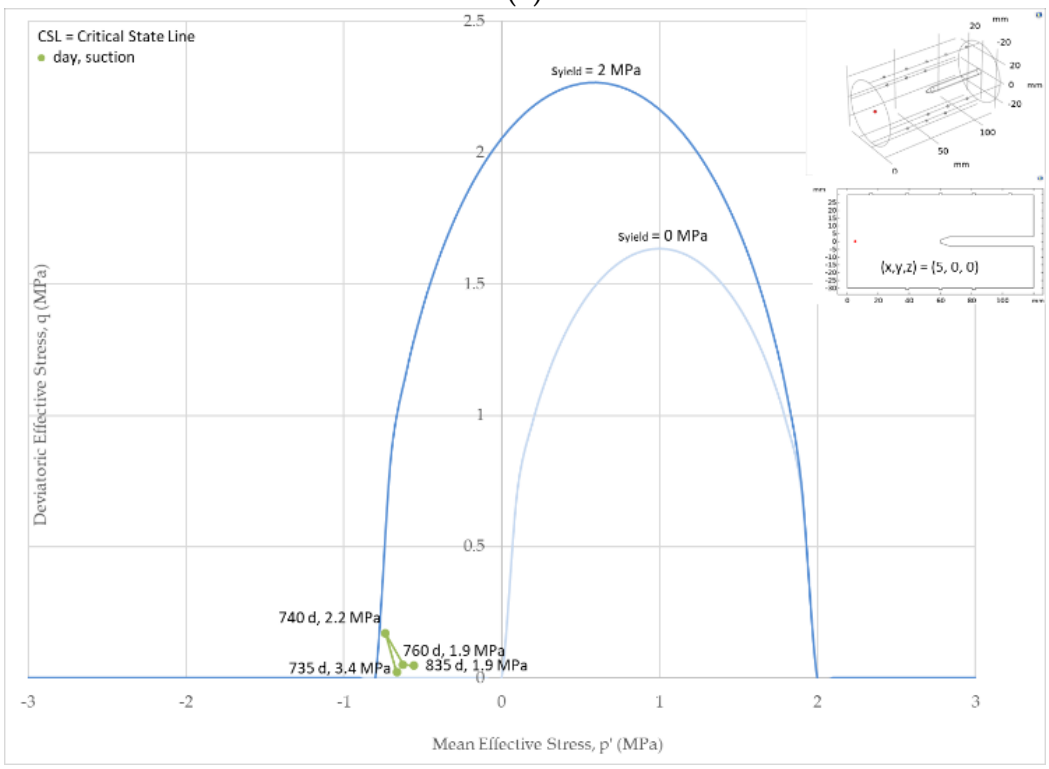

(b)

Figure 34. 3D Spherical Flow Case: EPD Model – Stress path analysis (**a**) near central injection rod and (**b**) near front axial end of specimen

For the NLPD model, the results of the stress path analyses conducted near the point of injection is presented in **Figure 35**(**a**), and is similar to the results described by the EPD model. At time t = 735 d, the initial stress state is at -0.6 MPa and under a suction of 2.4 MPa. There stress point initially moves in elastic compression, as the deviatoric stress increases with an increase in mean effective stress (while suction decreases). At day 752 the stress path intersects with the yield surface at a suction of 1.2 MPa and the onset of plastic deformation begins with dilation and strain-softening. At day 753 the suction value is now within the yield envelop and the deviatoric stress begins to increase again as mean effective stress now decreases. The stress point remains in elastic expansion (tension) while poregas pressure continues to increase as it migrates through the point.

The stress path near the front axial end is depicted in **Figure 35**(**b**). Similarly, with the EPD case, there stress point moves in elastic compression, and with very little change in stress-state as a result of little change in porepressures at this point.

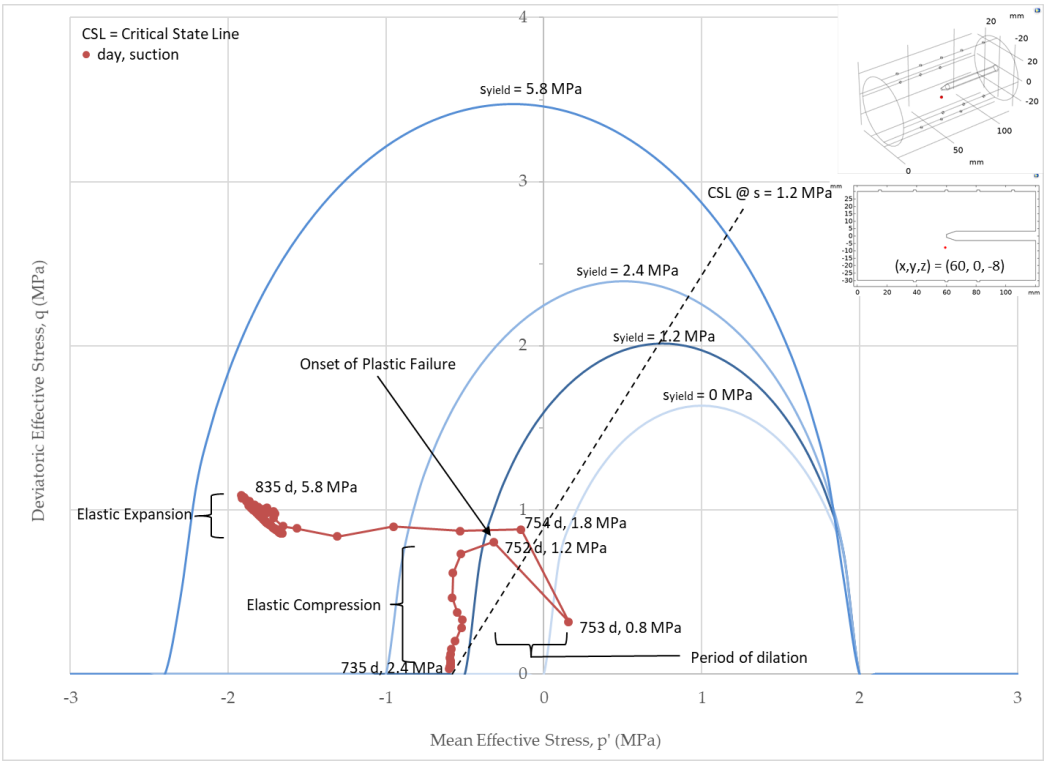

(a)

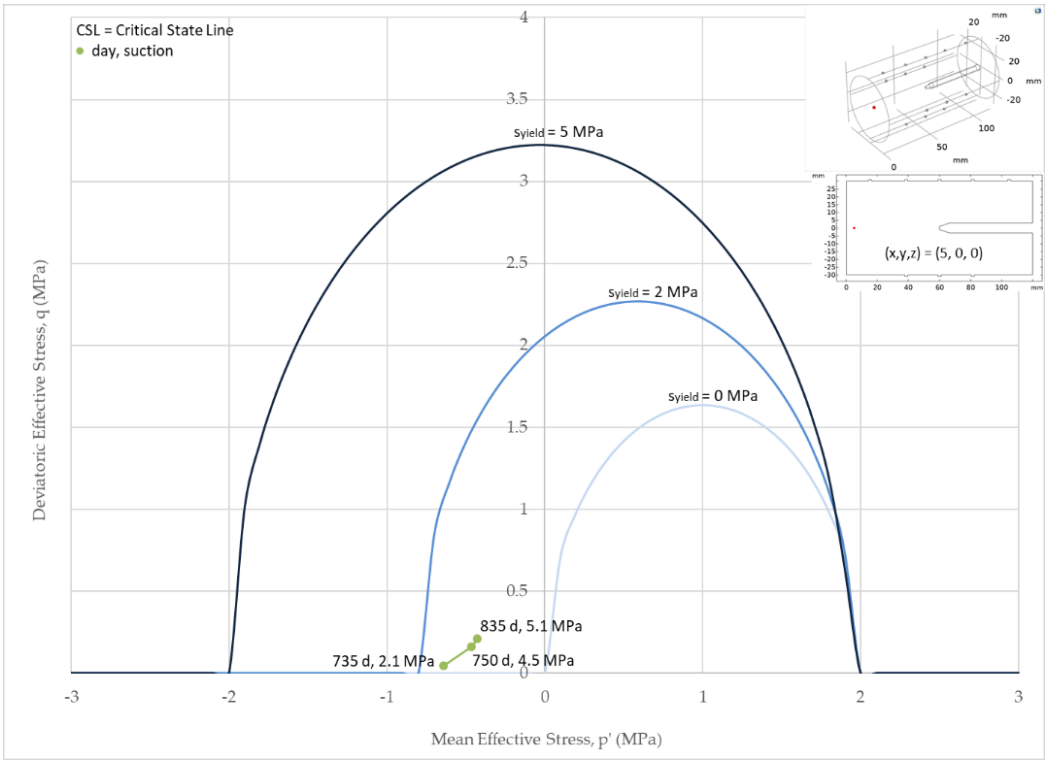

(b)

Figure 35. 3D Spherical Flow Case: NLPD Model – Stress path analysis (**a**) near central injection rod and (**b**) near front axial end of specimen

4.3. Model Improvements

A significant challenge of this work was presented by the large number of parameters required for calibration as evident by **Table 8**, **Table 9**, and **Table 10**. Due to a lack of geomechanical properties of the bentonite specimen obtained experimentally, model calibration, although informed by available values in literature, proved time consuming, particularly in ensuring the same calibration parameters could be consistently applied to both the 1D flow and 3D spherical flow case. During the calibration process, it was identified that only a few calibration parameters were key to generating gas flow, these included the AEV, the coefficient of the Klinkenberg effect, the strain at tensile strength and strain at compressive strength of the material which were used in ED Model, as well as the saturated consolidation pressure and corresponding void ratio necessary in order to characterize the compaction and swelling lines.

In future studies of multi-phase flow in highly compacted swelling geomaterials, key material properties are necessary and should be obtained as part of the experimental design. These include not only the standard elastic properties (i.e., Poisson's ratio, Young's Modulus), but also the tensile strength and compressive strength of the material as well as plastic properties of the soil. Measurement of the saturated consolidation pressure and corresponding void ratio as well as a reference pressure and corresponding void ratio at that reference pressure is necessary in order to characterize the compaction index and swelling index. A grain-size distribution would also help determine the level of heterogeneity within the specimen. Additionally, permeability tests to measure both intrinsic permeability of water and gas at several poregas pressures would also help provide much needed insight into the extent of the contribution of the Klinkenberg slip flow effect in swelling geomaterials such as bentonite.

Finally, when modelling the 3D spherical flow case, as the model initiated at time t = 735 days, some initial conditions were difficult to estimate, particularly that of the internal stresses and elastic deformations

presented within the sample. For this reason, when applying the plastic models, as there was little information of the evolution of the system before t = 735 days, a shift in the initial stresses had to be applied so that they fall within the yield envelope. For future modelling it is important to have well defined initial conditions for the experiment.

5. Conclusions

An important component in the design and long-term safety assessment of a DGR is the long-term performance of bentonite seals as barriers against gas migration. As gas generates from the degradation of organic waste and/or corrosion of metals, at some critical gas pressure, dilation of the bentonite could occur resulting in the creation of preferential flow pathways and a source of radionuclide exposure to people and the environment.

In an attempt to understand the physical mechanisms associated with dilation and two-phase flow, this study expands upon previous work by the authors [4, 73, 74] by assessing the influence of three different stress-strain constitutive models to simulate gas migration (two-phase flow) through low-permeability swelling soils. An ED model, an EPD model and a NLPD model were developed. For each of the models, validation studies were performed against experimental data from 1D flow and 3D-spherical flow tests through a saturated bentonite sample under a constant volume boundary stress condition. The experimental data demonstrated features of dilatancy-controlled gas flow. The modelled results were compared to key features of the experimental data, including the gas inflow and outflow behaviour, volume of gas stored within the specimen, and evolution of axial and radial stresses over the duration of the experiment. The extent of damage and influence on consolidation pressures were also examined.

Each of the models were also compared to one another to determine if one is more suitable for use in long-term safety assessments for supporting a safety case for a DGR. Overall, the ED model was capable of reproducing many of the general features exhibited by the experimental data for both the 1D and 3D spherical flow cases, with the NLPD model showing some promise.

Out of each of the models, the ED model was best able to reproduce the experimental results, being able to capture the gas inflow, total stress evolution, and volume of gas stored in the system over time reasonably well. The ED model was also able to reproduce the chaotic inflow behavior observed experimentally, a particular characteristic attributed to dilation of the clay and the creation of preferential flow pathways. Additionally, the ED model was also able to exhibit a self-sealing behavior characteristic of swelling soils. This was predominately associated with the method in which damage has been applied. Although outflow was observed, the time and magnitude of gas outflow did not match well with those measured by the experiment. This may have been associated with heterogeneity, and the orientation of the spatially applied random distribution of porosity in the model. Had a different random seed been applied, the modeled gas outflow profile may have better agreed with the experimental results. To test this, a probabilistic analysis should be conducted in a future study, whereby several models should be run using different randomly generated spatial orientations of heterogeneity (following the same normal distribution). This should result in a distribution of gas outflow profiles for which the experimental gas outflow may fall, and may support the validity of the model. Finally, the ED model was the simplest and most computationally robust model out of the three. This is attributed mainly to the use of an elastic model only with a simple method to introduce damage, and with fewer calibration parameters.

The EPD model did not perform well. It was not able to match any of the experimental results (i.e., gas inflow, gas outflow, stress evolution, volume of gas storage in system). This is due to the choice of a permeability function that results in lower increase in permeability associated with damage used in the EPD model, as compared to the ED model. The choice of this function is necessary in order to ensure convergence of the numerical solution.

In comparison, when introducing non-local plasticity, the NLPD model was able to obtain more favorable results and produce larger flows as a result of banding for the 1D-flow case, however the effect was not obtained when applied to the 3D spherical flow case. In comparison to the ED model, the NLPD model is the least robust. Since it applies a plastic model, the number of calibration parameters are nearly tripled in comparison to the ED model, and due to the additional parameterization, it is the most computational expensive. However, given its capability to generate large flow fields, the NLPD model is worth further investigation. The NLPD model demonstrates agreement with Critical State Theory and the conceptualization of two-phase flow which is being discussed in this paper. That is, an increase in pore-fluid pressure causes a reduction in effective stress resulting in dilation and extension of the clay particles, and the formation of preferential flow pathways and channeling.

The results also identified that in all the models, damage bands that represent areas of preferential flow do form. With respect to the EPD and NLPD models, however, due to convergence issues, the increase in permeability within those bands was a limiting factor. As a result, future studies should continue to investigate the ED and NLPD models, and consider the application of strain-localization and channeling in an attempt to simulate dilatancy-controlled gas flow. These studies should be conducted in conjunction with experiments that should consider visualization of the micro-structural changes of the bentonite, in addition to macroscopic output such as inflow, outflow, stress and pore pressure. Bentonite is characterized with different types of pore structures. Gas injection into a nearly-saturated bentonite can profoundly affect the relative frequency of the different pore types, and therefore the micro-structural changes associated with pore structure evolution need to be considered in the future.

CHAPTER 7: GENERAL DISCUSSION AND CONCLUSION

1. General Discussion

1.1. Numerical Challenges

A number of numerical challenges were encountered when implementing the mathematical models numerically in COMSOL® and are discussed here, along with any applied techniques to obtain a solution. The intent of this section is to enhance the current literature on using numerical methods, and particularly COMSOL® and the FEM to simulate two-phase flow in low-permeable swelling soils. The numerical modelling of gas migration in low permeable swelling soils poses many challenges, particularly with the coupling of the mechanical component to the hydraulic model. A number of numerical techniques were applied to obtain convergence in COMSOL®.

1.1.1. Discretization of Elements and Scaling

Regarding discretization of the elements, the use of cubic or higher order Lagrange shape functions were required over the default quadratic serendipity shape functions to solve the displacement field and flow equations in order to reach convergence. Lagrange shape functions allow for integration over internal nodes, which provides a more accurate solution, but with an added computational expense. A scaling function on the displacement field at the same order as the elastic strain (i.e., 0.001) was also applied and allowed for faster convergence to the solution. COMSOL® would sometimes apply this scaling function by default, which was necessary, in part, due to the small elastic strains which were observed by the models prior to gas injection.

1.1.2. Boundary Conditions

In each of the models, the experimental injection pressure and back pressure data were directly used as boundary conditions. Due to fluctuations in their measurement and to capture sharp increase in poregas pressure during gas injection, the use of strict BCs and forcing the Jacobian to be updated on each iteration was necessary. This resulted in higher computational effort, but a higher resolution solution with accurate implementation of the BCs. Additionally, some smoothing was required along the gas injection pressure and water backpressure boundary conditions during times when sharp pressure changes were experienced to obtain convergence.

1.1.3. Time Stepping and Mesh Size

COMSOL® allows the user to select an output time step. An output time step of 0.1 d was set in COMSOL® in order to capture the chaotic peak behavior which was observed by the experimental results. During the model runs, when a higher output time step of 1d was applied, the model results were not able to capture the full oscillations well as it resulted in too much smoothing of the numerical results. Output time steps of 0.01 d were also performed, and although the results provided even greater resolution of the chaos observed, in order to balance computational time and the resolution needed to capture main features of the experimental data, it was determined that an output time step of 0.1 d was adequate. Additionally, when modelling at a more refined mesh sizes, a smaller time step was required to reach convergence, as the reduction in time step helped stabilize periods of rapid changes in the model, typically related to rapid changes in the BCs and rapid changes in permeability due to damage. It should be noted that COMSOL® applies an effective time step smaller than, but based on the user defined time step.

Mesh size also played an important role in the numerical analysis. During the simulations, particularly of the 3D models, the application of too fine a mesh became computationally overly expensive, impractical for real application, and often proved difficult to converge. For this reason, there was often a balance of judgement when selecting mesh size and number of degrees of freedom to be solved.

1.1.4. Solver Techniques

Due to the highly coupled nature of multi-phase flow problems, in order for the numerical model simulations to converge, use of a Direct Fully Coupled solver was required. The author utilized both MUMPS and PARADISO which were available in COMSOL®, to determine if one would perform computationally faster than the other, and noted only slight differences in solution time and negligible difference in simulation results. Although use of Direct solvers is more computationally expensive, their application in this study proved most robust as most model runs could achieve convergence with their use, in comparison to when the authors attempted to use Iterative Segregated solvers.

1.1.5. Tolerance

For each model run, a user defined optimum relative tolerance had to be set in order to reach convergence. The selected relative tolerance had to be set low enough to minimize the relative error that could be generated by the numerical model, while simultaneously allowing for enough buffer to converge in areas with dynamic changes in poregas pressure.

1.1.6. Additional Techniques

When implementing the van Genuchten-Mualem model for the relative permeability relationships, the fitting parameter, L′, is recommended at an optimum value of 0.5 in literature [87], had to be set to 1 as COMSOL® had difficulties integrating exponential fractions. In order to evaluate the effect of this change, the authors assessed differences in the relative permeability curves between using a value of 0.5 and 1, as depicted in Figure 1 below. As can be shown, the influence was minimal and this was considered an acceptable solution.

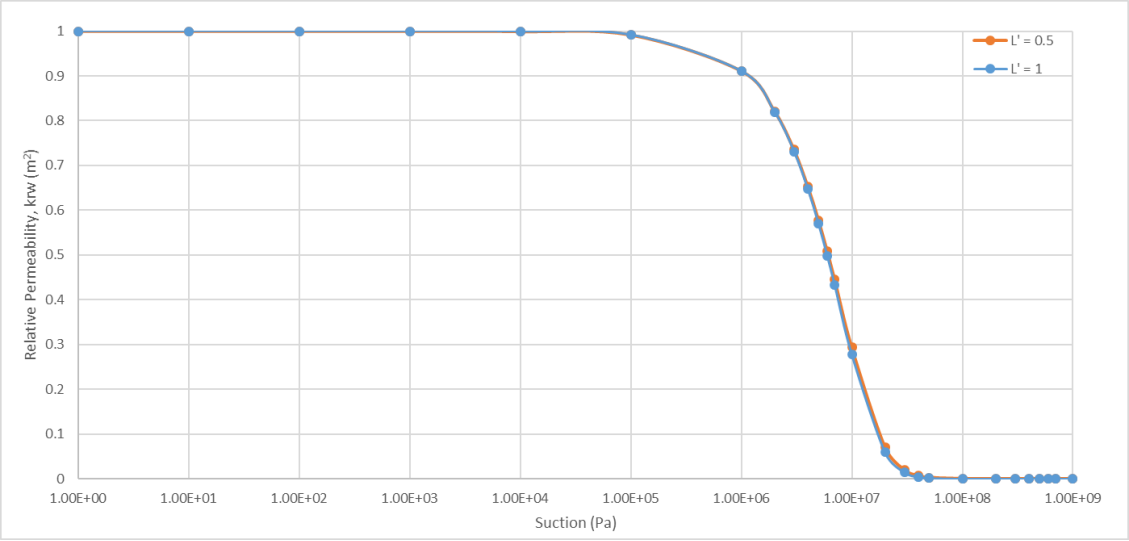

Figure 1. Relative permeability of water curves for two different, L′, fitting parameters

1.2. Heterogeneity and Probabilistic Analysis

At the onset of this study, the author anticipated that small material heterogeneities would exist in the highly compacted swelling geomaterial, even when under saturated conditions, and that these heterogeneities would contribute to the formation of preferential flow pathways and channeling. The impact of material heterogeneity on two-phase flow was assessed by applying statistical variability in soil porosity, which in turn effected local AEVs, SWCCs, and intrinsic permeabilities throughout the sample.

When plasticity was introduced, due to the relationship between initial reference void ratio and reference pressures, small heterogeneity was also introduced to the mechanical properties of the soil, including the initial consolidation pressure (Chapter 6).

In author's original study design, a final contribution of this work was to conduct a probabilistic analysis by running a number of models with different random normally distributed porosity distributions, creating different orientations of initial material heterogeneity. Conceptually it was assumed that this would result in simulations whereby the poregas would travel through the formation of different preferential flow pathways influenced by the degree of local heterogeneity of the hydraulic properties. In addition, this would allow for a statistical analysis of the distribution of inflow and outflow results obtained numerically, and would be followed by a comparison to the experimental results that were provided for the validation studies [59] [62] to see whether the experimental results would fall within the bounds of the statistical distribution.

A comparison of the influence of the extent of material heterogeneity provided in Chapter 5 and Chapter 6 (i.e., initial porosity distribution of 0.44 ± 0.06 vs 0.01, respectively) demonstrates that gas flow and fingering effects are greater when larger heterogeneities exist. However, both studies did not demonstrate the formation of discrete preferential flow pathways, particularly at small heterogeneities where the deviation around porosity was < 10%. For this reason, a probabilistic analysis through the application of different randomly distributed heterogeneity in the hydraulic properties of the specimen was not examined further.

It should be noted that the author also assessed the use of Fourier Transforms to generate random surfaces as an alternative mechanism to generate material heterogeneity. The generated random porosity was then applied to the material property of the soil in a similar technique that was applied to the statistical distribution approach. However, upon further consideration, it did not make physical sense, as variability in nature tends to follow normal or log-normal distributions, and it could be reasonably assumed that the particle size distribution of clays and corresponding pore-size distribution would also tend to follow a normal distribution. As a result, the use of random surfaces was not further considered.

1.3. Model Improvements

1.3.1. Heterogeneity Applied to Mechanical Properties

Through this work, it was identified that the approach applied to introducing material heterogeneity in this study did not provide the creation of distinct preferential flow pathways, but impacted the bulk gas flow. Future work will look at directly introducing material heterogeneity to several mechanical properties of the plastic model, including the coefficient of internal friction and the saturated consolidation pressure. It is anticipated that this model improvement will help to generate discrete preferential flow pathways. Use of the random surfaces using Fourier Transforms for this approach will also be revisited, along with a probabilistic analysis.

1.3.2. Consideration of the SWCC

As described in Chapter 2, the suction range for unsaturated bentonite clays can expand over the entire range of a classic SWCC and well exceed a suction of 10^6 kPa. The van Genuchten equation for the SWCCs was utilized in this study, and is a well-known for being numerically stable in most applications. However, it may not provide numerical stability when solved at even higher suction values for low-permeability swelling geomaterials. As a result, it may be more suitable to use the equation proposed by Fredlund & Xing [88], which can be modified to span over the entire expected suction range. The relationship between the volumetric water content and suction given by Fredlund & Xing can be expressed as,

$$\theta(\psi, a', n', m') = C(\psi)\frac{\theta_s}{\left\{\ln\left[e + \left(\frac{\psi}{a'}\right)^{n'}\right]\right\}^{m'}} \quad (11)$$

where similar to the van Genuchten equation, parameters a', n', and m' can be extracted from a graphical solution obtained by fitting a curve to experimental data or using the least-squares method [88]. The term $C(\psi)$ is a correction function which is defined as,

$$C(\psi) = 1 - \frac{\ln\left(1 + \frac{\psi}{\psi_r}\right)}{\ln\left(1 + \frac{1000000}{\psi_r}\right)} \quad (22)$$

where ψ_r is the suction corresponding to the residual water content, θ_r, and the value 1000000 is used ensure numerical stability when $\theta = 0$ [88]. The numerical value in the denominator can be adjusted accordingly based on the range of suction values.

Additionally, future studies should ensure that wetting and drying SWCCs have been derived and supported by experimental data for the specific bentonite to be modelled. This would help reduce uncertainties in the numerical model, associated with estimating the SWCC behaviour.

1.3.3. Consideration of Microstructure

In this thesis, a single porosity model has been considered. For sure the microstructure of the bentonite may have an influence on multi-phase. It is well known that expansive clays such as bentonites, with high montmorillonite content, have multiple pore-scales, including macro-pores, micro-pores, and nano-pores. The microstructure of the soils may influence multi-phase flow, and pore-scale effects should be considered in future models. For example, the SWCCs of such clays may be bi-modal or multi-modal, and as a result may have a significant effect on migration.

1.3.4. Consideration of Thermal Effects

For a DGR for used nuclear fuel, the waste will be heat generating. Therefore, a mathematical model that is suitable for measuring the deformation and migration of gas in the engineered buffer material near the source term, should consider thermal effects, which may influence material properties such as density of the porefluids and their viscosities, allow for some thermal expansion of the clay, and support desiccation of buffer.

1.3.5. Additional Approaches to Numerical Modelling

This thesis approached the problem of modelling two-phase flow using a continuum model simulated using the Finite Element Method. However, other modelling approaches, such as the Discrete Element Method (DEM) or the streamline numerical simulation method may be more suitable for this type of problem and should be further investigated.

2. Final Conclusions

The long-term management of radioactive waste is one of the most conscious problems facing our society today, and will continue to be so for generations to come. In a deep geological repository for the disposal of radioactive waste, the most critical component to ensuring long-term safety of people and the environment, over time frames that expand tens of thousands to hundreds of thousands of years, is by limiting radionuclide transport to every reasonable extent possible. DGRs are designed using a multiple barrier approach, with the use of an engineered barriers system designed and natural host rock selected to

provide this containment. One potential source of radionuclide exposure at the surface, could be from the migration of gases generated over these long periods, through engineered buffer, shaft seals, and host rock.

The compilation of works presented in this thesis offer a systematic and novel approach to understanding the processes involved in multi-phase flow. These works investigate the development of a highly coupled hydro-mechanical mathematical model to describe multi-phase flow (of gas and water) at critical gas pressures where the creation of microfractures and the formation of preferential flow pathways are expected to occur. The mathematical model was derived from the theoretical framework of poromechanics, incorporated Darcy's Law for both the porewater and poregas, and applied a modified Bishop's effective stress principle.

In the first contribution (Chapter 3), the author developed a fully-coupled, hydro-mechanical linear-elastic mathematical model for advective-diffusive visco-capillary controlled two-phase flow through a geomaterial in order to model the first two transport mechanisms proposed by Marschall et al. [5]. Results from a 1-dimensional flow constant volume boundary condition experiment was used to validate the model. A number of parametric studies were investigated to assess the contribution of advection of poregas, diffusion of dissolved gas in porewater, advection of dissolved gas in porewater, and inclusion of mechanical deformation (linear elasticity) on flow behaviour with increasing gas pressures over time. Additionally, sensitivity analyses were conducted to gain an understanding of the influence of a number of soil properties on flow behaviour, such as the effect of modifying the air-entry value (AEV), intrinsic permeability, and initial porosity of the soil specimen. Finally, the study investigated the use of an elastic damage model to better represent the experimental results.

Although the model results reproduced some of the general features noted in the experimental results, the model was not able to simulate dilatancy-controlled gas flow. The study concluded that in order to promote dilatancy-controlled gas flow additional mechanisms need to be considered within the model. The authors proposed that additional processes controlling hydraulic flow and more detailed analysis of the coupling between mechanical deformation and gas transport, were required to generate the magnitude of intrinsic permeability required to achieve the large gas flows observed experimentally. The authors also suggested that consideration of heterogeneity within the soil sample may help induce preferential flow and that the inclusion of a swelling stress term to incorporate the swelling and shrinking behaviour exhibited by expansive soils may also promote increased gas flow with increases in suction. Finally, the author proposed that future improvements to the model incorporate a self-healing mechanism in order to represent observed self-sealing behavior of bentonites.

In the second contribution of this work (Chapter 4), the author conducted a verification study of the mathematical model in order to ensure it was being implemented correctly numerically in the COMSOL® FEM software. Analytical solutions for a 1D steady-state gas flow and 1D transient gas flow problem were derived using the framework of poromechanics. Using FEM, the numerical model was used to simulate 1D flow through a confined cylindrical sample of near-saturated low-permeable soil under a constant volume boundary stress condition. Verification of the numerical model was performed by comparing the pore-gas pressure evolution and stress evolution to that of the results of the analytical solutions. For both the steady-state and transient problems, the poregas pressure, displacement, mean effective stress, deviatoric effective stress, and p'-q' stress path results obtained from the numerical model were also compared to those of the analytical solutions. For each parameter, the results of the numerical model closely matched those of the analytical solutions, providing added confidence that the proposed mathematical model is being correctly implemented in the COMSOL® FEM software.

In the third contribution (Chapter 5), the author investigated several of the processes identified in the previous contribution, which may be associated with dilation and two-phase flow in a swelling geomaterial. Through process simulation and analysis, the author assessed the effect of introducing material heterogeneity to the hydraulic properties of the soil, the Klinkenberg "slip flow" effect, and swelling and desiccation of the soil on flow behavior and the potential for the formation of gas fingers.

The analysis was performed by comparing results of a number of study scenarios against experimental data from a 1D flow test through a saturated bentonite sample under a constant volume boundary stress condition. The modelled results were compared to key features of the experimental data, including the gas inflow and outflow, volume of gas stored in the system, and evolution of total axial and radial stresses. Although the models were not able to reproduce dilation-controlled gas flow, substantial insight into the enhanced model features was obtained.

The results showed that heterogeneity in the hydraulic properties of the material may play a role in supporting the development of localization and preferential flow, however the introduction of heterogeneity alone was not enough to trigger preferential flow, and other advanced processes are required to generate preferential flow and exasperate dilation.

Introduction of the Klinkenberg "slip flow" effect significantly increased gas permeability and migration through the system. It also promoted the notable chaotic behavior in both gas inflow and outflow observed by the experimental results. However, key model features including sharp changes in inflow rate could not be achieved by the Klinkenberg effect. When coupled with heterogeneity, the model accurately simulated the total stresses evolution observed by the experimental results, a stark improvement from the author's previous work. However, the Klinkenberg "slip flow" effect, may not provide as much of a contribution to gas migration through preferential flow pathways, as the authors had initially hypothesized. When looking at the volume of gas stored in the system, the experimental results showed expected behavior of preferential flow whereby gas flowing into the sample follows discrete pathways resulting in nearly immediate gas outflow and little gas storage within the sample. The model results on the other hand, demonstrated a plug flow behavior, whereby saturation of the bentonite sample was observed. This suggests that although the Klinkenberg effect may play a role in two-phase flow, it cannot be used to explain the rapid increase in permeability and the formation of preferential flow pathways, as the effect tends to saturate the sample.

Introduction of a swelling strain played a minor role in the shape and timing of gas inflow, gas outflow, and volume of gas stored within the system. Though its presence did improve each of the results slightly, the author noted that investigation into the use of non-linear swelling, may provide better agreement with the experimental data.

With respect to the investigation into the formation of gas fingers, the modelling results were able to produce gas fingers. This was a result of differences in viscosities of each fluid (helium and water) considered within their own transport equations (Darcy's law), the inclusion of heterogeneity in pore size, and the selected mesh size. The results showed that the extent of gas fingering was strongly related to changes in permeability within the soil specimen. Additionally, when fingering was present, the size of the gas fingers was short and their formation short lived, likely as the effect of gravity, diffusion and suction hindered formation of long discrete fingers, as had been identified by previous studies on gas fingering [64]. The results of this work further supported the conclusions of the authors first study that other highly coupled HM mechanisms of mechanical deformation are required in order to generate dilatancy and more localized flow.

In light of this, in the fourth contribution of this study (Chapter 6), the author assessed the contribution of several types of stress-strain constitutive models on flow behavior. In their conceptual model, the author anticipated dilation to be coupled to plastic deformation and in particular strain softening of the soil, as described by Critical State Theory. In their conceptual model, the effects of combining damage to a non-linear poro-elastoplastic model and in considering non-local plasticity is of particular interest to complement the author's conceptual model linking dilation in unsaturated soils, under the presence of suction and reduced effective stress, to plastic deformation.

In order to test this theory the author conducted a detailed assessment of several different mechanisms of mechanical deformation with strong coupling between flow and stress state triggered by mechanical damage and plasticity. These included assessments of an elastic damage model with self-healing

behaviour, a local poro-elastoplastic model with damage, and a non-local poro-elastoplastic model with damage.

The models were validated against experimental data from a 1D flow test and a 3D spherical flow test, whereby as in the previous contributions, the modelled results were compared to the experimental gas inflow and outflow, volume of gas stored in the system, and evolution of total axial and radial stresses. A stress-path analysis was also conducted by the author to test their conceptualization of the onset of dilation.

The results of the fourth paper showed promise in the use of the elastic damage model in safety assessments for DGRs. The simulation results, particularly for the 3D spherical flow case, provided good agreement with the experimental inflow, stress evolution, and gas storage. The model was able to reproduce chaotic gas inflows that are characteristic of dilatancy-controlled gas flow, and exhibited self-sealing behavior. Although gas outflow was achieved, additional analysis and further improvements to the model are required. The use of a non-local plasticity model with damage also provided promising results, however additional work into its applicability in safety assessments is required.

Future studies will seek to further improve the elastic damage and non-local plastic model with damage. Finally, multiple model iterations of randomly introduced material heterogeneity will be assessed in an attempt to characterize, through a probabilistic assessment, the chaotic nature of the formation of dilation pathways.

In conclusion, the body of work presented in this thesis provides fundamental insight into processes which may be influencing multi-phase flow in swelling geomaterials. A mathematical model to describe the flow of gas and water in a low-permeability swelling geomaterial has been developed and shows promise for application in safety assessments for long-term disposal of radioactive waste, however several model improvements and additional validation analyses are required.

REFERENCES

[1] T. Nguyen and A. Le, "Simultaneous gas and water flow in a damage-susceptible bedded argillaceous rock," *Can. Geotech. J.,* no. 52, pp. 18-32, 2015.

[2] N. Khalili and M. H. Khabbaz, "A unique relatiship for χ for the determination of the shear strength of unsaturated soils," *Géotechnique,* vol. 48, no. 5, pp. 681-687, 1998.

[3] J. Crank, The Mathematics of Diffusion, Second Edition ed., Oxford: Clarendon Press, 1975.

[4] E. E. Dagher, T. S. Nguyen and J. A. Infante Sedano, "Development of a mathematical model for gas migration (two-phase flow) in natural and engineered barriers for radioactive waste disposal," in *Multiple Roles of Clays in Radioactive Waste Confinement*, S. Norris, E. Neeft and M. Van Geet, Eds., London, Geological Society, Special Publications, 2018.

[5] P. Marschall, S. Horseman and T. Gimmi, "Characterisation of Gas Transport Properties of the Opalinus Clay, a Potential Host Rock Formation for Radioactive Waste Disposal," *Oil and Gas Science and Technology - Rev. IFP,* vol. 60, no. 1, pp. 121-139, 2005.

[6] LLRWMO, Inventory of Radioactive Waste in Canada, Ottawa: Low-Level Radioactive Waste Management Office, 2012.

[7] CSA Group, "CSA N292.0-14, General principles for the management of radioactive waste and irradiated fuel," CSA Group, Mississauga, 2014.

[8] Canada Department of Justice, "Nuclear Safety and Control Act," 2000. [Online]. Available: http://laws-lois.justice.gc.ca/eng/acts/N-28.3/. [Accessed 03 09 2016].

[9] P. Sellin and O. X. Leupin, "The use of Clay as an Engineered Barrier in Radioactive-Waste Management - A Review," *Clays and Clay Minerals,* vol. 61, no. 6, pp. 477-498, 2013.

[10] Canada Department of Justice, "Nuclear Fuel Waste Act," 2002. [Online]. Available: http://laws-lois.justice.gc.ca/eng/annualstatutes/2002_23/FullText.html. [Accessed 03 September 2016].

[11] NWMO, "About Adaptive Phased Management," 2016. [Online]. Available: https://www.nwmo.ca/en/Canadas-Plan/About-Adaptive-Phased-Management-APM. [Accessed 3 September 2016].

[12] CNSC, "Regulating Canada's Geological Repositories," 2014. [Online]. Available: http://nuclearsafety.gc.ca/eng/resources/fact-sheets/regulating-canadas-geological-repositories-fact-sheet.cfm. [Accessed 03 September 2016].

[13] DECOVALEX, "DECOVALEX: DEvelopment of COupled models and their VALidation against EXperiments," 2016. [Online]. Available: http://www.decovalex.org. [Accessed 19 March 2016].

[14] CNSC, "Regulatory Guide G-320: Assessing the Long Term Safety of Radioactive Waste Management," Canadian Nuclear Safety Commission, Ottawa, 2006.

[15] IAEA, "IAEA Safety Standards - Specific Safety Guide No. SSG-23: The Safety Case and Safety Assessment for the Disposal of Radioactive Waste," International Atomic Energy Agency, Vienna, 2012.

[16] J. Rutqvist, "Coupled Thermo-Hydro-Mechanical Behavior of Natural and Clay Barriers," in *Developments in Clay Science - Volume 6: Natural and Engineered Clay Barriers*, C. Tournassat, C. I. Steefel, C. I. Bourg and F. Bergaya, Eds., Amsterdam, Elsevier Ltd., 2015, pp. 329-355.

[17] CNSC, "Regulatory Guide G-320, Assessing the Long Term Safety of Radioactive Waste Management," Ottawa, 2006.

[18] S. Norris, "EC FORGE project: updated consideration of gas generation and migration in the safety case," in *Gas Generation and Migration in Deep Geological Radioactive Waste Repositories*, R. P. Shaw, Ed., Geological Society, London, Special Publications, 415, 2015.

[19] R. P. Shaw, Ed., Gas Generation and Migration in Deep Geological Radioactive Waste Repositories, Geological Society, London, Special Publications, 415, 2015.

[20] R. Cuss, J. Harrington, R. Giot and C. Auvray, "Experimental observations of mechanical dilation at the onset of gas flow in Callovo-Oxfordian claystone," in *Clays in Natural and Engineered Barriers for Radioactive Waste Confinement*, vol. 400, S. Norris, J. Bruno, M. Cathelineau, P. Delage, C. Fairhurst, E. C. Gaucher, E. H. Hohn, A. Kalinichev, P. Lalieux and P. Sellin, Eds., London, Geological Society, 2014, pp. 507-519.

[21] E. Ahusborde, B. Amaziane and M. Jurak, "Three-dimensional numerical simulation by upscaling of gas migration through engineered and geological barriers for a deep repository for radioactive waste," in *Gas Generation and Migration in Deep Geological Radioactive Waste Repositories*, R. P. Shaw, Ed., Geological Society, London, Special Publication, 415, 2015, pp. 123-141.

[22] S. T. Horseman, J. F. Harrington and P. Sellin, "Gas migration in clay barriers," *Engineering Geology,* vol. 54, pp. 139-149, 1999.

[23] P. Sellin, Ed., Experiments and Modelling on the behaviour of EBS. FORGE Reprot D3.38, 2014.

[24] R. P. Shaw, "The Fate of Repository Gases (FORGE) project," in *Gas Generation and Migration in Deep Geological Radioactive Waste Repositories*, R. P. Shaw, Ed., Geological Society, London, Special Publications, 415, 2015, pp. 1-7.

[25] J. F. Harrington and S. T. Horseman, "Gas transport properties of clays and mudrocks," in *Muds and Mudstones: Physical and Fluid Flow Properties*, A. C. Aplin, A. J. Fleet and J. H. MacQuaker, Eds., London, The Geological Society of London, 1999, pp. (Vol 158) 107-124.

[26] S. T. Horseman, J. F. Harrington and P. Sellin, "Water and Gas Movement in Mx80 Bentonite Buffer Clay," *Symposium on the Scientific Basis for Nuclear Waste Management XXVII (Kalmar), Materials and Research Society,* vol. 807, pp. 715-720, 2003.

[27] J. F. Harrington, R. de la Vaissiére, D. J. Noy, R. J. Cuss and J. Talandier, "Gas flow in Callovo-Oxfordian claystone (COx): results from laboratory and field-scale measurements," *Mineralogical Magazine,* vol. 76, no. 8, pp. 3303-3318, 2012.

[28] C. C. Graham, J. F. Harrington, R. J. Cuss and P. Sellin, "Gas migration experiments in bentonite: implications for numerical modelling," *Mineralogical Magazine,* vol. 76, no. 8, pp. 3279-3292, 2012.

[29] D. P. Bennett, R. J. Cuss, P. J. Vardon, J. F. Harrington, M. Sedighi and H. R. Thomas, "Exploratory data analysis of the Large Scale Gas Injection Test (Lasgit) dataset, focusing on'second-order' events

around macro-scale gas flows," in *Gas Generation and Migration in Deep Geological Radioactive Waste Repositories*, R. P. Shaw, Ed., Geological Society, London, Special Publications, 415, 2015, pp. 225-239.

[30] R. O. Davis and A. P. Selvadurai, Plasticity and Geomechanics, Cambridge: Cambridge University Press, 2002.

[31] M. Sahimi, M. R. Rasaei and M. Haghighi, "Gas Injection and Fingering in Porous Media," in *Theory and Applications of Transport in Porous Media Volume 20: Gas Transport in Porous Media*, C. K. Ho and S. W. Webb, Eds., Dorderecht, Springer, 2006, pp. 133-168.

[32] W. R. Rodwell, A. W. Harris, S. T. Horseman, P. Lalieux, W. Muller, L. Ortiz Amaya and K. Pruess, "Gas Migration and Two-Phase Flow through Engineered and Geological Barriers for a Deep Repository for Radioactive Waste - A Joint EC/NEA Status Report," EC/NEA, 1999.

[33] P. J. Nash, B. T. Swift, M. Goodfield and W. R. Rodwell, "Modelling Gas Migration in Compacted Bentonite: A report produced for the GAMBIT Club," POSIVA, Helsinki, 1998.

[34] A. R. Hoch, K. A. Cliffe, B. T. Swift and W. R. Rodwell, "Modelling Gas Migrationin Compacted Bentonite: GAMBIT Club Phase 3 Final Report," POSIVA, Olkiluoto, Finland, 2004.

[35] M. Fall, O. Nasir and T. Nguyen, "A coupled hydro-mechanical model for simulation of gas migration in host sedimentary rocks for nuclear waste repositories," *Engineering Geology,* vol. 176, pp. 24-44, 2014.

[36] C. A. Davy, F. Skoczylas, P. Lebon and T. Dubois, "Gas migration properties through a bentonite/argillite interface," *Applied Clay Sciences,* vol. 42, pp. 639-648, 2009.

[37] S. Tripathy, M. Y. Tadza and H. R. Thomas, "Soil-water characteristic curves of clays," *Canadian Geotechnical Journal,* vol. 51, pp. 869-883, 2014.

[38] R. Pusch, "Use of Bentonite for Isolation of Radioactive Waste Products," *Clay Minerals,* vol. 27, pp. 353-361, 1992.

[39] M. V. Villar and A. Lloret, "Influence of dry density and water content on the swelling of a compacted bentonite," *Applied Clay Science,* vol. 39, pp. 38-49, 2008.

[40] A. Itälä, "Chemical Evolution of Bentonite Buffer in a Final Repository of Spent Nuclear Fuel during the Thermal Phase," *VTT Publications 721,* 2009.

[41] S. L. Barbour, "Nineteenth Canadian Geotechnical Colloquium: The soil-water characteristic curve: a historical perspective," *Canadian Geotechnical Journal,* vol. 35, no. 5, pp. 873-894, 1998.

[42] L. Börgesson, M. Chijimatsu, T. Fujita, T. S. Nguyen, J. Rutqvist and L. Jing, "Thermo-hydro-mechanical characterisation of a bentonite-based buffer material by laboratory tests and numerical back analyses," *International Journal of Rock Mechanics and Sciences,* vol. 38, pp. 95-104, 2001.

[43] D. G. Fredlund, "Unsaturated soil mechanics in engineering practice," *Journal of Geotechnical and Geoenvironmental Engineering,* vol. 132, no. 3, pp. 286-321, 2006.

[44] W. M. Ye, M. Wan, B. Chen, Y. G. Chen, Y. J. Cui and J. Wang, "Temperature effects on the unsaturated permeability of the densely compacted GMZ01 bentonite under confined conditions," *Engineering Geology,* vol. 126, pp. 1-7, 2011.

[45] M. Villar, "MX-80 Bentonite: Thermo-Hydro-Mechanical Characterisation Perfomred at CIEMAT in the Context of the PRototype Project," 2004.

[46] D. W. Oscarson, D. A. Dixon and H. B. Hume, "Mass transport through defected bentonite plugs," *Applied Clay Science,* vol. 11, pp. 127-124, 1996.

[47] F. T. Madsen, "Clay mineralogical investigations related to nuclear waste disposal," *Clay Minerals,* vol. 33, pp. 109-129, 1998.

[48] K. Pedersen, M. Motamedi, O. Karnland and T. Sandén, "Mixing and sulphate-reducing activity of bacteria in swelling, compacted bentonite clay under high-level radioactive waste repository conditions," *Journal of Applied Microbiology,* vol. 89, no. 6, pp. 1038-1047, 2000.

[49] A. Seiphoori, A. Ferrari and L. Laloui, "Characterization of THM Behaviour of Compacted MX-80 Granular Bentonite Using Double-wall Triaxial Cell," in *International EAGE Workshop on Geomechanics and Energy*, Lausanne, 2013.

[50] Grimsel Test Site (Switzerland), "Full-Scale Engineered Barriers Experiment (FEBEX)," Grimsel Test Site (Switzerland), 2020. [Online]. Available: https://www.grimsel.com/gts-phase-v/febex/febex-i-introduction-. [Accessed 11 04 2020].

[51] Low-Level Radioactive Waste Management Office, Inventory of Radioactive Waste in Canada, Ottawa: Low-Level Radioactive Waste Management Office, 2012.

[52] M. T. van Genuchten, "A Closed-form Equation for Predicting the Hydraulic Conductivity of Unsaturated Soils," *Sol Science Society of America Journal,* vol. 44, pp. 892-898, 1980.

[53] S. Huang, S. L. Barbour and D. G. Fredlund, "Development and verification of a coefficient of permeability function for a deformable unsaturated soil," *Candian Geotechnical Journal,* vol. 35, pp. 411-425, 1998.

[54] G. E. Laliberte, A. T. Corey and R. H. Brooks, Properties of Unsaturated Porous Media, Hydrology Paper No. 17, Fort Collins, CO: Colorado State University, 1966.

[55] P. C. Carman, Flow of Gases Through Porous Media, New York: Academic Press Inc., 1956.

[56] F. J. Valdes-Parada, J. A. Ochoa-Tapia and J. Alvarez-Ramirez, "Validity of the permeability Carman-Kozeny equation: A volume averaging approach," *Physica A,* vol. 388, pp. 789-798, 2009.

[57] R. Pall and N. N. Moshenin, "Permeability of Porous Media as a Function of Porosity and Particle Size Distribution," *TRANSACTIONS of the ASAE,* pp. 742-745, 1980.

[58] C. K. Ho and S. W. Webb, Eds., Gas Transport in Porous Media, Dordrecht: Springer, 2006.

[59] C. A. Tang, L. G. Tham, P. Lee, T. H. Yang and L. C. Li, "Coupled analysis of flow, stress and damage (FSD) in rock failure," *International Journal of Rock Mechanics & Mining Sciences,* vol. 39, pp. 477-489, 2002.

[60] K. A. Daniels and J. F. Harrington, "The response of compact bentonite during a 1D gas flow test, British Geological Survey Open Report, OR/17/067," British Geological Survey, 2017.

[61] M. Villar, "MX-80 Bentonite: Thermo-Hydro-Mechanical Characterisation Performed at CIEMAT in the Context of the Prototype Project," 2004.

[62] A. Man and J. B. Martino, "NWMO TR-2009-20: Thermal, Hydraulic and Mechanical Properties of Sealing Materials," Atomic Energy of Canada Limited, Ottawa, 2009.

[63] J. F. Harrington, C. C. Graham, R. J. Cuss and S. Norris, "Gas network development in a precompacted bentonite experiment: Evidence of generation and evolution," *Applied Clay Science,* vol. 147, pp. 80-89, 2017.

[64] M. Blunt and M. Christie, "How to Predict Viscous Fingering in Three Component Flow," *Transport in Porous Media,* vol. 12, pp. 207-236, 1993.

[65] J. Moortgat, "Viscous and Gravitational Fingering in Multiphase Compositional and Compressible Flow," *Advances in Water Resources,* vol. 89, pp. 53-66, 2016.

[66] E. E. Dagher, J. A. Infante Sedano and T. S. Nguyen, "A Mathematical Model of Gas and Water Flow in a Swelling Geomaterial - Part 1 - Verification with Analytical Solution," *Minerals (2020),* vol. 10, no. 1, p. 30, 2019a.

[67] C. A. Wibberley, "Hydraulic diffusivity of fault gouge zones and implications for thermal pressurization during seismic slip," *Earth, Planets and Space,* vol. 54, pp. 1153-1171, 2002.

[68] H. Noda and T. Shimamoto, "Thermal pressurization and slip-weakening distance of a fault; an example of Hanoare Fault, southwest Japan," *Bulletin of the Seismological Society of America,* vol. 95, pp. 1224-1233, 2005.

[69] C. A. Wibberley and T. Shimamoto, "Earthquake slip weakening and asperities explained by thermal pressurization," *Nature,* vol. 436, pp. 689-692, 2005.

[70] L. J. Klinkenberg, "The permeability of Porous media to liquids and gases," *American Petroleum Institute, Drilling and Productions Practices,* pp. 200-213, 1941.

[71] O. Nasir, T. S. Nguyen, J. D. Barnichon and A. Millard, "Simulation of hydromechanical behaviour of benotointe seals for containment of radioactive wastes," *Canadian Geotechnical Journal,* vol. 54, pp. 1055-1070, 2017.

[72] F. O. Jones and W. W. Owens, "A laboratory study of low permeaability gas sands," *Journal of Petroleum Technology,* vol. 32, no. 09, pp. 1631-1640, 1980.

[73] W. C. Zhu, J. Liu, J. C. Sheng and D. Elsworth, "Analysis of coupled gas flow and deformation process with desorption and Klinkenberg effects in coal seams," *International Journal of Rock Mechanics & Mining Sciences,* vol. 44, pp. 971-980, 2007.

[74] E. E. Dagher, J. A. Infante Sedano and T. S. Nguyen, "A Mathematical Model of Gas and Water Flow in a Swelling Geomaterial - Part 1 - Verification with Analytical Solution," *Minerals (2020),* vol. 10, no. 1, p. 30, 2020a.

[75] E. E. Dagher, J. A. Infante Sedano and T. S. Nguyen, "A Mathematical Model of Gas and Water Flow in a Swelling Geomaterial - Part 2 - Process Simulation," *Minerals (2020),* vol. 10, no. 1, p. 32, 2020b.

[76] T. S. Nguyen and J. D. Barnichon, "Calibration of the hydro-mechanical properties of bentonite seals from laboratory characterization tests - Task A0 of DECOVALEX-2015," Canadian Nuclear Safety Commission, 2012.

[77] A. Lloret and E. E. Alonso, "State surfaces for partially saturated soils," in *Proceedings of the 11th International Conference on Soil Mechanics and Foundation Engineering*, Balkema, 1985.

[78] K. H. Roscoe and J. B. Burland, "On the generalized stress-strain behaviour of the 'wet' clay," in *Engineering Plasticity*, J. Heyman and F. A. Leckie, Eds., Cambridge, Cambridge University Press, 1968, pp. 535-609.

[79] E. E. Alonso, A. Gens and A. Josa, "A constitutive model for partially saturated soils," *Geotechnique,* vol. 40, no. 3, pp. 405-430, 1990.

[80] D. M. Pedroso and M. M. Farias, "Extended Barcelona Basic Model for unsaturated soils under cyclic loadings," *Computers and Geomechanics,* vol. 38, pp. 731-740, 2011.

[81] J. H. Argyris, G. Faust, J. Szimmat and K. Willam, "Recent developments in the finite element analysis of prestressed reactor vessels," *Nuclear Engineering and Design,* vol. 28, pp. 42-75, 1974.

[82] D. Sheng, S. W. Sloan and H. S. Yu, "Aspects of finite element implementation of critical state models," *Computational Mechanics,* vol. 26, no. 2, pp. 185-196, 2000.

[83] E. E. Alonso, E. Romero and C. Hoffmann, "Hydromechanical behaviour of compacted granular expansive mixtures: experimental and constitutive study," *Géotechnique,* vol. 61, no. 4, pp. 329-344, 2011.

[84] T. S. Nguyen, Z. Li, G. Su, M. B. Nasseri and R. P. Young, "Hydro-mechanical behavior of an argillaceous limestone considered as a potential host formation for radioactive waste disposal," *Journal of Rock Mechanics and Geotechnical Engineering,* vol. 10, pp. 1063-1081, 2018.

[85] M. Jirásek, "Objective Modeling of strain localization," *Revue française de génie civil,* vol. 6, no. 6, pp. 1119-1132, 2002.

[86] M. A. Mánica, A. Gens, J. Vaunat and D. F. Ruiz, "Analysis of strain localization with a nonlocal plasticity model," in *XIV International Conference on Computational Plasticity. Fundamentals and Applications*, Barcelona, 2017.

[87] S. W. Van Sciver, Helium Cryogenics, International Cryogenics Monograph Series, Springer Science+Business Media, 2012.

[88] E. E. Dagher, J. A. Infante Sedano and T. S. Nguyen, "A Mathematical Model of Gas and Water Flow in a Swelling Geomaterial - Part 2 - Process Simulation," *Minerals (2020),* vol. 10, no. 1, p. 32, 2020b.

[89] D. G. Fredlund, A. Xing and S. Huang, "Predicting the permeability function for unsaturated soils using the soil water characteristic curve," *Canadian Geotechnical Journal,* vol. 31, pp. 533-546, 1994.

[90] D. G. Fredlund and A. Xing, "Equations for the soil-waer characteristic curve," *Canadian Geotechnical Journal,* vol. 31, no. 4, pp. 521-532, 1994.